Polariton Propagation and Coherent Many-Particle Effects in Semiconductor Heterostructures

Stefan Schumacher

Institute for Theoretical Physics

University of Bremen

2005

Polariton Propagation and Coherent Many-Particle Effects in Semiconductor Heterostructures

Vom Fachbereich für Physik und Elektrotechnik

der Universität Bremen

zur Erlangung des akademischen Grades

Doktor der Naturwissenschaften (Dr. rer. nat.)

genehmigte Dissertation

von

Dipl. Phys. Stefan Schumacher

aus Bremen

1. Gutachter:	Prof. Dr. rer. nat. G. Czycholl
2. Gutachter:	Prof. Dr. rer. nat. F. Jahnke

Eingereicht am:	18.01.2005
Tag des Promotionskolloquiums:	24.02.2005

Abstract

Within the last few decades, semiconductor optics has attracted considerable attention due to its many applications ranging from semiconductor lasers to single photon emitting devices. The proper theoretical description of a propagating light field which is coupled to the excitonic resonances of the semiconductor material has been a longstanding problem. It is complicated by the presence of surfaces and interfaces in semiconductor heterostructures which prevents an analytical solution of the resulting polariton problem. A microscopic formulation of the coupled light and matter dynamics is required that includes the influence of sample boundaries on the electronic system as well as on the optical fields.

In a regime where the optical transmission and reflection spectra are strongly influenced by propagation effects, a theoretical description of the polariton problem is formulated. A direct solution of the non-local excitonic dynamics together with Maxwell's equations yields a microscopic description of propagating light fields in heterostructures with a finite spatial extension. A new approach is developed in this work, in order to reduce the effort of the numerically very demanding problem. The evaluation is done in terms of exciton eigenstates which are directly determined for the confinement geometry. Finite-height confinement potentials for the electron and hole motion as well as Fabry-Perot effects for the optical fields are included in the microscopic description.

Theoretical results are discussed in detail for the linear optical regime and a direct theory-experiment comparison is presented. Optical transmission spectra are analyzed for a series of high quality ZnSe/ZnSSe heterostructures with different thicknesses of the ZnSe layers. The theoretical results are in excellent agreement with the measurements, giving a deeper understanding of polariton propagation in shallow-confinement heterostructures.

To achieve the microscopic description of propagation effects in the nonlinear optical regime the dynamics-controlled truncation formalism is applied. The complicated interplay of propagation effects and optically induced many-particle correlations is analyzed for the samples. In contrast to the linear optical regime, biexcitonic correlations yield a strong coupling of different polariton resonances. This is demonstrated for a typical pump and probe setup and in a four wave mixing geometry. In order to confirm the important observations, nonlinear transmission experiments have been initiated and performed. Excellent agreement with the theoretical results has been achieved.

Contents

General Introduction and Motivation

Recent progress in semiconductor growth technology has made heterostructures and nanotechnology more and more accessible for a wide variety of applications in computer and telecommunication technology. In particular, semiconductor optics has attracted considerable attention due to its many applications ranging from semiconductor lasers[1] to single photon emitting devices[2] as well as for the characterization of semiconductor structures. From a more fundamental point of view, semiconductor optics is an appropriate technique to gain a better understanding of physical processes underlying the intrinsic properties of semiconductor structures and materials. One of the fundamental problems of semiconductor optics is the propagation of light through a sample with surfaces. In the linear optical regime, for propagation near the band-gap energy, a microscopic theoretical description has only recently been formulated[3,4] and applied[5,6] to a realistic semiconductor heterostructure. The present work will address this problem and extend the discussion to the nonlinear optical regime. Polariton effects arising from the interplay of the interband polarization of a semiconductor material and propagating light fields are studied. A more detailed discussion of the polariton problem is given on page 25.

This work is divided into two parts and it is organized as follows: The first part is dedicated to the linear optical regime. Polariton spectra are investigated within a microscopic theory and a phenomenological model based on additional boundary conditions. A detailed comparison with a series of experimental transmission spectra for ZnSe/ZnSSe heterostructures is given. In the second part of this work an extension of the microscopic theory to the nonlinear optical regime is presented. The interplay of propagation effects and optically induced many-particle correlations is analyzed under the influence of sample boundaries. Excitonic and biexcitonic nonlinearities are treated within the dynamics-controlled truncation formalism.[7–9] The extension of the microscopic theory to the nonlinear regime allows for the analysis of optical experiments on ultra short time scales, where, in particular, the interplay of polariton effects and biexcitonic correlations is investigated for different optical setups.

Most of the direct band-gap semiconductor materials exhibit a strong dipole coupling of the electronic system to an external optical field in the spectral range of the fundamental band-gap energy. For the analysis of their optical properties it is important to use a proper description of the coupled light-matter system. For weak external fields in the linear optical regime interband polarizations can be analyzed in terms of excitonic processes. However, due to the dipole coupling of semiconductor material and light, excitonic polarizations excited by an incoming external light field can decay radiatively, which yields a change of the external light field itself. Therefore, photons and excitons are coupled to each other.

Since perturbation approaches are not appropriate for a theoretical description of strong coupling, it is convenient to introduce a new quasi-particle, the polariton. It corresponds to the common eigenstates of the coupled light and exciton system and has originally been introduced by Hopfield in 1958.[10] Momentum conservation in an idealized bulk semiconductor allows the analytical diagonalization of the coupled light-matter Hamiltonian which yields the well-known polariton dispersion.[11] It describes the modes of light propagation in the vicinity of excitonic resonances for the considered semiconductor material. Although being important for a fundamental understanding of polariton effects, this analytical solution is not applicable to semiconductor structures with a finite spatial extension because of the missing translation invariance and the consequently missing momentum conservation for the exciton center of mass motion.

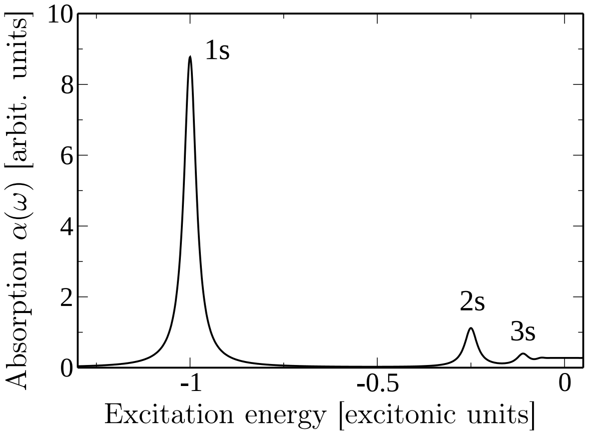

Figure 1: Calculated excitonic absorption $\alpha(\omega)$ for an idealized bulk material. The excitation energy is normalized to the bulk exciton binding energy and measured relative to the bulk band-gap energy.

Figure 1 shows the Hydrogen-like excitonic absorption spectrum of an idealized bulk semiconductor material with homogeneously broadened exciton resonances. Figure 2 shows typical experimental transmission spectra for ZnSe semiconductor layers with thicknesses of 20 nm, 28 nm, and 40 nm, respectively. The resonances in the optical spectra correspond to the structure of the polaritonic spectrum for light propagation through the samples. In comparison with the bulk exciton spectrum in Fig. 1, the experimental results clearly reveal a more complicated structure. The resonances between 2.805 eV and 2.82 eV on the horizontal axis can be attributed to heavy-hole (hh) exciton transitions and are labeled with consecutive numbers. The transmission spectra in Fig. 2 strongly depend on the layer thickness due to the quantum mechanical confinement of the carriers in the semiconductor layer. Although similar findings have been reported earlier for a variety of semiconductor materials,[12–17] the proper theoretical description has been a longstanding problem. Complications arise from the inclusion of sample surfaces where an external light field is coupled to the polariton modes and where the polaritons radiatively decay into photons. In the past, macroscopic approaches have been introduced, which rely on using the excitonic susceptibility of the spatially homogeneous (infinitely extended) medium. In this case the inclusion of sample surfaces requires so-called additional boundary conditions (ABCs). Nevertheless, depending on the material system, the interpretation of polariton spectra in terms of phenomenological models yields unsatisfactory results and necessitates the use of more or less unrealistic material parameters. A first theoretical description on a microscopic level has only recently been formulated and applied to a GaAs layer in Refs. 5, 6.

In this work, semiconductor heterostructures in a slab geometry are investigated, which contain interfaces as well as surfaces. They are suitable to investigate typical experimental setups for transmission or reflection measurements. Chapters 1 and 2 are devoted to a fundamental theoretical description of electronic and optical properties of the investigated semiconductor structures.

Part I, *Linear Polariton Propagation*, starts with an introduction and outline on page 25, followed by the microscopic description of excitons and polaritons in a semiconductor layer with finite thickness in Chapter 3. In Section 3.5 the application of the commonly used macroscopic model for polariton propagation based on Pekar's additional boundary conditions is outlined. In Chapter 4 results of the linear polariton propagation are discussed. In particular, a detailed comparison of polariton spectra obtained from the microscopic theory and the macroscopic approach is given in Section 4.1. The results allow an insight into the differences of both models and reveal some fundamental shortcomings of the macroscopic model that restrict its applicability. In Section 4.2, a direct comparison of theoretical and experimental polariton spectra is given for a series of ZnSe/ZnSSe heterostructures with different ZnSe layer thicknesses. In particular, the investigation of realistic heterostructures makes it necessary to extend the microscopic theory by including finite-height confinement potentials for the carrier motion as well as Fabry-Perot effects for the optical field.

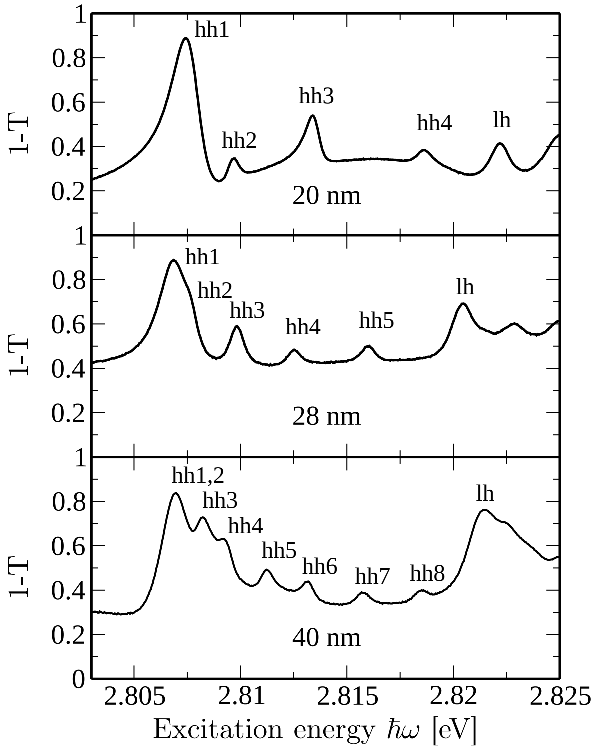

Figure 2: Experimental transmission spectra for a series of high quality ZnSe layers with thicknesses of 20 nm, 28 nm, and 40 nm. For details concerning samples and experiment see Section 4.2.

Part II, *Nonlinear Optics*, starts with an introduction and outline on page 67. In Chapter 5 the microscopic theory for polariton propagation is extended to the nonlinear optical regime. By use of the dynamics-controlled truncation approach, a consistent microscopic formulation is achieved. In particular, it incorporates propagation effects and coherent optical nonlinearities which are both strongly affected by the sample boundaries of the semiconductor heterostructure. The chapter concludes with a detailed discussion of fundamental theoretical results concerning the spectral properties of excitons and biexcitons in the confinement geometry. In Chapter 6 the theory is then applied to nonlinear pulse propagation and to typical optical setups in pump and probe as well as in four wave mixing geometry. A direct theory-experiment comparison is presented for the example of a 20 nm ZnSe layer. Results are summarized and discussed in Chapter 7.

1. Semiconductor Heterostructures

In order to analyze the optical properties of a semiconductor material an appropriate description of the electronic bandstructure is required. Figure 1.1 shows typical electronic bandstructures $\varepsilon_n(\mathbf{k})$ for II-VI and III-V bulk materials with zincblende structure. Examples are shown for ZnSe (left) and GaAs (right) along selected symmetry axes of the first Brillouin zone. The unit cell of the zincblende crystal structure is identical to that of a fcc (face-centered-cubic) crystal lattice, but with an atomic basis which consists of two atoms at the lattice points. As we are interested in optical properties around the fundamental band-gap energy the theory can be restricted to the two energetically highest valence bands ($E < 0$) and the lowest conduction band ($E > 0$), see Fig. 1.1. All interband transitions involving other bands are spectrally well separated from the fundamental band-gap energy and can therefore be neglected here. Due to the small momenta of photons in the investigated spectral window compared to typical electronic momenta $\mathbf{k}$, optically induced electronic transitions from a valence band to the conduction band occur nearly vertical in the considered direct band-gap materials. Henceforth, only a small part of the electronic dispersion near the zone center (Γ-point, $\mathbf{k} = 0$) yields a relevant contribution to the optically excited interband transitions under investigation.

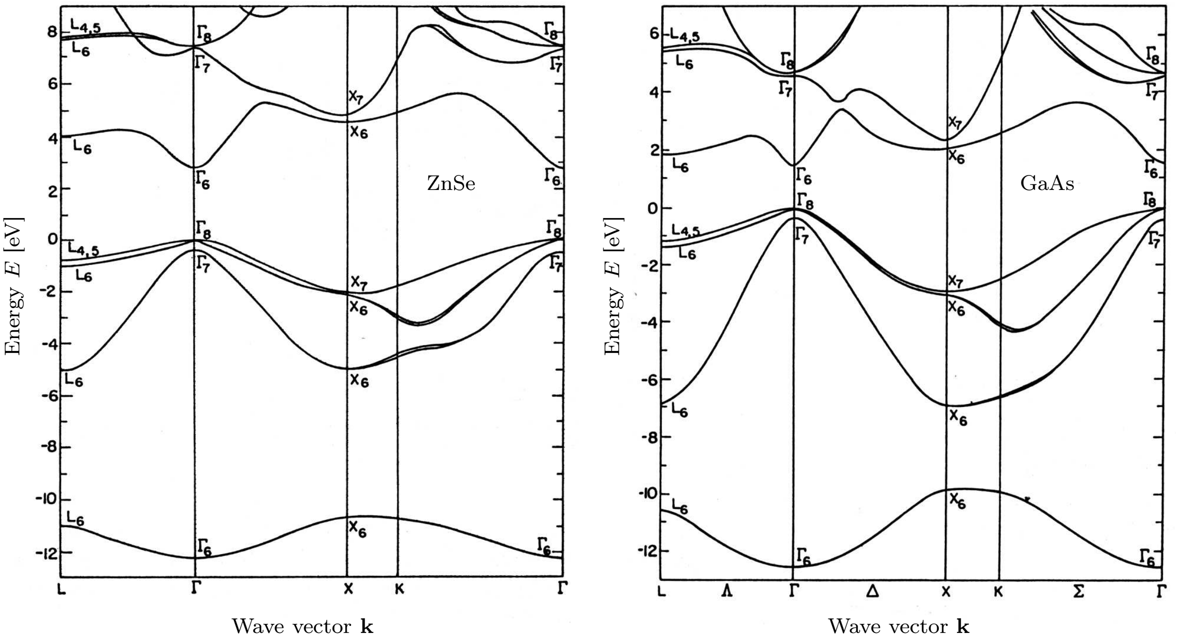

Figure 1.1: Bandstructure of bulk ZnSe (left) and GaAs (right) along selected symmetry axes of the first Brillouin zone. Figures are taken from Ref. 18.

To simplify things further the electronic dispersion around the Γ-point is replaced by a parabolic one:

$$\varepsilon_n(\mathbf{k}) \approx \varepsilon_n(0) + \frac{\hbar^2}{2} \sum_{ij} \left(m_n^{*-1}\right)_{ij} k_i k_j \,.$$

In this approximation the electrons move like free particles in the crystal structure but with an effective mass tensor $\left(m_n^{*-1}\right)_{ij} = \frac{1}{\hbar^2} \frac{\partial^2}{\partial k_i \partial k_j} \varepsilon_n(\mathbf{k})$ for each band n. The simplest case is that of a diagonal tensor with all diagonal elements being equal. This leads to the intuitive picture of electrons with isotropic effective masses propagating through the semiconductor. Figure 1.2 schematically shows the remaining, relevant part of the electronic bandstructure that is considered in the following. In the past, the discussed simplifications to the electronic bandstructure have successfully been applied to the calculation of optical properties for several semiconductor materials[5, 11, 19] and are well-suited for the material systems considered in this work, i.e. GaAs and ZnSe. We model the electronic bandstructure by one conduction band with electronic total angular momentum $j = \frac{1}{2}$ and one valence band with $j = \frac{3}{2}$ for $\mathbf{k} = 0$. The electronic states can be classified by the z-component m_j of the total angular momentum j. Around the Γ-point, due to spin-orbit coupling, the valence band is split into two bands with different effective masses, a light-hole (lh) band with $m_j = \pm\frac{1}{2}$ and a heavy-hole (hh) band with $m_j = \pm\frac{3}{2}$, see Fig. 1.2.[a)] In the electron-hole picture the z-component m_j of the total angular momentum of electrons in the conduction band and of holes in the valence bands will be denoted by $\mathrm{e} \in \{-\frac{1}{2}, +\frac{1}{2}\}$ and $\mathrm{h} \in \{-\frac{3}{2}, -\frac{1}{2}, +\frac{1}{2}, +\frac{3}{2}\}$, respectively.

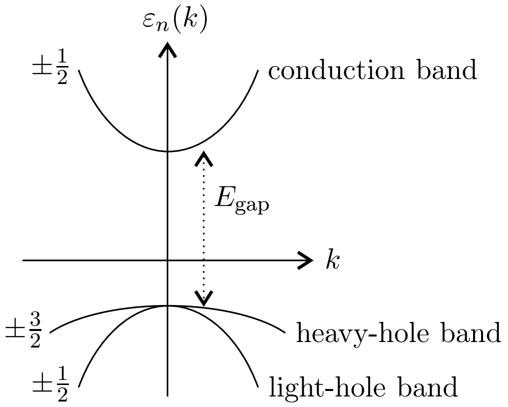

Figure 1.2: Schematic visualization of a selected part of the electronic bandstructure in effective mass approximation.

So far, only a description of electronic properties of bulk materials has been given. Since we are interested in the optical properties of semiconductor heterostructures a brief discussion of the treatment of spatial inhomogeneities and their influence on the above mentioned assumptions is needed. In principle, due to the destroyed translation invariance of the system, a full solution of the electronic problem within the crystal potential of the heterostructure would be necessary to obtain the electronic dispersion and the desired one-particle basis. Instead of this we use the so-called envelope approximation.[11] Making use of the discrete translation symmetry of the crystal lattice in the bulk material, the one-particle basis states $\psi_{\mathbf{k}n\sigma}(\mathbf{r})$ fulfill Bloch's theorem: $\psi_{\mathbf{k}n\sigma}(\mathbf{r}) = \mathrm{e}^{i\mathbf{kr}} u_{n\mathbf{k}}(\mathbf{r}) \chi_\sigma$. Here $u_{n\mathbf{k}}(\mathbf{r})$ is the lattice periodic Bloch factor and χ_σ is the spin wave function.[b)] In envelope approximation, the spatial part of the one-particle

---

[a)] The split-off valence band with $j = \frac{1}{2}$ and $m_j = \pm\frac{1}{2}$ is shifted to lower energies by spin-orbit coupling. This band is of no relevance for the optically excited transitions in the energy range investigated here.

[b)] The separation of the spin wave function χ_σ and the spatial degrees of freedom is only valid in a spin-independent external potential.

wave functions $\psi^{\text{env}}_{n\sigma}(\mathbf{r})$ is approximated by a product of a lattice periodic part $u_n(\mathbf{r})$ and an envelope function $\varphi_n(\mathbf{r})$:

$$\psi^{\text{env}}_{n\sigma}(\mathbf{r}) = \varphi_n(\mathbf{r}) u_n(\mathbf{r}) \chi_\sigma \, .$$

In this approximation, the lattice periodic function $u_n(\mathbf{r})$ is given by the Bloch factor of the bulk material at the zone center $u_{n\mathbf{k}=0}(\mathbf{r})$, the envelope functions $\varphi_n(\mathbf{r})$ vary only slowly over the length scale of one unit cell. They fulfill a one-particle Schrödinger equation in effective mass approximation[11] for each band n with an external potential only slowly varying over one unit cell of the crystal. Hence, in this approximation the destroyed translation symmetry in semiconductor heterostructures only enters via an effective external potential for the envelope functions while the effective masses are taken from the bulk material. In the past, the envelope approximation has successfully been applied to the description of optical properties of a variety of semiconductor heterostructures, e.g., in Refs. 6, 20, 21.[c)]

For the description of optical properties, the coupling of a classical light field to the quantum mechanical electronic system of the semiconductor heterostructure is needed. In dipole approximation the coupling of electronic interband transitions to external optical fields is determined by the dipole matrix elements $\mathbf{d}_{\text{eh}}$ between the considered bands. For the investigated semiconductor materials and near the Γ-point, these dipole matrix elements are in a good approximation $\mathbf{k}$-independent[11] and can, in envelope approximation, be taken from the literature for the bulk materials. However, the coupling strength between carriers and the optical field in a given semiconductor heterostructure is strongly influenced by the spatial structure of the carrier envelope functions and the resulting overlap with the electric field as discussed in Section 3.2. For the bulk material the only relevant and non-vanishing dipole matrix elements for the considered semiconductor materials are:[19]

$$\begin{aligned}
\mathbf{d}_{+\frac{1}{2}+\frac{3}{2}} &= d_{\text{eh}} \mathbf{e}_- \, , \\
\mathbf{d}_{-\frac{1}{2}-\frac{3}{2}} &= d_{\text{eh}} \mathbf{e}_+ \, , \\
\mathbf{d}_{-\frac{1}{2}+\frac{1}{2}} &= \frac{1}{\sqrt{3}} d_{\text{eh}} \mathbf{e}_- \, , \\
\mathbf{d}_{+\frac{1}{2}-\frac{1}{2}} &= \frac{1}{\sqrt{3}} d_{\text{eh}} \mathbf{e}_+ \, . \qquad (1.1)
\end{aligned}$$

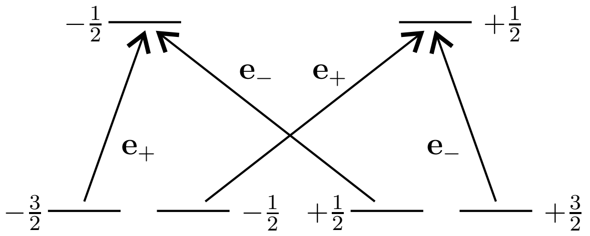

Figure 1.3: Optical dipole selection rules for circularly polarized light. The spin degenerate conduction band ($m_j = \pm 1/2$) and light ($m_j = \pm 1/2$) and heavy ($m_j = \pm 3/2$) hole valence bands are included.

Here, the optical dipole selection rules $\Delta m_j = \pm 1$ are expressed in terms of the circular polarization vectors $\mathbf{e}_\pm = 1/\sqrt{2}(\mathbf{e}_x \pm i\mathbf{e}_y)$ perpendicular to the propagation direction of the transversal electromagnetic fields; $\mathbf{e}_x$, $\mathbf{e}_y$ are the standard Cartesian basis vectors. The corresponding interband transitions are visualized in Fig. 1.3.

[c)] A more profound and by far more involved way to obtain the electronic structure of semiconductor heterostructures is the use of a tight-binding approach,[22, 23] which, however, is beyond the scope of this work.

In the present work, a semiconductor heterostructure is considered which homogeneously extends in the x-y-plane and has a finite thickness in the z-direction as illustrated in Fig. 1.4. The electromagnetic fields solely propagate in z-direction and are homogeneous in the x-y-plane. Hence, there is only a spatial inhomogeneity of the system in the z-direction. Within the x-y-plane the system exhibits a translation and rotation invariance. The carriers in the conduction and valence band are confined in the semiconductor layer of material A with thickness L which is embedded between layers of a larger band-gap material B. The incoming light field resonantly interacts with the layer material A.

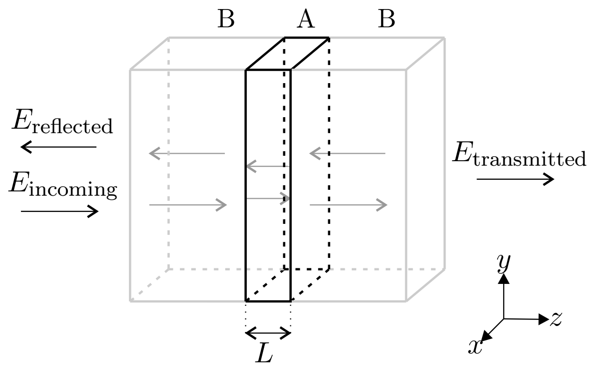

Figure 1.4: Illustration of the considered semiconductor heterostructure in a slab geometry. For more details see text.

Typically, the crystal structure of the layer material A is grown fully strained, i.e. with the lattice constant of the surrounding material B and thus not with the equilibrium lattice constant of the layer material. For the typically used material systems, e.g. ZnSe/ZnSSe or GaAs/AlGaAs, the strain deformation of the cubic crystal structure yields energy shifts in the electronic bandstructure.[1] In particular, these strain-shifts lift the degeneracy of the valence band states in Fig. 1.2 for different $|m_j|$ at the Γ-point.[d)] Therefore, signatures of electronic interband transitions between the heavy-hole band and the conduction band are spectrally well separated from the corresponding light-hole transitions in typical optical experiments. For compressive biaxial strain of the layer material, heavy-hole conduction band transitions are observed at lower energies than light-hole conduction band transitions. The opposite is true for tensile biaxial strain.[1] In order not to overburden the theory and to concentrate on more important details in the following, the description will be restricted to the description of a two-band model with spin degenerate heavy-hole valence and conduction band. This simplified model turns out to describe the experimental results in this work very well, see Section 4.2. The extension to more than one valence band is straight forward and can be done, if necessary, using a 4x4 Luttinger Hamiltonian[24,25] in its spherically symmetric form for the kinetic contribution of carriers in the valence bands.[6]

In the following chapter the theory to calculate optical properties of the considered semiconductor heterostructure illustrated in Fig. 1.4 is deduced. The starting point is the electronic Hamiltonian in envelope approximation with dipole coupling to an external electromagnetic field.

[d)] In thin layers the quantum confinement also yields a relevant contribution to the splitting of one-particle states in the valence bands with different effective masses which also lifts the degeneracy for different $|m_j|$.

2. Interband Polarization

To calculate the polarization that an optical field induces in a semiconductor material an appropriate microscopic description is required. We start with the Hamiltonian of the electronic system interacting with an external light field:

$$\mathcal{H} = \mathcal{H}_{\text{kin}} + \mathcal{H}_{\text{dipole}} + \mathcal{H}_{\text{Coulomb}} \,. \tag{2.1}$$

It consists of three parts: The kinetic energy of electrons and holes $\mathcal{H}_{\text{kin}}$, their dipole coupling to the external light field $\mathcal{H}_{\text{dipole}}$, and the Coulomb interaction of the carriers $\mathcal{H}_{\text{Coulomb}}$. To simulate a typical setup we consider a semiconductor layer in a slab geometry with finite thickness in the z-direction and infinite, homogeneous extension in the x-y-plane as described in the previous chapter and depicted in Fig. 1.4. A barrier material surrounds the layer of interest to create a heterostructure with a spatial confinement potential for the electrons and holes in conduction and valence bands, respectively. To describe the spatially inhomogeneous system it is convenient to define suitable creation $\psi^{i\dagger}_{\mathbf{k}}(z)$ and annihilation $\psi^{i}_{\mathbf{k}}(z)$ operators in the Heisenberg picture, that create or annihilate an electron ($i = \text{e}$) with in-plane momentum $\mathbf{k} = (k_x, k_y)$ or a hole ($i = \text{h}$) with in-plane momentum $-\mathbf{k}$ at position z. To simplify the notation, the time dependence of operators, density matrix elements and the electric field will only be made explicit if necessary. The quantum numbers $\text{e} \in \{-\frac{1}{2}, +\frac{1}{2}\}$ and $\text{h} \in \{-\frac{3}{2}, +\frac{3}{2}\}$ simultaneously denote the electronic bands and the quantum number m_j of the electronic total angular momentum z-component. The operators fulfill the fermionic commutation relations

$$\begin{aligned}
\Big[\psi^{i}_{\mathbf{k}}(z,t), \psi^{j\dagger}_{\mathbf{k}'}(z',t)\Big]_+ &= \delta(z-z')\delta_{\mathbf{k}\mathbf{k}'}\delta_{ij} \,, \\
\Big[\psi^{i}_{\mathbf{k}}(z,t), \psi^{j}_{\mathbf{k}'}(z',t)\Big]_+ &= 0 \quad \text{and} \\
\Big[\psi^{i\dagger}_{\mathbf{k}}(z,t), \psi^{j\dagger}_{\mathbf{k}'}(z',t)\Big]_+ &= 0 \,.
\end{aligned} \tag{2.2}$$

Using these definitions the kinetic part of the Hamiltonian (2.1) takes the form

$$\mathcal{H}_{\text{kin}} = \sum_{\mathbf{k}} \int \mathrm{d}z \Big[\sum_{\text{e}} \psi^{\text{e}\dagger}_{\mathbf{k}}(z) \varepsilon^{\text{e}}_{\mathbf{k},z} \psi^{\text{e}}_{\mathbf{k}}(z) + \sum_{\text{h}} \psi^{\text{h}\dagger}_{\mathbf{k}}(z) \varepsilon^{\text{h}}_{\mathbf{k},z} \psi^{\text{h}}_{\mathbf{k}}(z) \Big] \,, \tag{2.3}$$

with the one-particle energy operators $\varepsilon^{i}_{\mathbf{k},z_i} = \frac{\hbar^2\mathbf{k}^2}{2m^*_i} - \frac{\hbar^2}{2m^*_i}\frac{\partial^2}{\partial z_i^2} + E_{\text{gap}}\delta_{i\text{e}} + V^{i}_{\text{ext}}(z_i)$ in effective mass approximation; m^*_{e} and m^*_{h} denote the effective mass of electrons and holes, respectively. The one-particle energy operators are matrix elements with respect to the chosen in-plane $\mathbf{k}$-basis and operators in real space for the z-direction. The external potential $V^{i}_{\text{ext}}(z)$ is used to model the band offsets in the heterostructure illustrated in Fig. 1.4.

The interband dipole interaction of the electronic system with the external optical field is given by

$$\mathcal{H}_{\text{dipole}} = -\sum_{\mathbf{k}\text{eh}} \int \mathrm{d}z \Big[\psi^{\text{e}\dagger}_{\mathbf{k}}(z)\psi^{\text{h}\dagger}_{\mathbf{k}}(z)\mathbf{d}_{\text{eh}}\mathbf{E}(z) + \psi^{\text{h}}_{\mathbf{k}}(z)\psi^{\text{e}}_{\mathbf{k}}(z)\mathbf{d}^{*}_{\text{eh}}\mathbf{E}(z)\Big] , \tag{2.4}$$

with the dipole matrix element $\mathbf{d}_{\text{eh}}(\mathbf{k}, z_{\text{e}} - z_{\text{h}}) = \mathbf{d}_{\text{eh}}\delta(z_{\text{e}} - z_{\text{h}})$, which is local in real space and $\mathbf{k}$-independent. According to the dipole approximation, there is only a slight variation of the electric field $\mathbf{E}(z)$ on the length scale of one unit cell. It can be approximated by a piecewise constant field distribution, for further details see Ref. 1. The electromagnetic field homogeneously extends in the x-y-plane, so that propagation is only in the z-direction. Due to the in-plane homogeneity we only have $\mathbf{k}$-diagonal contributions to the dipole Hamiltonian, hence only electron-hole pairs with vanishing in-plane center of mass momentum $|\mathbf{q}| = 0$ are optically excited. Optical intraband transitions are not observed in or near the visible part of the spectrum, so they are not considered here.

The Coulomb interaction of electrons and holes in envelope approximation is given by

$$\begin{aligned}\mathcal{H}_{\text{Coulomb}} = \frac{1}{2}\sum_{\mathbf{k}\mathbf{k}'\mathbf{q}} \int \mathrm{d}z\mathrm{d}z'\, V^{zz'}_{\mathbf{q}} \Big[&\sum_{\text{ee}'} \psi^{\text{e}\dagger}_{\mathbf{k}+\mathbf{q}}(z)\psi^{\text{e}'\dagger}_{\mathbf{k}'-\mathbf{q}}(z')\psi^{\text{e}'}_{\mathbf{k}'}(z')\psi^{\text{e}}_{\mathbf{k}}(z) \\ &+\sum_{\text{hh}'} \psi^{\text{h}\dagger}_{\mathbf{k}+\mathbf{q}}(z)\psi^{\text{h}'\dagger}_{\mathbf{k}'-\mathbf{q}}(z')\psi^{\text{h}'}_{\mathbf{k}'}(z')\psi^{\text{h}}_{\mathbf{k}}(z) \\ &-2\sum_{\text{eh}} \psi^{\text{e}\dagger}_{\mathbf{k}+\mathbf{q}}(z)\psi^{\text{h}\dagger}_{\mathbf{k}'-\mathbf{q}}(z')\psi^{\text{h}}_{\mathbf{k}'}(z')\psi^{\text{e}}_{\mathbf{k}}(z)\Big] ,\end{aligned} \tag{2.5}$$

with the Coulomb matrix elements

$$V^{zz'}_{\mathbf{q}} = \frac{e_0^2}{2\varepsilon_0 n_{\text{bg}}^2}\frac{\mathrm{e}^{-|\mathbf{q}||z-z'|}}{|\mathbf{q}|} , \tag{2.6}$$

which are deduced in Appendix A.1. Here e_0 is the absolute value of the electronic charge, ε_0 is the vacuum dielectric constant and n_{bg} is the non-resonant background refractive index of the semiconductor material. Interband transitions induced by the Coulomb interaction that change the particle numbers in conduction and valence bands are not taken into account since they are very unlikely due to the large band-gap energy. Note, that this assumption is essential for the application of the dynamics-controlled truncation scheme in Part II. In envelope approximation electron-hole exchange terms are neglected in Eq. (2.5). This yields the loss of the singlet-triplet splitting for each single electron-hole pair.

To give a microscopic description of the interaction of the electronic system and an external electromagnetic field the resonant contribution to the macroscopic polarization[6]

$$\mathbf{P}(Z,t) = \sum_{\text{eh}\mathbf{k}} \int \mathrm{d}z_{\text{rel}}\, \mathbf{d}^{*}_{\text{eh}}\delta(z_{\text{e}} - z_{\text{h}})p^{\text{eh}}_{(\mathbf{k},z_{\text{e}},z_{\text{h}})} = \sum_{\text{eh}\mathbf{k}} \mathbf{d}^{*}_{\text{eh}}p^{\text{eh}}_{(\mathbf{k},Z,Z)} = \sum_{\text{eh}\mathbf{k}} \mathbf{e}_{\text{eh}}d^{*}_{\text{eh}}p^{\text{eh}}_{(\mathbf{k},Z,Z)} \tag{2.7}$$

is required, with the electron-hole relative $z_{\mathrm{rel}} = z_{\mathrm{e}} - z_{\mathrm{h}}$ and center of mass (COM) $Z = (z_{\mathrm{e}} m_{\mathrm{e}}^* + z_{\mathrm{h}} m_{\mathrm{h}}^*)/(m_{\mathrm{e}}^* + m_{\mathrm{h}}^*)$ coordinates, respectively. To calculate the expectation value of the dipole operator in Eq. (2.7), the following definition of the reduced one-particle density matrix has been used:[a]

$$\rho_{\mathbf{k}}(z, z') = \begin{pmatrix} \left\langle \psi_{\mathbf{k}}^{\mathrm{e}\dagger}(z)\psi_{\mathbf{k}}^{\mathrm{e}'}(z') \right\rangle & \left\langle \psi_{\mathbf{k}}^{\mathrm{e}\dagger}(z)\psi_{\mathbf{k}}^{\mathrm{h}\dagger}(z') \right\rangle \\ \left\langle \psi_{\mathbf{k}}^{\mathrm{h}}(z')\psi_{\mathbf{k}}^{\mathrm{e}}(z) \right\rangle & \left\langle \psi_{\mathbf{k}}^{\mathrm{h}\dagger}(z)\psi_{\mathbf{k}}^{\mathrm{h}'}(z') \right\rangle \end{pmatrix} = \begin{pmatrix} f_{(\mathbf{k},z,z')}^{\mathrm{ee}'} & p_{(\mathbf{k},z,z')}^{*\mathrm{eh}} \\ p_{(\mathbf{k},z,z)}^{\mathrm{eh}} & f_{(\mathbf{k},z,z')}^{\mathrm{hh}'} \end{pmatrix}, \tag{2.8}$$

where $p_{(\mathbf{k},z,z')}^{\mathrm{eh}}$ is the excitonic transition amplitude (excitonic polarization) and $f_{(\mathbf{k},z,z')}^{\mathrm{ee}'}$ and $f_{(\mathbf{k},z,z')}^{\mathrm{hh}'}$ are the electron and hole occupation functions[b], respectively. To calculate the time evolution of the macroscopic polarization (2.7) within a microscopic theory, the dynamics of the excitonic transition amplitude $p_{(\mathbf{k},z,z')}^{\mathrm{eh}}$ is required. It is given by:

$$\frac{\partial}{\partial t} p_{(\mathbf{k},z,z')}^{\mathrm{eh}} = \left\langle \dot{\psi}_{\mathbf{k}}^{\mathrm{h}}(z)\psi_{\mathbf{k}}^{\mathrm{e}}(z') + \psi_{\mathbf{k}}^{\mathrm{h}}(z)\dot{\psi}_{\mathbf{k}}^{\mathrm{e}}(z') \right\rangle . \tag{2.9}$$

The time evolution of the annihilation operators is determined by Heisenberg's equation of motion.[26] For an arbitrary operator $A(t)$ with no explicit time dependence the evolution is given by

$$\frac{\mathrm{d}}{\mathrm{d}t} A(t) = \dot{A}(t) = \frac{i}{\hbar} \left[\mathcal{H}, A(t) \right] . \tag{2.10}$$

Making use of Eq. (2.10), the Hamiltonian (2.1), and the anti-commutation relations (2.2), the equations of motion for the annihilation operators read:

$$\begin{aligned} \frac{\partial}{\partial t} \psi_{\mathbf{k}}^{\mathrm{e}}(z) = \frac{i}{\hbar} \Bigg[& - \varepsilon_{\mathbf{k},z}^{\mathrm{e}} \psi_{\mathbf{k}}^{\mathrm{e}}(z) + \sum_{\mathrm{h}} \mathbf{d}_{\mathrm{eh}} \mathbf{E}(z) \psi_{\mathbf{k}}^{\mathrm{h}\dagger}(z) \\ & + \sum_{\mathbf{k}'\mathbf{q}} \int \mathrm{d}z'\, V_{\mathbf{q}}^{zz'} \Big(\sum_{\mathrm{h}} \psi_{\mathbf{k}'}^{\mathrm{h}\dagger}(z') \psi_{\mathbf{k}'+\mathbf{q}}^{\mathrm{h}}(z') \psi_{\mathbf{k}+\mathbf{q}}^{\mathrm{e}}(z) + \sum_{\mathrm{e}'} \psi_{\mathbf{k}'+\mathbf{q}}^{\mathrm{e}'\dagger}(z') \psi_{\mathbf{k}+\mathbf{q}}^{\mathrm{e}}(z) \psi_{\mathbf{k}'}^{\mathrm{e}'}(z') \Big) \Bigg] , \end{aligned}$$

and

$$\begin{aligned} \frac{\partial}{\partial t} \psi_{\mathbf{k}}^{\mathrm{h}}(z) = \frac{i}{\hbar} \Bigg[& - \varepsilon_{\mathbf{k},z}^{\mathrm{h}} \psi_{\mathbf{k}}^{\mathrm{h}}(z) - \sum_{\mathrm{e}} \mathbf{d}_{\mathrm{eh}} \mathbf{E}(z) \psi_{\mathbf{k}}^{\mathrm{e}\dagger}(z) \\ & + \sum_{\mathbf{k}'\mathbf{q}} \int \mathrm{d}z' V_{\mathbf{q}}^{zz'} \Big(\sum_{\mathrm{h}'} \psi_{\mathbf{k}'}^{\mathrm{h}'\dagger}(z') \psi_{\mathbf{k}-\mathbf{q}}^{\mathrm{h}}(z) \psi_{\mathbf{k}'+\mathbf{q}}^{\mathrm{h}'}(z') + \sum_{\mathrm{e}} \psi_{\mathbf{k}'-\mathbf{q}}^{\mathrm{e}\dagger}(z') \psi_{\mathbf{k}'}^{\mathrm{e}}(z') \psi_{\mathbf{k}+\mathbf{q}}^{\mathrm{h}}(z) \Big) \Bigg] . \end{aligned}$$

---

[a] The relevant one-particle density matrix (2.8) is $\mathbf{k}$-diagonal, since, corresponding to Eq. (2.4), propagation is only in the z-direction and since Coulomb interaction does not spoil the system symmetry.

[b] The name "occupation function" for $f_{(\mathbf{k},z,z')}^{\mathrm{ee}'}$ and $f_{(\mathbf{k},z,z')}^{\mathrm{hh}'}$ is kept here, although, strictly speaking, they do not represent occupation functions if the creation and the annihilation operator in these expectation values contribute for different quantum numbers.

With Eq. (2.9) this results in the equation of motion for the excitonic transition amplitude:[c)]

$$
\begin{aligned}
i\hbar\frac{\partial}{\partial t}p^{\mathrm{eh}}_{(\mathbf{k},z_{\mathrm{e}},z_{\mathrm{h}})} =&\big(\varepsilon^{\mathrm{e}}_{\mathbf{k},z_{\mathrm{e}}}+\varepsilon^{\mathrm{h}}_{\mathbf{k},z_{\mathrm{h}}}\big)p^{\mathrm{eh}}_{(\mathbf{k},z_{\mathrm{e}},z_{\mathrm{h}})}-\sum_{\mathbf{k}'}V^{z_{\mathrm{e}}z_{\mathrm{h}}}_{\mathbf{k}-\mathbf{k}'}p^{\mathrm{eh}}_{(\mathbf{k}',z_{\mathrm{e}},z_{\mathrm{h}})}-\mathbf{d}_{\mathrm{eh}}\mathbf{E}(z_{\mathrm{e}})\delta(z_{\mathrm{e}}-z_{\mathrm{h}})\\
&+\sum_{\mathrm{h}'}\mathbf{d}_{\mathrm{eh}'}\mathbf{E}(z_{\mathrm{e}})\Big\langle\psi^{\mathrm{h}'\dagger}_{\mathbf{k}}(z_{\mathrm{e}})\psi^{\mathrm{h}}_{\mathbf{k}}(z_{\mathrm{h}})\Big\rangle+\sum_{\mathrm{e}'}\mathbf{d}_{\mathrm{e}'\mathrm{h}}\mathbf{E}(z_{\mathrm{h}})\Big\langle\psi^{\mathrm{e}'\dagger}_{\mathbf{k}}(z_{\mathrm{h}})\psi^{\mathrm{e}}_{\mathbf{k}}(z_{\mathrm{e}})\Big\rangle\\
&-\sum_{\mathbf{k}'\mathbf{q}}\int\mathrm{d}z\Bigg[V^{zz_{\mathrm{h}}}_{\mathbf{q}}\Bigg(\sum_{\mathrm{h}'}\Big\langle\psi^{\mathrm{h}'\dagger}_{\mathbf{k}'+\mathbf{q}}(z)\psi^{\mathrm{h}}_{\mathbf{k}+\mathbf{q}}(z_{\mathrm{h}})\psi^{\mathrm{h}'}_{\mathbf{k}'}(z)\psi^{\mathrm{e}}_{\mathbf{k}}(z_{\mathrm{e}})\Big\rangle\\
&\qquad-\sum_{\mathrm{e}'}\Big\langle\psi^{\mathrm{e}'\dagger}_{\mathbf{k}'-\mathbf{q}}(z)\psi^{\mathrm{h}}_{\mathbf{k}+\mathbf{q}}(z_{\mathrm{h}})\psi^{\mathrm{e}'}_{\mathbf{k}'}(z)\psi^{\mathrm{e}}_{\mathbf{k}}(z_{\mathrm{e}})\Big\rangle\Bigg)\\
&\qquad-V^{zz_{\mathrm{e}}}_{\mathbf{q}}\Bigg(\sum_{\mathrm{h}'}\Big\langle\psi^{\mathrm{h}'\dagger}_{\mathbf{k}'}(z)\psi^{\mathrm{h}}_{\mathbf{k}}(z_{\mathrm{h}})\psi^{\mathrm{h}'}_{\mathbf{k}'+\mathbf{q}}(z)\psi^{\mathrm{e}}_{\mathbf{k}+\mathbf{q}}(z_{\mathrm{e}})\Big\rangle\\
&\qquad-\sum_{\mathrm{e}'}\Big\langle\psi^{\mathrm{e}'\dagger}_{\mathbf{k}'+\mathbf{q}}(z)\psi^{\mathrm{h}}_{\mathbf{k}}(z_{\mathrm{h}})\psi^{\mathrm{e}'}_{\mathbf{k}'}(z)\psi^{\mathrm{e}}_{\mathbf{k}+\mathbf{q}}(z_{\mathrm{e}})\Big\rangle\Bigg)\Bigg]\,. \qquad (2.11)
\end{aligned}
$$

Unfortunately, this equation which describes the dynamics of the excitonic transition amplitude is not closed. First of all it is coupled to the electron and hole occupation functions $\langle\psi^{\mathrm{e}'\dagger}_{\mathbf{k}}(z_{\mathrm{h}})\psi^{\mathrm{e}}_{\mathbf{k}}(z_{\mathrm{e}})\rangle$ and $\langle\psi^{\mathrm{h}'\dagger}_{\mathbf{k}}(z_{\mathrm{e}})\psi^{\mathrm{h}}_{\mathbf{k}}(z_{\mathrm{h}})\rangle$, which is unproblematic. In addition we encounter the well-known many-particle hierarchy problem in the dynamics of the density matrix elements:[7–9]

Due to the inherent many-particle Coulomb interaction (2.5) of the electronic system, the dynamics of the excitonic transition amplitude is coupled to the dynamics of so-called *four-point* functions, namely expectation values $\langle\ldots\rangle$ of a combination of four electron- or hole-creation or -annihilation operators (see lines 3-6 in Eq. (2.11)). The dynamics of these four-point functions is then coupled to that of *six-point* functions and so on.

The simplest approach to overcome this infinite many-particle hierarchy is the use of the Hartree-Fock decoupling scheme, where four-point functions are factorized into products of two-point functions.[11,27] This type of decoupling yields a closed set of coupled equations for the excitonic transition amplitude and the electron and hole occupation functions, the so-called Semiconductor Bloch Equations.[11,19] Although it is possible to self-consistently solve this set of equations up to arbitrary order in the optical fields, within this approach, the description of the original many-particle system is restricted to effective two-particle processes only. Correlations of higher order are altogether neglected in this approximation. Many-particle effects beyond the Hartree-Fock approximation can be described by correlated many-particle processes and therefore necessarily involve more-point functions. It is not even possible to understand all nonlinearities of third order in the optical field in a model that is restricted to effective two-particle effects only.

[c)] The Coulomb matrix elements $V^{z_{\mathrm{e}}z_{\mathrm{h}}}_{\mathbf{k}-\mathbf{k}'}$ contain $|\mathbf{k}-\mathbf{k}'| = \sqrt{k^2+k'^2-2kk'\cos\left(\phi_k-\phi_{k'}\right)}$, where the angle $\phi_k-\phi_{k'}$ is enclosed by $\mathbf{k}$ and $\mathbf{k}'$.

Fortunately, for exclusive optical, coherent excitation it turns out that all many-particle effects can be characterized by a certain order in the optical field. Coherence in the time evolution of the electronic system is realized if it is determined by the Hamiltonian (2.1), as long as the electronic system is in its ground state prior to the optical excitation and no non-optical excitation is applied. For more details see Chapter 5 and Appendix A.2. In principle, the so-called Dynamics-Controlled Truncation (DCT) allows a systematic and exact truncation of the many-particle hierarchy for a fully coherently driven electronic system.[7–9] Formally, this approach yields a perturbation theory with respect to the electric field amplitude, leading to a power series for the macroscopic polarization:[d)]

$$P = \chi^{(1)} E^1 + \chi^{(3)} E^3 + \chi^{(5)} E^5 + \ldots . \tag{2.12}$$

This expression is obtained by expanding the system susceptibility $\chi(E)$, that relates the macroscopic polarization P to the electric field E via $P = \chi(E)E$, in terms of powers in the electric field. In general, this approach is advantageous for the coherent optical regime since it is not based on a perturbation treatment of Coulomb correlations. It yields consistent and exact results as long as the intensity of the exciting optical fields is not beyond the validity of the theory which depends on the number of considered terms in the power series (2.12). However, for practical applicability a restriction to "low-order nonlinearities" is necessary. Even going beyond third order contributions in Eq. (2.12) is quite cumbersome and has only been done for one-dimensional model systems[28] or for a certain class of higher order nonlinearities.[29–31] Another limiting factor is the fact, that for higher excitation intensities the influence of incoherent carrier populations becomes more important or even dominant over the coherent contributions which are accessible within the DCT approach. An even more involved theory that yields meaningful results beyond the coherent regime and for higher excitation intensities has been suggested in Refs. 32, 33. It reproduces the dynamics-controlled truncation results in the low intensity limit but with a strongly increased numerical effort which is at present numerically beyond the realms of possibilities for the realistic system considered here.

This work will focus on many-particle effects of first and third order in the optical field within a $\chi^{(1)}$- and a $\chi^{(3)}$-theory. Part I is dedicated to rather weak external fields in the linear optical regime. The extension of the theory to the description of third order nonlinearities will be covered in Part II.

Linearization of the general equation of motion (2.11) for the interband polarization in a semiconductor for weak optical fields yields the inhomogeneous exciton equation:

$$\begin{aligned} i\hbar\frac{\partial}{\partial t} p^{\mathrm{eh}}_{(\mathbf{k},z_{\mathrm{e}},z_{\mathrm{h}})}(t) =& \big(\varepsilon^{\mathrm{e}}_{\mathbf{k},z_{\mathrm{e}}} + \varepsilon^{\mathrm{h}}_{\mathbf{k},z_{\mathrm{h}}}\big) p^{\mathrm{eh}}_{(\mathbf{k},z_{\mathrm{e}},z_{\mathrm{h}})}(t) \\ & - \sum_{\mathbf{k}'} V^{z_{\mathrm{e}} z_{\mathrm{h}}}_{\mathbf{k}-\mathbf{k}'} p^{\mathrm{eh}}_{(\mathbf{k}',z_{\mathrm{e}},z_{\mathrm{h}})}(t) - \mathbf{d}_{\mathrm{eh}} \mathbf{E}(z_{\mathrm{e}},t) \delta(z_{\mathrm{e}} - z_{\mathrm{h}}) . \end{aligned} \tag{2.13}$$

This equation can be obtained from the Hartree-Fock approximation and is exact in linear order in the optical field. Near the band-gap energy it contains all many-particle

---

[d)] The expansion should only be understood as a schematic visualization without any technical details. For optical excitations near the band edge, it directly follows from Eq. (2.11) that only odd orders of the electric field enter this expansion.

effects that are involved in linear optics. The only remaining dynamic quantity for the description of the semiconductor response to an external electromagnetic field is the excitonic transition amplitude $p^{\mathrm{eh}}_{(\mathbf{k},z_{\mathrm{e}},z_{\mathrm{h}})}$. Hence, in this regime all many-particle effects can be understood in an effective two-particle picture in terms of excitonic polarizations. Note, that in linear optics the equations of motion for interband transitions with different quantum numbers e, h are decoupled. Choosing circular light polarization they can be independently excited according to the dipole selection rules in Eq. (1.1) and Fig. 1.3. The amplitude of the driving term $\mathbf{d}_{\mathrm{eh}}\mathbf{E}(z_{\mathrm{e}},t)$ in Eq. (2.13) is called Rabi energy. It is determined by the incoming light field that is observed outside the sample where no interaction with the material polarization occurs, and by the dipole matrix element $\mathbf{d}_{\mathrm{eh}}$ for each interband transition connected to the indices e, h.

Before we proceed to find a solution of Eq. (2.13) for a spatially inhomogeneous system, in the next section the well-known results for excitonic properties in an idealized bulk system are reviewed.

2.1. Excitons in Bulk Semiconductors

The inhomogeneous exciton equation (2.13) has been deduced for the description of a system with spatial inhomogeneity in the z-direction. To describe optical properties of a spatially homogeneous system it is convenient to use the Fourier transformed version of Eq. (2.13) in real space. The electron-hole relative position vector $\tilde{\mathbf{r}} = \tilde{\mathbf{r}}_{\mathrm{e}} - \tilde{\mathbf{r}}_{\mathrm{h}} = (x_{\mathrm{e}} - x_{\mathrm{h}}, y_{\mathrm{e}} - y_{\mathrm{h}}, z_{\mathrm{e}} - z_{\mathrm{h}})$, and the center of mass (COM) coordinate $Z = (m^*_{\mathrm{e}} z_{\mathrm{e}} + m^*_{\mathrm{h}} z_{\mathrm{h}})/(m^*_{\mathrm{e}} + m^*_{\mathrm{h}})$ for the z-direction are introduced. Propagation is exclusively in the z-direction. Therefore, in the x-y-plane, there is no finite COM momentum transferred from the optical field to the excited electron-hole pairs. The transformation to real space is convenient since a full analogy of excitons in a bulk system to the well-known Hydrogen problem can be reached. The transformed exciton equation (2.13) for the infinitely extended medium reads:

$$i\hbar\frac{\partial}{\partial t}p^{\mathrm{eh}}_{(\tilde{\mathbf{r}},Z)}(t) = \left(-\frac{\hbar^2}{2\mu^*}\nabla^2_{\tilde{\mathbf{r}}} - \frac{\hbar^2}{2M^*}\frac{\partial^2}{\partial Z^2} + E_{\mathrm{gap}} - V(\tilde{\mathbf{r}})\right) p^{\mathrm{eh}}_{(\tilde{\mathbf{r}},Z)}(t) - d_{\mathrm{eh}}E^{\mathrm{eh}}(Z,t)\delta(\tilde{\mathbf{r}})\,. \tag{2.14}$$

Here, $\mu^* = (m^*_{\mathrm{e}} m^*_{\mathrm{h}})/(m^*_{\mathrm{e}} + m^*_{\mathrm{h}})$ and $M^* = m^*_{\mathrm{e}} + m^*_{\mathrm{h}}$ are the reduced and the total exciton mass, respectively. The relevant circularly polarized component of the exciting field, according to the dipole selection rules (1.1), is denoted by $E^{\mathrm{eh}}(Z,t)$. The Coulomb potential is given by $V(\tilde{\mathbf{r}}) = e_0^2/(4\pi\varepsilon_0 n^2_{\mathrm{bg}}|\tilde{\mathbf{r}}|)$. Formally, the homogeneous part of Eq. (2.14) has the structure of a two-particle Schrödinger equation. Within an idealized bulk material two decoupled eigenvalue equations are defined for the electron-hole relative and COM motion, respectively:

$$\left[-\frac{\hbar^2}{2\mu^*}\nabla^2_{\tilde{\mathbf{r}}} - V(\tilde{\mathbf{r}})\right]\tilde{\phi}_\nu(\tilde{\mathbf{r}}) = \varepsilon^{\mathrm{X}}_\nu \tilde{\phi}_\nu(\tilde{\mathbf{r}})\,, \tag{2.15}$$

$$\left[-\frac{\hbar^2}{2M^*}\frac{\partial^2}{\partial Z^2}\right]\varphi_{q_z}(Z) = \varepsilon^{\mathrm{X}}_{q_z}\varphi_{q_z}(Z)\,. \tag{2.16}$$

The exciton total energy is given by $E^{\text{total}}_{\nu q_z} = \varepsilon^{\text{X}}_{\nu} + \varepsilon^{\text{X}}_{q_z} + E_{\text{gap}}$. The solution $\tilde{\phi}_\nu(\tilde{\mathbf{r}})$ of Eq. (2.15) is known from the Hydrogen problem, but here with modified, effective parameters. A detailed discussion is given in, e.g., Ref. 26. The eigenvalues for the bound exciton states are

$$\varepsilon^{\text{X}}_{\nu} = -E^{\text{X}}_{\text{b}} \frac{1}{\nu^2}\,, \tag{2.17}$$

with integer numbers ν and the bulk exciton binding energy $E^{\text{X}}_{\text{b}} = E_{\text{Ryd}} \cdot \mu^*/(m_0 n^4_{\text{bg}})$. The atomic Rydberg energy is $E_{\text{Ryd}} = \frac{m_0 e_0^4}{8\varepsilon_0^2 h^2} \approx 13.6\,\text{eV}$. The typical length scale of the problem, the bulk exciton Bohr radius, is given by $a^{\text{X}}_0 = a_0 n^2_{\text{bg}} m_0/\mu^*$, with the atomic Bohr radius $a_0 = \frac{\varepsilon_0 h^2}{\pi m_0 e_0^2} \approx 0.529\,\text{Å}$. Values for the bulk exciton Bohr radius are typically in between 2 nm and 15 nm. Equation (2.16) describes the one-dimensional motion of a free particle with effective mass M^*. The plane wave solutions are given by

$$\varphi_{q_z}(Z) = \frac{1}{\sqrt{V}} \mathrm{e}^{i q_z Z}\,,$$

with energies $\varepsilon^{\text{X}}_{q_z} = \frac{\hbar^2 q_z^2}{2M^*}$. Note, that the wave functions $\tilde{\phi}_\nu(\tilde{\mathbf{r}})$ and $\varphi_{q_z}(Z)$ fulfill the required quantum mechanical boundary conditions for the bulk system, namely the resulting probability density is normalized in the system volume V. Exciton relative and COM motion are decoupled since the boundary condition only has to be applied to the relative motion, a solution $\tilde{\phi}_\nu(\tilde{\mathbf{r}})$ is required which vanishes for $|\tilde{\mathbf{r}}| \to \infty$.

The excitonic transition amplitude can be expanded in terms of the complete set of these eigenfunctions,

$$p^{\text{eh}}_{(\tilde{\mathbf{r}},Z)}(t) = \sum_{\nu q_z} p^{\text{eh}}_{\nu q_z}(t) \varphi_{q_z}(Z) \tilde{\phi}_\nu(\tilde{\mathbf{r}})\,, \tag{2.18}$$

with the expansion coefficients $p^{\text{eh}}_{\nu q_z}(t)$. Together with Eq. (2.14), and making use of the orthonormality of the exciton basis states, this expansion results in:

$$\left(i\hbar \frac{\partial}{\partial t} - \varepsilon^{\text{X}}_{\nu} - \varepsilon^{\text{X}}_{q_z} - E_{\text{gap}} \right) p^{\text{eh}}_{\nu q_z}(t) = -d_{\text{eh}} E^{\text{eh}}_{q_z}(t) \tilde{\phi}^*_\nu(\tilde{\mathbf{r}} = 0)\,. \tag{2.19}$$

Here the contribution of the electric field $\mathbf{E}_{q_z}(t) = \int \mathrm{d}z \varphi^*_{q_z}(z) \mathbf{E}(z,t)$ with momentum q_z has been introduced. Fourier transformation of Eq. (2.19) yields the expansion coefficients

$$p^{\text{eh}}_{\nu q_z}(\omega) = -\frac{d_{\text{eh}} E^{\text{eh}}_{q_z}(\omega) \tilde{\phi}^*_\nu(\tilde{\mathbf{r}} = 0)}{\hbar\omega + i\gamma - \varepsilon^{\text{X}}_{\nu} - \varepsilon^{\text{X}}_{q_z} - E_{\text{gap}}} \tag{2.20}$$

in frequency domain. The small imaginary part γ in the energy denominator was introduced to guarantee the causality in the system and prevents the expression (2.20) to become singular for real-valued frequencies ω. Furthermore, a finite imaginary part can be used to include a dephasing constant for the excitonic polarization on a phenomenological level.

After transformation of the macroscopic polarization $\mathbf{P}(z,t)$ in Eq. (2.7) and of the expansion (2.18) to frequency domain, the coefficients (2.20) can be used to evaluate the macroscopic polarization:

$$\begin{aligned}\mathbf{P}(z,\omega) &= \sum_{\mathrm{eh}} \mathbf{e}_{\mathrm{eh}} d^*_{\mathrm{eh}} p^{\mathrm{eh}}_{(\tilde{\mathbf{r}}=0,z)}(\omega) \\ &= \sum_{\mathrm{eh}} \mathbf{e}_{\mathrm{eh}} d^*_{\mathrm{eh}} \sum_{\nu q_z} p^{\mathrm{eh}}_{\nu q_z}(\omega) \varphi_{q_z}(z) \tilde{\phi}_\nu(\tilde{\mathbf{r}}=0) \\ &= -\sum_{\mathrm{eh}\nu} \mathbf{e}_{\mathrm{eh}} |d_{\mathrm{eh}}|^2 |\tilde{\phi}_\nu(\tilde{\mathbf{r}}=0)|^2 \int \mathrm{d}z' \sum_{q_z} \frac{\varphi_{q_z}(z)\varphi^*_{q_z}(z')E^{\mathrm{eh}}(z',\omega)}{\hbar\omega + i\gamma - \varepsilon^{\mathrm{X}}_\nu - \varepsilon^{\mathrm{X}}_{q_z} - E_{\mathrm{gap}}} \,. \end{aligned} \tag{2.21}$$

The polarization vectors $\mathbf{e}_{\mathrm{eh}}$ are defined according to the dipole selection rules (1.1). To obtain this result, $\sum_{\mathbf{k}} p^{\mathrm{eh}}_{(\mathbf{k},z_{\mathrm{e}}=z,z_{\mathrm{h}}=z)}(t) = p^{\mathrm{eh}}_{(\tilde{\mathbf{r}}=0,z)}(t)$ has been used. Equation (2.21) has the formal structure

$$\mathbf{P}(z,\omega) = \int \mathrm{d}z' \chi(z,z',\omega)\mathbf{E}(z',\omega)\,, \tag{2.22}$$

where the susceptibility $\chi(z,z',\omega)$ is defined by

$$\chi(z,z',\omega) = -\sum_\nu |d_{\mathrm{eh}}|^2 |\tilde{\phi}_\nu(\tilde{\mathbf{r}}=0)|^2 \sum_{q_z} \frac{\mathrm{e}^{iq_z(z-z')}}{\hbar\omega + i\gamma - \varepsilon^{\mathrm{X}}_\nu - \varepsilon^{\mathrm{X}}_{q_z} - E_{\mathrm{gap}}}\,. \tag{2.23}$$

Here, for the homogeneous system, the coupling of different space points z, z' by the susceptibility only depends on their distance $z-z'$, with $\chi(z,z',\omega) = \chi(z-z',\omega)$. Hence, due to the translation invariance, the susceptibility for electron-hole pair excitations is reduced to a local quantity and Eq. (2.22) gains the structure of a convolution. Its Fourier transformation to momentum space yields the product

$$\mathbf{P}_{q_z}(\omega) = \chi(q_z,\omega)\mathbf{E}_{q_z}(\omega)\,. \tag{2.24}$$

Therefore, a local relation between $\mathbf{P}_{q_z}(\omega)$ and $\mathbf{E}_{q_z}(\omega)$ can be deduced which is determined by the local susceptibility

$$\chi(q_z,\omega) = -\sum_\nu \frac{|d_{\mathrm{eh}}|^2 |\tilde{\phi}_\nu(\tilde{\mathbf{r}}=0)|^2}{\hbar\omega + i\gamma - \varepsilon^{\mathrm{X}}_\nu - \varepsilon^{\mathrm{X}}_{q_z} - E_{\mathrm{gap}}} \tag{2.25}$$

in momentum space. Only exciton states $\tilde{\phi}_\nu(\tilde{\mathbf{r}})$ with s-symmetry, that is with full rotation symmetry, contribute to the susceptibility for dipole coupling to the optical field; only these states fulfill $\tilde{\phi}_\nu(\tilde{\mathbf{r}}=0) \neq 0$. The coupling strength of the exciton states to the optical field is determined by $|d_{\mathrm{eh}}|$ and $|\tilde{\phi}_\nu(\tilde{\mathbf{r}}=0)|$. Both, exciton relative and COM motion (via $\varepsilon^{\mathrm{X}}_{q_z}$) influence the optical properties of the considered system and enter the susceptibility (2.25). To simplify the discussion of the result, we concentrate on the $q_z = 0$ contribution of the susceptibility in the following part of this section. Its imaginary part is directly connected to the absorption $\alpha(\omega)$ of the system:[11]

$$\alpha(\omega) = \frac{4\pi\omega}{n_{\mathrm{bg}}c_0}\mathrm{Im}\chi(q_z=0,\omega)\,.$$

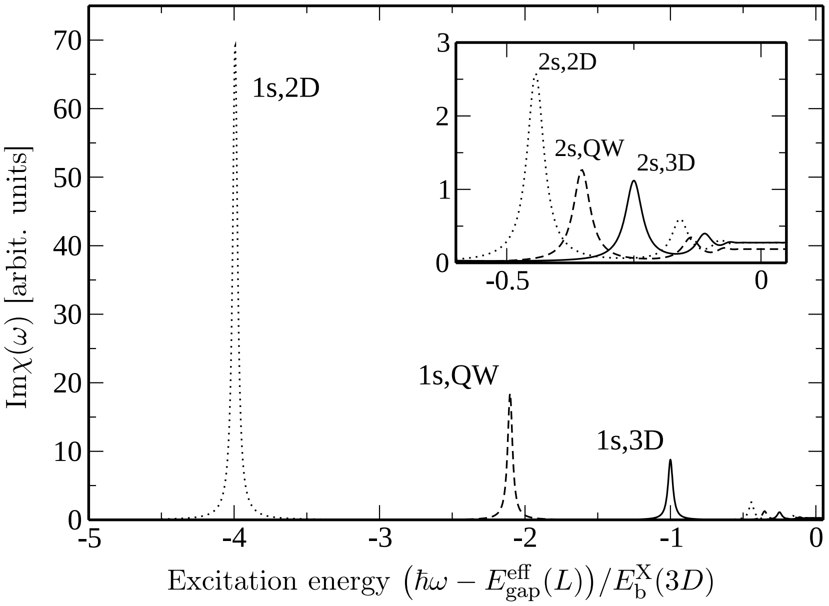

Figure 2.1: Calculated imaginary part of the excitonic susceptibility for an idealized bulk (3D) material (solid line), a two-dimensional (2D) system (dotted line), and a quantum-well (QW) with one exciton Bohr radius thickness (dashed line). Excitation energies are given relative to the effective band-gap energy $E_{\mathrm{gap}}^{\mathrm{eff}}(L)$ for each system and are given in units of the bulk exciton binding energy $E_{\mathrm{b}}^{\mathrm{X}}(3D)$.

Resonances of $\mathrm{Im}\chi(q_z = 0, \omega)$ are located at the position of the excitonic eigenenergies $\varepsilon_\nu^{\mathrm{X}} + E_{\mathrm{gap}}$. The phenomenological dephasing constant γ yields a homogeneous broadening of the resulting Lorentzians in the absorption $\alpha(\omega)$. The solid line in Fig. 2.1 shows the imaginary part of the excitonic susceptibility of a bulk material for typical GaAs parameters. The excitation energy is given relative to the bulk band-gap energy and normalized to the bulk exciton binding energy $E_{\mathrm{b}}^{\mathrm{X}}(3D)$. The bound exciton states contribute to the spectrum for excitation energies $E < 0$ and the influence of the excitonic continuum is observed for $E > 0$.

The solution of the eigenvalue equation (2.15) for an idealized two-dimensional system yields an analytical expression for the energies of bound excitons in two dimensions:

$$\varepsilon_\nu^{\mathrm{X}}(2D) = -E_{\mathrm{b}}^{\mathrm{X}}(3D)\frac{1}{(\nu - 1/2)^2} \quad \text{with} \quad \nu \in \{1, 2, \ldots\}\,. \tag{2.26}$$

Compared to the exciton binding energy in three dimensions (2.17), we encounter in Eq. (2.26) an exciton binding energy which is increased by a factor of four. The resulting absorption spectrum for an idealized two-dimensional system is included as dotted line in Fig. 2.1. For a better comparison, the excitation energy is given relative to the band-gap energy of the two-dimensional system and normalized to the bulk exciton binding energy $E_{\mathrm{b}}^{\mathrm{X}}(3D)$.

To conclude this discussion we investigate the absorption spectrum of a quasi two-dimensional quantum-well system. The quantum-well is surrounded by infinitely high potential barriers and its thickness is sufficiently small to validate a model where only one subband is taken into account for the motion of electron and hole perpendicular to the well. Details concerning the evaluation of the Coulomb matrix elements are given in Part II and Appendix A.1 of this work. The dashed line in Fig. 2.1 displays the calculated absorption spectrum for a well thickness of one exciton Bohr radius for GaAs. The properties, regarding position and height of the resonances, are in between the results of the two idealized limiting cases, the three- and the two-dimensional model systems.

For increased layer thickness propagation effects become important and the quantum confinement of carriers results in a complicated structure of the excitonic spectrum. Before a theory for polariton propagation in finite semiconductor heterostructures, including the influence of boundaries on a microscopic level, is introduced in Chapter 2, we continue the discussion of optical properties of an idealized bulk material in the next section.

2.2. The Polariton Concept

In the previous section, the discussion of optical properties focused on the $q_z = 0$ contribution of the excitonic susceptibility (2.25). But, strictly speaking, for strong dipole coupling, an analysis of the coupled light and exciton system is necessary where momentum is transferred from the propagating light field to the induced material polarization and vice versa. Maxwell's equations yield the Fourier transformed wave equation for the transversal electric field component with momentum q_z,

$$\left[n_{\mathrm{bg}}^2 \frac{\omega^2}{c_0^2} - q_z^2\right] \mathbf{E}_{q_z}(\omega) = -\frac{\omega^2}{\varepsilon_0 c_0^2} \mathbf{P}_{q_z}(\omega)\,. \tag{2.27}$$

The inhomogeneity is determined by the optically induced frequency and momentum dependent macroscopic polarization $\mathbf{P}_{q_z}(\omega)$. Making use of Eq. (2.24), which is based on the locality of the excitonic susceptibility for the homogeneous system, Eq. (2.27) can be transformed to

$$\left[\frac{\omega^2}{c_0^2} \varepsilon(q_z, \omega) - q_z^2\right] \mathbf{E}_{q_z}(\omega) = 0\,, \tag{2.28}$$

with $\varepsilon(q_z, \omega) = n_{\mathrm{bg}}^2 + \chi(q_z, \omega)/\varepsilon_0$. For simplicity, the following discussion is restricted to the contribution of the exciton ground state with the normalized wave function $\tilde{\phi}_{\nu=1}(\tilde{\mathbf{r}}) = \frac{2}{\sqrt{4\pi}} \left(a_0^{\mathrm{X}}\right)^{-3/2} \exp\left(-\frac{\tilde{r}}{a_0^{\mathrm{X}}}\right)$. With $|d_1|^2 = |d_{\mathrm{eh}}|^2 |\tilde{\phi}_1(\tilde{\mathbf{r}} = 0)|^2 = |d_{\mathrm{eh}}|^2/(\pi a_0^{\mathrm{X}3})$ the susceptibility (2.25) for optical excitation of an excitonic polarization in the 1s state reads:

$$\chi(q_z, \omega) = -\frac{|d_1|^2}{\hbar\omega + i\gamma - \varepsilon_1^{\mathrm{X}} - \varepsilon_{q_z}^{\mathrm{X}} - E_{\mathrm{gap}}}\,.$$

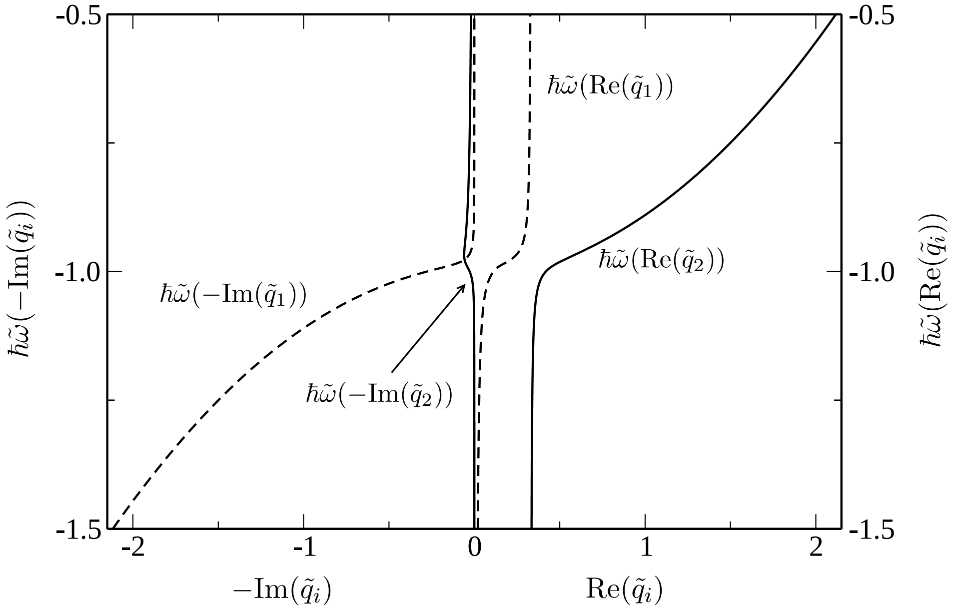

Figure 2.2: Bulk polariton dispersion for GaAs parameters. Excitonic units are chosen with $\tilde{q} = q \cdot a_0^{\mathrm{X}}$ and $\hbar\tilde{\omega} = (\hbar\omega - E_{\mathrm{gap}})/E_{\mathrm{b}}^{\mathrm{X}}$.

Therefore, making use of the momentum conservation for the coupled light-matter system, the propagation of light according to the solution of the wave equation (2.28) obeys the dispersion:

$$q_{1,2}^2(\omega) = \frac{1}{2}\left(q_{\mathrm{bg}}^2 + q_{\mathrm{X}}^2\right) \pm \sqrt{\frac{1}{4}\left(q_{\mathrm{bg}}^2 - q_{\mathrm{X}}^2\right)^2 + \kappa}\,. \tag{2.29}$$

The two branches $q_{1,2}(\omega)$ of this polariton dispersion describe the propagating solutions for the coupled light-matter system in the vicinity of the 1s exciton resonance. The dispersion of light, only influenced by the background refractive index n_{bg}, is given by $q_{\mathrm{bg}}^2 = \frac{\omega^2}{c_0^2} n_{\mathrm{bg}}^2$. The exciton COM motion is included by the parabolic dispersion $q_{\mathrm{X}}^2 = \frac{2M^*}{\hbar^2}(\hbar\omega - \varepsilon_1^{\mathrm{X}} - E_{\mathrm{gap}} + i\gamma)$. The light-matter coupling strength enters the dispersion (2.29) via the constant $\kappa = \frac{\omega^2}{c_0^2}\frac{2M^*}{\hbar^2\varepsilon_0}|d_1|^2$. For vanishing light-matter coupling $\kappa = 0$ and $\gamma \rightarrow 0$ the free dispersion of light and the free COM dispersion of the exciton motion are reproduced. The two polariton branches $q_{1,2}(\omega)$ are visualized in Fig. 2.2 for GaAs parameters. The contributions for real-valued wave vectors describe a propagating solution while those for imaginary wave vectors describe a damping of the propagating polariton modes which is included in the description via the dephasing constant γ.

In this section, an analytical solution for the propagating modes of light coupled to the excitonic resonances of an idealized bulk material has been found. However, the solution of the polariton problem within a finite semiconductor structure is complicated by the inclusion of boundaries which influence the electron-hole motion as well as the optical field. Within a spatially inhomogeneous system, the electron-hole relative and COM motion are entangled by the influence of boundary conditions.

The separation of the relative and COM degrees of freedom is no longer valid for an exciton confined in a finite semiconductor structure. Therefore, in the next chapter a full solution of the equation of motion (2.13) for the inhomogeneous system, influenced by boundary conditions on a microscopic level, is presented. A detailed discussion regarding the differences to the analytical solution for the homogeneous system is given. Section 3.5 deals with the commonly used phenomenological application of the analytical solution, which was formulated in the present section, to a finite semiconductor layer. Optical spectra are calculated in terms of the resulting phenomenological model. Unfortunately, within this simplified approach, a violation of the physical boundary conditions of a given system is unavoidable.

Part I:

Linear Polariton Propagation

Introduction and Outline

The theoretical description of a propagating light field interacting with the excitonic resonances of a semiconductor medium has been a longstanding problem. Complications arise from the proper inclusion of sample surfaces. At these surfaces an external light field is coupled to the polariton modes and the polaritons radiatively decay into photons. In the past, macroscopic approaches have been introduced, which continue to use the excitonic susceptibility of the spatially homogeneous, infinitely extended medium. In this case the inclusion of sample surfaces requires so-called additional boundary conditions (ABCs). The original proposal of Pekar[34] requires the macroscopic polarization to vanish at the semiconductor surface. Other approaches suggest that the spatial derivative[35] or a linear combination of the polarization and its derivative[36] should vanish at the sample surface. A recent discussion concerning the validity of the different kinds of ABCs is given in Ref. 37. Unfortunately the results for the excitonic transmission and reflection spectra strongly depend on the particular treatment of boundaries within the macroscopic models. This shortcoming can be avoided within a microscopic formulation of boundary conditions which are imposed on the solution of a two-particle Schrödinger equation for the electron-hole motion including Coulomb interaction. This Schrödinger equation is directly coupled to Maxwell's equations for the propagating light field. Only with microscopic boundary conditions it has been possible to simultaneously reproduce amplitude and phase measurements of the transmitted light field through a semiconductor layer.[5,6] Another recent investigation[38] has also demonstrated the critical role of microscopic boundary conditions where for simplicity a more or less realistic one-dimensional contact interaction between the electrons and holes has been used.

In this work, several aspects concerning the description of polaritons are discussed in terms of a microscopic theory. Starting from the electronic Hamiltonian, a microscopic theory for the interband polarization in a spatially inhomogeneous semiconductor heterostructure, excited by an optical field, has been formulated in the previous section. Based on this theory, the present part is dedicated to the detailed discussion of excitonic and in particular polaritonic properties in the linear optical regime. In Chapter 2, the equation of motion for the excitonic transition amplitude is discussed. The involved direct solution of this exciton equation together with Maxwell's equations is discussed in Section 3.1.

Sections 3.2 to 3.4 deal with new and alternative schemes for the solution of the microscopic theory. These approaches make the solution more feasible because they strongly reduce the numerical effort. As an alternative to the full numerical solution of the two-particle Schrödinger equation, we introduce the expansion in terms of exciton wave functions. In contrast to previous approaches[3, 39] this expansion is not done in terms of bulk exciton eigenfunctions but with a basis set where each single exciton wave function fulfills the microscopic boundary conditions. In Section 3.5 the most commonly used phenomenological model based on Pekar's ABCs is discussed and the conceptual shortcomings in this approach are enlightened. Results for linear polariton spectra of both approaches are compared in detail in Section 4.1. In particular, this comparison reveals that due to the finite spatial extension of the excitons, the system evolves so-called polarization free dead-layers near the sample surfaces. On a phenomenological level the dead-layer thickness can be included in macroscopic approaches as an additional parameter. The determination of the dead-layer thickness based on a Born-Oppenheimer approximation has previously been discussed in Ref. 40 and the results can be confirmed and extended by the findings in Section 4.1.2.

So far, the theoretical investigations have focused on infinitely high confinement potentials for the optically excited electrons and holes. In experiments, however, polariton propagation is investigated in layers surrounded by buffer material. These heterostructures provide a confinement potential that is relatively high in the GaAs/$\mathrm{Al_{0.3}Ga_{0.7}As}$ system of Refs. 5, 6 but considerably shallower in the ZnCdSe/ZnSe system[12] or in ZnSe/ZnSSe structures.[13] In Section 4.2 polariton effects in ZnSe/ZnSSe, as a typical example for shallow confinement, are studied within a direct comparison of transmission experiments and calculations using microscopic boundary conditions. Additionally, multiple reflections at the outer surfaces of the heterostructure are included in the solution of Maxwell's equations. Results are also shown for the macroscopic model based on Pekar's ABCs. In the presented case, the best fit of the Pekar model is obtained for an effective sample thickness that *exceeds* the true layer thickness. The microscopic calculations reveal this surprising result as an interplay between the extension of the exciton wave function into the shallow barriers and the reduction of the polarization near the barrier due to the finite spatial extension of the exciton wave functions.

3. The Exciton Equation

In Chapter 2, the inhomogeneous exciton equation (2.13) has been deduced for the description of linear optical properties of a semiconductor heterostructure in a slab geometry:

$$\begin{aligned} i\hbar\frac{\partial}{\partial t}p^{\mathrm{eh}}_{(\mathbf{k},z_\mathrm{e},z_\mathrm{h})}(t) =& \big(\varepsilon^{\mathrm{e}}_{\mathbf{k},z_\mathrm{e}} + \varepsilon^{\mathrm{h}}_{\mathbf{k},z_\mathrm{h}}\big)p^{\mathrm{eh}}_{(\mathbf{k},z_\mathrm{e},z_\mathrm{h})}(t) \\ &- \sum_{\mathbf{k}'} V^{z_\mathrm{e}z_\mathrm{h}}_{\mathbf{k}-\mathbf{k}'}p^{\mathrm{eh}}_{(\mathbf{k}',z_\mathrm{e},z_\mathrm{h})}(t) - \mathbf{d}_{\mathrm{eh}}\mathbf{E}(z_\mathrm{e},t)\delta(z_\mathrm{e}-z_\mathrm{h})\,. \end{aligned} \tag{3.1}$$

The homogeneous part of Eq. (3.1) can be abbreviated by introduction of an excitonic Hamiltonian $\mathcal{H}^{\mathrm{X}}$ acting on the excitonic transition amplitude $p^{\mathrm{eh}}_{(\mathbf{k},z_\mathrm{e},z_\mathrm{h})}$.[a)] Hence, the excitonic transition amplitude fulfills a time dependent two-particle Schrödinger equation with the electric field as a driving term:

$$i\hbar\frac{\partial}{\partial t}p^{\mathrm{eh}}_{(\mathbf{k},z_\mathrm{e},z_\mathrm{h})}(t) = \mathcal{H}^{\mathrm{X}}p^{\mathrm{eh}}_{(\mathbf{k},z_\mathrm{e},z_\mathrm{h})}(t) - \mathbf{d}_{\mathrm{eh}}\mathbf{E}(z_\mathrm{e},t)\delta(z_\mathrm{e}-z_\mathrm{h})\,. \tag{3.2}$$

Explicitly, the Hamiltonian $\mathcal{H}^{\mathrm{X}}$ is given by $\mathcal{H}^{\mathrm{X}}_{\mathbf{k}\mathbf{k}'} = \big(\varepsilon^{\mathrm{e}}_{\mathbf{k},z_\mathrm{e}} + \varepsilon^{\mathrm{h}}_{\mathbf{k},z_\mathrm{h}}\big)\delta_{\mathbf{k}\mathbf{k}'} - V^{z_\mathrm{e}z_\mathrm{h}}_{\mathbf{k}-\mathbf{k}'}$ and its action $\sum_{\mathbf{k}'}\mathcal{H}^{\mathrm{X}}_{\mathbf{k}\mathbf{k}'}p^{\mathrm{eh}}_{(\mathbf{k}',z_\mathrm{e},z_\mathrm{h})}$ on the excitonic polarization regarding the in-plane momentum $\mathbf{k}$ has been abbreviated by $\mathcal{H}^{\mathrm{X}}p^{\mathrm{eh}}_{(\mathbf{k},z_\mathrm{e},z_\mathrm{h})}$.

The following section deals with the solution of the exciton equation (3.2) and therefore with the linear optical properties of the discussed semiconductor heterostructure with finite spatial extension in the z-direction. Complications for the numerical solution arise from the non-locality of the problem: Transition amplitudes at different positions z_e, z_h are coupled by the action of the excitonic Hamiltonian in Eq. (3.2).

3.1. Linear Polariton Propagation: Direct Solution

The purpose of this section is to give an insight into the direct solution of Eq. (3.1). It is coupled to a transversal electromagnetic field propagating in the z-direction. For an arbitrary polarized state of the exciting light field, the induced excitonic polarization

---

a) Taking only one conduction and one valence band into account, the excitonic Hamiltonian $\mathcal{H}^{\mathrm{X}}$ does not depend on the angular momenta e, h since the electron-hole exchange interaction has been neglected in (2.1).

can always be written as a sum of two circularly polarized contributions:

$$\begin{aligned}\mathbf{P}(z,t) &= \sum_\sigma P_\sigma(z,t)\mathbf{e}_\sigma = P_+(z,t)\mathbf{e}_+ + P_-(z,t)\mathbf{e}_- \\ &= d^*_{\text{eh}} \sum_{\mathbf{k}} \left(p^+_{(\mathbf{k},z,z)}\mathbf{e}_+ + p^-_{(\mathbf{k},z,z)}\mathbf{e}_- \right) . \end{aligned} \tag{3.3}$$

According to the dipole selection rules in Eq. (1.1) and Fig. 1.3, the components are given by $p^+_{(\mathbf{k},z,z)} = p^{-1/2,-3/2}_{(\mathbf{k},z,z)}$ and $p^-_{(\mathbf{k},z,z)} = p^{+1/2,+3/2}_{(\mathbf{k},z,z)}$. The circular polarized basis vectors can be expressed in terms of the standard Cartesian basis vectors according to $\mathbf{e}_\pm = 1/\sqrt{2}(\mathbf{e}_x \pm i\mathbf{e}_y)$. We use the ansatz $\mathbf{E}(\mathbf{r},t) = \sum_\sigma E_\sigma(z,t)\mathbf{e}_\sigma$ and $\mathbf{B}(\mathbf{r},t) = \sum_\sigma B_\sigma(z,t)i\mathbf{e}_\sigma$, with $\sigma \in \{+,-\}$, for circularly polarized transversal electromagnetic fields. Therefore, propagation in the z-direction can be captured by the one-dimensional form of Maxwell's equations

$$n^2_{\text{bg}}(z)\frac{\partial}{\partial t}E_\pm(z,t) = -c_0^2\frac{\partial}{\partial z}B_\pm(z,t) - \frac{1}{\varepsilon_0}\frac{\partial}{\partial t}P_\pm(z,t) , \tag{3.4a}$$

$$\frac{\partial}{\partial t}B_\pm(z,t) = -\frac{\partial}{\partial z}E_\pm(z,t) , \tag{3.4b}$$

as described in Appendix B.2. Here, $n_{\text{bg}}(z)$ is the non-resonant background refractive index profile along the propagation direction. c_0 and ε_0 are the vacuum velocity of light and the vacuum dielectric constant, respectively. Note that Maxwell's equations (3.4a), (3.4b) are decoupled for each circular polarization. Hence, the dipole-allowed electronic interband transitions are decoupled in linear optics. Since the excitonic Hamiltonian in Eq. (3.2) does not depend on electron and hole angular momenta, it is sufficient to study here an arbitrary eh-component of the excitonic transition amplitude in Eq. (3.3), denoted by $p_{\mathbf{k}}(z_{\text{e}}, z_{\text{h}})$. Its excitation is due to the electromagnetic field in the corresponding circular polarization state with its z-dependent amplitudes designated by $E(z,t)$ and $B(z,t)$. The corresponding macroscopic polarization is denoted by $P(z,t)$.

At this point the rotation invariance of the system around the z-axis allows an analytical simplification of Eq. (3.1). Motivated by this symmetry, an angular momentum decomposition of the excitonic transition amplitude $p_{\mathbf{k}}(z_{\text{e}}, z_{\text{h}})$ in the x-y-plane yields

$$p_{\mathbf{k}}(z_{\text{e}}, z_{\text{h}}) = \frac{1}{\sqrt{2\pi}}\sum_m p^m_k(z_{\text{e}}, z_{\text{h}})\mathrm{e}^{im\phi_k} , \tag{3.5}$$

where the summation is with respect to the in-plane angular momentum quantum number m. Here $k = |\mathbf{k}|$ is the modulus of the in-plane momentum $\mathbf{k}$ which encloses an angle ϕ_k with the x-axis. The corresponding expansion for the Coulomb matrix elements reads

$$V^{z_{\text{e}}z_{\text{h}}}_{\mathbf{k}-\mathbf{k}'} = \frac{1}{2\pi}\sum_{mm'} \mathrm{e}^{-im\phi_k}V^{mm'}_{kk'}(z_{\text{e}} - z_{\text{h}})\mathrm{e}^{im'\phi_{k'}} , \tag{3.6}$$

with expansion coefficients that are diagonal with respect to the angular momentum quantum numbers m, m'

$$V^{mm'}_{kk'}(z_{\text{e}} - z_{\text{h}}) = V^{mm'}_{kk'}(z_{\text{e}} - z_{\text{h}})\delta_{mm'} , \tag{3.7}$$

compare Appendix A.1 and Ref. 6. Therefore, the angular momentum components $p_k^m(z_\mathrm{e}, z_\mathrm{h})$ of the excitonic transition amplitude $p_\mathbf{k}(z_\mathrm{e}, z_\mathrm{h})$ for different m are not coupled by the electron-hole Coulomb interaction (3.6). Using the expansions (3.5), (3.6) and the orthonormality of the $\mathrm{e}^{im\phi_k}$ [b], the exciton equation (3.1) is decoupled for each angular momentum component $p_k^m(z_\mathrm{e}, z_\mathrm{h})$ driven by the corresponding m^th Fourier component of the electric field $E_m(z,t) = \frac{1}{\sqrt{2\pi}} \int \mathrm{d}\phi_k E(z,t) \mathrm{e}^{-im\phi_k} = E(z,t)\delta_{m,0}$. So for a homogeneous electromagnetic field in the x-y-plane only the $m = 0$ contribution to the excitonic transition amplitude is driven in linear optics. Starting from the ground state of the electronic system, the initial conditions are given by $p_k^m(z_\mathrm{e}, z_\mathrm{h}, t = 0) = 0$ for all m. Hence, only the equation of motion for the $m = 0$ component $p_k^{m=0}(z_\mathrm{e}, z_\mathrm{h}) = p_k(z_\mathrm{e}, z_\mathrm{h})$ has to be considered, since all other components with $m \neq 0$ stay zero with (3.7).

Therefore, due to the rotation invariance around the propagation direction the relevant contribution to the excitonic transition amplitude $p_k(z_\mathrm{e}, z_\mathrm{h})$ only depends on the modulus k of the wave vector $\mathbf{k}$ in the x-y-plane. The Coulomb interaction of electron and hole is restricted to the $V_{kk'}^{00}(z_\mathrm{e} - z_\mathrm{h}) = V_{kk'}(z_\mathrm{e} - z_\mathrm{h})$ component. The resulting equation of motion for the excitonic transition amplitude takes the form:

$$\begin{aligned} i\hbar \frac{\partial}{\partial t} p_k(z_\mathrm{e}, z_\mathrm{h}, t) &= \left[E_\mathrm{gap} - i\gamma + \frac{\hbar^2 k^2}{2\mu^*} - \frac{\hbar^2}{2m_\mathrm{e}^*} \frac{\partial^2}{\partial z_\mathrm{e}^2} - \frac{\hbar^2}{2m_\mathrm{h}^*} \frac{\partial^2}{\partial z_\mathrm{h}^2} \right] p_k(z_\mathrm{e}, z_\mathrm{h}, t) \\ &\quad - \frac{1}{(2\pi)^2} \int_0^\infty \mathrm{d}k' \left[k' V_{kk'}(z_\mathrm{e} - z_\mathrm{h}) p_{k'}(z_\mathrm{e}, z_\mathrm{h}, t) \right] - d_\mathrm{eh} E(z_\mathrm{e}, t) \delta(z_\mathrm{e} - z_\mathrm{h}) \,. \end{aligned} \tag{3.8}$$

The Coulomb matrix elements are

$$V_{kk'}(z_\mathrm{e} - z_\mathrm{h}) = \frac{e_0^2}{2\varepsilon_0 n_\mathrm{bg}^2} \int_0^{2\pi} \mathrm{d}\phi \frac{\mathrm{e}^{-|\mathbf{k}-\mathbf{k}'||z_\mathrm{e} - z_\mathrm{h}|}}{|\mathbf{k} - \mathbf{k}'|} \,, \tag{3.9}$$

with $|\mathbf{k} - \mathbf{k}'| = \sqrt{k^2 + k'^2 - 2kk' \cos\phi}$. The angle ϕ is enclosed by $\mathbf{k}$ and $\mathbf{k}'$, $n_\mathrm{bg} = \sqrt{\varepsilon_\mathrm{bg}}$ is the background refractive index and γ is a phenomenological dephasing constant.

The excitonic dynamics within the semiconductor layer obeys Eq. (3.8) and is uniquely determined by *microscopic boundary conditions*. If the motion of electrons and holes within the layer is confined by infinitely high potential barriers at z_1, z_2, these boundary conditions are given by

$$\begin{aligned} p_k(z_\mathrm{e} = z_1, z_\mathrm{h}, t) &= p_k(z_\mathrm{e} = z_2, z_\mathrm{h}, t) = 0 \,, \\ p_k(z_\mathrm{e}, z_\mathrm{h} = z_1, t) &= p_k(z_\mathrm{e}, z_\mathrm{h} = z_2, t) = 0 \,. \end{aligned} \tag{3.10}$$

Hence, the excitonic transition amplitude vanishes if either electron or hole reaches the semiconductor surface. More general, for finite band offsets in the heterostructure as investigated in Section 4.7, the exciton wave function extends into the barrier material. It is forced to vanish at the outer sample surfaces by microscopic boundary conditions.

---

[b] $\frac{1}{2\pi} \int \mathrm{d}\phi_k \mathrm{e}^{-im\phi_k} \mathrm{e}^{im'\phi_k} = \delta_{mm'}$.

Effective electron mass	m_{e}^{*}	$= 0.067\,\mathrm{m}_0$
Effective hole mass	m_{h}^{*}	$= 0.457\,\mathrm{m}_0$
Bulk GaAs gap energy	E_{gap}	$= 1.42\,\mathrm{eV}$
Dipole coupling constant	d_{eh}/e_0	$= 0.5\,\mathrm{nm}$
Dephasing constant	γ	$= 0.04\,\mathrm{meV}$
Background refractive index	n_{bg}	$= 3.71$

Table 3.1.: GaAs material parameters according to Refs. 6, 19.

The time evolution of the electromagnetic field is determined by Maxwell's equations (3.4a) and (3.4b). The source term $\partial/\partial t P(z,t)$ in Eq. (3.4a) couples the electromagnetic field to the induced macroscopic polarization $P(z,t)$. With Eq. (2.7), and in terms of the excitonic transition amplitude, $P(z,t)$ is explicitly given by:

$$P(z,t) = \sum_{\mathbf{k}} d_{\mathrm{eh}}^{*}\, p_k(z,z,t) = \frac{1}{2\pi}\int\limits_{0}^{\infty} \mathrm{d}k\, k\, d_{\mathrm{eh}}^{*}\, p_k(z,z,t)\,. \tag{3.11}$$

Therefore, the coupled light and exciton dynamics obeys the set of partial differential equations (3.4a), (3.4b) and (3.8). These equations are coupled by the macroscopic polarization (3.11). They have to be solved with respect to the microscopic boundary conditions (3.10) for the excitonic transition amplitude and Maxwell's boundary conditions for the electromagnetic fields: The continuity for the in-plane components of electric and magnetic field and their first spatial derivatives are required.

Before we introduce a method to reduce the numerical effort to calculate the time evolution of Eq. (3.8) we first briefly discuss the results of a direct solution of the discretized versions of Eqs. (3.4a), (3.4b) and (3.8) in real space and momentum space in the time domain. Details concerning the numerically involved solution of the exciton equation (3.8) are given in Appendix B.1. A detailed discussion of the discretization of Maxwell's equations (3.4a), (3.4b) is given in Appendix B.2. The calculation starts with a vanishing excitonic polarization for $t = 0$. When the light pulse, described by Maxwell's equations (3.4a) and (3.4b) in their discretized form, reaches the sample at time t, an excitonic polarization $p_k(z_{\mathrm{e}}, z_{\mathrm{h}}, t)$ is induced that obeys the inhomogeneous exciton equation (3.8). Because of the locality of the dipole matrix element in Eq. (3.8), the electric field only acts as a direct source for the excitonic polarization for equal electron and hole coordinates $z_{\mathrm{e}} = z_{\mathrm{h}}$. The non-locality of the interacting two-particle problem manifests via the spatial derivatives for electron and hole coordinates which couple different space points during the time evolution of the excitonic polarization as described in Appendix B.1. Numerical integration of Eq. (3.8) with a small time step Δt yields the excitonic polarization at time $t + \Delta t$. The resulting macroscopic polarization (3.11) at time $t + \Delta t$ enters Maxwell's equations and causes a change of the fields themselves which then act again as a source to the excitonic polarization at time $t + \Delta t$. A self-consistent solution of this set of coupled differential equations in space and time can be found for sufficiently small time steps Δt as illustrated in Fig. 3.1.

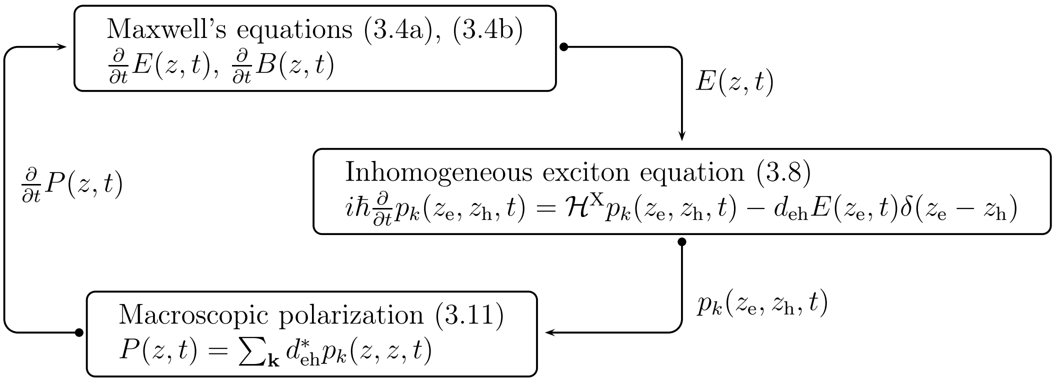

Figure 3.1: Illustration of the self-consistent solution of the coupled set of equations (3.4a), (3.4b) and (3.8) in the time domain. Along the arrows the quantities that couple the different equations are indicated.

Figure 3.2 shows a calculated transmission spectrum for a GaAs layer with a thickness of 10 exciton Bohr radii surrounded by infinitely high potential barriers. To avoid Fabry-Perot effects, here, an anti-reflection coating of the surfaces of the heterostructure has been simulated by use of the same constant background refractive index n_bg inside and outside the GaAs layer. Material parameters are given in Table 3.1. Fourier transformation yields the transmission $T(\omega)$ which is given by the transmitted, $I_\mathrm{trans}(\omega)$, divided by the incident, $I_\mathrm{inc}(\omega)$, light intensity

$$T(\omega)=\frac{I_\mathrm{trans}(\omega)}{I_\mathrm{inc}(\omega)}\,.$$

The excitation energy is given relative to the bulk band-gap energy E_gap and normalized to the corresponding bulk exciton binding energy E_b^X. In the transmission spectrum of a layer with finite thickness in Fig. 3.2, several resonances are present which have not been observed in the Hydrogen-like exciton spectrum of an idealized bulk semiconductor, displayed in Fig. 2.1. The calculated transmission shows several additional resonances, best seen between the energy positions of 1s and 2s exciton at -1 and -0.25, respectively. These resonances are due to the spatial confinement of the carrier motion in the z-direction. In analogy to a "center of mass quantization", the spatial confinement potential for electrons and holes in one dimension results in a discrete quantum mechanical energy spectrum. The level spacing sensitively depends on the layer thickness and the height of the confinement potential. Strictly speaking, the resonances visible in the transmission spectrum are the so-called *polariton modes* corresponding to the quantum mechanical eigenstates of the coupled light and exciton system influenced by the sample boundaries. The oscillator strength (height in the transmission spectrum) of the polaritonic resonances strongly depends on the spatial structure of the corresponding exciton states in the direction of propagation, and therefore on the layer thickness. This fact becomes more obvious in the following section.

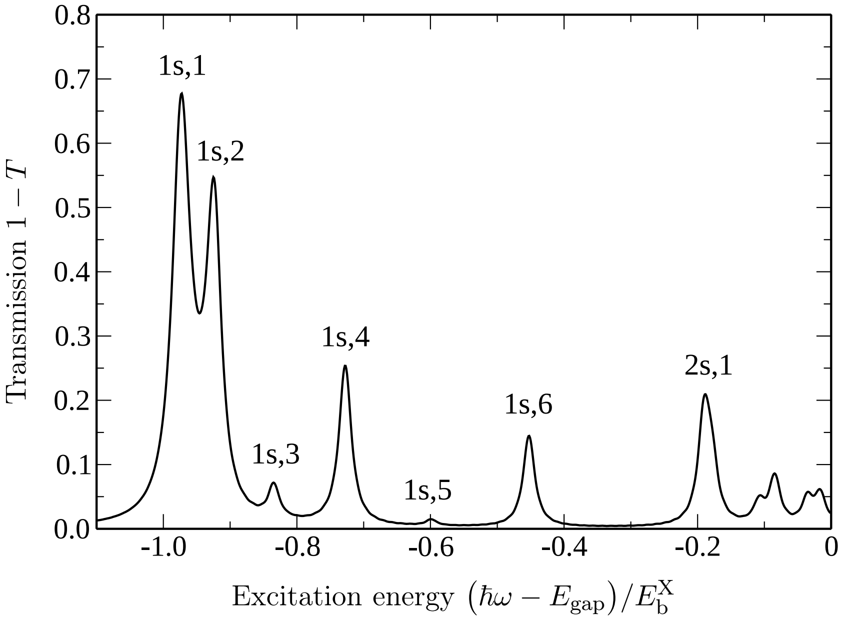

Figure 3.2: Calculated transmission spectrum for a GaAs layer with thickness of $10\,\mathrm{a}_0^{\mathrm{X}} \approx 125\,\mathrm{nm}$. The excitation energy is given relative to the bulk band-gap energy E_{gap} in units of the bulk exciton binding energy $E_{\mathrm{b}}^{\mathrm{X}}$.

In an experiment, the polariton resonances are most pronounced in high quality heterostructures with typical spatial extensions from $2\,\mathrm{a}_0^{\mathrm{X}}$ up to $20\,\mathrm{a}_0^{\mathrm{X}}$ at low temperatures (for example Helium-cooled at 4 K). High quality of the heterostructures is required to minimize the dephasing of the excitonic polarization by carrier scattering at defects in the crystal lattice structure; additionally at low temperatures scattering with phonons is strongly reduced. The typical polariton signatures result from the deviation of the system from an idealized bulk crystal, or, coming from the other extreme, from a quasi two-dimensional quantum-well. The dimensionality of these systems can be characterized to be somewhere in between two and three space dimensions.

3.2. The Exciton Basis – Time Domain

In the previous section a microscopic formulation of the coupled light and exciton dynamics has been given. However, the direct solution of the problem by discretization of the partial differential equations of motion in space and time is numerically very demanding.[6] Especially the numerical integration of the exciton equation (3.8) turns out to be very time-consuming because of the non-locality of the excitonic transition amplitude $p_k(z_{\mathrm{e}}, z_{\mathrm{h}}, t)$ in real space. Transition amplitudes for different coordinates $z_{\mathrm{e}}, z_{\mathrm{h}}$ are coupled to each other by the spatial derivatives in the kinetic part of the excitonic Hamiltonian. In this section, an alternative approach for the solution of the problem is presented, which strongly reduces the numerical effort.

In Eq. (3.2) the exciton equation formally has the structure of an inhomogeneous time dependent Schrödinger equation,

$$i\hbar\frac{\partial}{\partial t}p_{(\mathbf{k},z_\mathrm{e},z_\mathrm{h})}(t) = \mathcal{H}^\mathrm{X}p_{(\mathbf{k},z_\mathrm{e},z_\mathrm{h})}(t) - d_\mathrm{eh}E(z_\mathrm{e},t)\delta(z_\mathrm{e}-z_\mathrm{h})\,, \tag{3.12}$$

with the excitonic Hamiltonian $\mathcal{H}^\mathrm{X}$. Numerical details about the discretization of the Hamiltonian are given in Appendix B.1. Again we consider a circularly polarized light field. The excitonic transition amplitude $p_{(\mathbf{k},z_\mathrm{e},z_\mathrm{h})}(t)$ can be expanded in terms of the complete set of excitonic eigenfunctions $\phi_m(\mathbf{k},z_\mathrm{e},z_\mathrm{h})$. The eigenfunctions and corresponding eigenenergies ε_m obey the eigenvalue equation

$$\mathcal{H}^\mathrm{X}\phi_m(\mathbf{k},z_\mathrm{e},z_\mathrm{h}) = \varepsilon_m\phi_m(\mathbf{k},z_\mathrm{e},z_\mathrm{h})\,. \tag{3.13}$$

Note, that at this point our approach strongly deviates from earlier formulations[3, 38, 39] since we use an excitonic eigenbasis where the eigenfunctions $\phi_m(\mathbf{k},z_\mathrm{e},z_\mathrm{h})$ individually fulfill the microscopic boundary conditions (3.10). Expanding the excitonic transition amplitude with respect to this basis yields

$$p_\mathbf{k}(z_\mathrm{e},z_\mathrm{h},t) = \sum_m p_m(t)\phi_m(\mathbf{k},z_\mathrm{e},z_\mathrm{h})\,, \tag{3.14}$$

with time dependent coefficients $p_m(t)$. Inserting this expansion into the equation of motion (3.12),

$$i\hbar\frac{\partial}{\partial t}\sum_m p_m(t)\phi_m(\mathbf{k},z_\mathrm{e},z_\mathrm{h}) = \sum_m \varepsilon_m p_m(t)\phi_m(\mathbf{k},z_\mathrm{e},z_\mathrm{h}) - d_\mathrm{eh}E(z_\mathrm{e},t)\delta(z_\mathrm{e}-z_\mathrm{h})\,,$$

and using the orthonormality

$$\sum_\mathbf{k}\int \mathrm{d}z\mathrm{d}z'\phi^*_m(\mathbf{k},z,z')\phi_{m'}(\mathbf{k},z,z') = \delta_{mm'} \tag{3.15}$$

yields the equation of motion for the expansion coefficients:

$$\begin{aligned} i\hbar\frac{\mathrm{d}}{\mathrm{d}t}p_m(t) &= (\varepsilon_m - i\gamma)p_m(t) - \underbrace{d_\mathrm{eh}\int\left(\mathrm{d}z\,E(z,t)\sum_\mathbf{k}\phi^*_m(\mathbf{k},z,z)\right)}_{\Phi_m(t)} \\ &= (\varepsilon_m - i\gamma)p_m(t) - \Phi_m(t)\,. \end{aligned} \tag{3.16}$$

In analogy to Eq. (3.8) a phenomenological dephasing constant γ has been introduced. For the time evolution of the excitonic transition amplitude this approach yields one ordinary differential equation for each expansion coefficient $p_m(t)$. The source term $\Phi_m(t)$ for each coefficient $p_m(t)$ is given by the projection of the electric field amplitude $E(z,t)$ to the m^th excitonic eigenstate $\phi_m(\mathbf{k},z_\mathrm{e},z_\mathrm{h})$ and is therefore strongly dependent on its spatial structure. The solution of the homogeneous part of equation (3.16) can be given in terms of damped, oscillating solutions for each contributing eigenstate m:

$$p^\mathrm{free}_m(t) = \left(A\mathrm{e}^{+i\frac{\varepsilon_m}{\hbar}t} + B\mathrm{e}^{-i\frac{\varepsilon_m}{\hbar}t}\right)\mathrm{e}^{-\frac{\gamma}{\hbar}t}\,.$$

So, a description of the excitonic system as an ensemble of oscillators with frequencies $\omega_m = \varepsilon_m/\hbar$ has been formulated. It is self-consistently coupled to the electromagnetic field by the driving terms $\Phi_m(t)$ and the macroscopic polarization (3.11). In terms of excitonic eigenstates and with time dependent coefficients the latter one reads

$$P(z,t) = \sum_m p_m(t) \sum_{\mathbf{k}} d_{\mathrm{eh}}^* \phi_m(\mathbf{k}, z, z)\,. \tag{3.17}$$

Once having calculated the excitonic eigenenergies ε_m and eigenstates[c] $\phi_m(\mathbf{k}, z, z')$ for a given heterostructure, Eq. (3.16) can be solved as an alternative to the direct discretization of Eq. (3.8) presented in the previous section. The polarization of the system as response to an external electromagnetic field is determined by the dynamics of the expansion coefficients $p_m(t)$. Maxwell's equations (3.4a) and (3.4b) are not affected by the expansion of the excitonic problem and can be solved as outlined in the previous section. For typical transmission spectra as shown in Fig. 3.2, we are only interested in the lower energy part of the polaritonic spectrum. Therefore a restriction of the expansion (3.14) to a few of the energetically lowest exciton states is possible in a very good approximation. Within this approximation we are left with a finite number of ordinary differential equations for the time evolution of the expansion coefficients $p_m(t)$. The numerical effort depends on the number of considered states but is typically reduced by more than one order of magnitude compared to the direct solution. In fact, this approach nearly perfectly reproduces the results of the direct solution as long as all neglected exciton states are spectrally well-separated from the investigated part of the spectrum. This separation must at least exceed the homogeneous broadening of the resonances in the spectrum. For example, Fig. 3.3 shows the transmission spectrum of the previous section calculated with the direct solution (dashed line) and within the truncated exciton basis (solid line) with seven exciton states taken into account. The full transmission $1-T$ is shifted by 0.3 on the vertical axis for better visibility. Since we find nearly perfect agreement of both spectra, this comparison confirms the validity of the expansion (3.14) and the truncation of the chosen set of exciton eigenstates. Hence, in linear optics a decoupling of polariton states is found as long as they are spectrally well-separated.

Another advantage of the solution in the truncated exciton basis over the direct solution is the possibility to perform the numerically demanding solution of the excitonic eigenvalue problem (3.13) separately from the system dynamics (3.16) in time. The exciton eigenenergies and eigenstates can be stored for a given heterostructure. Following calculations can then easily be done for different dephasings γ or dipole coupling constants d_{eh} or for different excitation conditions. Additionally, the expansion of the dynamic quantities in terms of exciton eigenstates provides the basis for an extension of the microscopic theory to nonlinear optical effects in Part II. Especially the calculation of optical spectra for different excitation conditions without the need to solve the excitonic or biexcitonic problem each time becomes indispensable in nonlinear optics.

---

[c] Following Section 3.1 a restriction of the expansion (3.14) to in-plane s-shaped exciton eigenstates is exact as there is no driving term for states with non-vanishing in-plane angular momentum for the chosen geometry. Therefore the solution of the eigenvalue problem is only needed for exciton states with in-plane s symmetry.

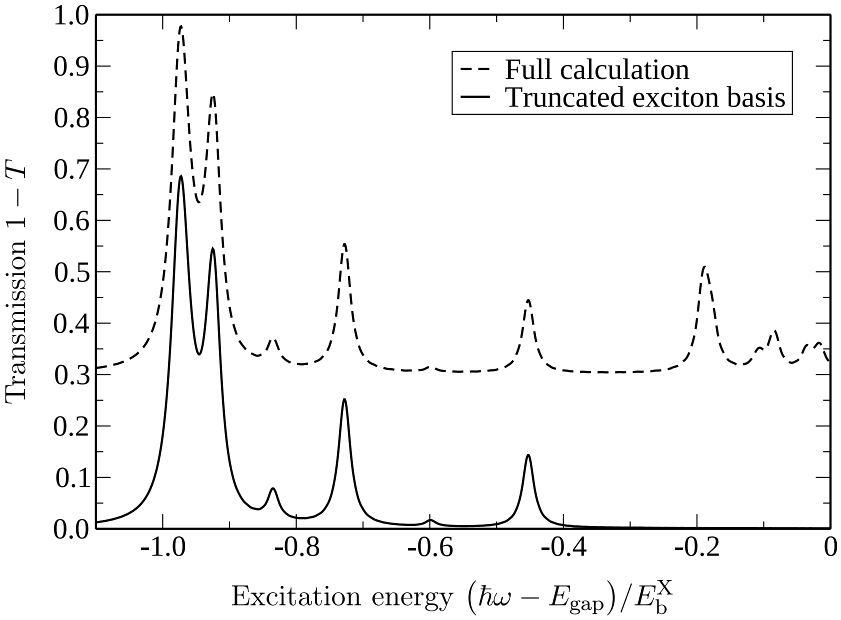

Figure 3.3: Comparison of transmission spectra for a GaAs layer with $10\,\text{a}_0^{\text{X}}$ thickness. Solid line: Calculation in the truncated exciton basis. Dashed line: Full calculation, for details refer to Section 3.1. The dashed line is shifted by 0.3 on the vertical axis for better visibility.

3.3. The Exciton Basis – Frequency Domain

In this section another alternative approach to the solution of the exciton equation (3.1) self-consistently coupled to Maxwell's equations is presented. In Section 3.3.1, the linear response of the system to the external field is deduced in terms of a frequency dependent, *non-local* excitonic susceptibility $\chi(z, z', \omega)$. The solution of the electromagnetic wave equation in frequency domain is discussed in Section 3.3.2.

3.3.1. Non-Local Susceptibility

In the first part of this section, the excitonic susceptibility is directly calculated from an eigenfunction expansion inserted into the inhomogeneous exciton equation in frequency domain. This is then put in a more general framework where the excitonic susceptibility is obtained from the general linear response theory.

Expansion of the Excitonic Transition Amplitude

Using the Fourier transformed excitonic transition amplitude $p_{(\mathbf{k},z_{\text{e}},z_{\text{h}})}(\omega)$ and the electric field $E(z,\omega)$ in frequency domain, the inhomogeneous exciton equation (3.2) reads

$$(\hbar\omega + i\gamma - \mathcal{H}^{\text{X}})p_{(\mathbf{k},z_{\text{e}},z_{\text{h}})}(\omega) = -d_{\text{eh}}\delta(z_{\text{e}} - z_{\text{h}})E(z_{\text{e}},\omega)\,, \tag{3.18}$$

with a phenomenological dephasing constant γ. Again we consider a circularly polarized light field as introduced in the previous sections.

The expansion of the excitonic transition amplitude in terms of exciton eigenfunctions $\phi_m(\mathbf{k}, z_\mathrm{e}, z_\mathrm{h})$ with, in contrast to Eq. (3.14), frequency dependent expansion coefficients $b_m(\omega)$ is given by:

$$p_{(\mathbf{k},z_\mathrm{e},z_\mathrm{h})}(\omega) = \sum_m b_m(\omega)\phi_m(\mathbf{k}, z_\mathrm{e}, z_\mathrm{h})\,. \tag{3.19}$$

With this expansion, Eq. (3.18) takes the form

$$\sum_m (\hbar\omega + i\gamma - \varepsilon_m) b_m(\omega)\phi_m(\mathbf{k}, z_\mathrm{e}, z_\mathrm{h}) = -d_\mathrm{eh}\delta(z_\mathrm{e} - z_\mathrm{h})E(z_\mathrm{e}, \omega)\,,$$

where ε_m and $\phi_m(\mathbf{k}, z_\mathrm{e}, z_\mathrm{h})$ fulfill the eigenvalue equation (3.13). The orthonormality of the $\phi_m(\mathbf{k}, z_\mathrm{e}, z_\mathrm{h})$ yields:

$$(\hbar\omega + i\gamma - \varepsilon_m) b_m(\omega) = -d_\mathrm{eh}\sum_\mathbf{k}\int \mathrm{d}z\, E(z,\omega)\phi_m^*(\mathbf{k}, z, z)\,.$$

Therefore the frequency dependent expansion coefficients are given by

$$b_m(\omega) = -d_\mathrm{eh}\sum_\mathbf{k}\frac{\int \mathrm{d}z\, E(z,\omega)\phi_m^*(\mathbf{k}, z, z)}{\hbar\omega + i\gamma - \varepsilon_m}\,. \tag{3.20}$$

Insertion of Eq. (3.20) into Eq. (3.19) yields the excitonic transition amplitude in the form

$$p_{(\mathbf{k},z_\mathrm{e},z_\mathrm{h})}(\omega) = -d_\mathrm{eh}\sum_m\frac{\sum_{\mathbf{k}'}\int \mathrm{d}z' E(z',\omega)\phi_m^*(\mathbf{k}', z', z')}{\hbar\omega + i\gamma - \varepsilon_m}\phi_m(\mathbf{k}, z_\mathrm{e}, z_\mathrm{h})\,.$$

The Fourier transformed, frequency dependent macroscopic polarization $P(z,\omega)$, Eq. (3.11), induced by the circularly polarized light, is given by:

$$\begin{aligned} P(z,\omega) &= \sum_\mathbf{k}\int \mathrm{d}z_\mathrm{rel}\, d_\mathrm{eh}^* p_{(\mathbf{k},z_\mathrm{e},z_\mathrm{h})}(\omega)\delta(z_\mathrm{e} - z_\mathrm{h}) \\ &= \int \mathrm{d}z' E(z',\omega)\Big(- |d_\mathrm{eh}|^2 \sum_m\sum_{\mathbf{k}\mathbf{k}'}\frac{\phi_m^*(\mathbf{k}', z', z')\phi_m(\mathbf{k}, z, z)}{\hbar\omega + i\gamma - \varepsilon_m}\Big)\,. \end{aligned} \tag{3.21}$$

From this, the frequency dependent non-local susceptibility for optically excited electron-hole pair transitions within a semiconductor layer can be defined in terms of exciton eigenstates by

$$\chi(z, z', \omega) = -|d_\mathrm{eh}|^2 \sum_m\sum_{\mathbf{k}\mathbf{k}'}\frac{\phi_m^*(\mathbf{k}', z', z')\phi_m(\mathbf{k}, z, z)}{\hbar\omega + i\gamma - \varepsilon_m}\,. \tag{3.22}$$

Note, that in our approach, the exciton eigenstates $\phi_m(\mathbf{k}, z_\mathrm{e}, z_\mathrm{h})$ fulfill the physical boundary conditions of the spatially inhomogeneous system and are not the bulk eigenstates used in the previous approaches of Refs. 3, 38, 39. The macroscopic polarization, Eq. (3.21), is given by:

$$P(z,\omega) = \int \mathrm{d}z' E(z',\omega)\chi(z, z', \omega)\,.$$

As already used in the previous sections, excitonic excitations for the chosen geometry are restricted to exciton states with vanishing in-plane angular momentum and therefore to states with in-plane s symmetry. Hence, only these states have to be included in the expansion (3.19). This yields the final result for the excitonic susceptibility for the given sample geometry:

$$\chi(z,z',\omega) = -\frac{|d_{\mathrm{eh}}|^2}{(2\pi)^2}\sum_m \int \mathrm{d}k\,\mathrm{d}k'\,kk'\frac{\phi_m^*(k',z',z')\phi_m(k,z,z)}{\hbar\omega + i\gamma - \varepsilon_m}\,.$$

In the next section the same result is deduced from the more general linear response theory following Ref. 27. Note, that the linear susceptibility (3.22) is independent of the polarization state of the exciting light field. Therefore the macroscopic polarization induced by a light field in an arbitrary polarization state is given by two contributions. Each contribution only depends on the z-dependent amplitude of the electric fields with the corresponding circular polarization. Hence, in linear optics the macroscopic polarization is polarized in the same manner as the exciting light field.

Linear Response Theory

Following Ref. 27, the resonant contribution to the susceptibility of the electronic system in its ground state $|0\rangle$ at temperature $T = 0$ is deduced. The linear response to an external perturbation via the operator B is given by

$$\chi(\omega + i\gamma) = -\sum_m \frac{\langle 0|\,B\,|m\rangle\,\langle m|\,A\,|0\rangle}{\hbar\omega + i\gamma - \varepsilon_m}\,, \tag{3.23}$$

where the observable of interest is given by the expectation value of the operator $\langle A\rangle$. In our approach only the resonant part of the susceptibility for frequencies $\omega > 0$ is taken into account as the non-resonant contribution is negligible because of the large band-gap energy. The many-particle states of the electronic system are denoted by $|m\rangle$.

We are interested in the macroscopic polarization of the system and the coupling of the electronic system to the external field via the dipole operator $e_0\mathbf{r}$. Therefore the operators A and B are both given by $\mathbf{A} = \mathbf{B} = e_0\mathbf{r}$, where $\mathbf{r} = \mathbf{r}_\mathrm{e} - \mathbf{r}_\mathrm{h}$ is the relative position vector between electron and hole. The expansion of $\mathbf{A}$, $\mathbf{B}$ in second quantization reads[d)]

$$\begin{aligned}\mathbf{A} = \mathbf{B} = e_0\mathbf{r} &= \sum_{\mathbf{k}} \int \mathrm{d}z_{\mathrm{rel}}\,\underbrace{\langle \mathbf{k},\mathrm{e},z_\mathrm{e}|\,e_0\mathbf{r}\,|\mathbf{k},\mathrm{h},z_\mathrm{h}\rangle}_{\mathbf{d}_{\mathrm{eh}}\delta(z_\mathrm{e}-z_\mathrm{h})}\,\psi_{\mathbf{k}}^{\mathrm{e}\dagger}(z_\mathrm{e})\psi_{\mathbf{k}}^{\mathrm{h}\dagger}(z_\mathrm{h}) + \mathrm{h.c.} \qquad (3.24)\\ &= \mathbf{d}_{\mathrm{eh}}\sum_{\mathbf{k}}\psi_{\mathbf{k}}^{\mathrm{e}\dagger}(Z)\psi_{\mathbf{k}}^{\mathrm{h}\dagger}(Z) + \mathrm{h.c.}\,,\end{aligned}$$

using electron-hole relative, z_{rel}, and center of mass, Z, coordinates with $z_\mathrm{e} = Z + \frac{m_\mathrm{h}}{M}z_{\mathrm{rel}}$ and $z_\mathrm{h} = Z - \frac{m_\mathrm{e}}{M}z_{\mathrm{rel}}$.

[d)] The expansion is done with respect to the electron-hole relative coordinates $\mathbf{k}$ and $z_{\mathrm{rel}} = z_\mathrm{e} - z_\mathrm{h}$ because the microscopic dipole is made up of these two particles.

As in Chapter 1, a $\mathbf{k}$-independent, and therefore in real space local, dipole matrix element $\langle \mathbf{k}, \mathrm{e}, z_\mathrm{e} | \, e_0 \mathbf{r} \, | \mathbf{k}, \mathrm{h}, z_\mathrm{h} \rangle = \mathbf{d}_\mathrm{eh} \delta(z_\mathrm{e} - z_\mathrm{h})$ is used. Due to the structure of the operators $\mathbf{A}$ and $\mathbf{B}$, here, only states contribute to the linear optical response where only one electron-hole pair is excited from the electronic ground state. Therefore the sum in Eq. (3.23) can be restricted to exciton states. Expansion of these effective two-particle states in terms of one-particle product states, starting from the ground state $|0\rangle$ yields:

$$|m\rangle = \sum_{\mathbf{k}} \int \mathrm{d}z_\mathrm{e} \mathrm{d}z_\mathrm{h} \, a^m_{\mathbf{k}}(z_\mathrm{e}, z_\mathrm{h}) \psi^{\mathrm{e}\dagger}_{\mathbf{k}}(z_\mathrm{e}) \psi^{\mathrm{h}\dagger}_{\mathbf{k}}(z_\mathrm{h}) \, |0\rangle \, . \tag{3.25}$$

Working in the exciton eigenbasis the expansion coefficients $a^m_{\mathbf{k}}(z_\mathrm{e}, z_\mathrm{h})$ in Eq. (3.25) are just given by the exciton eigenstates $\phi_m(\mathbf{k}, z_\mathrm{e}, z_\mathrm{h})$ used in the previous sections.

Insertion of the expansions (3.24) and (3.25) into Eq. (3.23) yields the frequency dependent non-local susceptibility for excitonic excitations by weak external optical fields:

$$\chi(z, z', \omega) = -|d_\mathrm{eh}|^2 \sum_m \sum_{\mathbf{k}\mathbf{k}'} \frac{\phi^*_m(\mathbf{k}', z', z') \phi_m(\mathbf{k}, z, z)}{\hbar\omega + i\gamma - \varepsilon_m} \, . \tag{3.26}$$

This is the same result that has already been deduced in the previous section in Eq. (3.22), directly from the inhomogeneous exciton equation. The result (2.23) for the excitonic susceptibility in a homogeneous system directly follows from Eq. (3.26) with the exciton eigenfunctions of the bulk material and noting that for the bulk material the substitution $\sum_{\mathbf{k}} \phi_m(\mathbf{k}, z, z) \rightarrow \tilde{\phi}_\nu(\tilde{\mathbf{r}} = 0) \mathrm{e}^{i q_z z}$ in Eq. (3.26) is valid. The summation in Eq. (3.26) is over the bulk quantum numbers now, $m \rightarrow \{\nu, q_z\}$.

An alternative approach to the exciton equation (3.1) has been deduced here by application of a linear response theory to the electronic system in its ground state perturbed by a weak external field. This theory is equivalent to the previous formulation in terms of the excitonic transition amplitude.

Figure 3.4 shows the real $\mathrm{Re}\,\chi(z, z', \omega)$ and the imaginary $\mathrm{Im}\,\chi(z, z', \omega)$ part of the non-local excitonic susceptibility for the lowest three resonances in the transmission spectrum of Fig. 3.3. The imaginary parts, that are connected to the absorption in the material, are depicted in the upper part of Fig. 3.4. They exhibit a structure looking similar to a product of standing waves for the z and the z' direction. This finding motivates a simplified interpretation of the system in terms of excitons with quantized center of mass momentum that might be able to describe its major properties. In fact, due to its simplicity, this picture is often used for the analysis of optical spectra of spatially confined excitons, see discussion in Section 3.5 and Chapter 4. Even though qualitative features can be understood in this simplified picture, within the microscopic theory we find a structure of the susceptibility that is more complicated and that is also strongly influenced by the exciton relative motion which enters the eigenstates in Eq. (3.26). These eigenstates are determined by the Hamiltonian $\mathcal{H}^\mathrm{X}$ in Eq. (3.2) which contains the full electron and hole motion in the z-direction. Note, that because of the finite spatial extension of the exciton relative motion surface regions with almost vanishing susceptibility are encountered before the surfaces at $z, z' = 0, 10\,\mathrm{a}^\mathrm{X}_0$ are actually

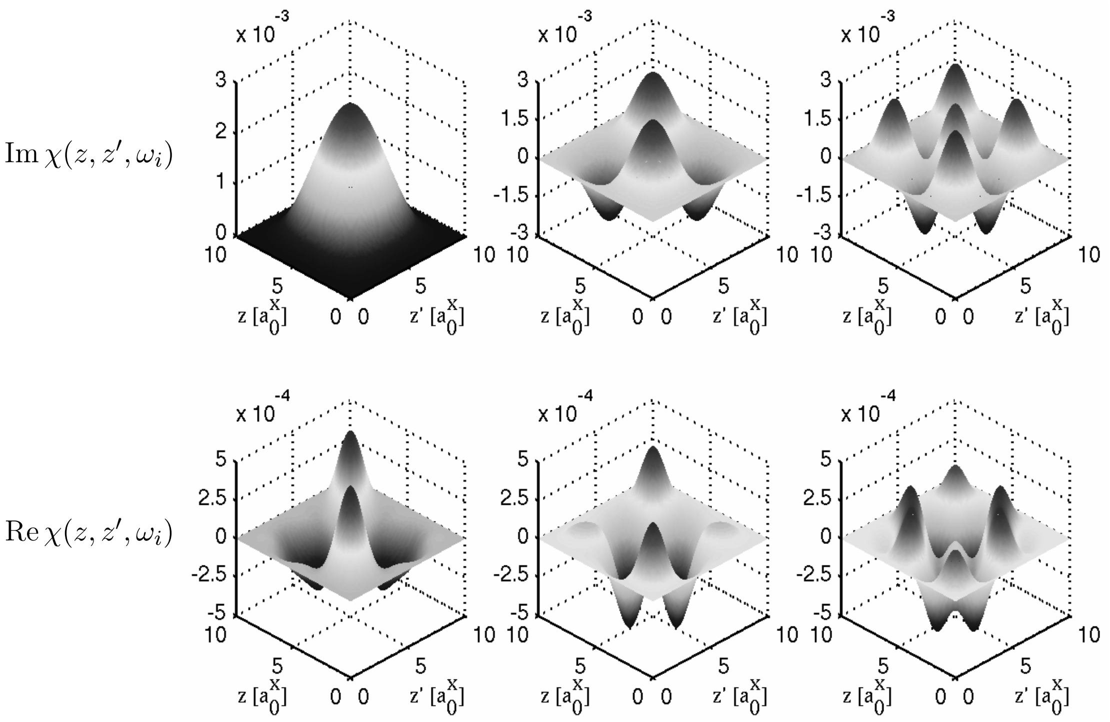

Figure 3.4: Non-local excitonic susceptibility for the lowest three resonance frequencies ω_i in Fig. 3.3. Increasing frequency from left to right. Top: Imaginary part $\mathrm{Im}\,\chi(z,z',\omega_i)$, bottom: Real part $\mathrm{Re}\,\chi(z,z',\omega_i)$.

reached in Fig. 3.4. The resulting polarization-free layers at the semiconductor surfaces are discussed in detailed in Section 4.1. An interpretation of the real part is not that intuitive, but note that both parts are symmetric with respect to interchange of z and z' and that the essential non-locality directly follows from the microscopic description of confined excitons. It should be emphasized again, that only for a system with translation invariance, a local excitonic susceptibility $\chi(z,z',\omega) = \chi(z-z',\omega)$ can be deduced because only in this case the exciton relative and COM motion can be separated.

3.3.2. The Wave Equation

Having deduced the excitonic susceptibility (3.26) in the previous section it can be used as an input for the calculation of optical spectra. For propagation in the z-direction, the wave equation for the transversal electric field $\mathbf{E}(z,\omega)$ in frequency domain is given by:[e]

$$\begin{aligned}\left[\frac{\partial^2}{\partial z^2} + n_{\mathrm{bg}}^2\frac{\omega^2}{c_0^2}\right]\mathbf{E}(z,\omega) &= -\frac{\omega^2}{\varepsilon_0 c_0^2}\mathbf{P}(z,\omega) \\ &= -\frac{\omega^2}{\varepsilon_0 c_0^2}\int \mathrm{d}z'\chi(z,z',\omega)\mathbf{E}(z',\omega)\,.\end{aligned} \tag{3.27}$$

---

[e] Only $\mathbf{E}(z,\omega)$ needs to be determined; the magnetic field directly follows from Maxwell's equations.

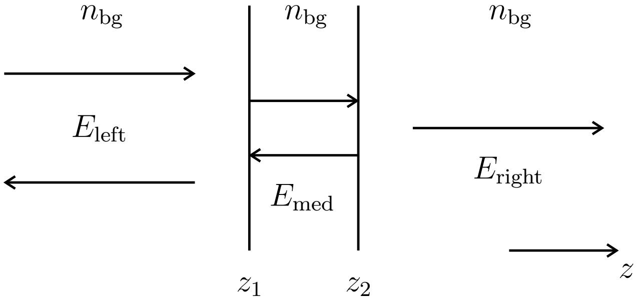

Figure 3.5: Illustration of the geometry that is considered for the solution of the one-dimensional wave equation.

Concentrating on the solution for the scalar z-dependent field amplitude $E(z,\omega)$ of one circularly polarized component of the electric field $\mathbf{E}(z,\omega)$, we end up with the scalar wave equation:

$$\left[\frac{\partial^2}{\partial z^2} + n_{\mathrm{bg}}^2 \frac{\omega^2}{c_0^2}\right] E(z,\omega) = -\frac{\omega^2}{\varepsilon_0 c_0^2} \int \mathrm{d}z' \chi(z,z',\omega) E(z',\omega)\,. \tag{3.28}$$

The solution has to be determined with respect to Maxwell's boundary conditions: Continuity of the in-plane component of the field itself and of its first spatial derivative is required. Again, a simplified model of a single semiconductor layer surrounded by infinitely high confinement potentials for electrons and holes is considered as illustrated in Fig. 3.5. An anti-reflection coating of the outer sample surfaces (not shown in Fig. 3.5) is simulated by use of the same background refractive indices inside and outside the sample as already described in the previous sections. For this slightly simplified model the solution of the wave equation in frequency domain is explicitly demonstrated. Using a transfer matrix method, this approach can easily be extended to more complicated structures including Fabry-Perot effects for the optical field as it is outlined in Section 4.2.2. A solution of Eq. (3.28) in momentum space, which could be used in bulk semiconductors in Section 2.2, is not appropriate here because of the inhomogeneity of the system and the consequently missing momentum conservation which results in a non-local excitonic susceptibility.

Figure 3.5 illustrates the considered situation for light propagation through the semiconductor layer. Outside of the sample, on the left, an ansatz with an incoming and a reflected plane wave contribution is used:

$$E_{\mathrm{left}}(z,\omega) = \mathrm{e}^{iq(\omega)z} + E_{\mathrm{r}}(\omega)\mathrm{e}^{-iq(\omega)z}\,, \tag{3.29}$$

with $q^2(\omega) = n_{\mathrm{bg}}^2 \frac{\omega^2}{c_0^2}$. The amplitude of the incoming field is normalized to unity. Outside of the sample, on the right, we only have a transmitted contribution with amplitude $E_{\mathrm{t}}(\omega)$:

$$E_{\mathrm{right}}(z,\omega) = E_{\mathrm{t}}(\omega)\mathrm{e}^{iq(\omega)z}\,. \tag{3.30}$$

Due to the coupling of the light field to the material polarization, the solution exhibits a more complicated structure inside the sample. It cannot just be captured by a linear combination of two plane waves. Formally the right hand side of the integro differential equation (3.28) can be handled as an inhomogeneity, although depending on the desired solution itself. A meaningful ansatz for the solution inside the sample is given by the sum of a particular solution of the inhomogeneous equation (3.28) and a general solution of its homogeneous part. A particular solution of the inhomogeneous equation can be found by the corresponding Green's function, which satisfies

$$\left[\frac{\partial^2}{\partial z^2} + n_{\mathrm{bg}}^2 \frac{\omega^2}{c_0^2}\right] G(z, z', \omega) = \delta(z - z') \,.$$

For the one-dimensional wave equation (3.28) it is given by[41]

$$G(z, z', \omega) = G(z - z', \omega) = -\frac{i}{2q(\omega)} \mathrm{e}^{iq(\omega)|z-z'|} \,.$$

The general solution of the homogeneous equation (3.28) is given by a propagating and a counter-propagating plane wave with amplitudes $a(\omega)$ and $b(\omega)$, respectively. Therefore the solution inside the sample is given by

$$\begin{aligned} E_{\mathrm{med}}(z, \omega) =& a(\omega)\mathrm{e}^{iq(\omega)z} + b(\omega)\mathrm{e}^{-iq(\omega)z} \\ & + \underbrace{\int \mathrm{d}z' G(z, z', \omega) \left[-\frac{\omega^2}{\varepsilon_0 c_0^2} \int \mathrm{d}z'' \chi(z', z'', \omega) E(z'', \omega)\right]}_{S(z,\omega)} \,. \end{aligned} \tag{3.31}$$

Continuity of $E(z, \omega)$ and its spatial derivative $E'(z, \omega)$ at the interfaces between the three regions yields four linear equations for the four unknown coefficients $a(\omega)$, $b(\omega)$, $E_{\mathrm{r}}(\omega)$ and $E_{\mathrm{t}}(\omega)$:[f)]

1. Continuity of $E(z, \omega)$ at $z = 0$:

$$1 + E_{\mathrm{r}}(\omega) = a(\omega) + b(\omega) + S(0, \omega) \tag{3.32a}$$

2. Continuity of $E(z, \omega)$ at $z = L$:

$$E_{\mathrm{t}}(\omega)\mathrm{e}^{iq(\omega)L} = a(\omega)\mathrm{e}^{iq(\omega)L} + b(\omega)\mathrm{e}^{-iq(\omega)L} + S(L, \omega) \tag{3.32b}$$

3. Continuity of $\frac{\partial}{\partial z} E(z, \omega)$ at $z = 0$:

$$iq(\omega) - iq(\omega)E_{\mathrm{r}}(\omega) = iq(\omega)a(\omega) - iq(\omega)b(\omega) + S'(z, \omega)\big|_{z=0} \tag{3.32c}$$

4. Continuity of $\frac{\partial}{\partial z} E(z, \omega)$ at $z = L$:

$$\begin{aligned} iq(\omega)E_{\mathrm{t}}(\omega)\mathrm{e}^{iq(\omega)L} =& iq(\omega)a(\omega)\mathrm{e}^{iq(\omega)L} \\ & - iq(\omega)b(\omega)\mathrm{e}^{-iq(\omega)L} + S'(z, \omega)\big|_{z=L} \end{aligned} \tag{3.32d}$$

[f)] As a short notation we use $S'(z, \omega) = \frac{\partial}{\partial z} S(z, \omega)$.

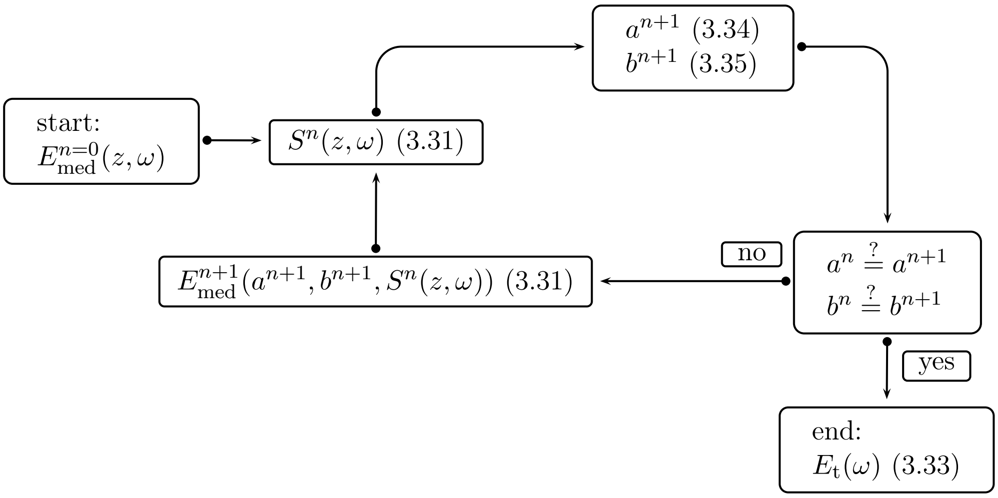

Figure 3.6: Self-consistency scheme for the solution of the polariton problem in frequency domain. The steps in the iterative solution are given by the superscript index n for all quantities that are adapted during the iteration process.

The formal solution of this system of linear equations (3.32a)-(3.32d) is straight forward and yields the amplitude $E_{\text{t}}(\omega)$ of the transmitted part of the field:

$$E_{\text{t}}(\omega) = -\frac{1}{2}\Bigg[S(0,\omega) - 2 - S(L,\omega)\mathrm{e}^{-iq(\omega)L} + \frac{1}{iq(\omega)}\left(S'(z,\omega)\big|_{z=0} - S'(z,\omega)\big|_{z=L}\mathrm{e}^{-iq(\omega)L}\right)\Bigg] . \quad (3.33)$$

However, the solution has to be computed self-consistently as the formal inhomogeneity, the right hand side of Eq. (3.28), depends on the desired solution itself. As illustrated in Fig. 3.6, the self-consistent solution also requires the amplitudes $a(\omega)$ and $b(\omega)$ for the propagating and counter-propagating plane wave contributions inside the sample,

$$a(\omega) = -\frac{1}{2}\left(S(0,\omega) + \frac{S'(z,\omega)\big|_{z=0}}{iq(\omega)} - 2\right), \quad (3.34)$$

$$b(\omega) = -\frac{1}{2}\mathrm{e}^{iq(\omega)L}\left(S(L,\omega) - \frac{S'(z,\omega)\big|_{z=L}}{iq(\omega)}\right). \quad (3.35)$$

The resulting transmission spectrum with $T = |E_{\text{t}}|^2$ is shown in Fig. 3.7 (solid line). Parameters are given in Table 3.1 on page 30. For a comparison, the spectrum calculated by the solution of Eq. (3.16) in time domain is included too (dashed line). Note, that nearly exact agreement is found although both solutions have been computed by completely different approaches. Especially the inherent physical self-consistency of the polariton problem is manifested in both approaches but enters the numerical evaluations in completely different ways.

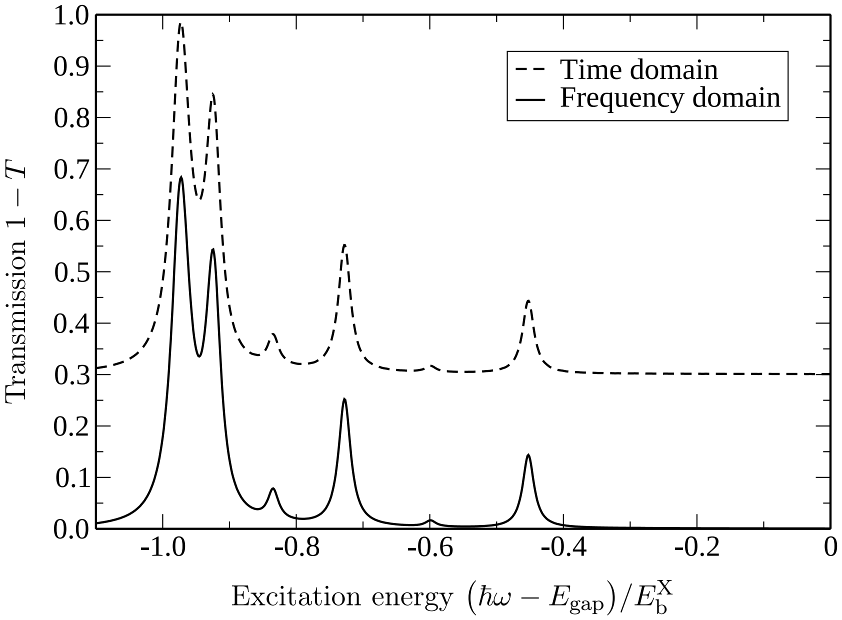

Figure 3.7: Comparison of transmission spectra for a GaAs layer with $10\,\mathrm{a}_0^{\mathrm{X}}$ thickness. Solid line: Calculation in frequency domain. Dashed line: Calculation in time domain, reproduced from Fig. 3.3. The dashed line is shifted by 0.3 on the vertical axis for better visibility.

In Section 3.1 the self-consistency is included in the calculation of the time evolution. For small time steps the source terms that couple the equations of motion are interchanged after each time step as illustrated in Fig. 3.1. This way, using sufficiently small time steps to reach numerical convergence of the results, a nearly "simultaneous" and self-consistent computation of the polariton dynamics is simulated.

The self-consistency in the solution presented in this section is manifested in the iterative solution of the Eqs. (3.32a)-(3.32d) as illustrated in Fig. 3.6. For the first step in the iterative solution, a starting value must be chosen for the electric field amplitude $E_{\rm med}^{n=0}(z,\omega)$ inside the medium. In the following iteration steps adapted amplitudes $a(\omega)$ and $b(\omega)$ [g] are used for each step in the iteration until convergence of the result is reached. Due to the linearity of Eq. (3.27), the solution can be found independently for each frequency ω of the incident light field.

For the GaAs model system investigated here, the numerical effort for the solution of the polariton problem in frequency domain is comparable to that for the solution in time domain introduced in Section 3.2. The most time-consuming part of the evaluation is the calculation of the exciton basis states and energies. However, for the analysis of experimental polariton spectra in Section 4.2 the inclusion of multiple reflections of the optical field between the outer sample surfaces of the heterostructure as illustrated in Fig. 1.4 on page 12 is required. These multiple reflections lead to Fabry-Perot effects. The approach in frequency domain easily allows this extension without further complications.

---

[g] Only these two amplitudes enter the calculation of $S(z,\omega)$ because the susceptibility $\chi(z,z',\omega)$ vanishes outside the sample.

An inclusion of these effects in time domain would require a large number of grid points in real space for the numerical solution of Maxwell's equations, which makes an accurate description very time-consuming. In frequency domain, however, the inclusion is straight forward and needs by far less execution time. So, here, the frequency domain is clearly superior to the time domain for the investigation of more complicated heterostructures.

3.4. The One-Particle Product Basis

To finish the general discussion concerning the solution of the exciton equation (3.1), another approach for the calculation of the exciton eigenenergies and eigenstates is introduced in this section. So far, in Sections 3.1 to 3.3, a direct numerical discretization scheme in real and momentum space has been used for the excitonic Hamiltonian. This approach yields large$^{\mathrm{h})}$ sparse matrices due to the necessarily large number of grid points in real space to reach good numerical convergence$^{\mathrm{i})}$. An alternative approach is the calculation of the Hamiltonian matrix with respect to a discrete one-particle basis for the z-direction. The one-particle states are used to properly account for the spatial inhomogeneity. We start with the excitonic Hamiltonian in real space representation:

$$\mathcal{H}^{\mathrm{X}} = -\frac{\hbar^2}{2m_{\mathrm{e}}^*}\nabla^2_{\mathbf{r}_\mathrm{e}} - \frac{\hbar^2}{2m_{\mathrm{h}}^*}\nabla^2_{\mathbf{r}_\mathrm{h}} - V(\mathbf{r}_\mathrm{e}-\mathbf{r}_\mathrm{h}) + V^{\mathrm{e}}_{\mathrm{ext}}(z_\mathrm{e}) + V^{\mathrm{h}}_{\mathrm{ext}}(z_\mathrm{h}) + E_{\mathrm{gap}}\,.$$

An appropriate one-particle basis to capture the electron (hole) in-plane motion and its motion in the z-direction is given by a product of a plane wave contribution with in-plane momentum $\mathbf{k}_\mathrm{e}$ ($\mathbf{k}_\mathrm{h}$) and the envelope function $\chi(z_\mathrm{e})$ ($\varphi(z_\mathrm{h})$). The latter one obeys the one-dimensional Schrödinger equation

$$\Big(-\frac{\hbar^2}{2m_{\mathrm{e}}^*}\frac{\partial^2}{\partial z^2} + V^{\mathrm{e}}_{\mathrm{ext}}(z) + E_{\mathrm{gap}}\Big)\chi_n(z) = \varepsilon^{\mathrm{e}}_n\chi_n(z)\,, \tag{3.36}$$

$$\Big(-\frac{\hbar^2}{2m_{\mathrm{h}}^*}\frac{\partial^2}{\partial z^2} + V^{\mathrm{h}}_{\mathrm{ext}}(z)\Big)\varphi_n(z) = \varepsilon^{\mathrm{h}}_n\varphi_n(z) \tag{3.37}$$

for electrons (e) and holes (h), respectively. It contains the external confinement potential $V^{\mathrm{e}}_{\mathrm{ext}}(z)$ ($V^{\mathrm{h}}_{\mathrm{ext}}(z)$) in the semiconductor heterostructure.

[h)] Depending on the layer thickness and the numerical accuracy typical dimensions of the discretized Hamiltonian matrix are of the order of 10^5 up to 10^6.

[i)] To obtain the Hamiltonian matrix for the numerical evaluation in the previous approach, the spatial derivatives in the z-direction are approximated by difference quotients with finite step size.

Separation of in-plane electron-hole relative and COM motion yields the excitonic Hamiltonian matrix in the one-particle product basis $(i, j, \mathbf{k})$ with in-plane relative momentum $\mathbf{k}$:[j)]

$$\begin{aligned} H^{ijkl}_{\mathbf{k}\mathbf{k}'} = \langle ij\mathbf{k}|\mathcal{H}|lk\mathbf{k}'\rangle =& \left(\frac{\hbar^2 k^2}{2\mu^*} + \varepsilon^{\mathrm{e}}_i + \varepsilon^{\mathrm{h}}_j\right)\delta_{il}\delta_{jk}\delta_{\mathbf{k}\mathbf{k}'} \\ &+ \int \mathrm{d}z_{\mathrm{e}}\mathrm{d}z_{\mathrm{h}}\chi^*_i(z_{\mathrm{e}})\varphi^*_j(z_{\mathrm{h}})V^{z_{\mathrm{e}}z_{\mathrm{h}}}_{\mathbf{k}-\mathbf{k}'}\varphi_k(z_{\mathrm{h}})\chi_l(z_{\mathrm{e}})\,. \end{aligned} \tag{3.38}$$

Infinitely high confinement potentials for electrons and holes yield $\chi_i(z) = \varphi_i(z)$. Then, the Coulomb matrix elements read

$$V^{ijkl}_{\mathbf{k}\mathbf{k}'} = \int \mathrm{d}z_{\mathrm{e}}\mathrm{d}z_{\mathrm{h}}\varphi^*_i(z_{\mathrm{e}})\varphi^*_j(z_{\mathrm{h}})V^{z_{\mathrm{e}}z_{\mathrm{h}}}_{\mathbf{k}-\mathbf{k}'}\varphi_k(z_{\mathrm{h}})\varphi_l(z_{\mathrm{e}})\,, \tag{3.39}$$

with $V^{ijkl}_{\mathbf{k}\mathbf{k}'} = V^{ikjl}_{\mathbf{k}\mathbf{k}'} = V^{ljki}_{\mathbf{k}\mathbf{k}'}$ for real-valued one-particle wave functions $\varphi_i(z)$. For infinitely high confinement potentials, the solutions of the one-particle problems in Eqs. (3.36) and (3.37), are:

$$\varphi_n(z) = \sqrt{\frac{2}{L}}\sin k_n z \qquad \text{with} \qquad k_n = \frac{\pi n}{L}\,, \tag{3.40}$$

$$\varepsilon^{\mathrm{e}}_n = \frac{\hbar^2\pi^2}{2m^*_{\mathrm{e}}}\frac{n^2}{L^2} + E_{\mathrm{gap}} \qquad \text{and} \qquad \varepsilon^{\mathrm{h}}_n = \frac{\hbar^2\pi^2}{2m^*_{\mathrm{h}}}\frac{n^2}{L^2}\,. \tag{3.41}$$

For layer thicknesses of $5\,\mathrm{a}^{\mathrm{X}}_0$ and $10\,\mathrm{a}^{\mathrm{X}}_0$, Fig. 3.8 shows the lowest eigenvalues of the Hamiltonian matrix (3.38) depending on the number of one-particle states taken into account. Additionally, the "exact" eigenvalues, obtained by the direct discretization used in the previous sections, are included as a reference. The result reveals two important features: First of all we encounter a convergence of the eigenenergies with increasing number of discrete one-particle states towards the reference values. The second point is that we find a faster convergence for the thinner layer ($5\,\mathrm{a}^{\mathrm{X}}_0$) than for the thicker one ($10\,\mathrm{a}^{\mathrm{X}}_0$). Caused by the increasing level spacing of the one-particle energies in Eq. (3.41) for decreasing layer thickness, the contributions of higher one-particle states are reduced with decreasing layer thickness.

In this section, we have presented an alternative way to compute the exciton eigenenergies and eigenstates by changing the quantum mechanical basis. However, for practical purposes an important question is which method is the most efficient one. Of course, the basic idea for the calculation with respect to the discrete one-particle basis is to neglect higher one-particle states. Hence, the evaluations are done in a truncated basis with a small number of one-particle basis states in a good approximation for the lowest exciton states. Nevertheless, the number of one-particle states that have to be considered to reach good numerical convergence strongly depends on the layer thickness.

[j)] In analogy to the previous sections, only states with in-plane COM momentum $|\mathbf{q}| = 0$ have to be considered here.

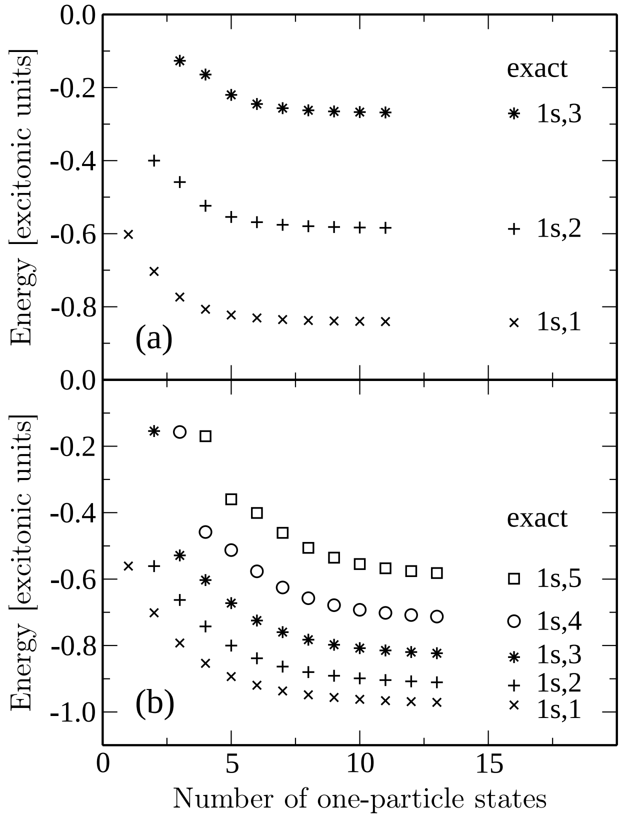

Figure 3.8: Dependence of the exciton energies calculated with respect to a truncated one-particle basis. Results are shown for (a) 5 a_0^X and for (b) 10 a_0^X thickness of the GaAs layer. The "exact" energies obtained by the corresponding calculations in real space following Section 3.2 are included as a reference. Energies are given in excitonic units according to the horizontal axis in Fig. 3.7

Good results within the discrete one-particle basis can only be obtained for rather thin layers. In this case, higher one-particle states can be neglected being interested in a proper description of the lowest exciton states only. Nevertheless, for thicker layers the Hamiltonian matrix (3.38) rapidly grows and it is important to keep in mind that it only contains a rather small number of zero elements compared to the Hamiltonian directly discretized in real space.

In conclusion, for practical purposes, the method presented first provides more reliable results with less numerical effort than the calculation in a discrete one-particle basis. However, the basic idea to work in a standing wave like basis for the z-direction is used in Chapter 5 for the calculation of Coulomb matrix elements. For the solution of the excitonic problem all computations throughout this work are performed by discretization of the Hamiltonian in real space as described in Appendix B.1.

3.5. Macroscopic Theory: Pekar's ABCs

In the previous sections of this chapter a microscopic theory for the description of exciton polaritons in thin semiconductor layers has been deduced. The theoretical analysis of polariton spectra in the past and even nowadays is mostly done in terms of phenomenological models. This section gives an insight into a phenomenological and macroscopic approach. Without a microscopic description of the excitonic dynamics influenced by realistic boundary conditions, which are uniquely given by the physical properties of the system, a solution of the phenomenological models can only be found by introduction of the so-called *additional boundary conditions* (ABCs). These boundary conditions cannot be justified on a microscopic level and are only imposed on macroscopic quantities of the system, e.g., the macroscopic polarization or the polarization flux. Due to the lack of microscopic justification, a phenomenological ansatz has to be made for the ABCs. After the original introduction of the additional boundary condition concept by Pekar in 1958,[34] different proposals for these boundary conditions have been presented: Originally, Pekar postulated a vanishing macroscopic polarization at the semiconductor surface.[34] Another proposal is that of a vanishing polarization flux at the surface[35] or even of an appropriate linear combination of both of these quantities.[36] Recently, in Ref. 42 even another macroscopic formulation has been suggested to compensate the shortcomings of models with missing microscopic foundation. Based on the solution of the exciton problem in the bulk material presented in Section 2.1, these models are much easier to handle and numerically much less involved and demanding than the microscopic theory presented in the previous sections of this chapter. Although calculations within macroscopic models phenomenologically reproduce the main features that are observed in experimental transmission spectra,[13] quantitative agreement is only obtained in some cases and for wrong or unrealistic material parameters.[6,43] Especially the layer thickness has to be adjusted.

In this work, the original Pekar ABCs are used for calculations within a macroscopic model since they led to best results in comparison with the microscopic theory and the experiment in Ref. 6. In this section the application of Pekar's ABCs to the semiconductor model system introduced in the previous sections is summarized.

The considered situation for propagation of light through a single semiconductor layer is equivalent to Section 3.3.2, Fig. 3.5. Again, we make use of the homogeneity of the system in the x-y-plane which reduces the solution of the electromagnetic wave equation to a one-dimensional problem. On the left, we have an incoming and a reflected plane wave contribution:

$$E_{\mathrm{left}}(z,\omega) = \mathrm{e}^{iq_{\mathrm{l}}z} + E_{\mathrm{r}}(\omega)\mathrm{e}^{-iq_{\mathrm{l}}z} \quad \text{with} \quad q_{\mathrm{l}} = n_{\mathrm{bg}}\frac{\omega}{c_0}\,. \tag{3.42a}$$

The amplitude of the incoming wave is normalized to unity. The transmitted part on the right is given by:

$$E_{\mathrm{right}}(z,\omega) = E_{\mathrm{t}}(\omega)\mathrm{e}^{iq_{\mathrm{r}}z} \quad \text{with} \quad q_{\mathrm{r}} = n_{\mathrm{bg}}\frac{\omega}{c_0}\,. \tag{3.42b}$$

Inside the layer, the solution for the electric field is influenced by its coupling to the optically induced excitonic polarization. Therefore, a more detailed investigation of the excitonic problem is necessary to find an appropriate ansatz: In general, the solution of the interacting two-particle problem in a confinement situation cannot be separated into relative and COM motion. Therefore, for an exact treatment a solution of the full problem as done in the previous sections of this chapter cannot be avoided. Nevertheless, following the ansatz of Pekar, we deduce a theory that is founded on the well-known solution for the electron-hole relative motion (Hydrogen problem) for an idealized bulk system, compare Sections 2.1 and 2.2. Ignoring the constraints by surfaces or interfaces, the relative motion is separated from the COM motion. Therefore, the exciton relative and COM motion are decoupled, although we are interested in a system with finite spatial extension, and despite the knowledge that this decoupling, in principle, is not valid. This way, the exciton problem is reduced to the solution of the confined COM motion of a point-like particle with the total exciton mass M^*, while the electron-hole relative motion intrinsically enters the exciton binding energy. Within this approach, the ansatz for the electric field in the sample, with propagating E_{p}^{+} and counter-propagating E_{p}^{-} contributions, is:

$$E_{\mathrm{med}}(z,\omega) = \sum_{\mathrm{p}=1,2} \left(E_{\mathrm{p}}^{+}(\omega)\mathrm{e}^{iq_{\mathrm{p}}(\omega)z} + E_{\mathrm{p}}^{-}(\omega)\mathrm{e}^{-iq_{\mathrm{p}}(\omega)z} \right). \tag{3.42c}$$

Here $q_{1,2}(\omega)$ are the two branches of the polariton dispersion for the coupled light and exciton system of the bulk material from Section 2.2.

This formulation naturally implies that the COM momentum q_z of the exciton is still a good quantum number and can be used to classify the propagating modes in the material. Obviously, in principle, this assumption is not valid for a system without translation symmetry in the direction of propagation. As a consequence of this shortcoming of the phenomenological ansatz, the continuity of the z-dependent electric field amplitude $E(z,\omega)$ and its first spatial derivative $\frac{\partial E(z,\omega)}{\partial z}$ at the interfaces z_1 and z_2 is not a sufficient requirement to find a unique solution for the transmitted field amplitude $E_{\mathrm{t}}(\omega)$. There are six unknown coefficients $E_{\mathrm{r}}(\omega)$, $E_{\mathrm{r}}(\omega)$ and $E_{\mathrm{p}=1,2}^{\pm}(\omega)$ in the equations (3.42a), (3.42b) and (3.42c) but only four continuity conditions at the two interfaces. To find a unique solution of the problem and to compensate the missing microscopic and physical justification of the ansatz (3.42c), additional boundary conditions have to be introduced on a phenomenological level. Originally these ABCs have been imposed on the macroscopic polarization of the system which is given by

$$P(z,\omega) = \sum_{\mathrm{p}=1,2} \chi(q_z,\omega)\big|_{q_z=q_{\mathrm{p}}(\omega)} \left[E_{\mathrm{p}}^{+}(\omega)\mathrm{e}^{iq_{\mathrm{p}}(\omega)z} + E_{\mathrm{p}}^{-}(\omega)\mathrm{e}^{-iq_{\mathrm{p}}(\omega)z} \right], \tag{3.43}$$

in terms of the local bulk exciton susceptibility $\chi(q_z,\omega)$, Eq. (2.25). Pekar's ABCs to the macroscopic polarization $P(z,\omega)$ are given by:

$$P(z = z_{1,2},\omega) = 0\,. \tag{3.44}$$

The macroscopic polarization vanishes at the surfaces at z_1 and z_2.

Using these ABCs, a solution of the Eqs. (3.42a)-(3.42c) and (3.43) becomes possible and yields the set of linear equations

$$E_{\mathrm{left}}(z_1,\omega) = E_{\mathrm{med}}(z_1,\omega): \quad \mathrm{e}^{iq_1 z_1} + E_{\mathrm{r}}(\omega)\mathrm{e}^{-iq_1 z_1} = \sum_{\mathrm{p}=1,2}\left[E_{\mathrm{p}}^{+}(\omega)\mathrm{e}^{iq_{\mathrm{p}} z_1} + E_{\mathrm{p}}^{-}(\omega)\mathrm{e}^{-iq_{\mathrm{p}} z_1}\right] \tag{3.45a}$$

$$E_{\mathrm{med}}(z_2,\omega) = E_{\mathrm{right}}(z_2,\omega): \quad E_{\mathrm{t}}(\omega)\mathrm{e}^{iq_{\mathrm{r}} z_2} = \sum_{\mathrm{p}=1,2}\left[E_{\mathrm{p}}^{+}(\omega)\mathrm{e}^{iq_{\mathrm{p}} z_2} + E_{\mathrm{p}}^{-}(\omega)\mathrm{e}^{-iq_{\mathrm{p}} z_2}\right] \tag{3.45b}$$

$$\frac{\partial E_{\mathrm{left}}(z,\omega)}{\partial z}|_{z_1} = \frac{\partial E_{\mathrm{med}}(z,\omega)}{\partial z}|_{z_1}: \quad iq_1\mathrm{e}^{iq_1 z_1} - iq_1 E_{\mathrm{r}}(\omega)\mathrm{e}^{-iq_1 z_1} = \sum_{\mathrm{p}=1,2}\left[iq_{\mathrm{p}}E_{\mathrm{p}}^{+}(\omega)\mathrm{e}^{iq_{\mathrm{p}} z_1} - iq_{\mathrm{p}}E_{\mathrm{p}}^{-}(\omega)\mathrm{e}^{-iq_{\mathrm{p}} z_1}\right] \tag{3.45c}$$

$$\frac{\partial E_{\mathrm{med}}(z,\omega)}{\partial z}|_{z_2} = \frac{\partial E_{\mathrm{right}}(z,\omega)}{\partial z}|_{z_2}: \quad iq_{\mathrm{r}}E_{\mathrm{t}}(\omega)\mathrm{e}^{iq_{\mathrm{r}} z_2} = \sum_{\mathrm{p}=1,2}\left[iq_{\mathrm{p}}E_{\mathrm{p}}^{+}(\omega)\mathrm{e}^{iq_{\mathrm{p}} z_2} - iq_{\mathrm{p}}E_{\mathrm{p}}^{-}(\omega)\mathrm{e}^{-iq_{\mathrm{p}} z_2}\right] \tag{3.45d}$$

$$P(z_1,\omega) = 0: \quad \sum_{\mathrm{p}=1,2}\chi(q_{\mathrm{p}},\omega)\left[E_{\mathrm{p}}^{+}(\omega)\mathrm{e}^{iq_{\mathrm{p}} z_1} + E_{\mathrm{p}}^{-}(\omega)\mathrm{e}^{-iq_{\mathrm{p}} z_1}\right] = 0 \tag{3.45e}$$

$$P(z_2,\omega) = 0: \quad \sum_{\mathrm{p}=1,2}\chi(q_{\mathrm{p}},\omega)\left[E_{\mathrm{p}}^{+}(\omega)\mathrm{e}^{iq_{\mathrm{p}} z_2} + E_{\mathrm{p}}^{-}(\omega)\mathrm{e}^{-iq_{\mathrm{p}} z_2}\right] = 0 \tag{3.45f}$$

The solution of Eqs. (3.45a)-(3.45f) yields the frequency dependent transmission through the semiconductor layer:

$$T(\omega) = |E_{\mathrm{t}}(\omega)|^2 .$$

Figure 3.9 shows a transmission spectrum for the example of a GaAs layer with thickness of 10 $\mathrm{a}_0^{\mathrm{X}}$. The additional boundary conditions (3.44) yield standing waves for the exciton COM motion with the discrete wave numbers q_n for a sample thickness L. The exciton eigenenergies are given by:

$$E_n^{\mathrm{X}} = \varepsilon_1^{\mathrm{X}} + E_{\mathrm{gap}} + \frac{\hbar^2}{2M^*}q_n^2 \quad \text{with} \quad q_n = \frac{\pi}{L}n \quad \text{with} \quad n \in \{1,2,\ldots\}\,. \tag{3.46}$$

The discrete structure of the energy spectrum for the COM motion yields additional resonances in the excitonic susceptibility and in the transmission spectrum in Fig. 3.9 compared to the case of an idealized bulk system in Fig. 2.1.

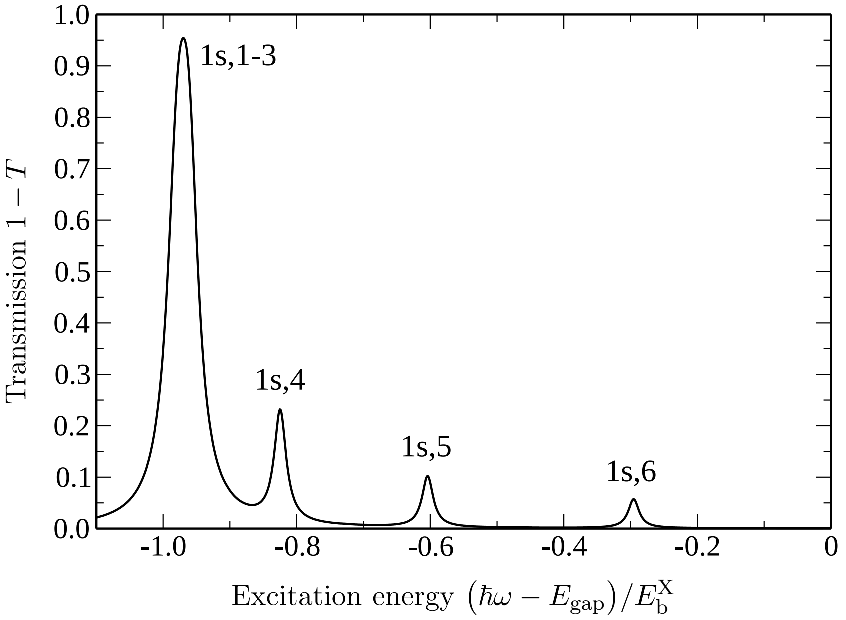

Figure 3.9: Transmission spectrum for a $10\,\mathrm{a}_0^{\mathrm{X}}$ GaAs layer with Pekar's ABCs. Material parameters are given in Table 3.1 on page 30.

Therefore, despite of its conceptional shortcomings a description of the optical response of confined excitons is obtained which qualitatively reproduces the main features of the polaritonic resonances in optical transmission spectra.[12,13] Thinking in terms of the phenomenological approach, the quantization is commonly referred to as "COM quantization" of the polariton propagation.[12–17]

A phenomenological solution for a propagating light field coupled to the 1s exciton resonance in a semiconductor heterostructure has been presented in this section. Nevertheless, one should be aware of the fact that the solution of the exciton for a bulk material was applied to a finite semiconductor layer which necessitates the use of ABCs for the macroscopic polarization. However, there is no differential equation which has to be fulfilled by the macroscopic polarization and on whose solution boundary conditions could be imposed. To apply physical meaningful boundary conditions on a microscopic level, the solution of the full two-particle problem for the electron-hole transition amplitude is unavoidable, although inconvenient due to the high numerical effort. The relative motion as well as the COM motion is influenced by the boundary conditions and they are coupled to each other in contradiction to the assumptions made for the macroscopic model in this section. The resulting shortcomings and the applicability of the macroscopic model in comparison to the microscopic theory and experimental results are investigated in detail in the next chapter.

4. Results: Linear Polariton Propagation

In Chapter 3 a microscopic theory for the calculation of linear transmission spectra has been introduced. A phenomenological formulation has been given in Section 3.5. Section 4.1 of this chapter is dedicated to the discussion and comparison of the results obtained by both approaches for the GaAs model system introduced in Chapter 3. Furthermore, the validity of the macroscopic approach is discussed for various material parameters and excitation conditions. In particular, the comparison of results leads to the introduction of the dead-layer concept that helps to augment the model based on Pekar's ABCs. To conclude the discussion of linear polariton spectra in Section 4.2, we investigate transmission spectra for ZnSe/ZnSSe heterostructures. This material system is studied as a typical example for shallow-confinement heterostructures. For this system a direct comparison of transmission experiments and calculations using microscopic boundary conditions is presented. Results obtained by the macroscopic model based on Pekar's ABCs are shown and discussed, too.

4.1. Microscopic Theory vs. Pekar's ABCs

4.1.1. Introduction of the Dead-Layer Concept

The solid line in Fig. 4.1 shows the transmission spectrum of a GaAs sample with a thickness of $L = 10\,\mathrm{a}_0^{\mathrm{X}}$ calculated within the microscopic theory. The result is reproduced from Fig. 3.2 on page 32. Resonant monochromatic excitation of the sample within the microscopic theory yields the space dependence of the macroscopic polarization $P(z,\omega)$ in z-direction. Results for the six lowest resonances are shown in Fig. 4.2. The polarization evolves standing wave like structures inside the layer which corresponds to the naive picture of a COM quantization of the exciton movement in z-direction in analogy to the discussion in Section 3.5. However, the system exhibits surface layers with negligible macroscopic polarization of the semiconductor due to the finite spatial extension of the exciton as a Coulomb bound state of electron and hole. The situation is complicated by the fact that the thickness of these layers differs for various resonance frequencies, which directly follows here from the microscopic theory. Note, that despite the symmetry of the exciton eigenstates with respect to $z = 5\,\mathrm{a}_0^{\mathrm{X}}$, the coupling to the propagating light field yields steady-state polarizations $|P(z,\omega)|$ which do not exhibit the symmetry of the corresponding exciton wave functions.

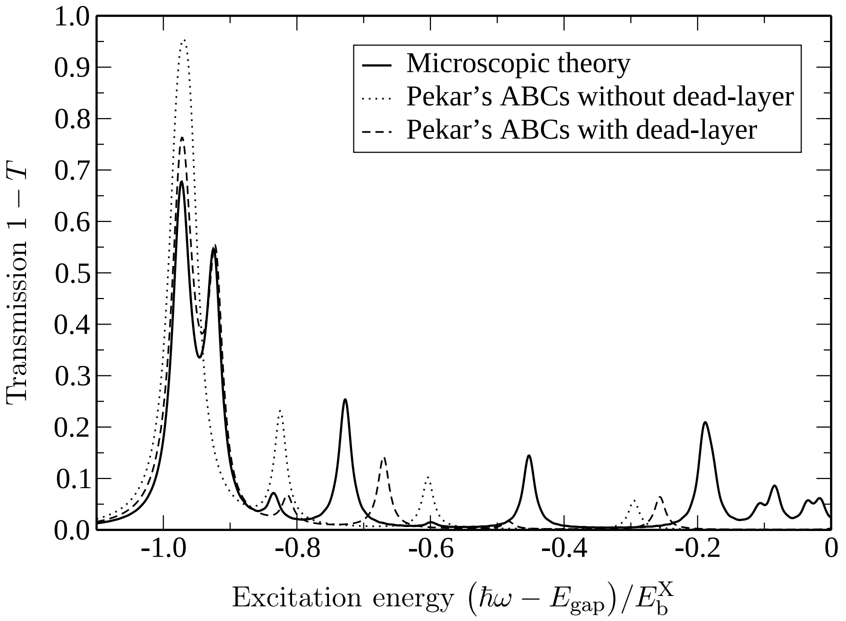

Figure 4.1: Calculated GaAs transmission spectrum for a sample thickness $L = 10\,\mathrm{a}_0^{\mathrm{X}}$. The excitation energy is given relative to the bulk band-gap energy E_{gap} and in units of the bulk exciton binding energy $E_{\mathrm{b}}^{\mathrm{X}}$.

When Pekar's ABCs are used to calculate optical spectra, the boundary conditions are only imposed on the COM motion within the slab, which leads to discrete exciton energies $E_n^{\mathrm{X}} = E_{\mathrm{b}}^{\mathrm{X}} + E_{\mathrm{gap}} + \frac{\hbar^2\pi^2}{2M^*}\frac{n^2}{L^2}$. The corresponding transmission spectrum has already been shown in Fig. 3.9 and is reproduced as dotted line in Fig. 4.1. To account for the finite spatial extension of the exciton states in this picture in an approximate way, the introduction of so-called dead-layers of thickness d with $|P(z)| \approx 0$ at the surfaces of the sample for $0 < z < d$ and $L - d < z < L$ is appropriate. Using the results of the microscopic theory displayed in Fig. 4.1, we estimate an effective sample thickness $L_{\mathrm{eff}} = L - 2d = 7.2\,\mathrm{a}_0^{\mathrm{X}}$ for the $n = 1$ resonance. The result of a calculation based on Pekar's ABCs using this dead-layer, determined for the first resonance $n = 1$, is shown as dashed line in Fig. 4.1. Although the structure of the "double-peak" main resonance is nearly reproduced, the energy positions of the higher exciton replica are shifted to higher energies in comparison to the microscopic spectrum. This is due to the fact that the higher polariton modes exhibit smaller dead-layers than the main resonance as shown in Fig. 4.2. The dead-layer determined for the $n = 1$ resonance is, strictly speaking, not an appropriate choice for the higher states.

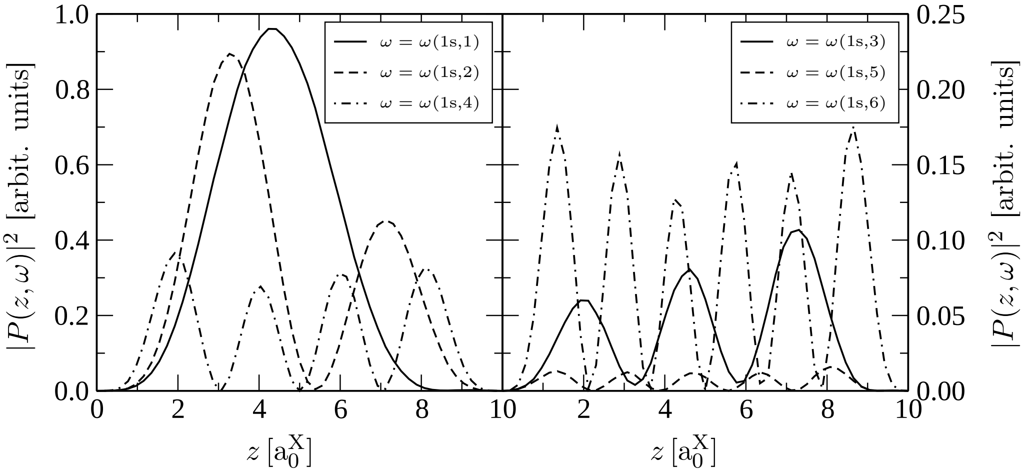

Figure 4.2: Spatial distribution of the macroscopic polarization for stationary, monochromatic excitation. The excitation frequency is tuned to the resonances of the system (solid line in Fig. 4.1).

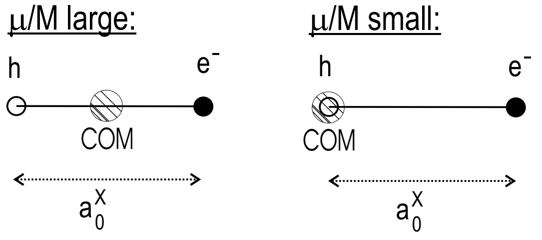

Figure 4.3: Illustration of the "rigid ball" model for the exciton. The two limiting cases are included. Left: Equal electron and hole masses. Right: Infinitely heavy hole. A detailed discussion is given in the text.

4.1.2. Dependence of the Dead-Layer on the Reduced Exciton Mass

Having introduced the dead-layer as a phenomenological parameter to augment Pekar's ABCs, the microscopic model is used to systematically determine the influence of material parameters and excitation frequency on the dead-layer thickness. The motion of electron and hole relative to the exciton COM coordinate can be characterized by the reduced exciton mass μ^* normalized to the total exciton mass M^*. This is motivated by the naive picture of electron and hole treated as "rigid balls" as illustrated in Fig. 4.3. If the electron and hole masses are approximately the same, the COM is situated in the center between electron and hole. Since the electron-hole transition amplitude must vanish if either electron or hole reaches the surface, the COM can approach the surface up to half an exciton Bohr radius. If the hole is much heavier than the electron, the COM is approximately at the hole position. In this case, to fulfill the boundary conditions, the COM distance to the surface is at least one exciton Bohr radius.

For a general discussion of this behavior the dependence of the dead-layer thickness on the reduced exciton mass, normalized to the total exciton mass μ^*/M^*, is investigated. The limiting cases of equal electron and hole masses and infinitely heavy holes correspond to $\mu^*/M^* = 0.25$ and $\mu^*/M^* = 0$, respectively. Recent investigations of the dead-layer for the exciton ground state in Ref. 40 have been based on an approximate decoupling of the exciton relative and COM motion by use of a Born-Oppenheimer procedure. Different dead-layers for various resonances have not been considered. In the following, we use the microscopic model calculations to extract the dead-layer thickness. For a layer thickness of $10\,\mathrm{a}_0^{\mathrm{X}}$ several transmission spectra for various reduced exciton masses are calculated. Since the determined dead-layer will be used to augment Pekar's ABCs, the determination process is as follows: By variation of the dead-layer thickness the position of the considered n^{th} resonance of the Pekar spectrum is adjusted to the corresponding peak in the spectrum of the microscopic calculation. This procedure corresponds to an adjustment of the effective layer thickness for the macroscopic model. Results for the dead-layer thickness are given in Fig. 4.4. Note, that the procedure is only meaningful as long as the influence of the quantum confinement on the electron-hole relative motion is not too strong. Otherwise, for thin layers, the dead-layer concept fails.

The calculations quantitatively reproduce the results presented in Ref. 40 for the exciton ground state (here $n = 1$) in a slab geometry. Furthermore, the expected growth of the dead-layer with decreasing reduced exciton masses is observed, as predicted from the simple rigid-ball model. For equal electron and hole masses ($\mu^*/M^* = 0.25$) the expected value of $0.5\,\mathrm{a}_0^{\mathrm{X}}$ for the dead-layer is nearly reached, but it increases faster for decreasing μ^*/M^* than the rigid-ball picture can explain. Additionally, there is a variation of the dead-layer thickness for the different resonances in each spectrum which becomes more important for decreasing μ^*/M^*. Because of this dependence, a constant dead-layer which well-fits the main resonance, shifts the higher polariton-states to higher energies in comparison to the microscopic theory. This is what has been observed in the results for the GaAs model system in Fig. 4.1.

Concluding these theoretical investigations, there is no justification for the use of a constant dead-layer to reproduce a whole spectrum of bound exciton states with Pekar's ABCs. Depending on material system, the interpretation of polariton spectra in terms of phenomenological models can lead to a more or less unrealistic sample thickness or other unreasonable material parameters as discussed in the following section.

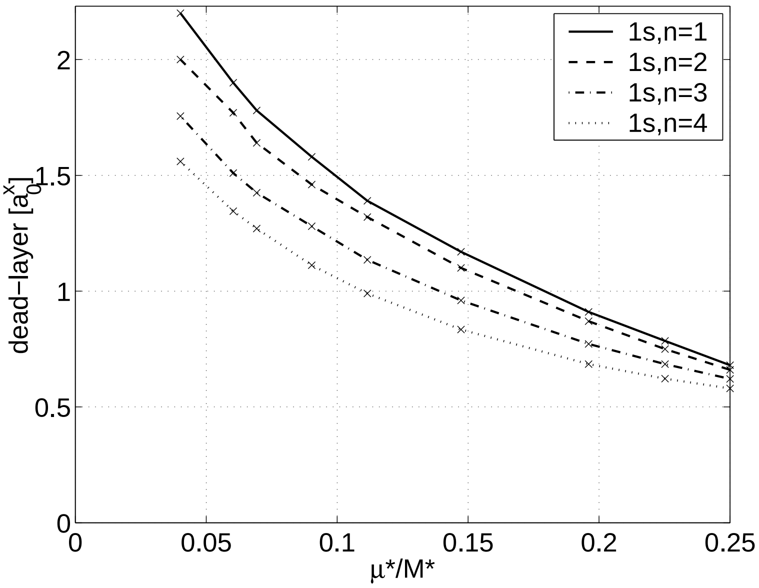

Figure 4.4: Dead-layer dependence on the reduced exciton mass μ^* normalized to the total exciton mass M^* for a sample thickness of $10\,\mathrm{a}_0^{\mathrm{X}}$. The dead-layer is given in units of the exciton Bohr radius $\mathrm{a}_0^{\mathrm{X}}$ for each μ^*/M^*. The lines are included as a guide to the eye.

4.2. Theory vs. Experiment

In the previous section the analysis of polariton spectra has been done for systems with infinitely high potential barriers surrounding the semiconductor layer that resonantly interacts with the optical fields. However, in realistic heterostructures the confinement of electrons and holes is provided by finite-height confinement potentials. The height of theses potentials strongly depends on the investigated material system. The assumption of infinitely high confinement potentials does hold in a good approximation, e.g., for the GaAs/Al$_{0.3}$Ga$_{0.7}$As material system investigated in Refs. 5, 6. However, for instance, for ZnCdSe/ZnSe[44] or ZnSe/ZnSSe[13] heterostructures the confinement potentials are considerably shallower.

To extend the previous discussions, in this section polariton spectra are investigated for a material system where the assumption of infinitely high confinement potentials does not hold anymore but rather shallow confinement potentials are provided for electrons in the conduction band and for holes in the valence band. In order to give a direct theory-experiment comparison for a shallow-confinement situation three ZnSe/ZnS$_{\mathrm{x}}$Se$_{1-\mathrm{x}}$ samples with nominal thicknesses for the ZnSe layer of 20 nm, 28 nm and 40 nm have been grown. Section 4.2.1 gives some insight in the growth process by molecular beam epitaxy, the ex-situ characterization by high resolution X-ray diffraction, the sample preparation, and the setup for the measurement of optical transmission spectra. The heterostructures are schematically illustrated in Fig. 4.5. The ZnSe layer resonantly interacts with the incident light field. More details concerning structural and electronic properties are given in Sections 4.2.1 and 4.2.2.

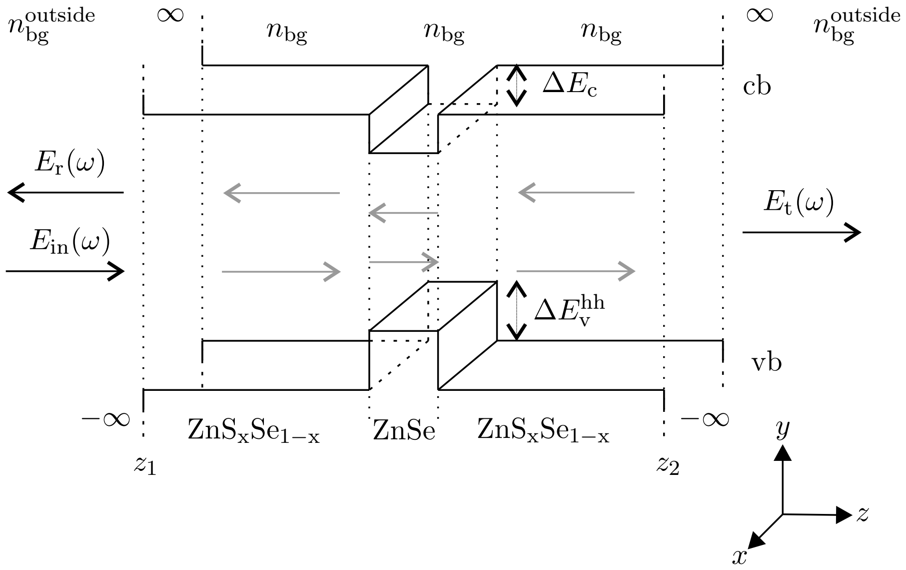

Figure 4.5: Illustration of the considered semiconductor heterostructure in a slab geometry. Conduction band (cb) and heavy-hole valence band (vb) alignments are visualized. The system homogeneously extends in the x-y-plane and has a finite thickness $|z_2 - z_1|$ in the z-direction. For more details see text.

4.2.1. Sample Growth, Characterization, Preparation, and Optical Setup

Three ZnSe/ZnSSe samples with nominal thicknesses of 20, 28, and 40 nm for the ZnSe layer were grown by molecular beam epitaxy (MBE). Preceding the growth process of the ZnSe/ZnSSe heterostructure, a 180 nm thick GaAs buffer layer was deposited on the GaAs(001) substrate. The ZnSe layer was embedded between two $\mathrm{ZnS_xSe_{1-x}}$ layers with nominal sulfur content $\mathrm{x} = 6\,\%$. The structure was grown lattice-matched to the GaAs substrate and the thickness of the ZnSSe buffer layers was $1\,\mu$m on the GaAs side and 500 nm on the top side.

The samples were characterized using a high resolution X-ray diffractometer. The results confirm a good lattice-match of the structure to the GaAs substrate. The resulting composition of the ZnSSe barriers as well as the thickness of the ZnSe layers could be extracted from the experiment by simulation of the resulting X-ray patterns. They are given in Table 4.1.

For transmission experiments the GaAs substrate was removed by chemical etching. For the measurement of linear transmission spectra a conventional setup was used, a Xeon lamp, a cryostat, a spectrometer with a resolution of 10^{-4} eV, and a photomultiplier. The samples were free-standing and immersed in a liquid helium bath with a temperature of 4 K. Additional technical details are given in Ref. 43.

Nominal ZnSe layer thickness [nm]	20	28	40
Experimentally determined:			
ZnSe layer thickness [nm]	21.5	29.0	43.5
Barrier sulfur content x [%]	5.2	5.0	5.8
Parameters for microscopic theory:			
ZnSe layer thickness [nm]	20.7	29.4	43.7
Heavy-hole val. band offset $\Delta E_{\mathrm{v}}^{\mathrm{hh}}$ [meV]	21.2	20.6	23.2
Conduction band offset ΔE_{c} [meV]	2.7	2.1	4.6
Parameters for Pekar's ABCs:			
ZnSe layer thickness [nm]	22.5	31.5	45.5

Table 4.1.: Structural sample parameters determined by high resolution X-ray diffraction and input parameters for the microscopic theory for the different samples. Band offsets are determined as outlined in Section 4.2.2. The layer thicknesses for the microscopic theory agree with the experimental ones, within an error of ±0.8 nm. For the macroscopic model the layer thicknesses are chosen so that the best result is obtained for a reproduction of the experimental transmission spectra.

The samples were grown by Arne Gust and the characterization by high resolution X-ray diffraction was done by Gabriela Alexe under supervision of Prof. Dr. D. Hommel at the Institute for Solid State Physics, Semiconductor Epitaxy Group, University of Bremen. The optical measurements and the sample preparation have been performed by Iryna Kudyk under supervision of Dr. H. I. Rückmann and Prof. Dr. J. Gutowski at the Institute for Solid State Physics, Semiconductor Optics Group, University of Bremen.

4.2.2. Modelling the ZnSe/ZnSSe Heterostructure

So far, the theoretical investigations have focused on infinitely high confinement potentials for the optically excited electrons and holes. To give an appropriate theoretical description of the ZnSe/ZnSSe heterostructures, here, two fundamental extensions to the formulation of the microscopic theory in Section 3.3 have to be made. First of all, a model with infinitely high potential barriers surrounding the ZnSe layer cannot be used. According to the physical properties of the heterostructure, illustrated in Fig. 4.5, the transitions from ZnSe to ZnSSe are modeled by the use of finite band offsets ΔE_{c}, $\Delta E_{\mathrm{v}}^{\mathrm{hh}}$ in the external potentials for electron and hole. Since the carrier wave functions exhibit a finite extension into the barrier material, care has to be taken to reach good numerical convergence of the results for the considered exciton energies and wave functions. A sufficiently large region outside the ZnSe layer must be taken into account for their calculation to avoid artifacts due to the finite total size of the numerical grid. Additionally, in contrast to Section 3.3.2, Fabry-Perot effects due to multiple reflections of light between the outer surfaces of the heterostructure at z_1 and z_2 in Fig. 4.5 are taken into account. The solution of the wave equation, using a transfer matrix method, is outlined in the following.

The Wave Equation and Fabry-Perot Modes

To take into account different background refractive indices inside and outside the semiconductor heterostructure illustrated in Fig. 4.5 the solution of the polariton problem as described in Section 3.3.2 has to be extended. In contrast to Section 3.3.2 here five space regions have to be distinguished where an ansatz for the desired solution for the electric field is made. The solution outside the sample ($z < z_1$ and $z > z_2$) can still be described by simple plane waves in analogy to Eqs. (3.29) and (3.30) in Section 3.3.2 but with wave numbers $q(\omega) = \frac{\omega}{c_0} n_{\mathrm{bg}}^{\mathrm{outside}}$ according to the background refractive index $n_{\mathrm{bg}}^{\mathrm{outside}}$ outside the sample. The solution inside the medium in the regions where no resonant interaction of the optical field with the semiconductor material takes place is determined by plane wave solutions too, but with $q(\omega) = \frac{\omega}{c_0} n_{\mathrm{bg}}$. The ansatz for the solution in the space region where a non-vanishing resonant excitonic polarization is induced by the light field is chosen in analogy to Eq. (3.31) in Section 3.3.2. Continuity of the electric field and its first spatial derivative is used to connect the solutions in the different space regions by use of a transfer matrix method[45] which results in a self-consistent solution of the polariton problem again. The inclusion of different background refractive indices n_{bg} inside and $n_{\mathrm{bg}}^{\mathrm{outside}}$ outside the semiconductor material results in multiple reflections of the light field at the surfaces at z_1 and z_2 resulting in so-called Fabry-Perot effects in the optical transmission spectra. The Fabry-Perot effects strongly depend on the overall thickness of the heterostructure and determine the absolute values of the transmitted light intensity. The influence of Fabry-Perot effects on the investigated transmission spectra for ZnSe/ZnSSe heterostructures is discussed in Section 4.2.3.

The Bandstructure and Parameters

This subsection is devoted to the material parameters that are used to model the electronic bandstructure and its offsets at the semiconductor interfaces. The effective masses for the heavy-hole valence band that follow from the Luttinger Hamiltonian in axial approximation are[1]

$$
\begin{aligned}
m^*_{\mathrm{hh}\|} &= \frac{m_0}{\gamma_1 + \gamma_2} = 0.327\,\mathrm{m}_0\,, \\
m^*_{\mathrm{hh}z} &= \frac{m_0}{\gamma_1 - 2\gamma_2} = 0.813\,\mathrm{m}_0\,,
\end{aligned}
$$

for the in-plane motion and the motion in growth direction, respectively.[a)] The Luttinger parameters γ_1 and γ_2 are given in Table 4.2, m_0 is the bare electron mass. Different effective masses for electrons and holes in the ZnSe and ZnSSe materials are not considered because they would yield only minor changes to our results: (i) Changes

---

[a)] The one-particle energies in the Hamiltonian (2.1) have to be modified to take into account different effective masses $m^*_{\mathrm{hh}\|}$, $m^*_{\mathrm{hh}z}$ for the hole in-plane motion and the motion in the z direction, respectively. Consequently, this modification results in an exciton equation (3.1) where inhomogeneous hole masses are included.

Band-gap energy	$E_{\mathrm{gap}}(\mathrm{ZnSe})$	$= 2.82593\,\mathrm{eV}$
Dephasing constant	γ	$= 0.35\,\mathrm{meV}$
Dipole coupling	d_{eh}/e_0	$= 3.7\,\text{Å}$
Backgr. refractive index	n_{bg}	$= 2.95$
Effective electron mass[51]	$m_{\mathrm{e}}^* = m_{\mathrm{e}\parallel}^* = m_{\mathrm{e}z}^*$	$= 0.147\,m_0$
Luttinger parameter[51]	γ_1	$= 2.45$
Luttinger parameter[51]	γ_2	$= 0.61$

Table 4.2.: ZnSe material parameters for the microscopic theory, equal for all samples. Material parameters entering the macroscopic model are discussed in the text. The bare electron mass is denoted by m_0.

in the electron mass are negligible due to the small sulfur contents $\mathrm{x} < 6\,\%$. (ii) The hole states, contributing to the optical spectra, only slightly penetrate the barrier due to the relatively large heavy-hole band offsets $\Delta E_{\mathrm{v}}^{\mathrm{hh}} \gg \Delta E_{\mathrm{c}}$ and the large effective heavy-hole mass. In a good approximation, the optical band-gap bowing for a ternary compound, consisting of the elements A, B and C, is given by[1]

$$E_{\mathrm{gap}}^{\mathrm{AB_xC_{1-x}}} = (1-\mathrm{x})E_{\mathrm{gap}}^{\mathrm{AC}} + \mathrm{x}E_{\mathrm{gap}}^{\mathrm{AB}} - b\mathrm{x}(1-\mathrm{x})\,. \tag{4.1}$$

Here $E_{\mathrm{gap}}^{\mathrm{AC}}$ and $E_{\mathrm{gap}}^{\mathrm{AB}}$ are the band-gap energies of the pure binary constituents, and $E_{\mathrm{gap}}^{\mathrm{AB_xC_{1-x}}}$ is the resulting band-gap energy of the ternary compound with a content x of material B. For the ZnSe/ZnSSe material system a variety of bowing parameters b has been reported.[46] Here, an intermediate value of $b = 0.43\,\mathrm{eV}$ is used as a representative average of the literature values. Band-gap energies of the pure binary bulk materials are[47]

$$E_{\mathrm{gap}}^{\mathrm{ZnS}}(T = 5\,\mathrm{K}) = 3.84\,\mathrm{eV}\,,$$
$$E_{\mathrm{gap}}^{\mathrm{ZnSe}}(T = 5\,\mathrm{K}) = 2.82\,\mathrm{eV}\,.$$

The ZnSe band-gap energy coincides quite well with the result for our samples given in Table 4.2.[b)] For the unstrained bulk materials the valence band offset from ZnSe to ZnS is $\Delta E_{\mathrm{v}}(\mathrm{ZnSe},\mathrm{ZnS}) = 530\,\mathrm{meV}$.[48] Similar values have been reported elsewhere.[49,50] With the band-gap energies this yields a conduction band offset of $\Delta E_{\mathrm{c}}(\mathrm{ZnSe},\mathrm{ZnS}) = 490\,\mathrm{meV}$. We assume that the ratio of valence and conduction band offsets from pure ZnSe to $\mathrm{ZnS_xSe_{1-x}}$ does not depend on the sulfur concentration x for the unstrained bulk materials.

[b)] Keep in mind the strain enlargement of the band-gap energy in the considered heterostructures which is discussed in the following.

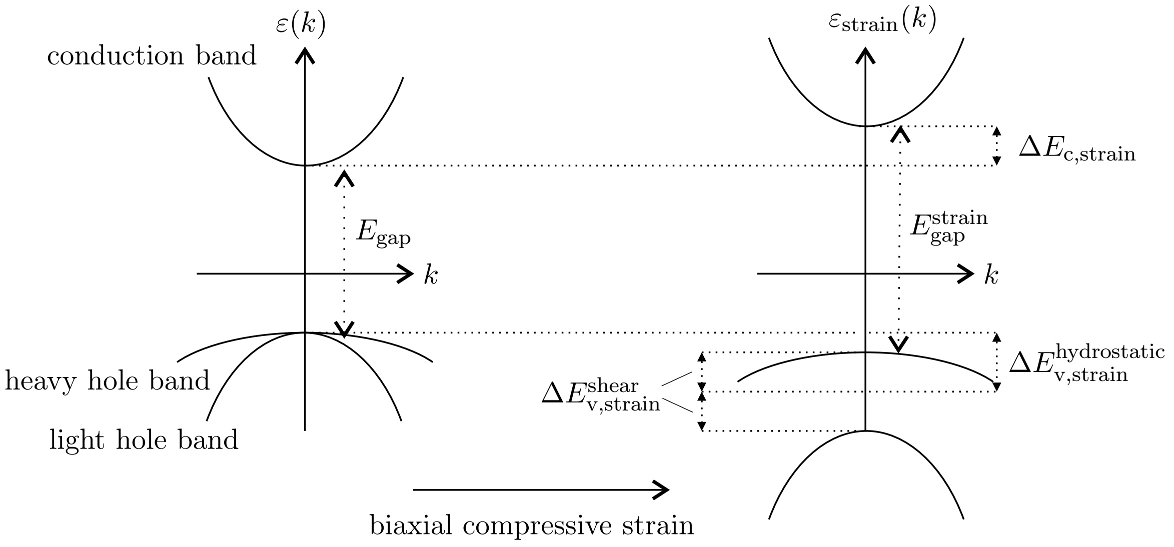

Figure 4.6: Schematic illustration of the energy shifts in the electronic bandstructure of a biaxially compressively strained zincblende crystal.

Due to pseudomorphic growth on GaAs(001) substrate, the ZnSe layer is biaxially compressively strained. This yields energy shifts of its conduction and valence bands[52, 53] as illustrated in Fig. 4.6. The resulting energy shifts for conduction and heavy-hole valence band are given by[1]

$$\Delta E_{\mathrm{c,strain}} = 2a_{\mathrm{c}}\Big(1-\frac{C_{12}}{C_{11}}\Big)\varepsilon_{xx}\,, \tag{4.2}$$

$$\begin{aligned}\Delta E^{\mathrm{hh}}_{\mathrm{v,strain}} &= \Delta E^{\mathrm{hydrostatic}}_{\mathrm{v,strain}} - \Delta E^{\mathrm{shear}}_{\mathrm{v,strain}}\\ &= 2a_{\mathrm{v}}\Big(1-\frac{C_{12}}{C_{11}}\Big)\varepsilon_{xx} - b_{\mathrm{v}}\Big(1+2\frac{C_{12}}{C_{11}}\Big)\varepsilon_{xx}\,.\end{aligned} \tag{4.3}$$

Due to the changed volume of the strained crystal unit cell, a hydrostatic deformation potential is obtained for the conduction and the valence band. An additional shear deformation potential applies for the valence band shift due to the changed symmetry in the strained crystal structure. The hydrostatic deformation potential decreases the band offsets for both bands and thus enlarges the band-gap energy of the ZnSe material.

The shear deformation potential increases the offset for the heavy-hole valence band and thus decreases the band-gap energy as illustrated in Fig. 4.6. The required material parameters for ZnSe are[49, 53] $a_{\mathrm{c}} = -5.9\,\mathrm{eV}$, $a_{\mathrm{v}} = -1.0\,\mathrm{eV}$, $b_{\mathrm{v}} = -1.14\,\mathrm{eV}$ for the deformation potential constants, and $C_{11} = 929\,\mathrm{kbar}$, $C_{12} = 562\,\mathrm{kbar}$ for the elastic stiffness tensor elements. The strain tensor element $\varepsilon_{xx} = (a_{\parallel,\mathrm{ZnSe}} - a^0_{\mathrm{ZnSe}})/(a^0_{\mathrm{ZnSe}})$ follows from the in-plane lattice constants of the fully strained ($a_{\parallel,\mathrm{ZnSe}} = a_{\mathrm{GaAs}}$) and unstrained ($a^0_{\mathrm{ZnSe}}$) ZnSe material. The band offsets for the different samples follow from Eqs. (4.1), (4.2) and (4.3), with the sulfur concentration in Table 4.1. They slightly vary around carrier confinement potentials of 3 meV for the conduction band and 22 meV for the heavy-hole valence band, compare Table 4.1.

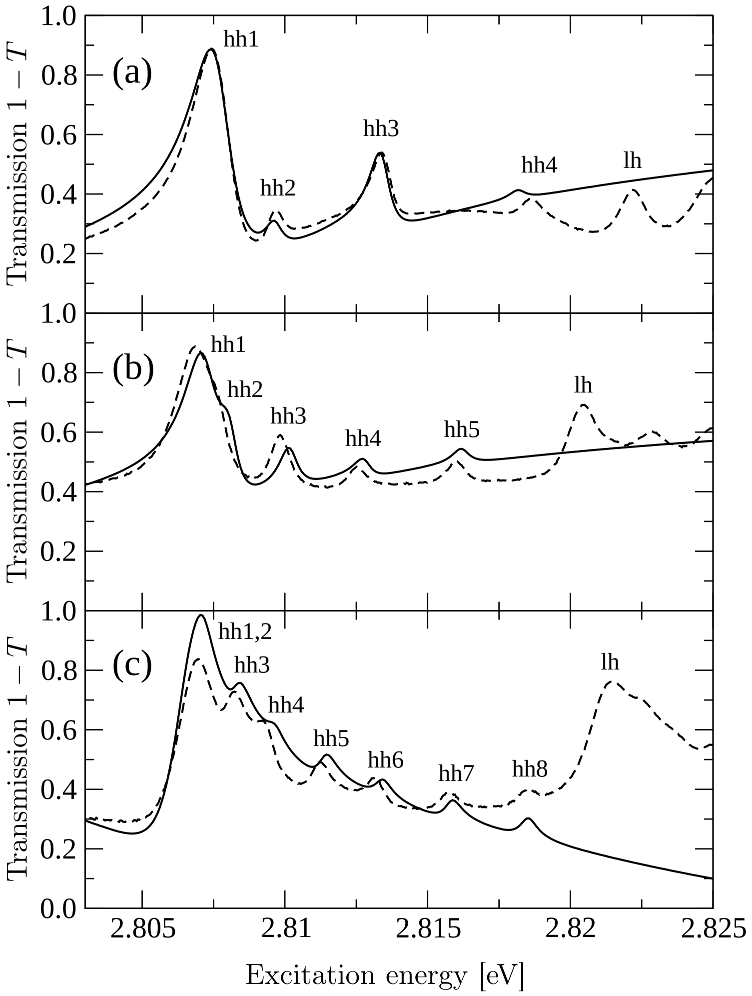

Figure 4.7: Transmission spectra for the (a) 20 nm, (b) 28 nm, and (c) 40 nm sample. Dashed line: Experiment. Solid line: Microscopic theory with Fabry-Perot effects.

The small conduction band offset coincides with previous results for ZnSe/ZnSSe heterostructures with larger sulfur concentrations.[44,52] Note, that in these systems exciton states are localized at the position of the ZnSe layer by the confinement of the hole motion; the electron is mainly "bound" to the ZnSe layer by the electron-hole Coulomb interaction.[54]

4.2.3. Results

In this section the optical transmission spectra for the three samples described in Sections 4.2.1 and 4.2.2 are investigated. The measured transmission spectra in the vicinity of the excitonic resonances of the ZnSe layer are shown as dashed lines in Fig. 4.7 for the (a) 20 nm, (b) 28 nm, and (c) 40 nm sample, respectively. Because of the high quality of the heterostructures even the weaker polariton resonances are clearly resolved. All peaks that can uniquely be attributed to resonances of the 1s heavy-hole polariton in the finite ZnSe layer are labeled with hh and consecutive numbers.

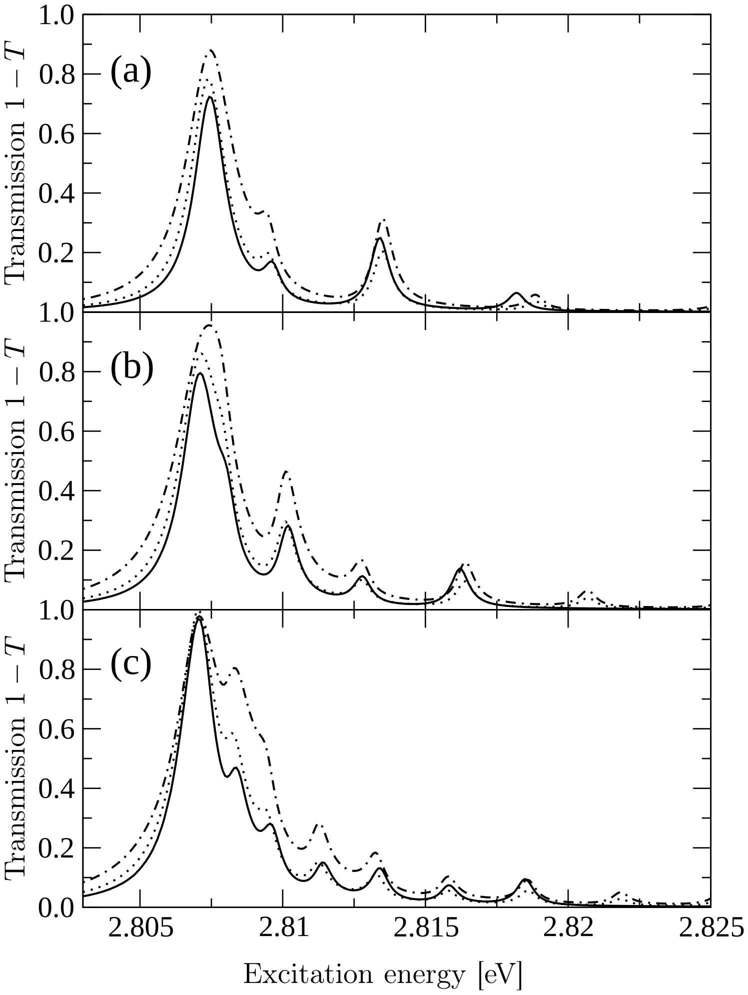

Figure 4.8: Transmission spectra for the (a) 20 nm, (b) 28 nm, and (c) 40 nm sample without Fabry-Perot effects. Solid line: Microscopic theory, $d_{\mathrm{eh}}/e_0 = 3.7\,\text{Å}$. Dotted line: Pekar's ABCs, $d_{\mathrm{eh}}/e_0 = 2.89\,\text{Å}$. Dashed-dotted line: Pekar's ABCs, $d_{\mathrm{eh}}/e_0 = 3.7\,\text{Å}$.

While light-hole resonances are not considered in the calculations, at least the lowest light-hole (lh) resonance, and even higher resonances in the 40 nm layer, can be seen in the experiment. In each subfigure, the resulting spectrum from the microscopic theory is given by the solid line. Input parameters are taken from Tables 4.1 and 4.2. In a good approximation to the experimental setup, a vacuum background refractive index $n_{\mathrm{bg}}^{\mathrm{outside}} = 1$ is used outside the sample. The results demonstrate that the microscopic theory well reproduces the experimental findings for the considered part of the spectrum. The deviations for higher energies result from the not considered light-hole exciton contributions, higher heavy-hole exciton states, and the neglected frequency dependent dispersion of the ZnSSe layers in this frequency range. Here we make use of the fact that in the linear regime various polariton resonances are decoupled, as it has been shown in Section 3.2. The dephasing constant γ and the band-gap energy $E_{\mathrm{gap}}(\mathrm{ZnSe})$ for the heavy-hole conduction band transition in the strained ZnSe layer (Table 4.2) are adjusted according to the experimental values.

The surfaces of the heterostructure form a resonator for the optical field. The resulting Fabry-Perot modes are superimposed to the polariton resonances. To concentrate exclusively on the polariton effects in the ZnSe layer, the solid lines in Fig. 4.8 show results of the microscopic calculation without Fabry-Perot effects. This corresponds to an ideal antireflection coating of the outer sample surfaces as it has been used throughout the preceding part of this work. For the macroscopic model, isotropic effective masses m_{e}^*, $m_{\mathrm{hh}}^* = m_{\mathrm{hh}z}^*$ for electrons and holes have to be used to facilitate the analytical solution, formulated in Section 3.5, which necessitates a slightly shifted band-gap energy $E_{\mathrm{gap}}^{\mathrm{Pekar}} = 2.8289\,\mathrm{eV}$ in comparison to the microscopic theory. The results are shown as dashed-dotted lines for a dipole coupling $d_{\mathrm{eh}}/e_0 = 3.7\,\text{Å}$ and as dotted lines for $d_{\mathrm{eh}}/e_0 = 2.89\,\text{Å}$, respectively.

The dipole coupling $d_{\mathrm{eh}}/e_0 = 3.7\,\text{Å}$ corresponds to the value of the microscopic theory. However, for the macroscopic model it turns out to be not appropriate. This is due to the assumption of homogeneity that enters the macroscopic model and that is not fulfilled for the system here. For a meaningful comparison with the microscopic theory, an effectively reduced dipole coupling constant is extracted from the microscopic theory in the following way: Within a homogeneous system the reduced exciton mass μ^* is connected to the bulk exciton binding energy $E_{\mathrm{b}}^{\mathrm{X}}(3D)$ given in Section 2.1 by

$$\mu^* = \frac{32\pi^2 \varepsilon_0^2 n_{\mathrm{bg}}^4 \hbar^2}{e_0^4} E_{\mathrm{b}}^{\mathrm{X}}(3D)\,.$$

Using the exciton binding energy $E_{\mathrm{b}}^{\mathrm{X}} = 19\,\mathrm{meV}$ obtained from the microscopic theory for the anisotropic system, it is possible to extract an effective reduced exciton mass μ_{eff}^*. This yields an effective exciton Bohr radius

$$a_{0,\mathrm{eff}}^{\mathrm{X}} = \frac{4\pi n_{\mathrm{bg}}^2 \varepsilon_0 \hbar^2}{\mu_{\mathrm{eff}}^* e_0^2}\,,$$

which, together with the dipole coupling constant $d_{\mathrm{eh}}/e_0 = 3.7\,\text{Å}$, provides an effective longitudinal-transversal splitting

$$\Delta_{\mathrm{LT}}^{\mathrm{mic}} = \frac{|d_{\mathrm{eh}}|^2}{\pi n_{\mathrm{bg}}^2 \varepsilon_0 a_{0,\mathrm{eff}}^{\mathrm{X}3}}\,. \tag{4.4}$$

With the assumption $\Delta_{\mathrm{LT}}^{\mathrm{Pekar}} = \Delta_{\mathrm{LT}}^{\mathrm{mic}}$ we obtain an effectively reduced dipole coupling constant $d_{\mathrm{eh}}/e_0 = 2.89\,\text{Å}$ for the macroscopic model. Our discussion shows, that within a macroscopic model for a homogeneous system applied to an inhomogeneous semiconductor heterostructure the dipole coupling constant is underestimated. In principle, the commonly used determination of dipole coupling constants from the longitudinal-transversal splitting is not appropriate here since Eq. (4.4) is only valid for homogeneous materials.

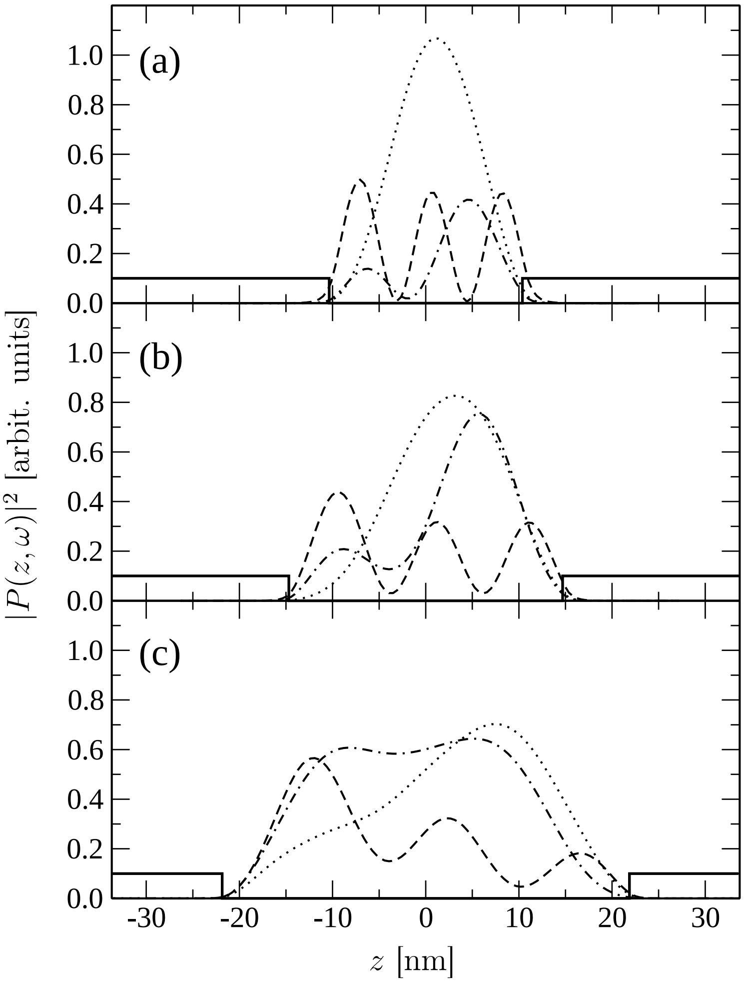

Figure 4.9: Steady-state polarization for monochromatic, resonant excitation of the three lowest polariton modes in the microscopic theory without Fabry-Perot effects for the (a) 20 nm, (b) 28 nm, and (c) 40 nm sample. The excitation frequency is tuned to the first (dotted line), second (dashed-dotted line), or third (dashed line) resonance, respectively. The solid lines illustrate the confinement potential for carriers in the ZnSe layer.

For each calculation based on Pekar's ABCs the layer thickness is adjusted for best reproduction of the energy positions of the polariton resonances in the experimental spectrum. The resulting values are given in Table 4.1. The values for the layer thickness chosen for the macroscopic model are *even larger* than the values that are experimentally determined as well as used for the microscopic calculation. At first glance this seems to be in contradiction to the fact that for infinitely high potential barriers of the ZnSe layer, a polarization-free dead-layer near the surface has been found in Section 4.1.

For a better understanding of these apparent inconsistencies in the application of Pekar's ABCs, Fig. 4.9 shows the spatially resolved macroscopic excitonic polarization $P(z,\omega)$ obtained from the microscopic theory for resonant monochromatic excitation of the lowest three polariton states. Due to the relatively small height of the confinement potentials in the ZnSe/ZnSSe system, the exciton wave functions can even penetrate slightly into the barrier region. This shows that for shallow confinement potentials the "effective" sample thickness used in the macroscopic calculations based on ABCs can even exceed the true layer thickness, and that in this case the dead-layer concept presented in Section 4.1 breaks down.

It is interesting to note that in a layer with high confinement potential the thickness of the region of reduced polarization varied for different polariton resonances of a given sample, Fig. 4.2. In the cases displayed in Fig. 4.9 this variation is much less pronounced. Especially for the 40 nm sample the effective thickness is almost the same for the displayed polariton modes. This also explains previous interpretations of experiments for ZnSe/ZnSSe heterostructures[13] in terms of Pekar's ABCs using the same effective thickness for all resonances of a given sample. As it turns out now, the used sample thickness exceeds the true value. However, the spatial dependence of the macroscopic polarization $P(z, \omega)$ in Fig. 4.9 clearly deviates from a simple picture of quantization of the COM motion which shows the intricate interplay of relative and COM motion with the propagating light field.

To summarize this chapter, in Section 4.1 a detailed comparison of polariton spectra calculated within a microscopic theory and in terms of a macroscopic approach based on Pekar's ABCs has been given. Attention has been focused to the shortcomings resulting from the lack of microscopic justification of the macroscopic model. A fundamental understanding of the deviations of both approaches has been obtained from the macroscopic polarization of the system. To account for a finite extension of the exciton states, polarization free dead-layers at the semiconductor surfaces have been introduced to augment the macroscopic model in comparison with the results of the microscopic theory. However, the dead-layer thickness has to be included as an additional phenomenological parameter and, even worse, this parameter is not uniquely given but it varies with the excitation frequency. This variation and the dependence on the reduced exciton mass has been deduced from the microscopic theory.

In Section 4.2 the microscopic theory has been applied to polariton propagation in a shallow confinement potential situation for which ZnSe/ZnSSe heterostructures served as a typical example. Results for the polariton modes in transmission spectra reproduce the experimental observations while calculations based on Pekar's ABCs require unrealistic modifications of the material parameters. This is due to the fact that Pekar's ABCs assume an infinite-height confinement potential where the realistic inclusion of the exciton relative motion has been found to require a polarization-free dead-layer. For shallow-confinement situations, a breakdown of these concepts has been demonstrated since the application of Pekar's ABCs requires an effective sample thickness which even exceeds the thickness of the confinement potential. Generally the use of macroscopic ABC models inherits uncertainties in the used sample thickness to adjust the spectral position and oscillatory strength of *all* polariton resonances of the same spectrum. In particular, the studied ZnSe/ZnSSe structures demonstrate the counteracting influence of a shallow confinement potential, the band offset, and the carrier masses that result in exciton wave functions having nearly the same effective spatial extension. This is, however, by no means trivial and strongly dependent on the material system.

Part II:

Nonlinear Optics

Introduction and Outline

The second part of this work is dedicated to the microscopic description of polariton propagation in the *nonlinear* optical regime. In linear optics the only dynamic quantity which determines the optical properties of the system is the excitonic transition amplitude. Here, in nonlinear optics, the dynamics-controlled truncation[7–9] (DCT) approach is used for a systematic truncation of the infinite many-particle hierarchy in the equation of motion for the excitonic polarization. This approach results in a perturbation theory in which all relevant many-particle correlations can, without further approximation, be taken into account. In the low-intensity regime and on ultra short time scales with a duration of the optical excitation typically shorter than one picosecond, the assumptions on which the DCT theory is based are very well fulfilled: Coherence for the electronic system which is optically excited from its ground state can almost perfectly be realized. So far, theories based on this scheme have successfully been applied to quasi two-dimensional quantum-well systems, e.g., in Refs. 20, 55–58, or to one-dimensional model systems.[28,59] The investigation of optical experiments gives an insight into the fundamental quantum mechanical processes excited in the semiconductor material. In particular, on ultra short time scales, coherent electronic excitations can be investigated before the coherence is destroyed by their coupling to, e.g., crystal lattice vibrations (phonons), or by scattering at imperfections in the crystal structure, or by carrier-carrier scattering with incoherent carrier populations.

However, in analogy to the linear optical regime discussed in Part I of this work, the description of optical excitations in semiconductor heterostructures makes it necessary to introduce boundary conditions for both the induced material polarization as well as for the optical fields. In typical quantum-well structures, where the spatial extension of the heterostructures is small compared to the wave length of the incident light field, propagation effects lead to radiative broadening[60] of excitonic resonances and in multiple quantum-well systems to a radiative coupling of several quantum-wells.[20] Systems of multiple quantum-wells coupled to the modes of a surrounding optical cavity, where the boundary conditions for the electromagnetic fields are of great importance, have been discussed in, e.g., Refs. 56, 61. Beyond the quantum-well limit, however, propagation effects in the nonlinear regime have only been discussed ignoring the influence of sample boundaries[62,63] or in a regime where incoherent carrier dynamics is dominant.[64,65]

Furthermore, commonly the analysis of propagation effects is done with boundary conditions that are only imposed on a macroscopic level,[12,59,65] in terms of additional boundary conditions (ABCs) as already discussed in Section 3.5. However, for semiconductor heterostructures with spatial extension of the order of several exciton Bohr radii, the structure of optical spectra is strongly influenced by propagation effects[43,65] and the proper treatment of sample boundaries becomes, as already discussed in the preceding chapters of this work, indispensable.

The nonlinear theory presented here is based on the DCT formalism and is applied to realistic heterostructures that can be characterized to be in between two and three space dimensions. The formulation incorporates both, propagation and coherent many-particle effects for these semiconductor layers. It properly accounts for the finite spatial extension of the exciton and biexciton states within a spatially inhomogeneous system. Based on this theory, nonlinear transmission spectra for single light pulses, in pump and probe and in four wave mixing geometry are presented and discussed in detail. To obtain a consistent theory it is necessary to restrict the calculations to third order nonlinearities and even the systematic inclusion of fifth order effects for the realistic system considered here, would be nearly impossible. So far, extensions beyond the third order have been discussed only for one-dimensional model systems[28] or for a certain class of higher order correlations[29–31] in quasi two-dimensional quantum-well systems.

In this work, the discussion of optical nonlinearities starts in Chapter 5. In Section 5.1 the equations of motion for the relevant dynamic quantities, namely the excitonic transition amplitude and the biexcitonic correlation function, are deduced. To make a solution of the resulting equations of motion possible, a description of the excitonic and biexcitonic problem in the exciton eigenbasis is derived in Section 5.2. The required matrix elements are calculated in the new basis, where, in analogy to Chapter 3, the eigenstates individually fulfill the physical boundary conditions of the system. An eigenfunction expansion that has successfully been applied to quantum-well systems[32,66,67] is reproduced in the quasi two-dimensional limit. In contrast to quantum-well systems,[29,58,67] however, the expansion of biexciton states in terms of exciton eigenfunctions can here systematically be extended beyond the exciton ground state. In Section 5.3 the resulting matrix elements are discussed and, in particular, the dependence of the biexciton binding energy on the layer thickness is studied. Chapter 6 is dedicated to the equations of motion which are explicitly given to simulate optical experiments for single pulse transmission, in pump and probe as well as in four wave mixing geometry.

In Chapter 7 the theory is applied to the calculation of optical spectra. The complicated interplay of propagation effects and excitonic as well as biexcitonic nonlinearities is discussed in detail. Pronounced signatures of the bound biexciton state and the exciton-exciton scattering continuum are found in the optical spectra. Theses signatures show a strong dependence on the polarization of the exciting light fields. In particular, the Coulomb interaction of different polariton modes is found to strongly influence the observed nonlinearities in contrast to the linear optical regime. To conclude the discussions, a direct theory-experiment comparison for nonlinear transmission spectra of a single laser pulse is presented. Excellent agreement of theoretical results and measurements is observed.

5. Dynamics-Controlled Truncation

To extend the discussion of optically induced interband polarizations beyond the limits of the linear exciton equation (2.13), we start again with the exact equation of motion for the excitonic transition amplitude $p^{\rm eh}_{(\mathbf{k},z_{\rm e},z_{\rm h})}$ which has been introduced in Eq. (2.11):

$$\begin{aligned} i\hbar\frac{\partial}{\partial t}p^{\rm eh}_{(\mathbf{k},z_{\rm e},z_{\rm h})} =& \big(\varepsilon^{\rm e}_{\mathbf{k},z_{\rm e}} + \varepsilon^{\rm h}_{\mathbf{k},z_{\rm h}}\big)p^{\rm eh}_{(\mathbf{k},z_{\rm e},z_{\rm h})} - \sum_{\mathbf{k}'} V^{z_{\rm e}z_{\rm h}}_{\mathbf{k}-\mathbf{k}'}p^{\rm eh}_{(\mathbf{k}',z_{\rm e},z_{\rm h})} - \mathbf{d}_{\rm eh}\mathbf{E}(z_{\rm e})\delta(z_{\rm e}-z_{\rm h}) \\ &+ \sum_{\rm h'}\mathbf{d}_{\rm eh'}\mathbf{E}(z_{\rm e})\Big\langle \psi^{\rm h'\dagger}_{\mathbf{k}}(z_{\rm e})\psi^{\rm h}_{\mathbf{k}}(z_{\rm h})\Big\rangle + \sum_{\rm e'}\mathbf{d}_{\rm e'h}\mathbf{E}(z_{\rm h})\Big\langle \psi^{\rm e'\dagger}_{\mathbf{k}}(z_{\rm h})\psi^{\rm e}_{\mathbf{k}}(z_{\rm e})\Big\rangle \\ &- \sum_{\mathbf{k}'\mathbf{q}}\int {\rm d}z\Bigg[V^{zz_{\rm h}}_{\mathbf{q}}\Bigg(\sum_{\rm h'}\Big\langle \psi^{\rm h'\dagger}_{\mathbf{k}'+\mathbf{q}}(z)\psi^{\rm h}_{\mathbf{k}+\mathbf{q}}(z_{\rm h})\psi^{\rm h'}_{\mathbf{k}'}(z)\psi^{\rm e}_{\mathbf{k}}(z_{\rm e})\Big\rangle \\ &\qquad - \sum_{\rm e'}\Big\langle \psi^{\rm e'\dagger}_{\mathbf{k}'-\mathbf{q}}(z)\psi^{\rm h}_{\mathbf{k}+\mathbf{q}}(z_{\rm h})\psi^{\rm e'}_{\mathbf{k}'}(z)\psi^{\rm e}_{\mathbf{k}}(z_{\rm e})\Big\rangle\Bigg) \\ &\qquad - V^{zz_{\rm e}}_{\mathbf{q}}\Bigg(\sum_{\rm h'}\Big\langle \psi^{\rm h'\dagger}_{\mathbf{k}'}(z)\psi^{\rm h}_{\mathbf{k}}(z_{\rm h})\psi^{\rm h'}_{\mathbf{k}'+\mathbf{q}}(z)\psi^{\rm e}_{\mathbf{k}+\mathbf{q}}(z_{\rm e})\Big\rangle \\ &\qquad - \sum_{\rm e'}\Big\langle \psi^{\rm e'\dagger}_{\mathbf{k}'+\mathbf{q}}(z)\psi^{\rm h}_{\mathbf{k}}(z_{\rm h})\psi^{\rm e'}_{\mathbf{k}'}(z)\psi^{\rm e}_{\mathbf{k}+\mathbf{q}}(z_{\rm e})\Big\rangle\Bigg)\Bigg]\,. \end{aligned} \tag{5.1}$$

As already discussed in Chapter 2, the dynamics of the excitonic transition amplitude is coupled to that of the electron $\langle \psi^{\rm e'\dagger}_{\mathbf{k}}(z_{\rm h})\psi^{\rm e}_{\mathbf{k}}(z_{\rm e})\rangle$ and hole $\langle \psi^{\rm h'\dagger}_{\mathbf{k}}(z_{\rm e})\psi^{\rm h}_{\mathbf{k}}(z_{\rm h})\rangle$ occupation functions and to that of higher order Coulomb correlations (lines 3-6 in Eq. (5.1)). In order to overcome this many-particle hierarchy problem of the interacting electronic system, a "factorization" of the expectation values in (5.1) is used. Note, that strictly speaking not a factorization is applied here, but all the relevant expectation values are systematically truncated in a certain order in the exciting light fields as described in the following. This way, a consistent $\chi^{(3)}$-theory is derived, including all optically excited third-order nonlinearities in the coherent limit.

Coherent excitations contain information about phase and amplitude of the exciting light fields. In typical semiconductor layers at low temperatures (for example Helium cooled, 4 K), and with a high crystalline perfection, the phase information is lost on typical time scales in the range of several femtoseconds (fs) up to a few picoseconds (ps). The loss of coherence results in a decay of the optically induced macroscopic polarization in the semiconductor material. The coherence is destroyed by scattering processes of the optical excitations with phonons, with incoherent, not directly optically excited carrier populations, or by scattering at imperfections in the crystal lattice. To obtain a theory, applicable to time scales where incoherent contributions are insignificant, the dynamics-controlled truncation (DCT) approach[7–9] is used here.

Within this approach a truncation of the many-particle hierarchy in a certain order in the optical field for all contributions in Eq. (5.1) is possible. It takes advantage of the coherence of the electronic system for exclusive optical excitation where all many-particle effects can be classified by a certain order in the optical field.[a)]

For a fully coherent situation, all electronic excitations are described by a correlated transition of a finite number of electron-hole pairs, driven by the optical field. All relevant expectation values can be expressed in terms of polarization-like contributions up to an arbitrary order in the optical field as described in Appendix A.2. Polarization-like expectation values exclusively contain *pairs* of electron and hole creation or annihilation operators in analogy to the excitonic polarization. Depending on the intensity of the exciting light field the theory can be restricted to effects of a certain order in the optical field. Thus, the general relation $P = \chi(E)E$ of the macroscopic polarization P to the electric field E, determined by the system susceptibility $\chi(E)$, can be illustrated by a schematic power series in terms of the electric field:

$$P = \chi^{(1)}E + \chi^{(3)}E^3 + \chi^{(5)}E^5 + \dots . \tag{5.2}$$

Truncation of this power series behind the i^{th} term results in a so-called $\chi^{(i)}$-theory. Since the theory is based on a perturbation approach with respect to the exciting electromagnetic fields, it is limited to sufficiently low intensities. Nevertheless, all Coulomb correlations that are relevant in a given order in the optical field are included in the theoretical description. In the case of an experiment the intensity of the optical field can be varied to obtain results in the $\chi^{(i)}$-limit. In principle, thinking of a power series (5.2), a many-particle theory can be deduced up to an arbitrary order in the optical field. However, an extension of the theory beyond third order many-particle effects is really awkward and has, so far, only been analyzed for one-dimensional model systems[28] or for a certain, selected class of higher order nonlinearities.[29–31] In this work, however, the theory is restricted to the $\chi^{(3)}$-limit and therefore to third order optical nonlinearities in the material polarization P.

5.1. Equations of Motion in the Coherent $\chi^{(3)}$-Limit

The first line in Eq. (5.1) describes the linear contribution to the excitonic dynamics that has extensively been studied in the preceding part of this work. Going beyond the linear order in the external field $E(z)$, it is coupled to the dynamics of the electron and hole occupation functions (line 2 in Eq. (5.1)). Lines 3-6 in Eq. (5.1) contain many-particle correlations that cannot be analyzed within an effective two-particle picture. Since the theory is restricted to coherent optical nonlinearities, an appropriate factorization of the occupation functions and four-point expectation values can be found by the dynamics-controlled truncation of the many-particle hierarchy. As details are given in

---

[a)] Incoherent effects, e.g., due to non-optical electronic excitations, cannot be captured within this theory. For details refer to Ref. 19 or to Appendix A.2.

Appendix A.2, only two essential requirements underlying the following theory shall be summarized here:

- the electronic system is in its ground state prior to the optical excitation
- the Hamiltonian that determines the dynamics of the system is given by Eq. (2.1) on page 13, thus, no non-optical excitation occurs and Coulomb interaction conserves the number of carriers in conduction and valence bands individually

Making use of these fundamental assumptions, in Appendix A.2 the following expressions for the quantities in Eq. (5.1) are found.

In the coherent limit, the occupation functions

$$\left\langle \psi_{\mathbf{k}}^{\mathrm{e}'\dagger}(z_{\mathrm{h}}) \psi_{\mathbf{k}}^{\mathrm{e}}(z_{\mathrm{e}}) \right\rangle = \sum_{\mathrm{h}} \int \mathrm{d}z \, p^{*\mathrm{e}'\mathrm{h}}_{(\mathbf{k},z_{\mathrm{h}},z)} p^{\mathrm{eh}}_{(\mathbf{k},z_{\mathrm{e}},z)} + \mathcal{O}(E^4)\,, \tag{5.3}$$

$$\left\langle \psi_{\mathbf{k}}^{\mathrm{h}'\dagger}(z_{\mathrm{e}}) \psi_{\mathbf{k}}^{\mathrm{h}}(z_{\mathrm{h}}) \right\rangle = \sum_{\mathrm{e}} \int \mathrm{d}z \, p^{*\mathrm{eh}'}_{(\mathbf{k},z,z_{\mathrm{e}})} p^{\mathrm{eh}}_{(\mathbf{k},z,z_{\mathrm{h}})} + \mathcal{O}(E^4) \tag{5.4}$$

can be factorized in terms of products of excitonic polarizations and an additional contribution that is at least of fourth order in the external field. The "factorization" of electron-screened and hole-screened[b)] transition amplitudes is given by:

$$\begin{aligned} \left\langle \psi_{\mathbf{k}_1}^{\mathrm{e}'\dagger}(z) \psi_{\mathbf{k}_2}^{\mathrm{e}'}(z) \psi_{\mathbf{k}_3}^{\mathrm{h}}(z_{\mathrm{h}}) \psi_{\mathbf{k}_4}^{\mathrm{e}}(z_{\mathrm{e}}) \right\rangle = & \sum_{\mathrm{h}'} \int \mathrm{d}z' p^{*\mathrm{e}'\mathrm{h}'}_{(\mathbf{k}_1,z,z')} \left\langle \psi_{\mathbf{k}_1}^{\mathrm{h}'}(z') \psi_{\mathbf{k}_2}^{\mathrm{e}'}(z) \psi_{\mathbf{k}_3}^{\mathrm{h}}(z_{\mathrm{h}}) \psi_{\mathbf{k}_4}^{\mathrm{e}}(z_{\mathrm{e}}) \right\rangle \\ & + \mathcal{O}(E^5)\,, \end{aligned} \tag{5.5}$$

$$\begin{aligned} \left\langle \psi_{\mathbf{k}_1}^{\mathrm{h}'\dagger}(z) \psi_{\mathbf{k}_2}^{\mathrm{h}'}(z) \psi_{\mathbf{k}_3}^{\mathrm{h}}(z_{\mathrm{h}}) \psi_{\mathbf{k}_4}^{\mathrm{e}}(z_{\mathrm{e}}) \right\rangle = & \sum_{\mathrm{e}'} \int \mathrm{d}z' p^{*\mathrm{e}'\mathrm{h}'}_{(\mathbf{k}_1,z',z)} \left\langle \psi_{\mathbf{k}_2}^{\mathrm{h}'}(z) \psi_{\mathbf{k}_1}^{\mathrm{e}'}(z') \psi_{\mathbf{k}_3}^{\mathrm{h}}(z_{\mathrm{h}}) \psi_{\mathbf{k}_4}^{\mathrm{e}}(z_{\mathrm{e}}) \right\rangle \\ & + \mathcal{O}(E^5)\,. \end{aligned} \tag{5.6}$$

In order to deduce a $\chi^{(3)}$-theory it is sufficient to take merely into account the leading order of Eqs. (5.3)-(5.6) in Eq. (5.1). In conclusion, the relevant four-point expectation values contributing to the excitonic dynamics (5.1) can be factorized in terms of a product of an excitonic polarization $p^{\mathrm{eh}}_{(\mathbf{k},z,z')}$ and a polarization-like four-particle expectation value that brings into play the correlated transition of two electron-hole pairs, the biexcitonic transition amplitude $\left\langle \psi_{\mathbf{k}_2}^{\mathrm{h}'}(z) \psi_{\mathbf{k}_1}^{\mathrm{e}'}(z') \psi_{\mathbf{k}_3}^{\mathrm{h}}(z_{\mathrm{h}}) \psi_{\mathbf{k}_4}^{\mathrm{e}}(z_{\mathrm{e}}) \right\rangle$.

[b)] The name is connected to the structure of these expectation values. They contain the two operators $\psi_{\mathbf{k}_3}^{\mathrm{h}}(z_{\mathrm{h}})\psi_{\mathbf{k}_4}^{\mathrm{e}}(z_{\mathrm{e}})$ that describe the annihilation of one electron-hole pair and an additional electron $\psi_{\mathbf{k}_1}^{\mathrm{e}'\dagger}(z)\psi_{\mathbf{k}_2}^{\mathrm{e}'}(z)$ or hole $\psi_{\mathbf{k}_1}^{\mathrm{h}'\dagger}(z)\psi_{\mathbf{k}_2}^{\mathrm{h}'}(z)$ number operator, respectively.

Regarding the structure of the resulting equations of motion, in analogy to Ref. 19, the introduction of the biexcitonic correlation function

$$\begin{aligned} b^{\mathrm{e'h'}\;(\mathbf{k}_2,z_2,\mathbf{k}_1,z_1)}_{\mathrm{eh}\;\;(\mathbf{k}_4,z_4,\mathbf{k}_3,z_3)} &= \left\langle \psi^{\mathrm{h'}}_{\mathbf{k}_1}(z_1)\psi^{\mathrm{e'}}_{\mathbf{k}_2}(z_2)\psi^{\mathrm{h}}_{\mathbf{k}_3}(z_3)\psi^{\mathrm{e}}_{\mathbf{k}_4}(z_4)\right\rangle \\ &- \left\langle \psi^{\mathrm{h'}}_{\mathbf{k}_1}(z_1)\psi^{\mathrm{e'}}_{\mathbf{k}_2}(z_2)\right\rangle\left\langle \psi^{\mathrm{h}}_{\mathbf{k}_3}(z_3)\psi^{\mathrm{e}}_{\mathbf{k}_4}(z_4)\right\rangle \\ &+ \left\langle \psi^{\mathrm{h'}}_{\mathbf{k}_1}(z_1)\psi^{\mathrm{e}}_{\mathbf{k}_4}(z_4)\right\rangle\left\langle \psi^{\mathrm{h}}_{\mathbf{k}_3}(z_3)\psi^{\mathrm{e'}}_{\mathbf{k}_2}(z_2)\right\rangle \end{aligned} \tag{5.7}$$

is convenient at this point. Using the leading order of the factorizations in Eqs. (5.3)-(5.6) and the definition (5.7) together with Eq. (5.1), the equation of motion for the excitonic transition amplitude up to third order in the optical field reads:

$$\begin{aligned} i\hbar\frac{\partial}{\partial t}p^{\mathrm{eh}}_{(\mathbf{k},z_{\mathrm{e}},z_{\mathrm{h}})} &= \left(\varepsilon^{\mathrm{e}}_{\mathbf{k},z_{\mathrm{e}}}+\varepsilon^{\mathrm{h}}_{\mathbf{k},z_{\mathrm{h}}}\right)p^{\mathrm{eh}}_{(\mathbf{k},z_{\mathrm{e}},z_{\mathrm{h}})} - \sum_{\mathbf{k}'} V^{z_{\mathrm{e}}z_{\mathrm{h}}}_{\mathbf{k}-\mathbf{k}'}p^{\mathrm{eh}}_{(\mathbf{k}',z_{\mathrm{e}},z_{\mathrm{h}})} - \mathbf{d}_{\mathrm{eh}}\mathbf{E}(z_{\mathrm{e}})\delta(z_{\mathrm{e}}-z_{\mathrm{h}}) \\ &+ \sum_{\mathrm{e'h'}}\Big[\mathbf{d}_{\mathrm{eh'}}\mathbf{E}(z_{\mathrm{e}})\int \mathrm{d}z\, p^{*\mathrm{e'h'}}_{(\mathbf{k},z,z_{\mathrm{e}})}p^{\mathrm{e'h}}_{(\mathbf{k},z,z_{\mathrm{h}})} + \mathbf{d}_{\mathrm{e'h}}\mathbf{E}(z_{\mathrm{h}})\int \mathrm{d}z\, p^{*\mathrm{e'h'}}_{(\mathbf{k},z_{\mathrm{h}},z)}p^{\mathrm{eh'}}_{(\mathbf{k},z_{\mathrm{e}},z)}\Big] \\ &+ \sum_{\mathbf{k}'\mathrm{e'h'}}\int \mathrm{d}z_{\mathrm{e'}}\mathrm{d}z_{\mathrm{h'}}\Big[\Big(V^{z_{\mathrm{e'}}z_{\mathrm{h}}}_{\mathbf{k}-\mathbf{k}'}p^{*\mathrm{e'h'}}_{(\mathbf{k},z_{\mathrm{e'}},z_{\mathrm{h'}})} - V^{z_{\mathrm{h'}}z_{\mathrm{h}}}_{\mathbf{k}-\mathbf{k}'}p^{*\mathrm{e'h'}}_{(\mathbf{k}',z_{\mathrm{e'}},z_{\mathrm{h'}})}\Big)p^{\mathrm{eh'}}_{(\mathbf{k},z_{\mathrm{e}},z_{\mathrm{h'}})}p^{\mathrm{e'h}}_{(\mathbf{k}',z_{\mathrm{e'}},z_{\mathrm{h}})} \\ &\qquad + \Big(V^{z_{\mathrm{h'}}z_{\mathrm{e}}}_{\mathbf{k}-\mathbf{k}'}p^{*\mathrm{e'h'}}_{(\mathbf{k},z_{\mathrm{e'}},z_{\mathrm{h'}})} - V^{z_{\mathrm{e'}}z_{\mathrm{e}}}_{\mathbf{k}-\mathbf{k}'}p^{*\mathrm{e'h'}}_{(\mathbf{k}',z_{\mathrm{e'}},z_{\mathrm{h'}})}\Big)p^{\mathrm{eh'}}_{(\mathbf{k}',z_{\mathrm{e}},z_{\mathrm{h'}})}p^{\mathrm{e'h}}_{(\mathbf{k},z_{\mathrm{e'}},z_{\mathrm{h}})}\Big] \\ &+ \sum_{\mathbf{k}'\mathbf{q}\mathrm{e'h'}}\int \mathrm{d}z_{\mathrm{e'}}\mathrm{d}z_{\mathrm{h'}}\Big[\Big(V^{z_{\mathrm{h'}}z_{\mathrm{h}}}_{\mathbf{q}}p^{*\mathrm{e'h'}}_{(\mathbf{k}'+\mathbf{q},z_{\mathrm{e'}},z_{\mathrm{h'}})} - V^{z_{\mathrm{e'}}z_{\mathrm{h}}}_{\mathbf{q}}p^{*\mathrm{e'h'}}_{(\mathbf{k}',z_{\mathrm{e'}},z_{\mathrm{h'}})}\Big)b^{\mathrm{e'h'}\;(\mathbf{k}'+\mathbf{q},z_{\mathrm{e'}},\mathbf{k}',z_{\mathrm{h'}})}_{\mathrm{eh}\;\;(\mathbf{k},z_{\mathrm{e}},\mathbf{k}+\mathbf{q},z_{\mathrm{h}})} \\ &\qquad + \Big(V^{z_{\mathrm{e'}}z_{\mathrm{e}}}_{\mathbf{q}}p^{*\mathrm{e'h'}}_{(\mathbf{k}'+\mathbf{q},z_{\mathrm{e'}},z_{\mathrm{h'}})} - V^{z_{\mathrm{h'}}z_{\mathrm{e}}}_{\mathbf{q}}p^{*\mathrm{e'h'}}_{(\mathbf{k}',z_{\mathrm{e'}},z_{\mathrm{h'}})}\Big)b^{\mathrm{e'h'}\;(\mathbf{k}',z_{\mathrm{e'}},\mathbf{k}'+\mathbf{q},z_{\mathrm{h'}})}_{\mathrm{eh}\;\;(\mathbf{k}+\mathbf{q},z_{\mathrm{e}},\mathbf{k},z_{\mathrm{h}})}\Big]. \end{aligned} \tag{5.8}$$

This equation of motion contains all coherent third order effects and therefore reveals exact results for sufficiently weak electromagnetic fields. The definition (5.7) of the biexcitonic correlation function is advantageous since Eq. (5.8) explicitly contains all contributions that can be obtained from a Hartree-Fock factorization[11] of the four-point expectation values in Eq. (5.1) in analogy to the Semiconductor Bloch Equations given in Ref. 11. These equations can be solved self-consistently up to an arbitrary order in the optical field but only include effective two-particle effects in the description of the electronic many-particle system. Consistent and exact results are only obtained in the linear limit as it has been used throughout the previous chapters of this work.

Line 2 in Eq. (5.8) describes a renormalization of the Rabi energy $\mathbf{d}_{\mathrm{eh}}\mathbf{E}$ for the excitonic transition amplitude $p^{\mathrm{eh}}_{(\mathbf{k},z_{\mathrm{e}},z_{\mathrm{h}})}$ resulting from the phase-space filling (Pauli-blocking). Hence, the dipole coupling strength is effectively reduced by the coherent contributions to the electron and hole occupation functions. Lines 3 and 4 contain the renormalization of the electron-hole Coulomb interaction which is already present in the linearized version of Eq. (5.1) and a renormalization of the band-gap energy for coherent excitation up to third order in the optical field. Here, all contributions beyond the Hartree-Fock result are due to the influence of correlated four-particle transitions and are given by the coupling to the biexcitonic correlation function in lines 5 and 6 of Eq. (5.8). The use of the definition (5.7) allows a more detailed analysis of the theory. Within this formulation, an explicit occurrence of correlated four-particle transitions in Eq. (5.8) is obtained. Therefore, during the numerical evaluation the distinction of effective two-particle and correlated four-particle (biexcitonic) nonlinearities that are beyond a third order Hartree-Fock theory is possible.

To describe the coupling of the excitonic dynamics to the biexcitonic correlation function an equation of motion for the latter one is required. We are interested in third order contributions to the excitonic transition amplitude $p^{\mathrm{eh}}_{(\mathbf{k},z_{\mathrm{e}},z_{\mathrm{h}})}$ in Eq. (5.8). Since the excitonic transition amplitude itself is at least of first order in the optical field, an equation of motion for the biexcitonic correlation functions $b^{\mathrm{e'h'}\;(\mathbf{k}_2,z_2,\mathbf{k}_1,z_1)}_{\mathrm{eh}\;(\mathbf{k}_4,z_4,\mathbf{k}_3,z_3)}$ in Eq. (5.8) that contains at least all second order contributions is required. Hence, all contributions, being in leading order beyond the second order, are neglected in the equation of motion for the biexcitonic correlation function. Using Heisenberg's equation of motion (2.10), a straight forward but somewhat lengthy calculation yields the dynamics of the biexcitonic correlation function (5.7) that is needed in Eq. (5.8):

$$
\begin{aligned}
i\hbar\frac{\partial}{\partial t} b^{\mathrm{e'h'}\;(\mathbf{k}',z_{\mathrm{e'}},\mathbf{k}'+\mathbf{q},z_{\mathrm{h'}})}_{\mathrm{eh}\;(\mathbf{k}+\mathbf{q},z_{\mathrm{e}},\mathbf{k},z_{\mathrm{h}})} &= \Big(\varepsilon^{\mathrm{e}}_{\mathbf{k}+\mathbf{q},z_{\mathrm{e}}} + \varepsilon^{\mathrm{h}}_{\mathbf{k},z_{\mathrm{h}}} + \varepsilon^{\mathrm{e'}}_{\mathbf{k}',z_{\mathrm{e'}}} + \varepsilon^{\mathrm{h'}}_{\mathbf{k}'+\mathbf{q},z_{\mathrm{h'}}}\Big) b^{\mathrm{e'h'}\;(\mathbf{k}',z_{\mathrm{e'}},\mathbf{k}'+\mathbf{q},z_{\mathrm{h'}})}_{\mathrm{eh}\;(\mathbf{k}+\mathbf{q},z_{\mathrm{e}},\mathbf{k},z_{\mathrm{h}})} \\
&\quad + \sum_{\mathbf{q}'} \Big[V^{z_{\mathrm{h'}}z_{\mathrm{h}}}_{\mathbf{q}'} b^{\mathrm{e'h'}\;(\mathbf{k}',z_{\mathrm{e'}},\mathbf{k}'+\mathbf{q}+\mathbf{q}',z_{\mathrm{h'}})}_{\mathrm{eh}\;(\mathbf{k}+\mathbf{q},z_{\mathrm{e}},\mathbf{k}-\mathbf{q}',z_{\mathrm{h}})} + V^{z_{\mathrm{e'}}z_{\mathrm{e}}}_{\mathbf{q}'} b^{\mathrm{e'h'}\;(\mathbf{k}'-\mathbf{q}',z_{\mathrm{e'}},\mathbf{k}'+\mathbf{q},z_{\mathrm{h'}})}_{\mathrm{eh}\;(\mathbf{k}+\mathbf{q}+\mathbf{q}',z_{\mathrm{e}},\mathbf{k},z_{\mathrm{h}})} \\
&\qquad - V^{z_{\mathrm{h'}}z_{\mathrm{e'}}}_{\mathbf{q}'} b^{\mathrm{e'h'}\;(\mathbf{k}'+\mathbf{q}',z_{\mathrm{e'}},\mathbf{k}'+\mathbf{q}+\mathbf{q}',z_{\mathrm{h'}})}_{\mathrm{eh}\;(\mathbf{k}+\mathbf{q},z_{\mathrm{e}},\mathbf{k},z_{\mathrm{h}})} - V^{z_{\mathrm{e'}}z_{\mathrm{h}}}_{\mathbf{q}'} b^{\mathrm{e'h'}\;(\mathbf{k}'+\mathbf{q}',z_{\mathrm{e'}},\mathbf{k}'+\mathbf{q},z_{\mathrm{h'}})}_{\mathrm{eh}\;(\mathbf{k}+\mathbf{q},z_{\mathrm{e}},\mathbf{k}+\mathbf{q}',z_{\mathrm{h}})} \\
&\qquad - V^{z_{\mathrm{h}}z_{\mathrm{e}}}_{\mathbf{q}'} b^{\mathrm{e'h'}\;(\mathbf{k}',z_{\mathrm{e'}},\mathbf{k}'+\mathbf{q},z_{\mathrm{h'}})}_{\mathrm{eh}\;(\mathbf{k}+\mathbf{q}+\mathbf{q}',z_{\mathrm{e}},\mathbf{k}+\mathbf{q}',z_{\mathrm{h}})} - V^{z_{\mathrm{h'}}z_{\mathrm{e}}}_{\mathbf{q}'} b^{\mathrm{e'h'}\;(\mathbf{k}',z_{\mathrm{e'}},\mathbf{k}'+\mathbf{q}+\mathbf{q}',z_{\mathrm{h'}})}_{\mathrm{eh}\;(\mathbf{k}+\mathbf{q}+\mathbf{q}',z_{\mathrm{e}},\mathbf{k},z_{\mathrm{h}})} \Big] \\
&\qquad + \Big(V^{z_{\mathrm{h'}}z_{\mathrm{h}}}_{\mathbf{q}} p^{\mathrm{e'h'}}_{(\mathbf{k}',z_{\mathrm{e'}},z_{\mathrm{h'}})} - V^{z_{\mathrm{e'}}z_{\mathrm{h}}}_{\mathbf{q}} p^{\mathrm{e'h'}}_{(\mathbf{k}'+\mathbf{q},z_{\mathrm{e'}},z_{\mathrm{h'}})} \Big) p^{\mathrm{eh}}_{(\mathbf{k}+\mathbf{q},z_{\mathrm{e}},z_{\mathrm{h}})} \\
&\qquad + \Big(V^{z_{\mathrm{e'}}z_{\mathrm{e}}}_{\mathbf{q}} p^{\mathrm{e'h'}}_{(\mathbf{k}'+\mathbf{q},z_{\mathrm{e'}},z_{\mathrm{h'}})} - V^{z_{\mathrm{h'}}z_{\mathrm{e}}}_{\mathbf{q}} p^{\mathrm{e'h'}}_{(\mathbf{k}',z_{\mathrm{e'}},z_{\mathrm{h'}})} \Big) p^{\mathrm{eh}}_{(\mathbf{k},z_{\mathrm{e}},z_{\mathrm{h}})} \\
&\qquad - \Big(V^{z_{\mathrm{h'}}z_{\mathrm{h}}}_{\mathbf{k}-\mathbf{k}'} p^{\mathrm{e'h}}_{(\mathbf{k}',z_{\mathrm{e'}},z_{\mathrm{h}})} - V^{z_{\mathrm{h'}}z_{\mathrm{e'}}}_{\mathbf{k}-\mathbf{k}'} p^{\mathrm{e'h}}_{(\mathbf{k},z_{\mathrm{e'}},z_{\mathrm{h}})} \Big) p^{\mathrm{eh'}}_{(\mathbf{k}+\mathbf{q},z_{\mathrm{e}},z_{\mathrm{h'}})} \\
&\qquad - \Big(V^{z_{\mathrm{e'}}z_{\mathrm{e}}}_{\mathbf{k}-\mathbf{k}'} p^{\mathrm{e'h}}_{(\mathbf{k},z_{\mathrm{e'}},z_{\mathrm{h}})} - V^{z_{\mathrm{e}}z_{\mathrm{h}}}_{\mathbf{k}-\mathbf{k}'} p^{\mathrm{e'h}}_{(\mathbf{k}',z_{\mathrm{e'}},z_{\mathrm{h}})} \Big) p^{\mathrm{eh'}}_{(\mathbf{k}'+\mathbf{q},z_{\mathrm{e}},z_{\mathrm{h'}})} \,. \qquad (5.9)
\end{aligned}
$$

In second order for the biexcitonic correlation function, the only dynamic quantity that enters the source terms (lines 5-8) of this equation is the excitonic transition amplitude $p^{\mathrm{eh}}_{(\mathbf{k},z_{\mathrm{e}},z_{\mathrm{h}})}$. Therefore a coupled but closed system of equations (5.8), (5.9) to calculate the coherent semiconductor response up to third order in the optical field is found. In analogy to the exciton equation (3.2) on page 27, the homogeneous part of Eq. (5.9) can be abbreviated by introduction of a biexcitonic Hamiltonian $\mathcal{H}^{\mathrm{ehe'h'}}_{\mathrm{XX}}$:

$$
\begin{aligned}
i\hbar\frac{\partial}{\partial t} b^{\mathrm{e'h'}\;(\mathbf{k}',z_{\mathrm{e'}},\mathbf{k}'+\mathbf{q},z_{\mathrm{h'}})}_{\mathrm{eh}\;(\mathbf{k}+\mathbf{q},z_{\mathrm{e}},\mathbf{k},z_{\mathrm{h}})} &= \mathcal{H}^{\mathrm{ehe'h'}}_{\mathrm{XX}} b^{\mathrm{e'h'}\;(\mathbf{k}',z_{\mathrm{e'}},\mathbf{k}'+\mathbf{q},z_{\mathrm{h'}})}_{\mathrm{eh}\;(\mathbf{k}+\mathbf{q},z_{\mathrm{e}},\mathbf{k},z_{\mathrm{h}})} \\
&\qquad + \Big(V^{z_{\mathrm{h'}}z_{\mathrm{h}}}_{\mathbf{q}} p^{\mathrm{e'h'}}_{(\mathbf{k}',z_{\mathrm{e'}},z_{\mathrm{h'}})} - V^{z_{\mathrm{e'}}z_{\mathrm{h}}}_{\mathbf{q}} p^{\mathrm{e'h'}}_{(\mathbf{k}'+\mathbf{q},z_{\mathrm{e'}},z_{\mathrm{h'}})} \Big) p^{\mathrm{eh}}_{(\mathbf{k}+\mathbf{q},z_{\mathrm{e}},z_{\mathrm{h}})} \\
&\qquad + \Big(V^{z_{\mathrm{e'}}z_{\mathrm{e}}}_{\mathbf{q}} p^{\mathrm{e'h'}}_{(\mathbf{k}'+\mathbf{q},z_{\mathrm{e'}},z_{\mathrm{h'}})} - V^{z_{\mathrm{h'}}z_{\mathrm{e}}}_{\mathbf{q}} p^{\mathrm{e'h'}}_{(\mathbf{k}',z_{\mathrm{e'}},z_{\mathrm{h'}})} \Big) p^{\mathrm{eh}}_{(\mathbf{k},z_{\mathrm{e}},z_{\mathrm{h}})} \\
&\qquad - \Big(V^{z_{\mathrm{h'}}z_{\mathrm{h}}}_{\mathbf{k}-\mathbf{k}'} p^{\mathrm{e'h}}_{(\mathbf{k}',z_{\mathrm{e'}},z_{\mathrm{h}})} - V^{z_{\mathrm{h'}}z_{\mathrm{e'}}}_{\mathbf{k}-\mathbf{k}'} p^{\mathrm{e'h}}_{(\mathbf{k},z_{\mathrm{e'}},z_{\mathrm{h}})} \Big) p^{\mathrm{eh'}}_{(\mathbf{k}+\mathbf{q},z_{\mathrm{e}},z_{\mathrm{h'}})} \\
&\qquad - \Big(V^{z_{\mathrm{e'}}z_{\mathrm{e}}}_{\mathbf{k}-\mathbf{k}'} p^{\mathrm{e'h}}_{(\mathbf{k},z_{\mathrm{e'}},z_{\mathrm{h}})} - V^{z_{\mathrm{e}}z_{\mathrm{h}}}_{\mathbf{k}-\mathbf{k}'} p^{\mathrm{e'h}}_{(\mathbf{k}',z_{\mathrm{e'}},z_{\mathrm{h}})} \Big) p^{\mathrm{eh'}}_{(\mathbf{k}'+\mathbf{q},z_{\mathrm{e}},z_{\mathrm{h'}})} \,.
\end{aligned}
$$

This equation is equivalent to an inhomogeneous time-dependent Schrödinger equation for a two-electron-two-hole system. The biexcitonic Hamiltonian $\mathcal{H}_{\mathrm{XX}}^{\mathrm{ehe'h'}}$ determines the spectral properties of biexcitonic correlations, including a bound biexciton state and the exciton-exciton scattering continuum. Note, that the inhomogeneity here is not due to the optical fields but due to products of two excitonic transition amplitudes, hence the biexcitonic correlation function is not directly optically driven.

The classification of many-particle effects by the number of involved electron-hole pairs is, strictly speaking, only valid for a fully coherently driven system. Therefore, a system is assumed where no non-optical excitation and no dephasing of the coherent polarizations due to incoherent scattering processes occurs. Only keeping these assumptions in mind, Eqs. (5.8) and (5.9) form a closed set of equations. Otherwise there would be a coupling to non polarization-like quantities as for example incoherent contributions to the electron or hole occupation functions that cannot be factorized into products of polarization-like expectation values.[7,19] However, for the numerical evaluation of the equations of motion (5.8) and (5.9), the introduction of dephasing processes for the coherent excitations on a phenomenological level becomes necessary. In principle, the inclusion of dephasing processes on a phenomenological level destroys the exact relations (5.3)-(5.6) that are underlying the theory presented here. Nevertheless, in the past it has been successfully applied to analyze optical experiments for quantum-well systems[20,29,58] on an ultra short time scale. So one should be aware of the fact that the exact relations are destroyed by the introduction of a dephasing but still hold in a good approximation on ultra short time scales. Since two excitonic polarizations contribute to the biexcitonic correlation function, in this work a dephasing constant for the biexcitonic correlation function is used that is two times the corresponding dephasing constant for the excitonic polarization. An extension of the theory systematically treating incoherent electronic contributions and dephasing processes is even more involved and can be deduced using the nonequilibrium Green's function technique.[32,33] This theory contains the DCT theory in the limit of weak optical fields and on ultra short time scales where incoherent occupations become insignificant. Nevertheless, a fundamental drawback of the resulting theory is the strongly increased numerical effort.

So far, a direct solution of the coupled exciton-biexciton dynamics in momentum space has only been done for a quasi two-dimensional quantum-well system.[20] Due to the finite spatial extension of the considered system here, even the direct solution of equation (5.8) for the excitonic transition amplitude in its linearized form turns out to be numerically very demanding; the direct solution of (5.8) and (5.9), including the full biexcitonic problem, is numerically not within the realms of possibility. Nevertheless, a transition to the exciton eigenbasis allows a solution of the coupled exciton-biexciton-light dynamics. Therefore, in the next section the expansions for the excitonic and biexcitonic problem in terms of exciton eigenstates and the resulting equations of motion for the time dependent expansion coefficients are deduced. Additionally, this allows again, as already used in Section 3.2 for the exciton problem, a separation of the stationary quantum mechanical two- and four-particle problem from the description of the system dynamics.

5.2. The Exciton Basis

In the following we focus on excitations of the electronic system in the vicinity of the fundamental excitonic resonance. The description of the exciton as well as the biexciton problem is done within the exciton eigenbasis. In linear optics, in Section 3.2, the restriction to only a finite number of exciton states $\phi_m(\mathbf{k}, z_\mathrm{e}, z_\mathrm{h})$ turned out to be a very good approximation to the full problem around the lowest excitonic resonances. However, in nonlinear optics, things are more complicated. First of all we are not able to calculate the exact solution for the biexcitonic problem as a reference. In addition to this, unfortunately but naturally, the two-electron-two-hole Hamiltonian $\mathcal{H}_{\mathrm{XX}}^{\mathrm{ehe'h'}}$ in Eq. (5.9) couples different exciton eigenstates since the two-electron-two-hole Coulomb interaction is not diagonal with respect to the two-exciton product basis. Therefore, in principle, an infinite number of exciton eigenstates $\phi_m(\mathbf{k}, z_\mathrm{e}, z_\mathrm{h})$ contributes to each biexciton state. Nevertheless, being interested in biexcitonic contributions to optical spectra in the vicinity of the lowest excitonic resonances only, a truncation of the exciton eigenbasis yields meaningful results here. For two-dimensional quantum-well systems a restriction of the exciton basis to the exciton ground state, the 1s state, has successfully been applied in the past.[29, 58, 66, 68] Around the 1s exciton resonance it captures the fundamental many-particle effects and dominant contributions to the nonlinear optical response of the system. An extension of this description of excitonic and biexcitonic nonlinearities to systems with finite spatial extension in the third space dimension is presented here.

The expansion of the excitonic transition amplitude $p^{\mathrm{eh}}_{(\mathbf{k},z_\mathrm{e},z_\mathrm{h})}$ in terms of exciton eigenstates $\phi_m(\mathbf{k}, z_\mathrm{e}, z_\mathrm{h})$, which are calculated with microscopic boundary conditions in Section 3.2, yields

$$p^{\mathrm{eh}}_{(\mathbf{k},z_\mathrm{e},z_\mathrm{h})}(t) = \sum_m p^{\mathrm{eh}}_m(t)\phi_m(\mathbf{k}, z_\mathrm{e}, z_\mathrm{h}) \,. \tag{5.10}$$

The time-dependent expansion coefficients $p^{\mathrm{eh}}_m(t)$ are connected to the corresponding interband transitions in the two-band model. Since electron and hole one-particle energies and their Coulomb interaction in (5.9) do not depend on the z-component of electron and hole angular momenta (e, h), spin-independent exciton eigenstates $\phi_m(\mathbf{k}, z_\mathrm{e}, z_\mathrm{h})$ are used in analogy to Section 3.2.

For the biexcitonic problem, following the ansatz in Ref. 19, symmetric and antisymmetric linear combinations of two-exciton product states are used with respect to interchange of electrons or holes, respectively. This is necessary to account for the symmetry of the resulting four-fermion states in a truncated exciton basis as discussed below. Using the following expansion for the biexcitonic correlation function proper antisymmetry with respect to particle interchange is guaranteed for each term in the expansion with fixed quantum numbers n, m.

Furthermore, in analogy to the Hydrogen molecule problem, a classification of the contributions to the biexcitonic correlation function[c)]

$$b_{\mathrm{eh}}^{\mathrm{e'h'}\lambda}{}^{(\mathbf{k}_2,z_2,\mathbf{k}_1,z_1)}_{(\mathbf{k}_4,z_4,\mathbf{k}_3,z_3)} = \sum_{nm}\Big[\phi_n(\alpha\mathbf{k}_4+\beta\mathbf{k}_3,z_4,z_3)\phi_m(\alpha\mathbf{k}_2+\beta\mathbf{k}_1,z_2,z_1)b_{nm}^{\mathrm{ehe'h'}\lambda}(\mathbf{k}_4-\mathbf{k}_3)$$
$$-\lambda\phi_n(\alpha\mathbf{k}_2+\beta\mathbf{k}_3,z_2,z_3)\phi_m(\alpha\mathbf{k}_4+\beta\mathbf{k}_1,z_4,z_1)b_{nm}^{\mathrm{ehe'h'}\lambda}(\mathbf{k}_2-\mathbf{k}_3)\Big] \tag{5.11}$$

according to the electronic singlet ($\lambda = -1$) and triplet ($\lambda = +1$) configuration is convenient, with

$$b_{\mathrm{eh}}^{\mathrm{e'h'}}{}^{(\mathbf{k}_2,z_2,\mathbf{k}_1,z_1)}_{(\mathbf{k}_4,z_4,\mathbf{k}_3,z_3)} = b_{\mathrm{eh}}^{\mathrm{e'h'}+}{}^{(\mathbf{k}_2,z_2,\mathbf{k}_1,z_1)}_{(\mathbf{k}_4,z_4,\mathbf{k}_3,z_3)} + b_{\mathrm{eh}}^{\mathrm{e'h'}-}{}^{(\mathbf{k}_2,z_2,\mathbf{k}_1,z_1)}_{(\mathbf{k}_4,z_4,\mathbf{k}_3,z_3)}\,.$$

Using this definition, the equations of motion for the biexcitonic expansion coefficients $b_{nm}^{\mathrm{ehe'h'}\lambda}(\mathbf{q})$ in Eq. (5.11) are decoupled for $\lambda = -1$ and $\lambda = +1$, since the total electron spin is conserved. Here $\alpha = m_{\mathrm{h}}^*/M^*$ and $\beta = m_{\mathrm{e}}^*/M^*$ are the ratio of the hole and the electron mass to the total exciton mass $M^* = m_{\mathrm{e}}^* + m_{\mathrm{h}}^*$, respectively. Regarding the in-plane motion the internal exciton quantum numbers n, m only account for the discrete exciton spectrum due to the electron-hole pair relative motion. Therefore, to include a non-vanishing in-plane center of mass momentum $\mathbf{q}$ for each single exciton, the expansion coefficients $b_{nm}^{\mathrm{ehe'h'}\lambda}(\mathbf{q})$ depend on n, m and the two-exciton relative momentum $\mathbf{q}$. For further details regarding this expansion see Appendix A.3.

Inserting the expansions (5.10) and (5.11) into Eqs. (5.8) and (5.9), a somewhat lengthy, but straightforward calculation yields the closed set of equations of motion for the excitonic p_m^{eh},

$$i\hbar\frac{\mathrm{d}}{\mathrm{d}t}p_m^{\mathrm{eh}} = \varepsilon_m p_m^{\mathrm{eh}} - \mathbf{d}_{\mathrm{eh}}\int \mathrm{d}z\,\mathbf{E}(z)\sum_{\mathbf{k}}\phi_m^*(\mathbf{k},z,z)$$
$$+\sum_{m'n\mathrm{e'h'}} p_{m'}^{*\mathrm{e'h'}}\Big[p_n^{\mathrm{e'h}}\int \mathrm{d}z_{\mathrm{e}}\,\mathbf{d}_{\mathrm{eh'}}\mathbf{E}(z_{\mathrm{e}})R^1_{mm'n}(z_{\mathrm{e}}) + p_n^{\mathrm{eh'}}\int \mathrm{d}z_{\mathrm{h}}\,\mathbf{d}_{\mathrm{e'h}}\mathbf{E}(z_{\mathrm{h}})R^2_{mm'n}(z_{\mathrm{h}})\Big]$$
$$+\sum_{m'nn'\mathrm{e'h'}} p_{m'}^{*\mathrm{e'h'}}p_n^{\mathrm{eh'}}p_{n'}^{\mathrm{e'h}}\,V^{\mathrm{HF}}_{mm'nn'} + \sum_{n\mathrm{e'h'}} p_n^{*\mathrm{e'h'}}\sum_{\mathbf{q}n'm'\lambda} W^{\mathrm{XX}\lambda*}_{n'm'mn}(\mathbf{q},0)\,b_{n'm'}^{\mathrm{ehe'h'}\lambda}(\mathbf{q})\,, \tag{5.12}$$

and biexcitonic $b_{nm}^{\mathrm{ehe'h'}\lambda}(\mathbf{q})$,

$$i\hbar\frac{\mathrm{d}}{\mathrm{d}t}b_{nm}^{\mathrm{ehe'h'}\lambda}(\mathbf{q}) = \sum_{n'm'\mathbf{q}'} H^{\mathrm{XX}\lambda}_{nmn'm'}(\mathbf{q},\mathbf{q}')b_{n'm'}^{\mathrm{ehe'h'}\lambda}(\mathbf{q}')$$
$$+\frac{1}{2}\sum_{n'm'rs\mathbf{q}'}\Big[(1-\lambda S)^{-1}_{nmrs}(\mathbf{q},\mathbf{q}')W^{\mathrm{XX}\lambda}_{rsn'm'}(\mathbf{q}',0)\big[p_{n'}^{\mathrm{eh}}p_{m'}^{\mathrm{e'h'}} + \lambda p_{n'}^{\mathrm{e'h}}p_{m'}^{\mathrm{eh'}}\big]\Big]\,, \tag{5.13}$$

[c)] The time-dependence of the excitonic $p_m^{\mathrm{eh}}(t)$ and biexcitonic $b_{nm}^{\mathrm{ehe'h'}\lambda}(\mathbf{q},t)$ expansion coefficients is not made explicit in the following.

coefficients. Since all numerical evaluations in the following are performed in the exciton eigenbasis, the expansion coefficients p_m^{eh} and $b_{nm}^{\mathrm{ehe'h'}\lambda}(\mathbf{q})$ will be referred to as excitonic transition amplitude (excitonic polarization) and biexcitonic correlation function, respectively. With the definitions $\mathbf{q}^+ = \mathbf{q} + \mathbf{q}'$ and $\mathbf{q}^- = \mathbf{q} - \mathbf{q}'$ the Coulomb matrix elements in the two-exciton product basis read:

$$W^{\mathrm{XX}\lambda}_{nmn'm'}(\mathbf{q},\mathbf{q}') = W^{\mathrm{C}}_{nmn'm'}(\mathbf{q},\mathbf{q}') + \lambda \cdot W^{\mathrm{XC}}_{nmn'm'}(\mathbf{q},\mathbf{q}')\,, \tag{5.14}$$

with

$$\begin{aligned} W^{\mathrm{C}}_{nmn'm'}(\mathbf{q},\mathbf{q}') = \sum_{\mathbf{k}\mathbf{k}'} \int & \mathrm{d}z_{\mathrm{e}}\mathrm{d}z_{\mathrm{h}}\mathrm{d}z_{\mathrm{e}'}\mathrm{d}z_{\mathrm{h}'}\, \phi^*_n(\mathbf{k}, z_{\mathrm{e}}, z_{\mathrm{h}})\phi^*_m(\mathbf{k}', z_{\mathrm{e}'}, z_{\mathrm{h}'}) \\ & \times\Big[V^{z_{\mathrm{h}'}z_{\mathrm{h}}}_{\mathbf{q}^-}\phi_{n'}(\mathbf{k}+\beta\mathbf{q}^-, z_{\mathrm{e}}, z_{\mathrm{h}})\phi_{m'}(\mathbf{k}'-\beta\mathbf{q}^-, z_{\mathrm{e}'}, z_{\mathrm{h}'}) \\ & +V^{z_{\mathrm{e}'}z_{\mathrm{e}}}_{\mathbf{q}^-}\phi_{n'}(\mathbf{k}-\alpha\mathbf{q}^-, z_{\mathrm{e}}, z_{\mathrm{h}})\phi_{m'}(\mathbf{k}'+\alpha\mathbf{q}^-, z_{\mathrm{e}'}, z_{\mathrm{h}'}) \\ & -V^{z_{\mathrm{e}'}z_{\mathrm{h}}}_{\mathbf{q}^-}\phi_{n'}(\mathbf{k}+\beta\mathbf{q}^-, z_{\mathrm{e}}, z_{\mathrm{h}})\phi_{m'}(\mathbf{k}'+\alpha\mathbf{q}^-, z_{\mathrm{e}'}, z_{\mathrm{h}'}) \\ & -V^{z_{\mathrm{h}'}z_{\mathrm{e}}}_{\mathbf{q}^-}\phi_{n'}(\mathbf{k}-\alpha\mathbf{q}^-, z_{\mathrm{e}}, z_{\mathrm{h}})\phi_{m'}(\mathbf{k}'-\beta\mathbf{q}^-, z_{\mathrm{e}'}, z_{\mathrm{h}'})\Big]\,, \end{aligned} \tag{5.15}$$

for the direct part, and

$$\begin{aligned} W^{\mathrm{XC}}_{nmn'm'}(\mathbf{q},\mathbf{q}') = \sum_{\mathbf{k}\mathbf{k}'} \int & \mathrm{d}z_{\mathrm{e}}\mathrm{d}z_{\mathrm{h}}\mathrm{d}z_{\mathrm{e}'}\mathrm{d}z_{\mathrm{h}'}\, \phi^*_n(\mathbf{k}+\alpha\mathbf{q}^-, z_{\mathrm{e}}, z_{\mathrm{h}})\phi^*_m(\mathbf{k}'+\beta\mathbf{q}^+, z_{\mathrm{e}'}, z_{\mathrm{h}'}) \\ & \times\Big[\phi_{n'}(\mathbf{k}', z_{\mathrm{e}'}, z_{\mathrm{h}})\Big[V^{z_{\mathrm{e}}z_{\mathrm{h}}}_{\mathbf{k}-\mathbf{k}'}\phi_{m'}(\mathbf{k}'+\alpha\mathbf{q}^-+\beta\mathbf{q}^+, z_{\mathrm{e}}, z_{\mathrm{h}'}) \\ & \qquad -V^{z_{\mathrm{h}'}z_{\mathrm{h}}}_{\mathbf{k}-\mathbf{k}'}\phi_{m'}(\mathbf{k}+\alpha\mathbf{q}^-+\beta\mathbf{q}^+, z_{\mathrm{e}}, z_{\mathrm{h}'})\Big] \\ & +\phi_{n'}(\mathbf{k}, z_{\mathrm{e}'}, z_{\mathrm{h}})\Big[V^{z_{\mathrm{h}'}z_{\mathrm{e}'}}_{\mathbf{k}-\mathbf{k}'}\phi_{m'}(\mathbf{k}+\alpha\mathbf{q}^-+\beta\mathbf{q}^+, z_{\mathrm{e}}, z_{\mathrm{h}'}) \\ & \qquad -V^{z_{\mathrm{e}}z_{\mathrm{e}'}}_{\mathbf{k}-\mathbf{k}'}\phi_{m'}(\mathbf{k}'+\alpha\mathbf{q}^-+\beta\mathbf{q}^+, z_{\mathrm{e}}, z_{\mathrm{h}'})\Big]\Big] \end{aligned} \tag{5.16}$$

for the two-exciton exchange interaction, respectively. The required Hartree-Fock Coulomb matrix elements in Eq. (5.12) are obtained from the two-exciton exchange matrix elements (5.16) in the $\mathbf{q} \to 0$, $\mathbf{q}' \to 0$-limit:

$$V^{\mathrm{HF}}_{mm'nn'} = W^{\mathrm{XC}*}_{n'nmm'}(0,0)\,.$$

The matrix elements for the phase space filling corrections (Pauli-blocking) to the Rabi-energy are:

$$R^1_{mm'n}(z) = \sum_{\mathbf{k}} \int \mathrm{d}z'\mathrm{d}z''\phi^*_m(\mathbf{k}, z, z'')\phi_{m'}(\mathbf{k}, z', z)\phi_n(\mathbf{k}, z', z'')\,, \tag{5.17}$$

$$R^2_{mm'n}(z) = \sum_{\mathbf{k}} \int \mathrm{d}z'\mathrm{d}z''\phi^*_m(\mathbf{k}, z'', z)\phi_{m'}(\mathbf{k}, z, z')\phi_n(\mathbf{k}, z'', z')\,. \tag{5.18}$$

The homogeneous part of the equation of motion (5.13) for the biexcitonic coefficients $b_{nm}^{\mathrm{ehe'h'}\lambda}(\mathbf{q})$ has the formal structure of a two-electron-two-hole Schrödinger equation. Diagonalization of the biexciton Hamiltonian matrix,

$$\begin{aligned} H^{\mathrm{XX}\lambda}_{nmn'm'}(\mathbf{q},\mathbf{q}') =& \big(\varepsilon_n(q)+\varepsilon_m(q)\big)\delta_{nn'}\delta_{mm'}\delta_{\mathbf{q}\mathbf{q}'} \\ &+\sum_{rs\mathbf{k}}(1-\lambda S)^{-1}_{nmrs}(\mathbf{q},\mathbf{k})W^{\mathrm{XX}\lambda}_{rsn'm'}(\mathbf{k},\mathbf{q}')\,, \end{aligned} \tag{5.19}$$

reveals information about the energy spectrum of the interacting four-particle system. The $\varepsilon_n(q)$ are the exciton eigenenergies for non-vanishing in-plane COM momentum $\mathbf{q}$, given in Appendix A.3. The presence of the exciton overlap matrix

$$\begin{aligned} S_{nmn'm'}(\mathbf{q},\mathbf{q}') = \sum_{\mathbf{k}}\int & \mathrm{d}z_\mathrm{e}\mathrm{d}z_\mathrm{h}\mathrm{d}z_{\mathrm{e}'}\mathrm{d}z_{\mathrm{h}'}\;\phi_n^*(\mathbf{k}+\alpha\mathbf{q},z_\mathrm{e},z_\mathrm{h})\phi_m^*(\mathbf{k}+\mathbf{q}'+\beta\mathbf{q},z_{\mathrm{e}'},z_{\mathrm{h}'}) \\ &\times\phi_{n'}(\mathbf{k}+\alpha\mathbf{q}',z_{\mathrm{e}'},z_\mathrm{h})\phi_{m'}(\mathbf{k}+\mathbf{q}+\beta\mathbf{q}',z_\mathrm{e},z_{\mathrm{h}'}) \end{aligned} \tag{5.20}$$

is due to the non-othonormality of the chosen set of basis states (5.11). In general, to find an exact solution of a quantum mechanical problem it is not necessary to use a non-orthogonal set of basis states, since it can always be transformed into an orthonormal one. In praxis, where a truncation of the considered basis is necessary, the use of a non-orthogonal set of basis states may be advantageous. Here, working in a truncated basis, the required fermionic symmetry of the biexciton states is no longer automatically fulfilled, in contrast to the result with respect to a complete two-exciton product basis.[d] By a proper choice of the basis states, artifacts due to the truncation of the basis can be reduced. Therefore, for the description of identical interacting particles, the introduction of non-orthogonal basis states (5.11) is necessary to avoid a violation of the fermionic symmetry of the resulting biexciton states in the truncated Hilbert space. A similar result is obtained for a two-dimensional system in Ref. 67, but here the matrix elements contain the additional space-dependence for the spatially inhomogeneous situation.

The evaluation of the Coulomb matrix elements in the two-exciton product basis turns out to be numerically very demanding. Details are given in Appendix B.3. Especially parts of the exchange interaction matrix element $W^{\mathrm{XC}}_{nmn'm'}(\mathbf{q},\mathbf{q}')$ (5.16) with its four-fold real space integral cannot be factorized at all. In order to guarantee reliable numerical results, an alternative technique is briefly discussed here. Expansion of the real space dependence of the exciton eigenfunctions $\phi_m(\mathbf{k},z_\mathrm{e},z_\mathrm{h})$ in terms of products of one-particle eigenstates $\chi_i(z_\mathrm{e})$ for electrons and $\varphi_j(z_\mathrm{h})$ for holes,

$$\phi_m(\mathbf{k},z_\mathrm{e},z_\mathrm{h}) = \sum_{ij} a^m_{ij}(\mathbf{k})\chi_i(z_\mathrm{e})\varphi_j(z_\mathrm{h})\,, \tag{5.21}$$

---

[d] Working in a complete two-exciton product basis, fermionic symmetry for the resulting two-electron-two-hole (biexcitonic) states is automatically fulfilled, since only pairs of identical particles contribute to these states.

yields a representation where multiple subbands i, j contribute to the matrix elements (5.15)-(5.18), (5.20). The expansion coefficients are given by

$$a_{ij}^{m}(\mathbf{k}) = \int \mathrm{d}z_{\mathrm{e}} \mathrm{d}z_{\mathrm{h}} \chi_i^*(z_{\mathrm{e}}) \varphi_j^*(z_{\mathrm{h}}) \phi_m(\mathbf{k}, z_{\mathrm{e}}, z_{\mathrm{h}}) \,. \tag{5.22}$$

Depending on the given layer thickness, an evaluation of the matrix elements according to the expansion (5.21) may be advantageous. A more detailed discussion of this approach is given in Appendix B.3.2 and the influence of higher subbands i, j is investigated in Section 5.3.2.

5.2.1. Angular Momentum Decomposition

Following Section 3.1, in linear optics only excitons with in-plane s-symmetry are excited by the dipole coupling to an optical field which is homogeneous in the x-y-plane. Coulomb interaction for each single electron-hole pair does not induce transitions to exciton states with non in-plane s-symmetry as shown in Appendix A.1. Therefore a restriction of the theory to s-shaped states is exact in linear optics.

In nonlinear optics a similar restriction to s exciton states in the expansions (5.10) and (5.11) is no longer exact. Though not directly optically excited, in principle, exciton-exciton Coulomb interaction yields contributions to the excitonic polarization $p^{\mathrm{eh}}_{(\mathbf{k}, z_{\mathrm{e}}, z_{\mathrm{h}})}$ from non s-shaped exciton states. Nevertheless, for quantum-well systems a restriction of excitonic and biexcitonic nonlinearities to the 1s subspace has successfully been applied to different excitation conditions.[29, 58, 66] As already discussed in Section 5.2, also in the nonlinear optical regime, the large spectral separation of the fundamental exciton resonance (1s) from the remaining part of the exciton spectrum allows its isolated description in a good approximation as long as no other exciton states are directly optically excited. To concentrate on the 1s exciton resonance and its polariton modes, in the following the expansions (5.10) and (5.11) are restricted to excitons with in-plane 1s symmetry.[e)]

To realize the above mentioned approximation, an angular momentum decomposition of the exciton-exciton relative motion in the biexcitonic correlation function

$$b_{nm}^{\mathrm{ehe'h'}\lambda}(\mathbf{q}) = \sum_{\mu} \mathrm{e}^{i\mu\phi_q} b_{nm}^{\mathrm{ehe'h'}\lambda\mu}(q) \,, \tag{5.23}$$

and the matrix elements

$$M_{nmn'm'}(\mathbf{q}, \mathbf{q}') = \sum_{\mu\mu'} \mathrm{e}^{i\mu\phi_q} M_{nmn'm'}^{\mu\mu'}(q, q') \mathrm{e}^{-i\mu'\phi_{q'}} \tag{5.24}$$

is used, following Ref. 67.

[e)] Note, that for the slab geometry the lower energy part of the exciton spectrum results from the 1s exciton state of the bulk material due to spatial confinement in the z-direction. The in-plane rotation invariance is conserved in the confinement geometry while the resulting states exhibit different space dependencies in the z-direction.

Here $M_{nmn'm'}(\mathbf{q},\mathbf{q}')$ represents one of the matrix elements in the two-exciton product basis needed in the equations of motion (5.12) and (5.13), for instance $W^{\mathrm{XX}\lambda}_{nmn'm'}(\mathbf{q},\mathbf{q}')$ (5.14). The exciton eigenfunctions $\phi_m(\mathbf{k},z_\mathrm{e},z_\mathrm{h})$ are eigenfunctions of the in-plane angular momentum operator with quantum numbers μ_n and μ_m for the two contributing excitons in states n,m. Taking into account the angular momentum μ for the two-exciton relative motion, the total in-plane angular momentum of the two-exciton system is $\mu_\mathrm{tot}=\mu+\mu_n+\mu_m$. Due to the rotation invariance of the semiconductor heterostructure around the z-axis, the in-plane total angular momentum μ_tot of the two-exciton system is conserved. Consequently, the Fourier coefficients $M^{\mu\mu'}_{nmn'm'}(q,q')$ in Eq. (5.24) are block-diagonal for fixed μ_tot:

$$M^{\mu\mu'}_{nmn'm'}(q,q')=\delta_{\mu+\mu_n+\mu_m,\mu'+\mu_{n'}+\mu_{m'}}\frac{1}{2\pi}\int\limits_0^{2\pi}\mathrm{d}\phi'\,\mathrm{e}^{i\mu'\phi'}M_{nmn'm'}(q,0,q',\phi')\,.$$

The Coulomb coupling of exciton states with different in-plane symmetry is neglected according to the discussion at the beginning of this section. Then usage of the expansions (5.23) and (5.24) with the equation of motion (5.13) yields decoupled sets of equations for the expansion coefficients $b^{\mathrm{ehe'h'}\lambda\mu}_{nm}(q)$ for fixed μ. Due to the system symmetry, including the in-plane homogeneity of the exciting optical fields, the in-plane total angular momentum μ_tot vanishes for each biexciton. Hence, the only relevant matrix elements in the two-exciton product basis read

$$M_{nmn'm'}(q,q')=M^{00}_{nmn'm'}(q,q')=\int\limits_0^{2\pi}\frac{\mathrm{d}\phi'_q}{2\pi}M_{nmn'm'}(q,0,q',\phi_{q'})\,, \tag{5.25}$$

and only the $b^{\mathrm{ehe'h'}\lambda}_{nm}(q)=b^{\mathrm{ehe'h'}\lambda\mu=0}_{nm}(q)$ contribution to the biexcitonic correlation function (5.23) is driven. Therefore, restricting the expansions (5.10) and (5.11) to in-plane s-shaped exciton states and hence using all matrix elements in their angular averaged version (5.25), the projection of the equations of motion (5.12) and (5.13) to the in-plane s subspace of exciton states is obtained.

5.3. Matrix Elements and Biexciton Binding Energy

The main purpose of this work is not to present a new or best method to calculate the biexciton ground state energy but to describe the fundamental many-particle effects important for coherent optical nonlinearities including propagation effects.

Nevertheless care must be taken to reach good numerical convergence of the biexciton binding energy to guarantee a proper evaluation of the Coulomb matrix elements in the two-exciton product basis. Results are presented for a GaAs model system with parameters given in Table 3.1 on page 30. In principle, the results quantitatively depend on the material parameters, especially on the electron-hole mass ratio $m^*_\mathrm{e}/m^*_\mathrm{h}$.[19] To make the following discussion as expressive as possible, all energies are normalized to the bulk exciton binding energy $\mathrm{E}^\mathrm{X}_\mathrm{b}$ and all lengths to the exciton Bohr-radius a^X_0.

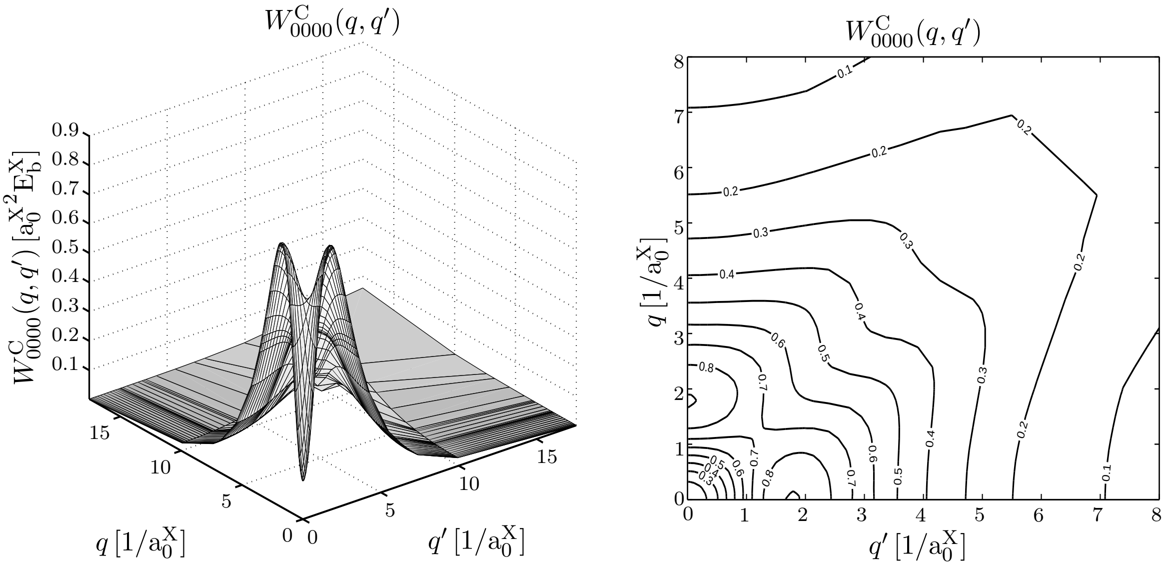

Figure 5.1: On-site matrix element $W^{\mathrm{C}}_{0000}(q,q')$ of the direct exciton-exciton Coulomb interaction (5.15). Left: Surface plot. Right: Contour plot.

5.3.1. Coulomb Matrix Elements

This chapter is dedicated to the exciton-exciton Coulomb interaction in the two-exciton product basis. For a fixed set of internal exciton quantum numbers n, m, n', m', the Coulomb matrix elements $W^{\mathrm{C}}_{nmn'm'}(q,q')$ (5.15) and $W^{\mathrm{XC}}_{nmn'm'}(q,q')$ (5.16) can be classified by on-site ($n = m = n' = m'$), inter-site diagonal ($n = n'$ and $m = m'$ and $n \neq m$), and off-diagonal blocks ($n \neq n'$ or $m \neq m'$).

Figures 5.1 and 5.2 show on-site blocks of the direct $W^{\mathrm{C}}_{nmn'm'}(q,q')$ and of the exchange $W^{\mathrm{XC}}_{nmn'm'}(q,q')$ Coulomb matrices for a GaAs layer with thickness of $5\,\mathrm{a}_0^\mathrm{X}$. In both figures, on the left the dependence of the Coulomb interaction on the two-exciton relative momenta q, q' is shown in a surface plot. On the right, a contour plot corresponding to the same data as the surface plot is depicted. Examples for inter-site diagonal and off-diagonal blocks are shown in Figs. B.2 to B.5 on page 137 in Appendix B.3.1.

For the spatially inhomogeneous system the direct Coulomb matrix elements do not vanish in the $q \to 0$, $q' \to 0$-limit, even not for the on-site matrix element $W^{\mathrm{C}}_{0000}(q,q')$ shown in Fig. 5.1. Due to the spatial inhomogeneity, according to Eq. (5.21), several subbands contribute to the exciton states, in contrast to the results in Ref. 67 for the two-dimensional quantum-well model. Since all Coulomb matrix elements in the two-exciton product basis vanish for large momenta q, q', their contributions for $q, q' > 20\,\mathrm{a}_0^\mathrm{X}$ are neglected in the following calculations. Note, that all the displayed matrix elements have a similar magnitude. All of them have to be taken into account and are of equal importance for the calculations in the remaining part of this work. More details concerning the evaluation of the matrix elements are given in Appendix B.3.1.

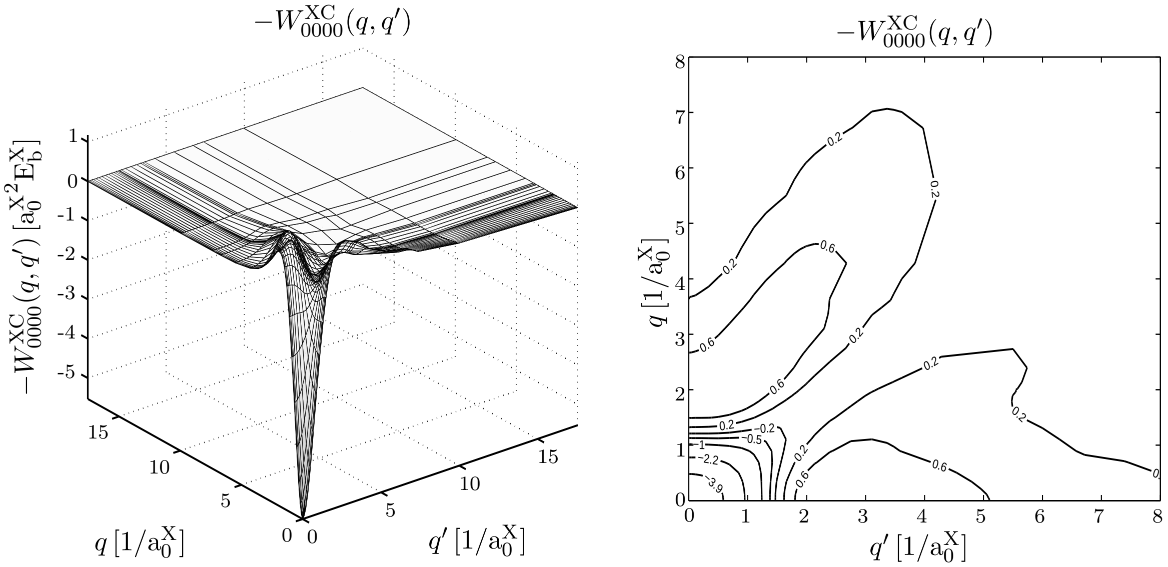

Figure 5.2: On-site matrix element $W^{\mathrm{XC}}_{0000}(q,q')$ of the exchange exciton-exciton Coulomb interaction (5.16). Left: Surface plot. Right: Contour plot.

5.3.2. Role of the Dimensionality

The theory that has been deduced in the previous part of this work is suitable for the description of excitons and biexcitons in a semiconductor layer with a thickness situated somewhere in between the two limiting cases of a bulk semiconductor and a two-dimensional quantum-well. In order to complete the discussion of the previous section, the dependence of the biexciton binding energy $E_\mathrm{b}^{\mathrm{XX}}$ on the layer thickness is discussed.

The exciton $E_\mathrm{b}^{\mathrm{X}}$ as well as the biexciton $E_\mathrm{b}^{\mathrm{XX}}$ binding energy strongly depend on the thickness L of the semiconductor layer in which electrons and holes are confined, Fig. 2.1 and Ref. 69. Additionally, in the two-exciton basis, the biexciton binding energy $E_\mathrm{b}^{\mathrm{XX}}$ depends on the number of exciton states that are taken into account to build the biexciton Hamiltonian matrix $H^{\mathrm{XX}\lambda}_{nmn'm'}(\mathbf{q},\mathbf{q}')$ (5.19). The number of exciton states is determined by the energy level spacing of the 1s shaped states due to the spatial confinement in the z-direction which depends on the layer thickness. There is one state for a layer thickness L of one and two exciton Bohr radii, two states for $L = 3\,\mathrm{a}_0^\mathrm{X}$, and three for $L = 4\,\mathrm{a}_0^\mathrm{X}$ and $L = 5\,\mathrm{a}_0^\mathrm{X}$. The bound biexciton state is found in the electron singlet subspace of the biexciton Hamiltonian (5.19).[f)]

The dependence of the calculated exciton (×) and biexciton (○) binding energy on the layer thickness L is displayed in Fig. 5.3. The corresponding data are given in Table 5.1 on page 86. In the semiconductor layer with finite thickness, by definition, the exciton binding energy is measured relative to the effective band-gap energy

---

[f)] This result is obtained here in analogy to the Hydrogen molecule problem. But note, that for the solution of the two-electron-two-hole problem a Born-Oppenheimer approximation cannot be applied due to the large electron-hole mass ratio $m_\mathrm{e}^*/m_\mathrm{h}^*$.

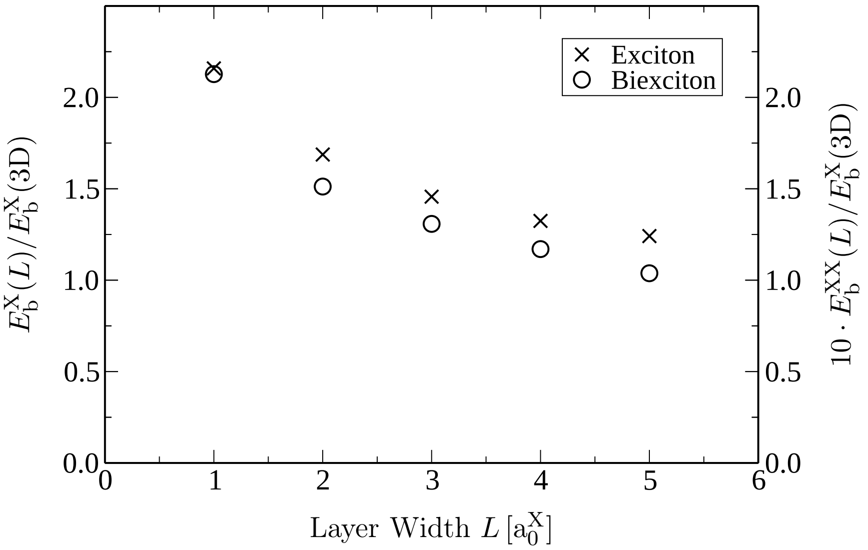

Figure 5.3: The figure shows the dependence of exciton $E_b^X(L)$ and biexciton $E_b^{XX}(L)$ binding energy on the layer thickness L. The exciton binding energy (×) is given with the vertical axis on the left and ten times the biexciton binding energy (○) is given with the vertical axis on the right. Results are normalized to the bulk exciton binding energy $E_b^X(3D)$, corresponding to the data in Table 5.1 on page 86.

$E_{\mathrm{gap}}^{\mathrm{eff}}(L) = E_{\mathrm{gap}}(3D) + \varepsilon_1^e(L) + \varepsilon_1^h(L)$ for a non-interacting electron-hole pair as illustrated in Fig. 5.4 (a). $\varepsilon_1^e(L)$ and $\varepsilon_1^h(L)$ are the lowest one-particle energies for electrons and holes, resulting from the confined motion in the z-direction in a layer with thickness L.[g] According to the above discussion, the biexciton binding energy $E_b^{XX}(L)$ is measured relative to the lowest energy $2E_{\mathrm{gap}}^{\mathrm{eff}}(L) - 2E_b^X(L)$ of two isolated excitons as illustrated in Fig. 5.4 (b).

With decreasing layer thickness, the quantum confinement yields an increase of the exciton as well as of the biexciton binding energy. The biexciton binding energy is about 10 % of the exciton binding energy for the investigated layer thicknesses which reproduces Haynes' rule of thumb[70] for this ratio. The ratio slightly increases with decreasing layer thickness as already reported in Refs. 69, 71. For the calculations in the two-exciton product basis the influence of excited exciton states on the biexciton binding energy becomes more important for increasing layer thickness due to their decreasing energy level spacing. For $4\,a_0^X$ the inclusion of two additional excited states increases the biexciton binding energy by 9.4 % whereas for $5\,a_0^X$ we encounter an increase of 10.5 %.

---

[g] For thin layers the spatial confinement yields a pronounced shift of the lowest one-particle energies $\varepsilon_1^e(L)$, $\varepsilon_1^h(L)$, namely the lowest subbands for electrons and holes in the heterostructure.

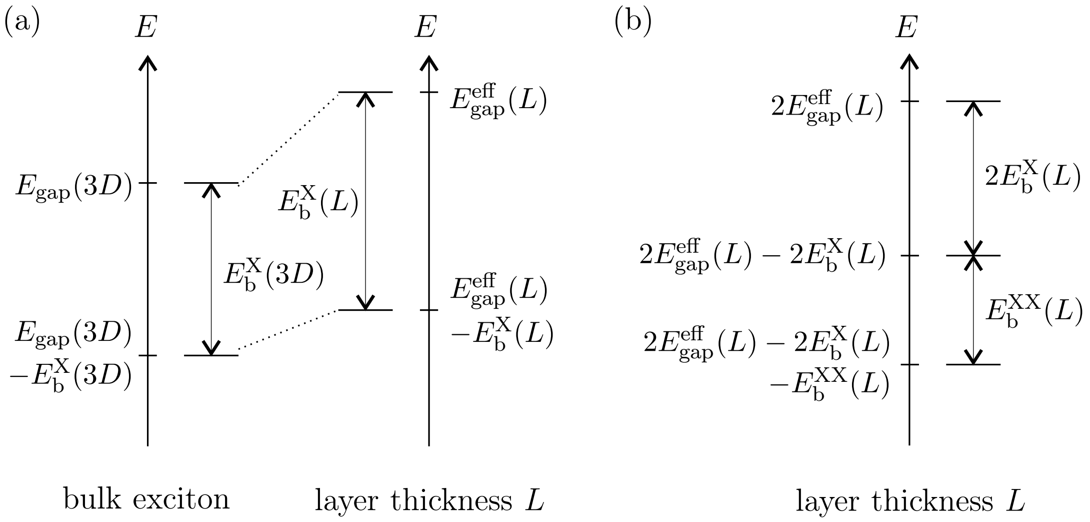

Figure 5.4: Schematic illustration of exciton and biexciton binding energy. (a) Visualization of the exciton binding energy in a bulk material and in a semiconductor layer with finite thickness L. (b) Visualization of the biexciton binding energy in a semiconductor layer with finite thickness L. For a detailed discussion see text.

According to Eq. (5.21), the influence of higher one-particle subbands i, j in the evaluation of the matrix elements $H_{nmn'm'}^{\mathrm{XX}\lambda}(\mathbf{q}, \mathbf{q}')$ in the two-exciton product basis on the biexciton binding energy $E_{\mathrm{b}}^{\mathrm{XX}}(L)$ is shown in Fig. 5.5. One exciton state (1X) is included in these calculations. The biexciton binding energies $E_{\mathrm{b}}^{\mathrm{XX}}(L, 1X)$ are normalized to the result $E_{\mathrm{b,max}}^{\mathrm{X}}(L, 1X)$ obtained for the inclusion of five electron and hole subbands i, j for each layer thickness L. The corresponding data are given in Table 5.2 on page 87.

For the considered layer thicknesses we find a convergence of the biexciton binding energy with increasing number of included subbands, while the importance of higher subbands is increased with increasing layer thickness. For instance, for $1\,\mathrm{a}_0^{\mathrm{X}}$ layer thickness more than 90 % of the binding energy are already reached with only the inclusion of the lowest subband, whereas for $5\,\mathrm{a}_0^{\mathrm{X}}$ the contributions from higher subbands increase the binding energy by about 60 %.

According to Eq. (5.22), the contributions $a_{ij}^1(k)$ [h] of the subbands i, j to the exciton ground state wave function $\phi_1(k, z_{\mathrm{e}}, z_{\mathrm{h}})$ are shown in Fig. 5.6 (a) for a layer thickness of $1\,\mathrm{a}_0^{\mathrm{X}}$ and in Fig. 5.6 (b) for $5\,\mathrm{a}_0^{\mathrm{X}}$. Only contributions from subbands i, j with $a_{ij}^1(0) \cdot 100 \geq a_{00}^1(0)$ are visualized. For a layer thickness of $1\,\mathrm{a}_0^{\mathrm{X}}$ the exciton ground state wave function is clearly dominated by the contribution $a_{00}^1(k)$ from the lowest electron ($i = 0$) and hole ($j = 0$) subbands. For a layer thickness of $5\,\mathrm{a}_0^{\mathrm{X}}$ the contributions from higher subbands are increased due to their decreased energy level spacing as already observed in Fig. 5.5 for the biexciton binding energy.

---

[h] Following Section 3.1 the exciton ground state wave function exhibits an in-plane rotation invariance and therefore only depends on the modulus k of the in-plane wave vector $\mathbf{k}$.

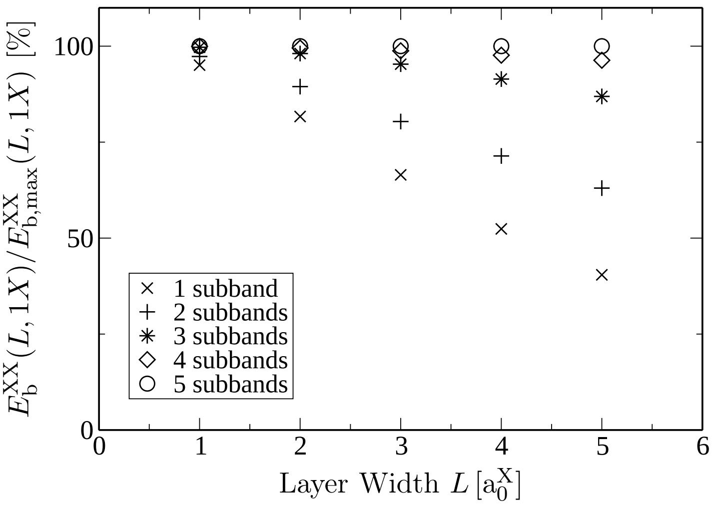

Figure 5.5: Dependence of the biexciton binding energy $E_\mathrm{b}^\mathrm{XX}(L,1X)$ on the number of subbands i,j in the expansion (5.21), while one exciton state is included in the calculations. The symbols correspond to one (×), two (+), three (∗), four (◇), and five (○) included subbands, respectively. For each layer thickness L the results are normalized to the biexciton binding energy $E_\mathrm{b,max}^\mathrm{XX}(L,1X)$ that is obtained by inclusion of five subbands. The data are given in Table 5.2 on page 87.

The description of biexciton states in terms of two-exciton product states yields physical meaningful results for the investigated systems. Nevertheless with a truncated set of exciton basis states, especially the biexciton binding energy is underestimated compared to, e.g., variational approaches. Variational approaches commonly yield the best results for the ground state energy of a given system.[19] The approach used here, also contains the description of excited biexciton states being important for the description of optical properties of the system. Alltogether, the biexciton binding energy is found to be about 10 % of the corresponding exciton binding energy, with a slightly growing ratio for decreasing sample thickness.[69,70] However, recent investigations predict a somewhat larger growth of the biexciton-exciton binding energy ratio for layer thicknesses approaching the quantum-well limit.[72–74] In Section 7.2 the 20 nm ZnSe layer, introduced in Section 4.2, is investigated in the nonlinear optical regime. Indeed, our results show a slightly too small biexciton binding energy compared to the experiment. All other features in the optical spectra are well-described by the theoretical results.

So far, a theory for nonlinear polariton propagation in spatially inhomogeneous semiconductors in the coherent limit has been introduced in this chapter. It incorporates both, propagation effects and excitonic as well as biexcitonic nonlinearities on a microscopic level. Microscopic boundary conditions for the induced material polarization and the optical fields have been properly included in the description. The calculation of transmission spectra for single light pulses and in pump and probe or in four wave mixing geometry is covered in the next chapter.

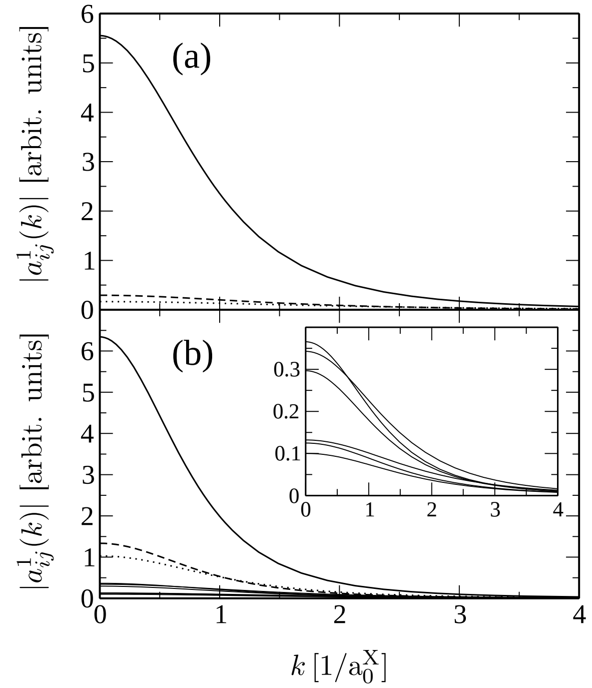

Figure 5.6: The figure shows the contributions $|a^1_{ij}(k)|$ from electron (i) and hole (j) subbands to the exciton ground state wave function $\phi_1(k, z_e, z_h)$, according to the definition in Eq. (5.22). (a) $a^1_{11}(k)$ (solid line), $a^1_{13}(k)$ (dashed line), and $a^1_{22}(k)$ (dotted line) for a layer thickness of $1\,a_0^X$. (b) $a^1_{11}(k)$ (solid line), $a^1_{13}(k)$ (dashed line), and $a^1_{22}(k)$ (dotted line) for a layer thickness of $5\,a_0^X$. The inset shows from top to bottom for $k = 0$ the subband contributions $a^1_{24}(k)$, $a^1_{33}(k)$, $a^1_{31}(k)$, $a^1_{44}(k)$, $a^1_{35}(k)$, and $a^1_{42}(k)$.

$L[a_0^X]$	$E_b^X(L)/E_b^X(3D)$	$E_b^{XX}(L)/E_b^X(3D)$	$E_b^{XX}(L)/E_b^X(L)$
1	2.1585	0.2127	0.0985
2	1.6873	0.1512	0.0896
3	1.4568	0.1308	0.0898
4	1.3243	0.1170	0.0883
5	1.2412	0.1038	0.0836

Table 5.1.: Dependence of exciton $E_b^X(L)$ and biexciton $E_b^{XX}(L)$ binding energy on the layer thickness L. Energies are normalized to the bulk exciton binding energy $E_b^X(3D)$ and lengths to the bulk exciton Bohr radius a_0^X.

subbands N	$E_\mathrm{b}^\mathrm{XX}(L)/E_\mathrm{b}^\mathrm{X}(3D)$	$E_\mathrm{b}^\mathrm{XX}(L,1X)/E_\mathrm{b}^\mathrm{X}(3D)$
$1\,\mathrm{a}_0^\mathrm{X}$ thickness:		
1	0.2022	0.2022
2	0.2070	0.2070
3	0.2121	0.2121
4	0.2126	0.2126
5	0.2127	0.2127
$2\,\mathrm{a}_0^\mathrm{X}$ thickness:		
1	0.1235	0.1235
2	0.1353	0.1353
3	0.1483	0.1483
4	0.1505	0.1505
5	0.1512	0.1512
$3\,\mathrm{a}_0^\mathrm{X}$ thickness:		
1	–	0.0823
2	0.1093	0.0995
3	0.1234	0.1180
4	0.1293	0.1223
5	0.1308	0.1238
$4\,\mathrm{a}_0^\mathrm{X}$ thickness:		
1	–	0.0557
2	0.0833	0.0759
3	0.1042	0.0972
4	0.1136	0.1038
5	0.1170	0.1063
$5\,\mathrm{a}_0^\mathrm{X}$ thickness:		
1	–	0.0374
2	0.0622	0.0583
3	0.0869	0.0804
4	0.0985	0.0891
5	0.1038	0.0925

Table 5.2.: Dependence of the biexciton binding energy $E_\mathrm{b}^\mathrm{XX}(L)$ on the number of considered subbands N and on the number of included exciton states for layer thicknesses $1\,\mathrm{a}_0^\mathrm{X} \leq L \leq 5\,\mathrm{a}_0^\mathrm{X}$. Results are given in the second column for the maximum number of exciton states (for explanation see text at the beginning of Section 5.3.2), and in the third column with only one of them ($1X$) taken into account, respectively. The energies are normalized to the bulk exciton binding energy $E_\mathrm{b}^\mathrm{X}(3D)$. In the case of $3\,\mathrm{a}_0^\mathrm{X} \leq L \leq 5\,\mathrm{a}_0^\mathrm{X}$, for calculations including excited exciton states (second column), a description with only one subband is not meaningful because of the complicated spatial structure of the excited exciton wave functions.

6. Nonlinear Optics

In linear optics, the two excitonic transitions driven by light fields with opposite circular polarization are not coupled to each other. Consequently, the total excitonic polarization $\mathbf{P}(z,t)$ in Eq. (3.3) on page 28 is just the sum of the two contributions $\mathbf{P}_{\pm}(z,t)$ excited by light with opposite circular polarization vectors $\mathbf{e}_{\pm}$, according to the dipole selection rules (1.1) on page 11. Therefore, in Part I circularly polarized optical fields have been considered. Here, in the nonlinear regime, the different dipole-allowed excitonic transitions are coupled to each other by the four-particle (biexcitonic) correlations in Eq. (5.8). In this chapter the dependence of optical properties on the polarization of the exciting light fields plays an important role. Before the equations of motion for the description of different optical setups are deduced in Sections 6.2 to 6.5, in Section 6.1 a short introduction to the polarization of light is given.

6.1. Polarization of Light

We start again with the basis vectors for circular polarization in the x-y-plane, $\mathbf{e}_{\pm} = \frac{1}{\sqrt{2}}(\mathbf{e}_x \pm i\mathbf{e}_y)$. In terms of these basis vectors the standard Cartesian basis vectors are

$$\mathbf{e}_x = \frac{1}{\sqrt{2}}(\mathbf{e}_+ + \mathbf{e}_-)\,, \qquad \mathbf{e}_y = \frac{1}{i\sqrt{2}}(\mathbf{e}_+ - \mathbf{e}_-)\,.$$

A normalized linear polarization vector $\mathbf{e}_{x_0y_0}$, which encloses an angle $\phi_{x_0y_0} = \arctan\frac{y_0}{x_0}$ with the x-axis, is given by

$$\begin{aligned}\mathbf{e}_{x_0y_0} &= \frac{x_0\mathbf{e}_x + y_0\mathbf{e}_y}{\sqrt{x_0^2+y_0^2}} \\ &= \frac{1}{\sqrt{2(x_0^2+y_0^2)}}\left((x_0 - iy_0)\mathbf{e}_+ + (x_0 + iy_0)\mathbf{e}_-\right) = A_+\mathbf{e}_+ + A_-\mathbf{e}_-\,,\end{aligned}$$

in terms of the circular polarization vectors and with amplitudes

$$A_+ = \frac{x_0 - iy_0}{\sqrt{2(x_0^2+y_0^2)}}\,, \qquad A_- = \frac{x_0 + iy_0}{\sqrt{2(x_0^2+y_0^2)}}\,. \tag{6.1}$$

The above definitions are advantageous as they naturally contain the amplitudes A_+, A_- for circularly polarized light components. This allows a direct evaluation of the dipole selection rules, given by Eq. (1.1), even for calculations with linear light polarization expressed by the coefficients x_0, y_0.

In general, light pulses with linear polarization are assumed:

$$\mathbf{E}(z,t) = E_+(z,t)\mathbf{e}_+ + E_-(z,t)\mathbf{e}_- \,.$$

The amplitudes $E_\pm(z,t)$ are chosen according to Eq. (6.1). With the dipole selection rules, two interband transitions are excited in the spectral range of the heavy-hole exciton resonance. The relevant excitonic transition amplitudes $p^{\mathrm{eh}}_{(\mathbf{k},z_\mathrm{e},z_\mathrm{h})}$ in Eq. (5.8), or p^{eh}_m in the exciton basis in Eq. (5.12), are labeled with

$$+ \mathrel{\hat{=}} \{\mathrm{e} = +3/2, \mathrm{h} = +1/2\}\,, \qquad - \mathrel{\hat{=}} \{\mathrm{e} = -3/2, \mathrm{h} = -1/2\}\,, \tag{6.2}$$

respectively. The relevant biexcitonic correlation functions $b^{\mathrm{e'h'}\;(\mathbf{k}_2,z_2,\mathbf{k}_1,z_1)}_{\mathrm{eh}\;\;(\mathbf{k}_4,z_4,\mathbf{k}_3,z_3)}$ in Eq. (5.9), or $b^{\mathrm{ehe'h'}\lambda}_{nm}(\mathbf{q})$ in the exciton basis in Eq. (5.13), are labeled according to their source terms.

6.2. Single Pulse Propagation

The simplest configuration to study nonlinear optical spectra is given by a single light pulse transmitted through the investigated semiconductor sample. In analogy to the measurement of transmission spectra in linear optics, the quantity of interest that contains information about the induced material polarization is the transmitted optical field. Here, in nonlinear optics, the third order material polarization is determined by the coupled set of equations of motion for the excitonic and the biexcitonic dynamics, Eqs. (5.8) and (5.9). Making use of the dipole selection rules (1.1) for a single light pulse, the equations of motion for the excitonic coefficients $p^\pm_m$ in the exciton basis are:

$$\begin{aligned}
i\hbar\frac{\mathrm{d}}{\mathrm{d}t}p^+_m =& \varepsilon_m p^+_m - d_{\mathrm{eh}} \int \mathrm{d}z\, E_+(z) \sum_{\mathbf{k}} \phi_m(\mathbf{k},z,z) \\
&+ d_{\mathrm{eh}} \sum_{m'n} \Big[\big(p^+_{m'}\big)^* p^+_n \int \mathrm{d}z\, E_+(z) \Big(R^1_{mm'n}(z) + R^2_{mm'n}(z) \Big) \Big] \\
&+ \sum_{m'nn'} \big(p^+_{m'}\big)^* p^+_n p^+_{n'} V^{\mathrm{HF}}_{mm'nn'} \\
&+ \sum_{n} \big(p^+_n\big)^* \sum_{\mathbf{q}n'm'\lambda} W^{\mathrm{XX}\lambda *}_{n'm'mn}(\mathbf{q},0) b^{++\lambda}_{n'm'}(\mathbf{q}) \\
&+ \sum_{n} \big(p^-_n\big)^* \sum_{\mathbf{q}n'm'\lambda} W^{\mathrm{XX}\lambda *}_{n'm'mn}(\mathbf{q},0) b^{+-\lambda}_{n'm'}(\mathbf{q})\,,
\end{aligned} \tag{6.3}$$

$$\begin{aligned}
i\hbar\frac{\mathrm{d}}{\mathrm{d}t}p_m^- =& \varepsilon_m p_m^- - d_{\mathrm{eh}}\int \mathrm{d}z\, E_-(z)\sum_{\mathbf{k}}\phi_m(\mathbf{k},z,z)\\
&+ d_{\mathrm{eh}}\sum_{m'n}\Big[\left(p_{m'}^-\right)^* p_n^- \int \mathrm{d}z\, E_-(z)\Big(R^1_{mm'n}(z)+R^2_{mm'n}(z)\Big)\Big]\\
&+ \sum_{m'nn'}\left(p_{m'}^-\right)^* p_n^- p_{n'}^- V^{\mathrm{HF}}_{mm'nn'}\\
&+ \sum_n \left(p_n^-\right)^* \sum_{\mathbf{q}n'm'\lambda} W^{\mathrm{XX}\lambda *}_{n'm'mn}(\mathbf{q},0)\, b^{--\lambda}_{n'm'}(\mathbf{q})\\
&+ \sum_n \left(p_n^+\right)^* \sum_{\mathbf{q}n'm'\lambda} W^{\mathrm{XX}\lambda *}_{n'm'mn}(\mathbf{q},0)\, b^{-+\lambda}_{n'm'}(\mathbf{q})\,. \qquad (6.4)
\end{aligned}$$

The equations of motion for the biexcitonic coefficients $b^{\pm\pm\lambda}_{nm}(\mathbf{q})$ contributing to Eqs. (6.3) and (6.4) are:

$$\begin{aligned}
i\hbar\frac{\mathrm{d}}{\mathrm{d}t}b^{++\lambda}_{nm}(\mathbf{q}) =& \sum_{n'm'\mathbf{q}'} H^{\mathrm{XX}\lambda}_{nmn'm'}(\mathbf{q},\mathbf{q}')\, b^{++\lambda}_{n'm'}(\mathbf{q}')\\
&+ \frac{1}{2}(1+\lambda)\sum_{n'm'rs\mathbf{q}'}(1-\lambda S)^{-1}_{nmrs}(\mathbf{q},\mathbf{q}')\, W^{\mathrm{XX}\lambda}_{rsn'm'}(\mathbf{q}',0)\, p^+_{n'} p^+_{m'}\,, \qquad (6.5)
\end{aligned}$$

$$\begin{aligned}
i\hbar\frac{\mathrm{d}}{\mathrm{d}t}b^{--\lambda}_{nm}(\mathbf{q}) =& \sum_{n'm'\mathbf{q}'} H^{\mathrm{XX}\lambda}_{nmn'm'}(\mathbf{q},\mathbf{q}')\, b^{--\lambda}_{n'm'}(\mathbf{q}')\\
&+ \frac{1}{2}(1+\lambda)\sum_{n'm'rs\mathbf{q}'}(1-\lambda S)^{-1}_{nmrs}(\mathbf{q},\mathbf{q}')\, W^{\mathrm{XX}\lambda}_{rsn'm'}(\mathbf{q}',0)\, p^-_{n'} p^-_{m'}\,, \qquad (6.6)
\end{aligned}$$

$$\begin{aligned}
i\hbar\frac{\mathrm{d}}{\mathrm{d}t}b^{+-\lambda}_{nm}(\mathbf{q}) =& \sum_{n'm'\mathbf{q}'} H^{\mathrm{XX}\lambda}_{nmn'm'}(\mathbf{q},\mathbf{q}')\, b^{+-\lambda}_{n'm'}(\mathbf{q}')\\
&+ \frac{1}{2}\sum_{n'm'rs\mathbf{q}'}(1-\lambda S)^{-1}_{nmrs}(\mathbf{q},\mathbf{q}')\, W^{\mathrm{XX}\lambda}_{rsn'm'}(\mathbf{q}',0)\, p^+_{n'} p^-_{m'}\,, \qquad (6.7)
\end{aligned}$$

$$\begin{aligned}
i\hbar\frac{\mathrm{d}}{\mathrm{d}t}b^{-+\lambda}_{nm}(\mathbf{q}) =& \sum_{n'm'\mathbf{q}'} H^{\mathrm{XX}\lambda}_{nmn'm'}(\mathbf{q},\mathbf{q}')\, b^{-+\lambda}_{n'm'}(\mathbf{q}')\\
&+ \frac{1}{2}\sum_{n'm'rs\mathbf{q}'}(1-\lambda S)^{-1}_{nmrs}(\mathbf{q},\mathbf{q}')\, W^{\mathrm{XX}\lambda}_{rsn'm'}(\mathbf{q}',0)\, p^-_{n'} p^+_{m'}\,. \qquad (6.8)
\end{aligned}$$

Note, that the Hartree-Fock contributions to the excitonic polarizations $p^\pm_m$ (lines 2 and 3 in Eqs. (6.3) and (6.4)) do not couple the spin subsystems ± defined in (6.2). A coupling of the two interband transitions excited with $\mathbf{e}_+$ and $\mathbf{e}_-$ light only occurs due to the biexcitonic correlations in Eqs. (6.3) and (6.4).

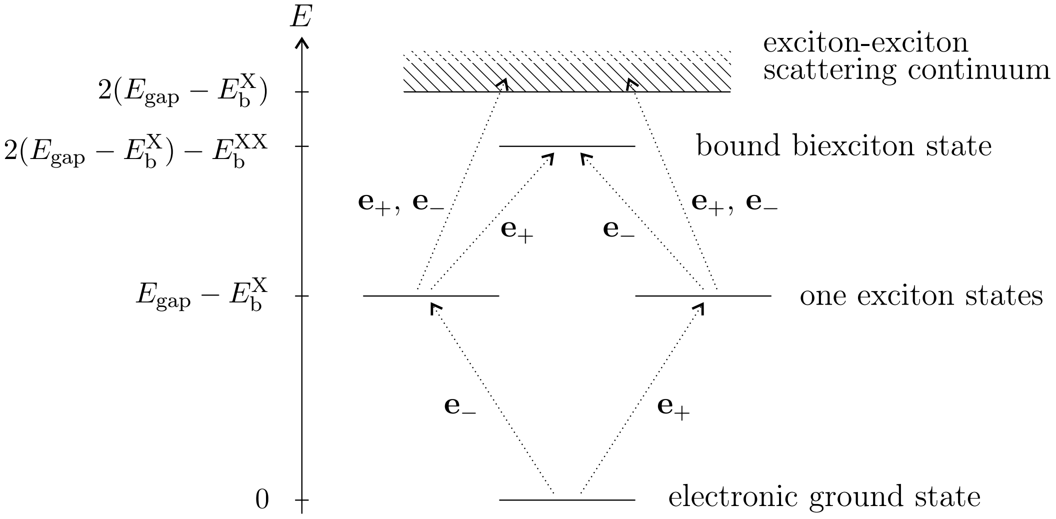

Figure 6.1: Schematic illustration of the excitation energies and selection rules for optical excitation of excitons and biexcitons.

For exclusively circular light polarization ($\mathbf{e}_+$ or $\mathbf{e}_-$), the biexcitonic correlations are determined either by Eq. (6.5) for $\mathbf{e}_+$ polarization or by Eq. (6.6) for $\mathbf{e}_-$ polarization, where in both equations the source term vanishes for the electronic singlet configuration with $\lambda = -1$. Therefore, we find that in this case no contributions from biexciton states with electronic singlet configuration are excited. Hence, especially the bound biexciton state does not contribute to the semiconductor response for exclusively circular light polarization. The excitation energies and selection rules for optical excitation of exciton and biexciton are schematically visualized in Fig. 6.1.

The set of coupled equations (6.3)-(6.8) represents a consistent description of optically induced excitonic and biexcitonic third order nonlinearities to the macroscopic polarization of the system. However, the self-consistent solution of these equations results in higher order contributions as well. Without propagation, namely without the self-consistent coupling of the material polarization and the optical field, the evaluation of the equations of motion can be performed in a way where the macroscopic polarization is strictly restricted to third order contributions in the optical field. Within this approach the excitonic polarizations that enter the nonlinear contributions to Eqs. (6.3) and (6.4) and the inhomogeneities in Eqs. (6.5)-(6.8) are strictly kept in linear order in the optical field and thus are determined from the linearized versions (line 1) of Eqs. (6.3) and (6.4).

Including propagation effects in the description, the exciting light field is influenced by the nonlinear material polarization and consequently contains nonlinear contributions itself. Therefore, for light intensities beyond the linear optical regime, a rigorous linearization of Eqs. (6.3) and (6.4) is no longer possible. In principle, a self-consistent solution of Eqs. (6.3)-(6.8) is necessary which automatically results in contributions to the macroscopic polarization of the system up to arbitrary order in the optical field.

Nevertheless, for the theoretical evaluations, the light intensity can be chosen sufficiently small to suppress the influence of higher order contributions and to consistently concentrate on the analysis of third order nonlinearities in the optical response. Calculations for higher light intensities can easily be performed but do no longer yield fully consistent results, since only a subclass of higher order nonlinearities is included in the theoretical description while others all neglected by the dynamics-controlled truncation of the many-particle hierarchy problem in Section 5.1.

6.3. Fourier Decomposition of Signals

For the description of typical optical experiments an extension of the theory presented in the previous section to more than one light pulse is necessary. For instance, two incoming light fields are chosen, suitable to simulate typical experimental setups in pump and probe or four wave mixing geometry, respectively. The pulses propagate in different directions $\mathbf{k}_1$ and $\mathbf{k}_2$.

A light pulse propagating in the direction of $\mathbf{k}$ can be constructed by superposition of plane wave contributions, all propagating in direction $\frac{\mathbf{k}}{|\mathbf{k}|}$ but with different modulus $|\mathbf{k}|$ of the wave vector $\mathbf{k}$:

$$\mathbf{E}_{\frac{\mathbf{k}}{|\mathbf{k}|}}(\mathbf{r},t) = \mathbf{e} \int\limits_{\frac{\mathbf{k}'}{|\mathbf{k}'|}=\frac{\mathbf{k}}{|\mathbf{k}|}} \mathrm{d}^3k'\, E_0(\mathbf{k}')\mathrm{e}^{i\mathbf{k}'\mathbf{r}}\mathrm{e}^{-ic|\mathbf{k}'|t}\,. \tag{6.9}$$

The spectral shape of the pulse with polarization vector $\mathbf{e}$ is determined by the coefficients $E_0(\mathbf{k}')$. The dispersion of light, $\omega = c|\mathbf{k}'|$, has been used for each plane wave contribution. For the subject of the present work, the spectral shape of all considered pulses is localized within a narrow spectral window around a certain central frequency ω. So, in order to capture the main features and to keep the following discussion of nonlinear signals as simple and illustrative as possible, the momentum space contribution to the pulse is approximated by $E_0(\mathbf{k}') \approx E_0\delta(|\mathbf{k}'| - |\mathbf{k}|)$ here. Therefore, the general expression in Eq. (6.9) for light pulses propagating in a certain direction is approximated by a simple plane wave contribution with wave vector $\mathbf{k}$.

Material polarizations are induced by the incident light pulses according to their propagation direction. Due to the nonlinearities in the material equations, here Eqs. (5.12) and (5.13) on page 76, optical excitation with at least two light pulses propagating in different directions induces excitonic polarizations in directions not being equal to one of those of the incident pulses. Formally, the nonlinearities in Eq. (5.12) yield contributions to the excitonic polarization in the directions $n_1\mathbf{k}_1 + n_2\mathbf{k}_2$, with $n_1, n_2 \in \{0, \pm1, \pm2 \ldots\}$, with the restriction $n_1 + n_2 = 1$ which directly follows from Eq. (5.12) and the rotating-wave approximation.[19,29] Due to the self-consistent coupling of optical field and material polarization, these “diffracted” polarizations themselves are the source for additional contributions to the optical field. In third order in the optical field, the nonlinearities in the material equations yield additional contributions to the excitonic polarization in the directions $2\mathbf{k}_2 - \mathbf{k}_1$ and $2\mathbf{k}_1 - \mathbf{k}_2$.

The dipole coupling of excitonic polarization and the optical field gives rise to contributions to the optical field in these directions as well. In order to deduce a consistent theory in third order, a weak pulse in $\mathbf{k}_1$-direction is applied which only yields a significant contribution to the excitonic polarization in linear order in its electric field amplitude. So, due to the weak $\mathbf{k}_1$ pulse, only the prominent four wave mixing signal in $2\mathbf{k}_2 - \mathbf{k}_1$ direction is observed.[75,76]

However, the idealized directions $n_1\mathbf{k}_1 + n_2\mathbf{k}_2$ of diffracted signals can, strictly speaking, only be deduced for plane wave signals. Thinking in terms of wave packets given by Eq. (6.9), contributions to nonlinear signals are just localized in the vicinity of the diffraction maxima observed in the directions $n_1\mathbf{k}_1 + n_2\mathbf{k}_2$. Nevertheless, in the following all contributions are contracted to these idealized directions in a very good approximation. This approach has successfully been applied to different excitation configurations in the past[20,75] and yields meaningful results as long as the slowly varying envelope approximation[19] (SVEA) is applicable to the investigated system.

Only a small deviation from perpendicular incidence to the semiconductor layer is considered here. The induced material polarization and the optical field in different directions are still described by the equations of motion for light propagation in the z-direction, deduced in the previous part of this work, together with the dipole selection rules (1.1). Maxwell's equations are solved in their one-dimensional form (3.4a), (3.4b), with $\mathbf{E}_{\mathbf{k}/|\mathbf{k}|}(\mathbf{r}, t) \approx \mathbf{E}_{\mathbf{k}/|\mathbf{k}|}(z, t)$ for $k_z \gg k_x, k_y$ and $|\mathbf{k}| \approx |k_z|$. The index $\mathbf{k}$ is only formally kept to distinguish the signals which are propagating in different directions. A change of the semiconductor response due to the small momentum of the optical fields in the x-y-plane is not considered. All relevant dynamic quantities are decomposed according to the directions $n_1\mathbf{k}_1 + n_2\mathbf{k}_2$. This decomposition yields coupled equations of motion for the Fourier components

$$p_m^{\mathrm{eh}n_1n_2}(t)\,, \qquad b_{nm}^{\mathrm{ehe'h'}\lambda n_1n_2}(t) \tag{6.10}$$

of the excitonic polarization and the biexcitonic correlation function, respectively, in the directions $n_1\mathbf{k}_1 + n_2\mathbf{k}_2$.

In Sections 6.4 and 6.5 the relevant equations of motion to determine the excitonic transition amplitudes $p_m^{\mathrm{eh}n_1n_2}$ and the biexcitonic correlation functions $b_{nm}^{\mathrm{ehe'h'}\lambda n_1n_2}$ are explicitly given to simulate experiments in pump and probe and in four wave mixing geometry.

6.4. Pump and Probe

A typical pump and probe setup is illustrated in Fig. 6.2. The two incident light pulses propagate in the directions $\mathbf{k}_1$ and $\mathbf{k}_2$, respectively, and are superimposed on the sample. The intensity of the probe pulse in $\mathbf{k}_1$ direction is weak enough that it alone would yield a linear transmission spectrum. The pump pulse in $\mathbf{k}_2$ direction gives rise to third order contributions to the material polarization in probe direction. A time-delay between pump and probe pulse may be applied. Behind the sample, the transmitted

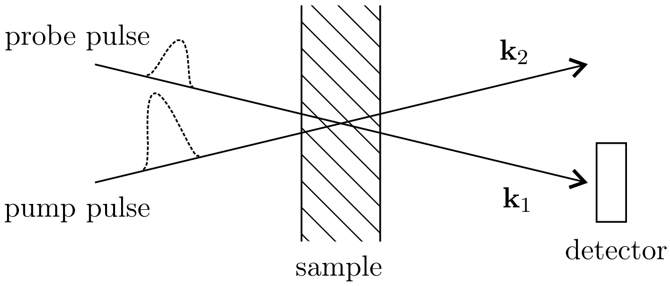

Figure 6.2: Schematic illustration of a typical pump and probe setup.

signal in probe direction is detected. This probe transmission contains information about the linear material response as well as about the third order material response. Since in pump and probe configuration the probe pulse enters the polarization only in linear order, information exclusively about the third order response can be obtained from the transmission change induced by the pump pulse. Commonly, the analysis of pump and probe experiments is done for two different polarization configurations: (i) pump and probe pulse are in the same circular polarization state, the co-circular configuration, and (ii) pump and probe pulse are in opposite circular polarization states, the opposite circular configuration. Making use of the dipole selection rules and the Fourier decomposition of signals described in the previous section, the relevant equations of motion for the co-circular $\mathbf{e}_+\mathbf{e}_+$ configuration read:

(i) Linear polarization in pump direction:

$$i\hbar\frac{\mathrm{d}}{\mathrm{d}t}p_m^{01+} = \varepsilon_m p_m^{01+} - d_{\mathrm{eh}} \int \mathrm{d}z\, E_+^{01}(z) \sum_{\mathbf{k}} \phi_m(\mathbf{k}, z, z)\,. \tag{6.11}$$

(ii) Third order polarization in probe direction:

$$\begin{aligned} i\hbar\frac{\mathrm{d}}{\mathrm{d}t}p_m^{10+} =& \varepsilon_m p_m^{10+} - d_{\mathrm{eh}} \int \mathrm{d}z\, E_+^{10}(z) \sum_{\mathbf{k}} \phi_m(\mathbf{k}, z, z) \\ &+ d_{\mathrm{eh}} \sum_{m'n} \Bigg[\left(p_{m'}^{01+}\right)^* p_n^{01+} \int \mathrm{d}z\, E_+^{10}(z) \Big(R^1_{mm'n}(z) + R^2_{mm'n}(z) \Big) \\ &\qquad + \left(p_{m'}^{01+}\right)^* p_n^{10+} \int \mathrm{d}z\, E_+^{01}(z) \Big(R^1_{mm'n}(z) + R^2_{mm'n}(z) \Big) \Bigg] \\ &+ \sum_{m'nn'} \left(p_{m'}^{01+}\right)^* \left[p_n^{01+} p_{n'}^{10+} + p_n^{10+} p_{n'}^{01+} \right] V^{\mathrm{HF}}_{mm'nn'} \\ &+ \sum_{n} \left(p_n^{01+}\right)^* \sum_{\mathbf{q}n'm'\lambda} W^{\mathrm{XX}\lambda *}_{n'm'mn}(\mathbf{q}, 0)\, b^{11++\lambda}_{n'm'}(\mathbf{q})\,. \end{aligned} \tag{6.12}$$

(iii) Relevant biexcitonic correlation function:

$$\begin{aligned} i\hbar\frac{\mathrm{d}}{\mathrm{d}t} b^{11++\lambda}_{nm}(\mathbf{q}) = &\sum_{n'm'\mathbf{q}'} H^{\mathrm{XX}\lambda}_{nmn'm'}(\mathbf{q},\mathbf{q}')\, b^{11++\lambda}_{n'm'}(\mathbf{q}') \\ &+ (1+\lambda) \sum_{n'm'rs\mathbf{q}'} (1-\lambda S)^{-1}_{nmrs}(\mathbf{q},\mathbf{q}')\, W^{\mathrm{XX}\lambda}_{rsn'm'}(\mathbf{q}',0)\big(p^{01+}_{n'} p^{10+}_{m'} + p^{10+}_{n'} p^{01+}_{m'}\big)\,. \end{aligned} \tag{6.13}$$

The equations of motion are given here for small light intensities where only third order nonlinearities yield a relevant contribution to the material polarization in probe direction. The polarization in probe direction is linear in the weak probe field and of second order in the pump field. Within the $\chi^{(3)}$-limit the pump polarization can be determined from the linear equation (6.11).

The corresponding equations of motion for opposite circular $\mathbf{e}_+\mathbf{e}_-$ configuration are:

(i) Linear polarization in pump direction:

$$i\hbar\frac{\mathrm{d}}{\mathrm{d}t} p^{01-}_{m} = \varepsilon_m p^{01-}_{m} - d_{\mathrm{eh}} \int \mathrm{d}z\, E^{01}_{-}(z) \sum_{\mathbf{k}} \phi_m(\mathbf{k},z,z)\,.$$

(ii) Third order polarization in probe direction:

$$\begin{aligned} i\hbar\frac{\mathrm{d}}{\mathrm{d}t} p^{10+}_{m} = &\varepsilon_m p^{10+}_{m} - d_{\mathrm{eh}} \int \mathrm{d}z\, E^{10}_{+}(z) \sum_{\mathbf{k}} \phi_m(\mathbf{k},z,z) \\ &+ \sum_{n} \big(p^{01-}_{n}\big)^{*} \sum_{\mathbf{q}n'm'\lambda} W^{\mathrm{XX}\lambda *}_{n'm'mn}(\mathbf{q},0)\, b^{11+-\lambda}_{n'm'}(\mathbf{q})\,. \end{aligned} \tag{6.14}$$

(iii) Relevant biexcitonic correlation function:

$$\begin{aligned} i\hbar\frac{\mathrm{d}}{\mathrm{d}t} b^{11+-\lambda}_{nm}(\mathbf{q}) = &\sum_{n'm'\mathbf{q}'} H^{\mathrm{XX}\lambda}_{nmn'm'}(\mathbf{q},\mathbf{q}')\, b^{11+-\lambda}_{n'm'}(\mathbf{q}') \\ &+ \frac{1}{2} \sum_{n'm'rs\mathbf{q}'} (1-\lambda S)^{-1}_{nmrs}(\mathbf{q},\mathbf{q}')\, W^{\mathrm{XX}\lambda}_{rsn'm'}(\mathbf{q}',0)\, p^{10+}_{n'} p^{01-}_{m'}\,. \end{aligned}$$

Note, that in $\mathbf{e}_+\mathbf{e}_-$ configuration no mean-field (Hartree-Fock, via the matrix elements V^{HF}, $R^1(z)$, $R^2(z)$) contributions to the third order probe polarization (6.14) are obtained. Similar to linear optics, on the Hartree-Fock level, the two spin-subsystems are decoupled as already seen in Section 6.2. Results obtained from an evaluation of these equations of motion for the probe pulse transmission through a semiconductor material are presented in Chapter 7.

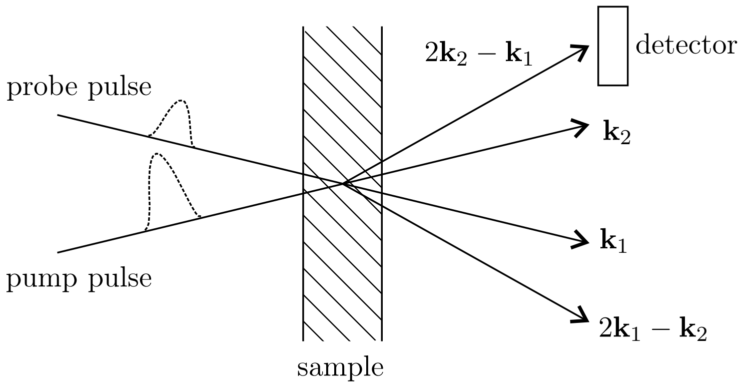

Figure 6.3: Schematic illustration of a typical four wave mixing setup.

6.5. Four Wave Mixing

In four wave mixing geometry a similar setup to that in the previous section is used. However, here, the quantity to measure is the diffracted signal in the four wave mixing direction $2\mathbf{k}_2 - \mathbf{k}_1$. A signal in this direction is at least of third order in the optical field. In contrast to the pump and probe setup the detected signal is not superimposed by a contribution in linear order in the optical field. Therefore, this configuration is particularly sensible to optical nonlinearities, to third order nonlinearities for a sufficiently weak optical pulse in $\mathbf{k}_2$ direction. In analogy to the pump and probe setup, the pulse in $\mathbf{k}_1$ direction is weak enough to guarantee a consistent description in third order in the optical field. The setup is schematically illustrated in Fig. 6.3. A general formulation is presented here regarding the polarization states of the two incident pulses. In particular, by use of the relations given in Section 6.1 linear pulse polarization is investigated while the angle that is enclosed by the polarization vectors of both pulses can easily be varied. The relevant equations of motion to calculate the third order four wave mixing signal in $2\mathbf{k}_2 - \mathbf{k}_1$ direction are:

(i) Excitonic polarizations in linear order in the optical field in $\mathbf{k}_1$ direction:

$$i\hbar \frac{\mathrm{d}}{\mathrm{d}t} p_m^{10+} = \varepsilon_m p_m^{10+} - d_{\mathrm{eh}} \int \mathrm{d}z \, E_+^{10}(z) \sum_{\mathbf{k}} \phi_m(\mathbf{k}, z, z) \,, \tag{6.15}$$

$$i\hbar \frac{\mathrm{d}}{\mathrm{d}t} p_m^{10-} = \varepsilon_m p_m^{10-} - d_{\mathrm{eh}} \int \mathrm{d}z \, E_-^{10}(z) \sum_{\mathbf{k}} \phi_m(\mathbf{k}, z, z) \,. \tag{6.16}$$

(ii) Excitonic polarizations in linear order in the optical field in $\mathbf{k}_2$ direction:

$$i\hbar \frac{\mathrm{d}}{\mathrm{d}t} p_m^{01+} = \varepsilon_m p_m^{01+} - d_{\mathrm{eh}} \int \mathrm{d}z \, E_+^{01}(z) \sum_{\mathbf{k}} \phi_m(\mathbf{k}, z, z) \,, \tag{6.17}$$

$$i\hbar \frac{\mathrm{d}}{\mathrm{d}t} p_m^{01-} = \varepsilon_m p_m^{01-} - d_{\mathrm{eh}} \int \mathrm{d}z \, E_-^{01}(z) \sum_{\mathbf{k}} \phi_m(\mathbf{k}, z, z) \,. \tag{6.18}$$

(iii) Nonlinear excitonic polarizations in $2\mathbf{k}_2 - \mathbf{k}_1$ direction:

$$\begin{aligned}
i\hbar\frac{\mathrm{d}}{\mathrm{d}t}p_m^{-12+} =& \varepsilon_m p_m^{-12+} + d_{\mathrm{eh}} \int \mathrm{d}z\, E_+^{-12}(z) \sum_{\mathbf{k}} \phi_m(\mathbf{k}, z, z) \\
&+ d_{\mathrm{eh}} \sum_{m'n} \left[\left(p_{m'}^{10+}\right)^* p_n^{01+} \int \mathrm{d}z\, E_+^{01}(z) (R^1_{mm'n}(z) + R^2_{mm'n}(z)) \right] \\
&+ \sum_{m'nn'} \left(p_{m'}^{10+}\right)^* p_n^{01+} p_{n'}^{01+} V^{\mathrm{HF}}_{mm'nn'} \\
&+ \sum_n \Bigg[\left(p_n^{10+}\right)^* \sum_{\mathbf{q}n'm'\lambda} W^{\mathrm{XX}\lambda*}_{n'm'mn}(\mathbf{q},0) b^{02++\lambda}_{n'm'}(\mathbf{q}) \\
&+ \left(p_n^{10-}\right)^* \sum_{\mathbf{q}n'm'\lambda} W^{\mathrm{XX}\lambda*}_{n'm'mn}(\mathbf{q},0) b^{02+-\lambda}_{n'm'}(\mathbf{q}) \Bigg] ,
\end{aligned} \tag{6.19}$$

$$\begin{aligned}
i\hbar\frac{\mathrm{d}}{\mathrm{d}t}p_m^{-12-} =& \varepsilon_m p_m^{-12-} + d_{\mathrm{eh}} \int \mathrm{d}z\, E_-^{-12}(z) \sum_{\mathbf{k}} \phi_m(\mathbf{k}, z, z) \\
&+ d_{\mathrm{eh}} \sum_{m'n} \left[\left(p_{m'}^{10-}\right)^* p_n^{01-} \int \mathrm{d}z\, E_-^{01}(z) (R^1_{mm'n}(z) + R^2_{mm'n}(z)) \right] \\
&+ \sum_{m'nn'} \left(p_{m'}^{10-}\right)^* p_n^{01-} p_{n'}^{01-} V^{\mathrm{HF}}_{mm'nn'} \\
&+ \sum_n \Bigg[\left(p_n^{10+}\right)^* \sum_{\mathbf{q}n'm'\lambda} W^{\mathrm{XX}\lambda*}_{n'm'mn}(\mathbf{q},0) b^{02-+\lambda}_{n'm'}(\mathbf{q}) \\
&+ \left(p_n^{10-}\right)^* \sum_{\mathbf{q}n'm'\lambda} W^{\mathrm{XX}\lambda*}_{n'm'mn}(\mathbf{q},0) b^{02--\lambda}_{n'm'}(\mathbf{q}) \Bigg] .
\end{aligned} \tag{6.20}$$

(iv) Biexcitonic correlation functions that contribute to the nonlinear excitonic polarization in $2\mathbf{k}_2 - \mathbf{k}_1$ direction in Eqs. (6.19) and (6.20):

$$\begin{aligned}
i\hbar\frac{\mathrm{d}}{\mathrm{d}t}b^{02++\lambda}_{nm}(\mathbf{q}) =& \sum_{n'm'\mathbf{q}'} H^{\mathrm{XX}}_{nmn'm'}(\mathbf{q},\mathbf{q}') b^{02++\lambda}_{n'm'}(\mathbf{q}') \\
&+ \frac{1}{2}(1+\lambda) \sum_{n'm'rs\mathbf{q}'} (1-\lambda S)^{-1}_{nmrs}(\mathbf{q},\mathbf{q}') W^{\mathrm{XX}\lambda}_{rsn'm'}(\mathbf{q}',0) p^{01+}_{n'} p^{01+}_{m'} ,
\end{aligned} \tag{6.21}$$

$$\begin{aligned}
i\hbar\frac{\mathrm{d}}{\mathrm{d}t}b^{02--\lambda}_{nm}(\mathbf{q}) =& \sum_{n'm'\mathbf{q}'} H^{\mathrm{XX}}_{nmn'm'}(\mathbf{q},\mathbf{q}') b^{02--\lambda}_{n'm'}(\mathbf{q}') \\
&+ \frac{1}{2}(1+\lambda) \sum_{n'm'rs\mathbf{q}'} (1-\lambda S)^{-1}_{nmrs}(\mathbf{q},\mathbf{q}') W^{\mathrm{XX}\lambda}_{rsn'm'}(\mathbf{q}',0) p^{01-}_{n'} p^{01-}_{m'} ,
\end{aligned} \tag{6.22}$$

$$
\begin{aligned}
i\hbar\frac{\mathrm{d}}{\mathrm{d}t}b^{02+-\lambda}_{nm}(\mathbf{q}) = &\sum_{n'm'\mathbf{q}'} H^{\mathrm{XX}}_{nmn'm'}(\mathbf{q},\mathbf{q}')b^{02+-\lambda}_{n'm'}(\mathbf{q}') \\
&+ \frac{1}{2}\sum_{n'm'rs\mathbf{q}'} (1-\lambda S)^{-1}_{nmrs}(\mathbf{q},\mathbf{q}')W^{\mathrm{XX}\lambda}_{rsn'm'}(\mathbf{q}',0)p^{01+}_{n'}p^{01-}_{m'}\ ,
\end{aligned}
\tag{6.23}
$$

$$
\begin{aligned}
i\hbar\frac{\mathrm{d}}{\mathrm{d}}b^{02-+\lambda}_{nm}(\mathbf{q}) = &\sum_{n'm'\mathbf{q}'} H^{\mathrm{XX}}_{nmn'm'}(\mathbf{q},\mathbf{q}')b^{02-+\lambda}_{n'm'}(\mathbf{q}') \\
&+ \frac{1}{2}\sum_{n'm'rs\mathbf{q}'} (1-\lambda S)^{-1}_{nmrs}(\mathbf{q},\mathbf{q}')W^{\mathrm{XX}\lambda}_{rsn'm'}(\mathbf{q}',0)p^{01-}_{n'}p^{01+}_{m'}\ .
\end{aligned}
\tag{6.24}
$$

Again, higher order contributions that would result from a self-consistent solution of the equations of motion are not considered. Therefore, the linear excitonic polarizations (6.15)-(6.18) in $\mathbf{k}_1$ and $\mathbf{k}_2$ direction form the driving terms for the nonlinear excitonic polarizations (6.19) and (6.20) in $2\mathbf{k}_2-\mathbf{k}_1$ direction as well as for the biexcitonic correlations (6.21)-(6.24) in $2\mathbf{k}_2$ direction. A self-consistent extension of these equations of motion for light intensities beyond the $\chi^{(3)}$-limit is investigated in Ref. 76.

7. Results: Nonlinear Optics

In the previous chapter the equations of motion for the theoretical description of nonlinear optical transmission spectra in different configurations have been given. Making use of the results discussed in Sections 5.2 and 5.3, in this section the method is applied to the calculation of nonlinear optical spectra for semiconductor heterostructures. The evaluation is done for layer thicknesses beyond the quasi two-dimensional quantum-well limit where propagation effects strongly influence the optical spectra. In the following section some basic results are discussed for a GaAs model system, whereas in Section 7.2 a direct theory-experiment comparison of transmission spectra is presented for a 20 nm ZnSe layer.

7.1. GaAs Model System

The model system that is investigated in this section consists of a single GaAs layer with a thickness of $5\,\mathrm{a}_0^\mathrm{X}$. The biexciton binding energy E_b^XX and the matrix elements in the two-exciton product basis have already been discussed for this system in Section 5.3. Material parameters are given in Table 3.1 on page 30. The dephasing constant is slightly increased to $\gamma = 0.6\,\mathrm{meV}$ in this section. This dephasing constant yields a somewhat faster decay of the material polarization in the time domain and an unsignificantly larger broadening of excitonic and biexcitonic resonances in the optical spectra. For practical purposes, this increased dephasing constant was initially used here to broaden the numerically discrete resonances that represent the exciton-exciton scattering continuum in the calculations. However, this parameter does not sensitively affect the final results and their discussion.

7.1.1. Single Pulse Propagation

The solid and dashed lines in Fig. 7.1 (a) show the linear optical transmission T_linear through the GaAs layer and the spectral shape of the 120 fs laser pulse, respectively. The excitation energy $\hbar\omega$ is given relative to the bulk band-gap energy E_gap and in units of the corresponding bulk exciton binding energy E_b^X.

For the chosen layer thickness, the confinement of carriers in the z-direction yields three polariton resonances in the displayed part of the spectrum. According to Section 5.2.1, they can be attributed to a splitting of the 1s exciton state and are labeled with consecutive numbers. The spectral position of biexciton states entering the calculations are depicted in Fig. 7.1 (b) for electronic singlet (×) and triplet (+) configuration.

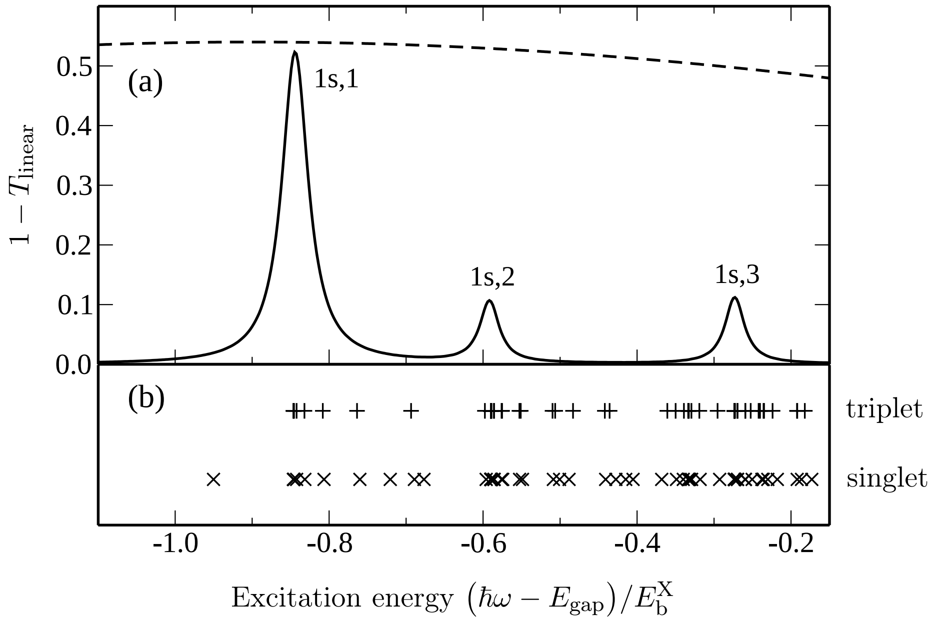

Figure 7.1: (a) Calculated linear transmission spectrum for a $5\,\mathrm{a}_0^{\mathrm{X}}$ GaAs layer (solid line), and spectral shape of the 120 fs laser pulse (dashed line). The polariton resonances are labeled according to the in-plane 1s symmetry of the involved exciton states and with consecutive numbers. (b) Spectral positions of biexciton states for electronic singlet (×) and triplet (+) configuration.

These energies for the biexciton states follow from the diagonalization of the biexcitonic Hamiltonian matrices (5.19) for the electronic singlet ($\lambda = -1$) and triplet ($\lambda = +1$) subspaces. The discrete structure of the biexcitonic spectrum on the higher energy side of the 1s,1 polariton resonance, the exciton-exciton scattering continuum, is a consequence of the numerical discretization of the two-exciton relative momentum $\mathbf{q}$ and of the confinement of electrons and holes in the slab geometry. The bound biexciton state on the lower energy side of the 1s,1 polariton resonance is found in the electronic singlet subspace in analogy to the Hydrogen-molecule problem as already discussed in Section 5.3.

The calculation of nonlinear transmission spectra is performed according to the equations of motion (6.3)-(6.8) for the material polarization given in Section 6.2. Sufficiently weak optical fields are applied here to give a consistent description of third order optical nonlinearities. A Rabi energy of $d_{\mathrm{eh}}|\mathbf{E}| = 0.01\,\mathrm{E}_{\mathrm{b}}^{\mathrm{X}}(3\mathrm{D})$[a] is chosen for the 120 fs laser pulse. For this light intensity, the nonlinear contributions to the transmitted signal are less than 1% of the linear transmission in Fig. 7.1 (a). Thus, appropriate for the visualization and discussion of the optical nonlinearities, the transmission change

---

[a] In order to connect the Rabi energy $\mathbf{d}_{\mathrm{eh}}\mathbf{E}$ directly to the light intensity $|\mathbf{E}|^2$ of the incoming laser pulses within our two-band model, the quantity $d_{\mathrm{eh}}|\mathbf{E}| = |\mathbf{d}_{\mathrm{eh}}||\mathbf{E}|$ is called Rabi energy in the following. According to Section 6.1, in the case of linear light polarization, the intensity of the incoming light field is equally distributed to the two circularly polarized components and therefore to the different dipole-allowed interband transitions.

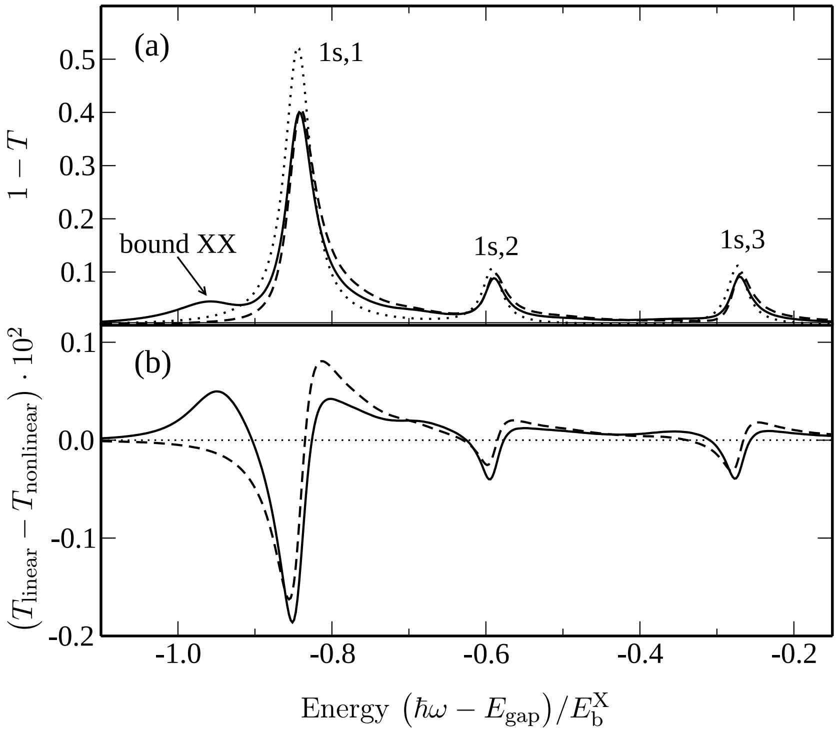

Figure 7.2: (a) The dotted line shows the linear transmission spectrum for a $5\,\mathrm{a}_0^{\mathrm{X}}$ GaAs layer (same as solid line in Fig. 7.1 (a)). Nonlinear transmission spectra for linear (solid line) and circular (dashed line) light polarization are included for a Rabi energy $d_{\mathrm{eh}}|\mathbf{E}| = 0.07\,\mathrm{E}_{\mathrm{b}}^{\mathrm{X}}$. (b) Differential single pulse transmission spectra for linear (solid line) and circular (dashed line) light polarization, corresponding to (a) but for a Rabi energy $d_{\mathrm{eh}}|\mathbf{E}| = 0.01\,\mathrm{E}_{\mathrm{b}}^{\mathrm{X}}$. For explanations see text.

$T_{\mathrm{linear}} - T_{\mathrm{nonlinear}}$ due to optically induced nonlinearities is displayed in Fig. 7.2 (b) for a single light pulse. The result is shown for linear (solid line) and circular (dashed line) light polarization, respectively.

For illustration purposes, the solid and the dashed lines in Fig. 7.2 (a) show the corresponding transmission spectra to Fig. 7.2 (b) for an increased Rabi energy of $d_{\mathrm{eh}}|\mathbf{E}| = 0.07\,\mathrm{E}_{\mathrm{b}}^{\mathrm{X}}(3\mathrm{D})$. For this elevated excitation intensity also higher order nonlinearities beyond the $\chi^{(3)}$-limit contribute to the nonlinear transmitted signals in Fig. 7.2 (a), see Section 6.2. Note, that the description does not yield fully consistent results in this case because other higher order nonlinearities like for example six-particle correlations have been neglected in the DCT factorization of expectation values in Chapter 5. Therefore, the following discussion of theoretical results will be done for a Rabi energy $d_{\mathrm{eh}}|\mathbf{E}| = 0.01\,\mathrm{E}_{\mathrm{b}}^{\mathrm{X}}(3\mathrm{D})$ and in terms of transmission changes (differential transmission spectra) to ensure that the results consistently remain in the $\chi^{(3)}$-limit.

The observed bleaching of polariton resonances in Fig. 7.2 results from Hartree-Fock as well as biexcitonic contributions to the third order optical response. As already discussed in Section 5.1 Pauli-blocking and the mean-field contributions to the exciton-exciton Coulomb interaction contribute on the effective two-particle (Hartree-Fock) level.

Biexcitonic (four-particle) correlations, which are included in the theory presented here, yield additional important contributions. The exciton-exciton Coulomb interaction involves exciton states with non-vanishing in-plane COM momentum in the semiconductor nonlinear optical response. The resulting broad background on the higher energy side of the 1s,1 resonance is due to excitation of this exciton-exciton scattering continuum. A transmission change energetically below the 1s,1 polariton resonance at the spectral position of the bound biexciton (bound XX) state is found for linear light polarization only. According to Section 6.1, linearly polarized light contains both circularly polarized components which allows the excitation of the bound biexciton state according to its electronic singlet symmetry as illustrated in Fig. 6.1 on page 92.

7.1.2. Pump and Probe

For the pump and probe configuration as described in Section 6.4 we have two incoming light pulses propagating perpendicular to the slab. However, the two propagation directions are slightly different, so that the pulses can be distinguished by their direction. The selection rules for both pulses are assumed to be those for normal incidence, as previously discussed in Section 6.3.

In the pump and probe configuration, the quantity of measurement is the optical transmission T_{probe} of the weak probe pulse. The transmission of the probe pulse depends on the nonlinearities to the material polarization that are induced by the pump pulse. The evaluation is done according to the equations of motion that have been discussed in Section 6.4. The material polarization in probe direction, Eq. (6.12) or (6.14), is linear in the probe field and of second order in the pump field for a sufficiently weak pump pulse. For the pump pulse, a Rabi energy $d_{\mathrm{eh}}|\mathbf{E}_{\mathrm{pump}}| = 0.01\,\mathrm{E}_{\mathrm{b}}^{\mathrm{X}}(3\mathrm{D})$ is used which ensures a consistent description in terms of the formulated $\chi^{(3)}$-theory. Therefore, the pump pulse induced changes in the probe pulse transmission (differential probe transmission) contain exclusive information about the third order optical response of the system. For the excitation, 120 fs pump and probe pulses are applied which reach the sample without time-delay.

Figure 7.3 shows calculated transmission changes for the probe pulse. The results for opposite circular $\mathbf{e}_+\mathbf{e}_-$ and co-circular $\mathbf{e}_+\mathbf{e}_+$ polarization of pump and probe pulse are shown as solid and dashed-dotted lines in Fig. 7.3 (a), respectively. The transmission changes around the higher polariton resonances are similar to those around the lowest one but with a decreased amplitude. In the $\mathbf{e}_+\mathbf{e}_-$ configuration the excitation of the bound biexciton resonance yields a line shape for the probe transmission changes which corresponds to a red-shift of the 1s,1 polariton resonance. For the $\mathbf{e}_+\mathbf{e}_+$ configuration a clear blue-shift is observed for the 1s,1 polariton resonance. A similar dependence on the light polarization has been reported for the differential probe absorption around the 1s exciton resonance in a quantum-well system in Ref. 20.

Coulomb interaction of polaritons in states with different spatial distribution in the z-direction plays an important role for the observed probe transmission changes in Fig. 7.3. In the following, the $\mathbf{e}_+\mathbf{e}_-$ configuration is chosen for its analysis since it allows

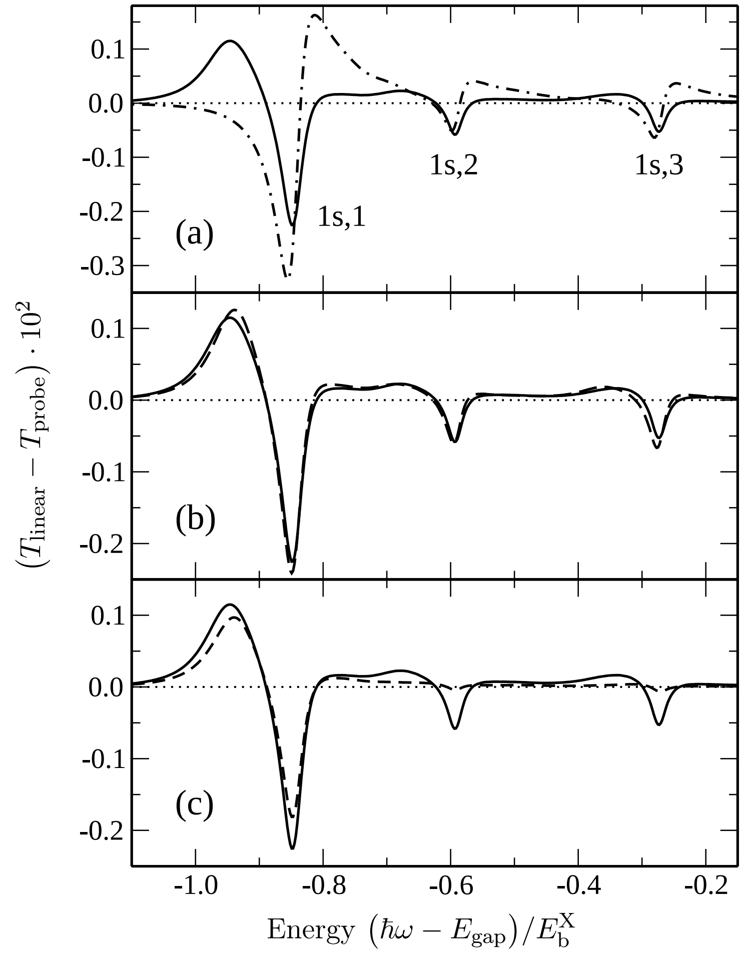

Figure 7.3: (a) Differential probe transmission for opposite circular $\mathbf{e}_{+}\mathbf{e}_{-}$ configuration (solid line) and co-circular $\mathbf{e}_{+}\mathbf{e}_{+}$ configuration (dashed-dotted line). (b) Differential probe transmission for $\mathbf{e}_{+}\mathbf{e}_{-}$ configuration including all Coulomb terms (solid line, same as solid line in (a) and (c)), and diagonal Coulomb interaction with respect to the internal exciton quantum numbers in the two-exciton product basis (dashed line). (c) No Coulomb interaction of different excitons (dashed line).

the exclusive investigation of biexcitonic correlations: For the $\mathbf{e}_{+}\mathbf{e}_{-}$ configuration the changes in the probe transmission are determined by biexcitonic correlations only; no mean-field effects contribute according to the equation of motion (6.14) in Section 6.4. In this configuration, the two dipole-allowed interband transitions (6.2) are exclusively excited by the opposite circularly polarized pump and probe pulses. On the Hartree-Fock level, both subsystems $+, -$ would be decoupled which would result in vanishing pump-induced transmission changes for the probe pulse.

The solid line in Fig. 7.3 (b) shows the transmission changes with full Coulomb interaction taken into account. The dashed line represents the result where only Coulomb interaction has been taken into account that is diagonal with respect to the internal exciton quantum numbers n, m of the two excitons contributing to the two-exciton product states in Eq. (5.11). Off-diagonal elements in the two-exciton Coulomb interaction

(5.15) and (5.16) have been neglected in the calculation, compare the discussions in Section 5.3. Only slight changes in the probe transmission are observed compared to the result with full Coulomb interaction (solid line). But note that despite the considerably large spectral separation of the exciton states for a layer thickness of $5\,\mathrm{a}_0^{\mathrm{X}}$, here, the biexciton binding energy is decreased by about $10\,\%$ neglecting off-diagonal Coulomb matrix elements in the two-exciton product basis as already discussed in Section 5.3.2.

The dashed line in Fig. 7.3 (c) shows the result where all Coulomb terms coupling excitons in different states n, m have artificially been turned off. According to the notation introduced in Section 5.3.1, inter-site and off-diagonal Coulomb matrix elements have been neglected in this calculation. We encounter only a slight quantitative change of the probe transmission around the lowest polariton resonance (1s,1) whereas for the higher resonances (1s,2 and 1s,3) the influence of the pump pulse almost vanishes. Therefore, Coulomb interaction between different exciton states is the main source for transmission changes around higher polariton resonances. Thinking in terms of two-exciton product states, due to the comparatively large oscillator strength of the exciton ground state (1s,1), the contributions from biexciton states which involve the exciton ground state are dominant in the nonlinear optical spectra. Contributions from biexciton states exclusively involving the excited exciton states (1s,2 and 1s,3) are much less pronounced. With increasing layer thickness higher polariton resonances become more important due to their decreasing energy level separation.

7.1.3. Four Wave Mixing

The evaluation of four wave mixing singals in this section are based on the equations of motion for the third order material polarization given in Section 6.5. The diffracted four wave mixing signal is observed in the $2\mathbf{k}_2-\mathbf{k}_1$ direction and is exclusively sensitive to third order nonlinearities in the optically induced material polarization. It is not superimposed by a linear background transmission of one of the incoming pulses.

Results are presented for the GaAs model system with a layer thickness of $5\,\mathrm{a}_0^{\mathrm{X}}$ as in the previous sections. To give a comparison to a quasi two-dimensional quantum-well system, results are also shown for a layer thickness of $1\,\mathrm{a}_0^{\mathrm{X}}$. Four wave mixing signals are analyzed as a function of the delay time t_{del} between the two incoming light pulses for different polarization states of these pulses. The detection is not sensitive to the polarization state of the diffracted signal in $2\mathbf{k}_2-\mathbf{k}_1$ direction. Again 120 fs laser pulses are applied with the same spectral shape as displayed in Fig. 7.1 (a). For the $5\,\mathrm{a}_0^{\mathrm{X}}$ system, both pulses are centered at an excitation energy of -0.6 in excitonic units. The energy scale for the quantum-well with $1\,\mathrm{a}_0^{\mathrm{X}}$ thickness is shifted to higher values due to the confinement of the carrier motion perpendicular to the quantum-well. Therefore, for this system, the pulses are centered on the spectral position of the exciton resonance at 7.71 in excitonic units.

Results are displayed in Fig. 7.4 for co-circular $\mathbf{e}_+\mathbf{e}_+$ polarization of the two incident light pulses, in Fig. 7.5 for co-linear $\mathbf{e}_x\mathbf{e}_x$ polarization, and in Fig. 7.6 for cross-linear $\mathbf{e}_x\mathbf{e}_y$ polarization. The contour plots show the spectrally resolved four wave mixing

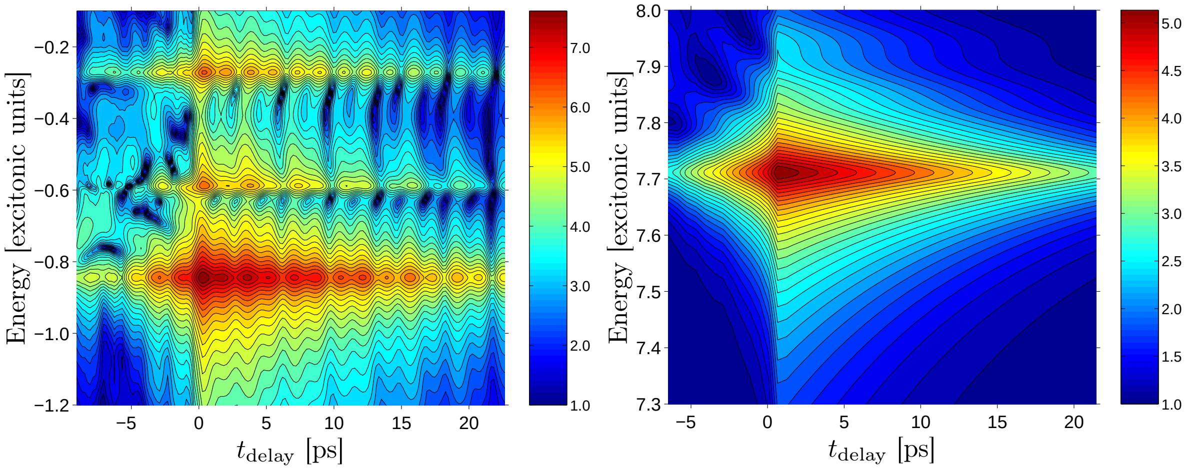

Figure 7.4: Left: Contour plot of the spectrally resolved four wave mixing intensity in co-circular $\mathbf{e}_+\mathbf{e}_+$ configuration as a function of the delay time t_{delay} between the two incoming light pulses for a GaAs layer with thickness of $5\,\mathrm{a}_0^{\mathrm{X}}$. The color coding represents the four wave mixing intensity in arbitrary units on a logarithmic scale according to the color bar. The energy scale on the vertical axis is chosen in excitonic units according to the horizontal axis in Fig. 7.1. Right: Same as figure on the left but for a layer thickness of $1\,\mathrm{a}_0^{\mathrm{X}}$.

intensity as a function of the delay time t_{del}. The color coding represents the magnitude of the four wave mixing intensity on a logarithmic scale. On the left of each figure, the results for $5\,\mathrm{a}_0^{\mathrm{X}}$ layer thickness are depicted and on the right the corresponding results for the quantum-well system with $1\,\mathrm{a}_0^{\mathrm{X}}$ layer thickness.

For the $5\,\mathrm{a}_0^{\mathrm{X}}$ sample, for all the three configurations a four wave mixing signal is detected at the spectral position of the three polariton resonances which are already present in the linear transmission spectrum in Fig. 7.1 (a). Qualitatively, around the spectral position of the lowest polariton resonance a similar polarization dependence of the four wave mixing signal is observed that is found for the $1\,\mathrm{a}_0^{\mathrm{X}}$ quantum-well system: (i) For the $\mathbf{e}_+\mathbf{e}_+$ configuration in Fig. 7.4 no resonant contribution to the signal is detected at the spectral position of the bound biexciton state, according to its electronic singlet configuration as already discussed in the previous sections. A fast decay of the signal for negative delay times $t_{\text{del}} < 0$ is found. (ii) For the $\mathbf{e}_x\mathbf{e}_x$ configuration in Fig. 7.5 the signal is dominated by contributions at the spectral positions of the polariton resonances while the signal at the spectral position of the bound biexciton resonance is weak in this configuration. (iii) For the $\mathbf{e}_x\mathbf{e}_y$ configuration in Fig. 7.6 a resonant contribution to the four wave mixing signal is visible at the spectral position of the bound biexciton resonance spectrally below the lowest polariton resonance. This feature is much more pronounced for the $1\,\mathrm{a}_0^{\mathrm{X}}$ system because of the larger biexciton binding energy and the smaller spectral window which is displayed in the figures. But, comparing Figs. 7.5 and 7.6, also for the $5\,\mathrm{a}_0^{\mathrm{X}}$ system a qualitative difference in the four wave mixing signals spectrally below the lowest polariton resonance is clearly visible. It can be attributed to the excitation of the bound biexciton resonance. A similar polarization dependence of four wave mixing signals has experimentally and theoretically been observed for a ZnSe quantum-well system in Refs. 76, 77.

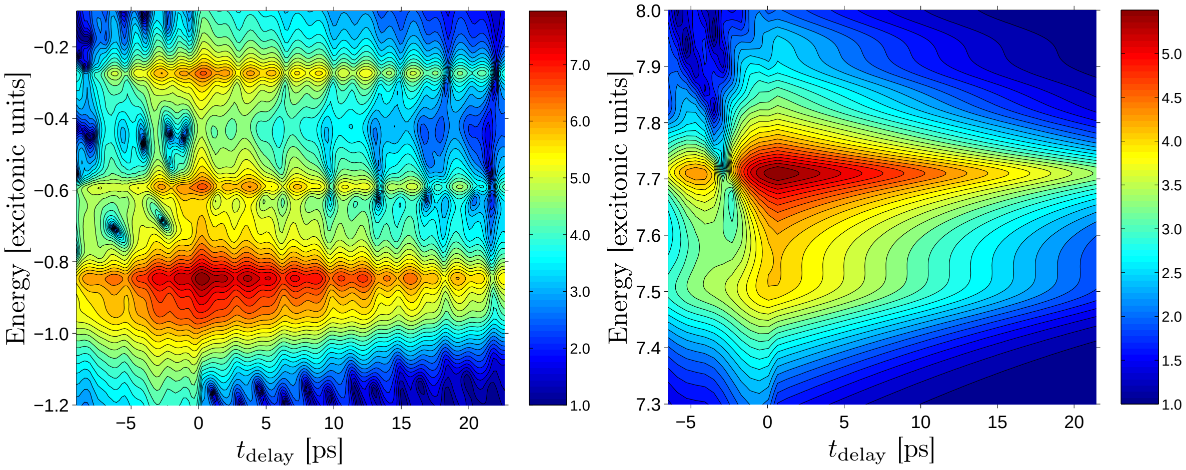

Figure 7.5: Same as Fig. 7.4 but for co-linear $\mathbf{e}_x\mathbf{e}_x$ polarization of the two incoming light pulses.

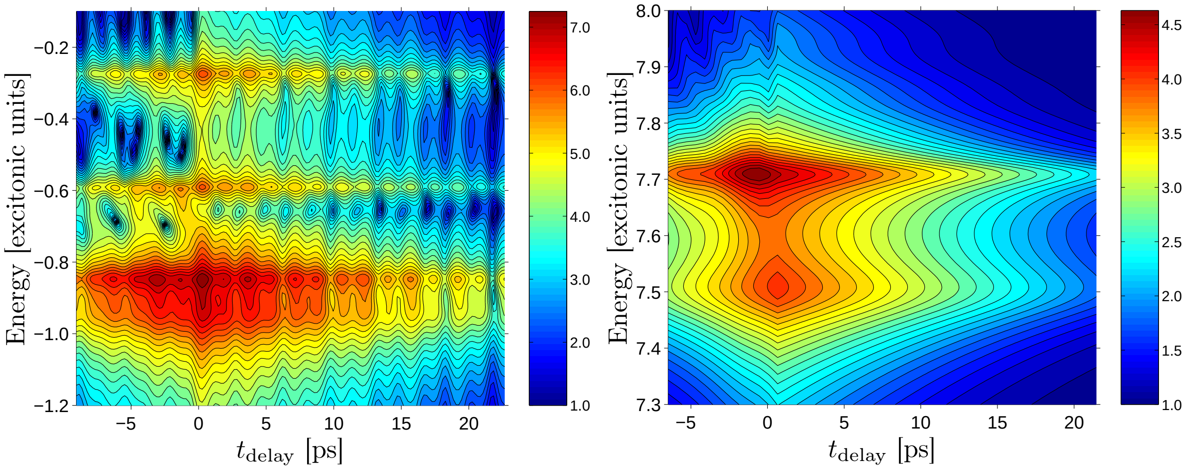

Figure 7.6: Same as Fig. 7.4 but for cross-linear $\mathbf{e}_x\mathbf{e}_y$ polarization of the two incoming light pulses.

Going more into detail, distinct differences in the four wave mixing spectra of both systems are observed. For the system with $5\,\mathrm{a}_0^{\mathrm{X}}$ layer thickness we find that the detected signal at the spectral position of each polariton resonance is strongly influenced by the excitation of the other resonances. In the displayed spectral range the signal is periodically modulated in the delay time t_{delay}. These oscillations are absent for the quantum-well system since only a single excitonic resonance contributes to the four wave mixing signal. The periods of the oscillations for $5\,\mathrm{a}_0^{\mathrm{X}}$ are determined by the energy separation of the different polariton resonances. Two main contributions to these oscillations are observed. The periods can be attributed to the energy difference between first and third polariton resonance and to the energy difference between the first and the second or the second and the third resonance, respectively. For higher excitation intensities oscillations have been observed for a quantum-well with a period in the delay time t_{delay} that could be attributed to the energy difference between the spectral position of the exciton resonance and the spectral position of the bound biexciton resonance.[29,76] Qualitative differences are observed for the four wave mixing signals around the spectral positions of the different polariton resonances for the $5\,a_0^X$ sample in Figs. 7.4 to 7.6. In particular, the signals in the vicinity of the second and the third resonance are superimposed by contributions that arise from the excitation of exciton-exciton scattering states involving the exciton ground state as well.

Compared to a quantum-well system, the resulting four wave mixing spectra for $5\,a_0^X$ exhibit a more complicated structure due to the excitation of several polariton resonances in the investigated spectral range. However, the qualitative polarization dependence of the four wave mixing signal in the vicinity of the lowest polariton resonance is similar to that of the quantum-well system. Nevertheless, an interpretation in terms of isolated polariton resonances is not valid beyond the quantum-well limit since a strong interaction of the contributions from different polaritonic resonances over the whole spectral range is observed.

7.2. Theory vs. Experiment

The theory presented in the preceding part of this work provides for the first time a rigorous microscopic description of biexcitonic nonlinearities and propagation effects in semiconductor heterostructures with a finite spatial extension. To conclude the discussions, a direct theory-experiment comparison of nonlinear polariton spectra has been initiated. Especially the ZnSe/ZnSSe heterostructure with a ZnSe layer thickness of 20 nm, already investigated in Section 4.2 in the linear optical regime, is well-suited for the application of the presented theory for nonlinear polariton propagation. Being the conceptually simplest configuration for the measurement of nonlinear spectra, the transmission through the sample is investigated for a single laser pulse with variable light intensity.

The experiments are performed using a frequency-doubled titanium-sapphire laser system. The 110 fs laser pulses are generated with a repetition rate of 82 MHz. Pockels-cells are used for the calibration of the polarization state of the laser pulses. The spectrometer and CCD device allow the detection of the signal over a wave length range of about 11 nm with a spectral resolution of $\Delta\lambda \lesssim 0.04\,\text{nm}$. The samples are prepared and handled as already described in Section 4.2.1. The optical experiments have been performed by Iryna Kudyk in the Semiconductor Optics Group of the Institute for Solid State Physics at the University of Bremen.

The measured transmission spectra are shown in Fig. 7.7 (a) for a pulse energy of 1.2 pJ (dashed-dotted line) and for 12.2 pJ for circular (dashed line) and linear (solid line) light polarization. A slight constant offset of about 0.1 in the nonlinear transmission spectra is observed. The reason for its occurrence is not completely clear by now, but it might be caused by slight fluctuations in the laser pulse intensity during the measurement. However, the structure of the transmission changes which are depicted in Fig. 7.7 (b) is not influenced by it. Therefore it does not affect the following discussion of the results at all. The spectral shape of the laser pulse is included as a dotted line.

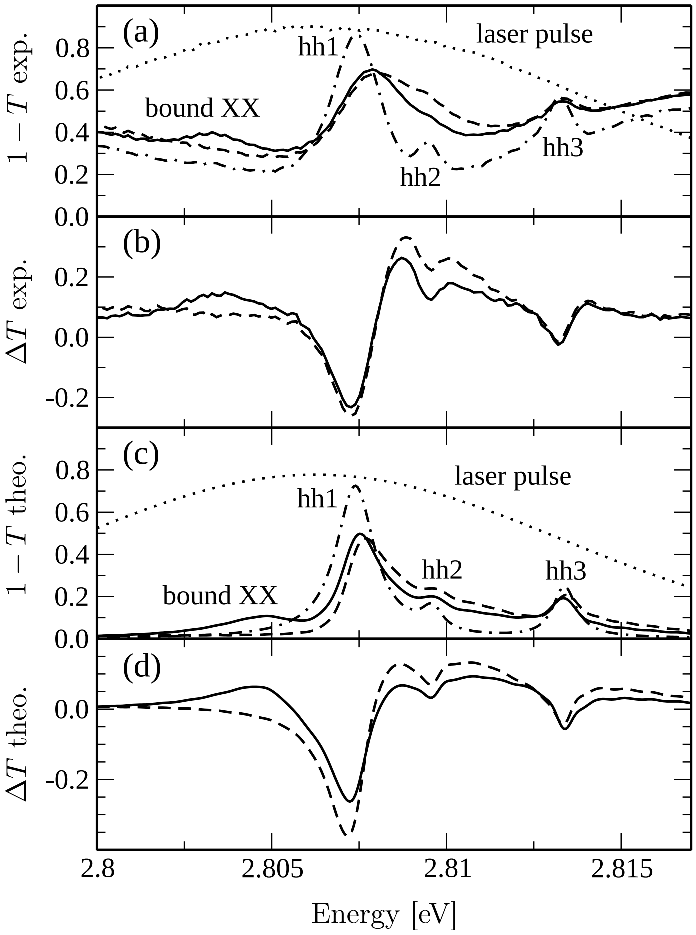

Figure 7.7: (a) Experimental linear (pulse energy 1.2 pJ) transmission spectrum for the 20 nm ZnSe sample (dashed-dotted line) and spectral shape of the 110 fs laser pulse (dotted line). Solid and dashed line show the nonlinear transmission spectra for a pulse energy of 12.2 pJ for linear (solid) and circular (dashed) light polarization. (b) Experimental transmission change $\Delta T = T_{\text{linear}} - T_{\text{nonlinear}}$ for the pulse intensity in the nonlinear regime corresponding to the data in (a). The solid line shows the result for linear and the dashed line for circular light polarization. (c), (d) Theoretical results corresponding to (a) and (b), respectively.

According to the data in Fig. 7.7 (a) the transmission changes for nonlinear pulse intensities are displayed in Fig. 7.7 (b) for linear (solid line) and circular (dashed line) light polarization. Three polariton resonances are observed in the linear transmission spectrum (dashed-dotted line). In analogy to the theoretical results presented in Section 7.1.1 a bound biexciton (bound XX) resonance is only observed in the nonlinear transmission for linear light polarization (solid line). The nonlinearities at the spectral position of the hh1 polariton resonance and above are more pronounced for circular light polarization.

The theoretical results corresponding to the experimental ones are displayed in Figs. 7.7 (c), (d). Material parameters for the calculation are taken from Section 4.2. The light intensity is chosen according to the observed nonlinearities in the experimental spectra. For the resulting rather high pulse intensities a self-consistent evaluation of the material equations given in Section 6.2 up to arbitrary order in the optical fields is required here as discussed at the end of Section 6.2. Consequently, the theoretical description can not be performed in the $\chi^{(3)}$-limit here, since a subclass of higher order nonlinearities is automatically included in the calculations. However, this way, optical spectra can also be described for higher excitation intensities in terms of the present theory.

The nonlinear transmission spectra exhibit all the features that have already been predicted by the evaluation of the theory in Section 7.1.1. A bleaching of the polariton resonances is observed, and a broad background on their higher energy side, as well as the bound biexciton resonance (bound XX) spectrally below the hh1 polariton resonance. The experimental results are in very good agreement with our theoretical predictions. Especially the polarization dependence of the nonlinear transmitted signals is reproduced by the measurements. The biexciton binding energy is slightly underestimated by the evaluation in the exciton basis as already discussed in Section 5.3.2. Nevertheless, the great advantage of the approach applied here is the simultaneous inclusion of the bound biexciton state and of the exciton-exciton scattering continuum in the theoretical description. The latter one is essential to reproduce the broad background on the higher energy side of the polaritonic resonances in the nonlinear transmission spectra.

In this section, the microscopic theory for nonlinear polariton propagation has successfully been applied to a realistic ZnSe/ZnSSe heterostructure. The applicability to realistic heterostructures has been achieved by a formulation of the excitonic and biexcitonic problem with respect to the exciton eigenbasis. The physical boundary conditions of the system that strongly influence the optical spectra are fully included in the theoretical description. For transmission spectra of a single laser pulse with linear and circular light polarization excellent agreement of theoretical and experimental results has been demonstrated.

Conclusions and Outlook

The dynamics of coherent excitations in semiconductors induced by optical fields was investigated in a regime where propagation effects play an important role. The presence of surfaces or interfaces in realistic heterostructures results in a non-local response function for the optical excitations. This non-locality massively complicates the solution of the coupled light-matter problem. In particular, in the linear optical regime it prevents an analytical solution of the well-known polariton problem. To circumvent its complicated solution, different approximation schemes have been developed in the past, which do not take into account the microscopic structure of the situation. However, in this work, a fully microscopic description of polaritons was formulated and analyzed in detail. Within this framework, the often used macroscopic approach to the polariton problem based on Pekar's ABCs was investigated and its shortcomings were discussed. Experiments have been initiated and performed during the preparation of this work which allowed a direct theory-experiment comparison of transmission spectra that are strongly influenced by polaritonic effects. The first part of this work was dedicated to the linear optical regime whereas the second part focused on nonlinear optical excitations.

In the first part of this work, a formulation of the non-local optical response function in terms of exciton eigenstates was presented. This approach makes a microscopic description of the polariton problem much more feasible for the application to realistic semiconductor heterostructures. In contrast to previous approaches in the literature, the exciton eigenfunctions were directly determined according to the confinement geometry and individually fulfill the physical boundary conditions of the investigated systems. In the linear optical regime, this formulation allows the individual excitation of polariton resonances as long as they are spectrally well-separated from other resonances in the optical spectra. A series of high quality ZnSe/ZnSSe heterostructures with different thicknesses of the ZnSe layer has been grown for the analysis of experimental transmission spectra. These samples made a detailed theory-experiment comparison possible. The ZnSe/ZnSSe heterostructures served as a typical example to study polariton propagation in heterostructures which provide shallow confinement potentials for the motion of electrons and holes. Excellent agreement with experimental results was achieved by the inclusion of finite-height potential barriers for the carrier motion as well as Fabry-Perot effects for the optical field in the theoretical description.

In the shallow-confinement situation the absence of polarization-free dead-layers at the ZnSe/ZnSSe interfaces was found. Furthermore, our investigations demonstrated why macroscopic models based on Pekar's ABCs seemed to work for the description of polaritons in ZnSe/ZnSSe heterostructures in the past. The discussions can also be extended to other semiconductor material systems. The importance of a microscopic description of the polariton problem has clearly been demonstrated.

In the second part of this work, an extension of the microscopic theory for polariton propagation to the description of nonlinear optical properties was presented. The inherent many-particle hierarchy in the dynamics of the optically excited electronic system was truncated in terms of the dynamics-controlled truncation formalism. A theory has been derived that incorporates both, propagation effects as well as optically induced excitonic and biexcitonic nonlinearities in the semiconductor material. The formulation is suitable for the description of optical experiments on ultra short time scales and allows to analyze the dynamics of coherent many-particle effects coupled to the propagating light fields on a microscopic level. The evaluation of the presented $\chi^{(3)}$-theory including the excitonic and the biexcitonic problem in the confinement geometry is a numerical challenge. An efficient formulation was achieved by the transition to the exciton eigenbasis. The exciton eigenstates contain the physical boundary conditions for excitons and biexcitons in the investigated heterostructures. The numerical calculations within the exciton basis remain very time-consuming but an evaluation of the theory was achieved by efficient parallelization on modern supercomputer systems. The theory was applied to the calculation of nonlinear transmission spectra which were analyzed for single light pulses as well as in pump and probe and in four wave mixing geometry. Pronounced biexcitonic signatures were found in the optical transmission spectra. This clearly demonstrates the importance of higher order Coulomb correlations in the theoretical description. Depending on the polarization state of the exciting light fields the bound biexciton resonance as well as the exciton-exciton scattering states strongly contribute to the nonlinear optical response of the system. In contrast to the findings in linear optics, exciton-exciton Coulomb interaction turns out to strongly couple different polariton modes in the nonlinear optical regime. In order to confirm the important theoretical results, the measurement of nonlinear optical transmission spectra for a 20 nm ZnSe sample has been initiated and performed during the preparation of this work. The application of our theory to this heterostructure shows excellent agreement with the experimental results. In advance to the measurements, especially the polarization dependence of the optically induced nonlinearities has been predicted by the theory.

The presented theory allows for the first time the simultaneous analysis of optically induced many-particle correlations and propagation effects beyond the quasi two-dimensional quantum-well limit. In this work, a direct theory-experiment comparison has been presented for the propagation of a single light pulse. Further interesting results can be expected from a forthcoming theory-experiment comparison in pump and probe and in four wave mixing configuration. Another application for the presented theory represents the coherent control of excitonic and biexcitonic polarizations which provides a wide spectrum of experimental applications. For the analysis of the coherent optical regime which was investigated in this work, the dynamics-controlled truncation formalism provides an excellent description of the system dynamics. To develop a theory for the description of optical excitations with higher excitation densities or exceeding the ultra short time scales, the non-equilibrium Green's function technique[32] can be applied. In this way an inclusion of incoherent contributions to the carrier occupation functions and the inclusion of dephasing processes on a microscopic level is possible. Nevertheless, the resulting theory would hardly be applicable to the system investigated in this work because of its strongly increased numerical effort. However, besides this system, semiconductor heterostructures with a reduced dimensionality such as quantum-wires and especially quantum-dots attract more and more attention for technological applications in optoelectronic devices. The more general theoretical concepts applied in this work, for instance the transition to the exciton eigenbasis and the dynamics-controlled truncation scheme, can directly be transferred to the analysis of these low-dimensional systems.

A. Calculation of Transition Amplitudes

A.1. Coulomb Matrix Elements

To deduce the Coulomb matrix elements (2.6) used for the slab geometry we start with the Coulomb interaction in momentum space:

$$V_{\tilde{\mathbf{q}}} = \frac{e_0^2}{\varepsilon_0 \varepsilon_\mathrm{r}} \frac{1}{\tilde{\mathbf{q}}^2} \quad \text{with} \quad \tilde{\mathbf{q}} = (q_x, q_y, q_z)\,.$$

Fourier transformation applied to the z-direction yields the desired representation of the Coulomb matrix elements in Eq. (2.6),

$$\begin{aligned} V_{\mathbf{q}}^{zz'} = \int \frac{\mathrm{d}q_z}{2\pi}\, \mathrm{e}^{-iq_z(z-z')} \frac{e_0^2}{\varepsilon_0\varepsilon_\mathrm{r}} \frac{1}{\tilde{\mathbf{q}}^2} = \int \frac{\mathrm{d}q_z}{2\pi}\, \mathrm{e}^{-iq_z(z-z')} \frac{e_0^2}{\varepsilon_0\varepsilon_\mathrm{r}} \frac{1}{\mathbf{q}^2 + q_z^2} \\ = \frac{e_0^2}{2\varepsilon_0 n_\mathrm{bg}^2} \frac{\mathrm{e}^{-|\mathbf{q}||z-z'|}}{|\mathbf{q}|}\,, \end{aligned}$$

with the in-plane momentum $\mathbf{q} = (q_x, q_y)$ and $\varepsilon_\mathrm{r} = n_\mathrm{bg}^2$. Here the identity[45]

$$\int \mathrm{d}k\, \mathrm{e}^{-ikx} \frac{1}{a^2 + k^2} = \frac{\pi}{a} \mathrm{e}^{-a|x|}$$

has been used for the integration. The Fourier coefficients $V_{kk'}^{mm'}(z_\mathrm{e} - z_\mathrm{h})$ in the in-plane angular momentum decomposition

$$V_{\mathbf{k}-\mathbf{k}'}^{z_\mathrm{e} z_\mathrm{h}} = \frac{1}{2\pi} \sum_{mm'} \mathrm{e}^{-im\phi_k} V_{kk'}^{mm'}(z_\mathrm{e} - z_\mathrm{h}) \mathrm{e}^{im'\phi_{k'}}$$

of the Coulomb matrix elements in Eq. (3.6), are given by

$$\begin{aligned} V_{kk'}^{mm'}(z_\mathrm{e} - z_\mathrm{h}) =& \frac{1}{2\pi} \int_0^{2\pi} \mathrm{d}\phi_k \int_0^{2\pi} \mathrm{d}\phi_{k'}\, \mathrm{e}^{im\phi_k} \mathrm{e}^{-im'\phi_{k'}} V_{\mathbf{k}-\mathbf{k}'}^{z_\mathrm{e} z_\mathrm{h}} \\ =& \delta_{mm'} \frac{e_0^2}{2\varepsilon_0 n_\mathrm{bg}^2} \int_0^{2\pi} \mathrm{d}\phi\, \mathrm{e}^{im'\phi} \frac{\mathrm{e}^{-|\mathbf{k}-\mathbf{k}'||z_\mathrm{e} - z_\mathrm{h}|}}{|\mathbf{k}-\mathbf{k}'|} = \delta_{mm'} V_{kk'}^{mm'}(z_\mathrm{e} - z_\mathrm{h})\,, \end{aligned}$$

with $|\mathbf{k} - \mathbf{k}'| = \sqrt{k^2 + k'^2 - 2kk' \cos\phi}$ in the last line.

A.2. The Dynamics-Controlled Truncation

This chapter is dedicated to the Dynamics-Controlled Truncation (DCT) of expectation values. This technique is used in Section 5.1 to overcome the many-particle hierarchy problem in the equation of motion for the excitonic polarization. For a proper truncation of the many-particle hierarchy in a certain order in the external field it is necessary to characterize each relevant expectation value by its leading order in the external field. Thinking of a power series in the external field for each expectation value, the leading order is the first non-vanishing term in the expansion and therefore the term where the lowest order of the external field appears.

First of all we consider an expectation value $\langle \dots \rangle$ of a normal-ordered product of electron and hole creation and annihilation operators where electron and hole operators always occur pairwise together. For this class of expectation values the leading order in the external field can easily be identified. The second step is to show that all other expectation values can be expressed in terms of expectation values with pairwise occurrence of electron and hole operators and an additional contribution of higher order in the external field. In order not to overburden the notation, the quantum numbers of the system are abbreviated by $e_i = \{e, \mathbf{k}, z_\mathrm{e}\}$, $h_i = \{h, \mathbf{k}, z_\mathrm{h}\}$ for the general discussion of the DCT scheme that is not limited to the special geometry considered in this work.

For instance, we consider an expectation value $\langle \psi^{e_1 \dagger} \psi^{h_1 \dagger} \psi^{h_2} \psi^{e_2} \psi^{h_3} \psi^{e_3} \rangle$ which contains one pair of electron and hole creation and two pairs of annihilation operators. The system is in its ground state prior to an optical excitation. Since the Coulomb interaction (2.5) in the system Hamiltonian (2.1) conserves the particle numbers in conduction and valence bands individually, the system stays in its ground state as long as it is not optically excited. This essential assumption is valid for a semiconductor material since Coulomb-induced interband transitions that change the particle numbers in valence and conduction bands are very unlikely because of the large band-gap energy. Therefore, the time evolution of the many-particle state in the interaction picture is determined by the action of the time evolution operator $\mathcal{S}$ on the ground state $|0\rangle$ of the electronic many-particle system:

$$\langle \psi^{e_1 \dagger} \psi^{h_1 \dagger} \psi^{h_2} \psi^{e_2} \psi^{h_3} \psi^{e_3} \rangle = \langle 0 | \mathcal{S}^\dagger(t,t_0) \bar{\psi}^{e_1 \dagger} \bar{\psi}^{h_1 \dagger} \bar{\psi}^{h_2} \bar{\psi}^{e_2} \bar{\psi}^{h_3} \bar{\psi}^{e_3} \mathcal{S}(t,t_0) | 0 \rangle \,. \tag{A.1}$$

Here $\bar{\psi}$ denotes operators in the interaction picture[26] that obey the free time-evolution determined by the kinetic part and the Coulomb interaction in the Hamiltonian (2.1). The time evolution of the many-particle states is given by the coupling to the external optical field entering the time-evolution operator $\mathcal{S}$ which obeys the differential equation

$$i\hbar \frac{\partial}{\partial t} \mathcal{S}(t,t_0) = \bar{\mathcal{H}}_\mathrm{dipole}(t) \mathcal{S}(t,t_0) \,,$$

with the dipole Hamiltonian

$$\bar{\mathcal{H}}_\mathrm{dipole}(t) = - \sum_\mathrm{eh} \left[\bar{\psi}^{\mathrm{e}\dagger} \bar{\psi}^{\mathrm{h}\dagger} \mathbf{d}_\mathrm{eh} \mathbf{E}(t) + \bar{\psi}^\mathrm{h} \bar{\psi}^\mathrm{e} \mathbf{d}^*_\mathrm{eh} \mathbf{E}(t) \right] . \tag{A.2}$$

Formal integration with the condition $\mathcal{S}(t_0, t_0) = 1$ yields the integral equation

$$\mathcal{S}(t, t_0) = 1 + \frac{1}{i\hbar} \int\limits_{t_0}^{t} \mathrm{d}t_1 \, \bar{\mathcal{H}}_{\mathrm{dipole}}(t_1) \mathcal{S}(t_1, t_0) \,. \tag{A.3}$$

An iterative solution of this equation is convenient. Using

$$\mathcal{S}(t_1, t_0) = 1 + \frac{1}{i\hbar} \int\limits_{t_0}^{t_1} \mathrm{d}t_2 \, \bar{\mathcal{H}}_{\mathrm{dipole}}(t_2) \mathcal{S}(t_2, t_0)$$

for $t_1 \leq t$, the first step of the iteration reads

$$\begin{aligned} \mathcal{S}(t, t_0) = 1 &+ \frac{1}{i\hbar} \int\limits_{t_0}^{t} \mathrm{d}t_1 \, \bar{\mathcal{H}}_{\mathrm{dipole}}(t_1) \\ &+ \frac{1}{(i\hbar)^2} \int\limits_{t_0}^{t} \mathrm{d}t_1 \int\limits_{t_0}^{t_1} \mathrm{d}t_2 \, \bar{\mathcal{H}}_{\mathrm{dipole}}(t_1) \bar{\mathcal{H}}_{\mathrm{dipole}}(t_2) \mathcal{S}(t_2, t_0) \,. \end{aligned}$$

Further iteration yields the final result that can be written in a compact notation,[78]

$$\mathcal{S}(t, t_0) = \hat{T} \exp\left(- \frac{i}{\hbar} \int\limits_{t_0}^{t} \mathrm{d}t' \, \bar{\mathcal{H}}_{\mathrm{dipole}}(t') \right) , \tag{A.4}$$

with the exponential given by its definition as a power series. $\hat{T}$ is the time-ordering symbol.

To obtain a non-vanishing contribution to the expectation value (A.1), the action of the time-evolution operator $\mathcal{S}$ on the ground state $|0\rangle$ and the action of the six electron and hole operators and of $\mathcal{S}^\dagger$ must cancel each other to bring the system back to the ground state $|0\rangle$ again. Note, that the electron and hole operators enter the Coulomb interaction (2.5) always in pairs of creation and annihilation operators. So the free time evolution of the operators $\bar{\psi}$ does not cause the electronic system to leave its ground state. Having in mind the structure of $\bar{\mathcal{H}}_{\mathrm{dipole}}$ (A.2) and reading the exponential in the time evolution operator (A.4) as a power series, the first non-vanishing term in Eq. (A.1) is of order $\mathcal{O}(E^3)$. The expansion of $\mathcal{S}$ contributes at least in second order and that of $\mathcal{S}^\dagger$ at least in first order in $\bar{\mathcal{H}}_{\mathrm{dipole}}$ (A.2) and therefore in the electric field amplitude $E(t)$. All contributions beyond the third order are at least of fifth order in the optical field. Therefore, the leading contribution to the considered expectation value (A.1) is of third order in the optical field, all other contributions are of higher order resulting from further expansion of the time evolution operators $\mathcal{S}$, $\mathcal{S}^\dagger$.

Insertion of a complete set of Fock states in between creation and annihilation operators yields[a)]

$$
\begin{aligned}
&\langle \psi^{e_1\dagger}\psi^{h_1\dagger}\psi^{h_2}\psi^{e_2}\psi^{h_3}\psi^{e_3}\rangle \\
&= \sum_{\mathrm{F}} \langle 0|\mathcal{S}^\dagger(t,t_0)\bar{\psi}^{e_1\dagger}\bar{\psi}^{h_1\dagger}\mathcal{S}(t,t_0)|F\rangle\langle F|\mathcal{S}^\dagger(t,t_0)\bar{\psi}^{h_2}\bar{\psi}^{e_2}\bar{\psi}^{h_3}\bar{\psi}^{e_3}\mathcal{S}(t,t_0)|0\rangle \\
&= \langle 0|\mathcal{S}^\dagger(t,t_0)\bar{\psi}^{e_1\dagger}\bar{\psi}^{h_1\dagger}\mathcal{S}(t,t_0)|0\rangle\langle 0|\mathcal{S}^\dagger(t,t_0)\bar{\psi}^{h_2}\bar{\psi}^{e_2}\bar{\psi}^{h_3}\bar{\psi}^{e_3}\mathcal{S}(t,t_0)|0\rangle + \mathcal{O}(E^5) \\
&\qquad\qquad\qquad = \langle \psi^{e_1\dagger}\psi^{h_1\dagger}\rangle\langle \psi^{h_2}\psi^{e_2}\psi^{h_3}\psi^{e_3}\rangle + \mathcal{O}(E^5)\,. \qquad \text{(A.5)}
\end{aligned}
$$

In the leading order, this yields the factorization of (A.1) which is exact with respect to the lowest contributing order in the optical field, here the third order. Not only third order contributions are considered by the factorization. A certain class of higher order contributions is included in the factorized expectation value (A.5) while others of higher order are neglected. The factorization (A.5) is exact being only interested in third order contributions because none of them is neglected here. Only the ground state contributes to the lowest order in the optical field, all contributions involving excited states of the system are at least of fifth order. A consistent factorization beyond the leading order (here beyond the third order) is possible but more involved, compare Ref. 19. In fifth order, it brings into play expectation values of up to six operators whereas in third order we are left with at most four-operator expectation values. In general, the characterization of any expectation value by its leading order in the optical field is possible. In analogy to the given example it can be seen that the leading order of an arbitrary expectation value is always given by,[7]

$$
\langle \ldots \rangle = \mathcal{O}(E^m) \qquad m = \max\{n_{\mathrm{e}}, n_{\mathrm{h}}\}\,, \qquad \text{(A.6)}
$$

while n_{e} is the number of electron operators and n_{h} the number of hole operators contained in the expectation value $\langle \ldots \rangle$, respectively. The leading order factorization (A.5) in terms of products of polarization-like expectation values can directly be applied if electron and hole operators occur pairwise. To extend the discussion to non polarization-like expectation values, in a second step, the particle number conservation in the system is used. The particle number operator $\hat{N}$ in the electron-hole picture is given by:

$$
\hat{N} = \sum_{\mathrm{e}\mathbf{k}} \int \mathrm{d}z\, \psi^{\mathrm{e}\dagger}_{\mathbf{k}}(z)\psi^{\mathrm{e}}_{\mathbf{k}}(z) + \sum_{\mathrm{h}\mathbf{k}} \int \mathrm{d}z \Big(1 - \psi^{\mathrm{h}\dagger}_{\mathbf{k}}(z)\psi^{\mathrm{h}}_{\mathbf{k}}(z)\Big)\,.
$$

[a)] Insertion of the Fock states at another position in the expectation value would automatically yield contributions beyond the leading order.

Insertion into the electron occupation function yields:

$$
\begin{aligned}
\left\langle \psi^{\mathrm{e}'\dagger}_{\mathbf{k}}(z_{\mathrm{h}})\psi^{\mathrm{e}}_{\mathbf{k}}(z_{\mathrm{e}})\hat{N}\right\rangle =& N\left\langle \psi^{\mathrm{e}'\dagger}_{\mathbf{k}}(z_{\mathrm{h}})\psi^{\mathrm{e}}_{\mathbf{k}}(z_{\mathrm{e}})\right\rangle \\
=&\sum_{\mathrm{e}''\mathbf{k}'}\int \mathrm{d}z\,\left\langle \psi^{\mathrm{e}'\dagger}_{\mathbf{k}}(z_{\mathrm{h}})\psi^{\mathrm{e}}_{\mathbf{k}}(z_{\mathrm{e}})\psi^{\mathrm{e}''\dagger}_{\mathbf{k}'}(z)\psi^{\mathrm{e}''}_{\mathbf{k}'}(z)\right\rangle \\
&+\sum_{\mathrm{h}\mathbf{k}'}\int \mathrm{d}z\,\left\langle \psi^{\mathrm{e}'\dagger}_{\mathbf{k}}(z_{\mathrm{h}})\psi^{\mathrm{e}}_{\mathbf{k}}(z_{\mathrm{e}})\right\rangle \\
&-\sum_{\mathrm{h}\mathbf{k}'}\int \mathrm{d}z\,\left\langle \psi^{\mathrm{e}'\dagger}_{\mathbf{k}}(z_{\mathrm{h}})\psi^{\mathrm{e}}_{\mathbf{k}}(z_{\mathrm{e}})\psi^{\mathrm{h}\dagger}_{\mathbf{k}'}(z)\psi^{\mathrm{h}}_{\mathbf{k}'}(z)\right\rangle \\
=& N\left\langle \psi^{\mathrm{e}'\dagger}_{\mathbf{k}}(z_{\mathrm{h}})\psi^{\mathrm{e}}_{\mathbf{k}}(z_{\mathrm{e}})\right\rangle - \sum_{\mathrm{e}''\mathbf{k}'}\int \mathrm{d}z\,\left\langle \psi^{\mathrm{e}'\dagger}_{\mathbf{k}}(z_{\mathrm{h}})\psi^{\mathrm{e}''\dagger}_{\mathbf{k}'}(z)\psi^{\mathrm{e}}_{\mathbf{k}}(z_{\mathrm{e}})\psi^{\mathrm{e}''}_{\mathbf{k}'}(z)\right\rangle \\
&+\sum_{\mathrm{e}''\mathbf{k}'}\int \mathrm{d}z\,\left\langle \psi^{\mathrm{e}'\dagger}_{\mathbf{k}}(z_{\mathrm{h}})\psi^{\mathrm{e}''}_{\mathbf{k}'}(z)\right\rangle \delta_{\mathbf{k}\mathbf{k}'}\delta_{\mathrm{e}\mathrm{e}''}\delta(z-z_{\mathrm{e}}) \\
&-\sum_{\mathrm{h}\mathbf{k}'}\int \mathrm{d}z\,\left\langle \psi^{\mathrm{e}'\dagger}_{\mathbf{k}}(z_{\mathrm{h}})\psi^{\mathrm{h}\dagger}_{\mathbf{k}'}(z)\psi^{\mathrm{h}}_{\mathbf{k}'}(z)\psi^{\mathrm{e}}_{\mathbf{k}}(z_{\mathrm{e}})\right\rangle .
\end{aligned}
$$

For the electron occupation function directly follows:

$$
\begin{aligned}
\left\langle \psi^{\mathrm{e}'\dagger}_{\mathbf{k}}(z_{\mathrm{h}})\psi^{\mathrm{e}}_{\mathbf{k}}(z_{\mathrm{e}})\right\rangle =&\sum_{\mathrm{h}\mathbf{k}'}\int \mathrm{d}z\,\left\langle \psi^{\mathrm{e}'\dagger}_{\mathbf{k}}(z_{\mathrm{h}})\psi^{\mathrm{h}\dagger}_{\mathbf{k}'}(z)\psi^{\mathrm{h}}_{\mathbf{k}'}(z)\psi^{\mathrm{e}}_{\mathbf{k}}(z_{\mathrm{e}})\right\rangle \\
&+\sum_{\mathrm{e}''\mathbf{k}'}\int \mathrm{d}z\,\left\langle \psi^{\mathrm{e}'\dagger}_{\mathbf{k}}(z_{\mathrm{h}})\psi^{\mathrm{e}''\dagger}_{\mathbf{k}'}(z)\psi^{\mathrm{e}}_{\mathbf{k}}(z_{\mathrm{e}})\psi^{\mathrm{e}''}_{\mathbf{k}'}(z)\right\rangle .
\end{aligned}
$$

The leading order factorization (A.5) together with (A.6) and the in-plane homogeneity of the system yields:

$$
\begin{aligned}
\left\langle \psi^{\mathrm{e}'\dagger}_{\mathbf{k}}(z_{\mathrm{h}})\psi^{\mathrm{e}}_{\mathbf{k}}(z_{\mathrm{e}})\right\rangle =&\sum_{\mathrm{h}\mathbf{k}'}\int \mathrm{d}z\,\left\langle \psi^{\mathrm{e}'\dagger}_{\mathbf{k}}(z_{\mathrm{h}})\psi^{\mathrm{h}\dagger}_{\mathbf{k}'}(z)\right\rangle\left\langle \psi^{\mathrm{h}}_{\mathbf{k}'}(z)\psi^{\mathrm{e}}_{\mathbf{k}}(z_{\mathrm{e}})\right\rangle \delta_{\mathbf{k}\mathbf{k}'} + \mathcal{O}(E^4) \\
=&\sum_{\mathrm{h}}\int \mathrm{d}z\, p^{*\mathrm{e}'\mathrm{h}}_{(\mathbf{k},z_{\mathrm{h}},z)}p^{\mathrm{eh}}_{(\mathbf{k},z_{\mathrm{e}},z)} + \mathcal{O}(E^4)\,, \qquad \text{(A.7)}
\end{aligned}
$$

with

$$
p^{*\mathrm{e}'\mathrm{h}}_{(\mathbf{k},z_{\mathrm{h}},z)} = \left\langle \psi^{\mathrm{e}'\dagger}_{\mathbf{k}}(z_{\mathrm{h}})\psi^{\mathrm{h}\dagger}_{\mathbf{k}'}(z)\right\rangle = \left\langle \psi^{\mathrm{h}}_{\mathbf{k}'}(z)\psi^{\mathrm{e}'}_{\mathbf{k}}(z_{\mathrm{h}})\right\rangle^{*} .
$$

The factorization of the hole occupation function reads:

$$
\left\langle \psi^{\mathrm{h}'\dagger}_{\mathbf{k}}(z_{\mathrm{e}})\psi^{\mathrm{h}}_{\mathbf{k}}(z_{\mathrm{h}})\right\rangle = \sum_{\mathrm{e}}\int \mathrm{d}z\, p^{*\mathrm{eh}'}_{(\mathbf{k},z,z_{\mathrm{e}})}p^{\mathrm{eh}}_{(\mathbf{k},z,z_{\mathrm{h}})} + \mathcal{O}(E^4)\,. \qquad \text{(A.8)}
$$

In its leading order the electron-screened transition amplitude factorizes according to:

$$\begin{aligned}
&\left\langle \psi^{\mathrm{e}'\dagger}_{\mathbf{k}_1}(z)\psi^{\mathrm{e}'}_{\mathbf{k}_2}(z)\psi^{\mathrm{h}}_{\mathbf{k}_3}(z_\mathrm{h})\psi^{\mathrm{e}}_{\mathbf{k}_4}(z_\mathrm{e})\right\rangle \\
&\qquad = \sum_{\mathrm{h}'\mathbf{k}} \int \mathrm{d}z' \left\langle \psi^{\mathrm{e}'\dagger}_{\mathbf{k}_1}(z)\psi^{\mathrm{h}'\dagger}_{\mathbf{k}}(z')\right\rangle \left\langle \psi^{\mathrm{h}'}_{\mathbf{k}}(z')\psi^{\mathrm{e}'}_{\mathbf{k}_2}(z)\psi^{\mathrm{h}}_{\mathbf{k}_3}(z_\mathrm{h})\psi^{\mathrm{e}}_{\mathbf{k}_4}(z_\mathrm{e})\right\rangle \delta_{\mathbf{k}\mathbf{k}_1} + \mathcal{O}(E^5) \\
&\qquad = \sum_{\mathrm{h}'} \int \mathrm{d}z' p^{*\mathrm{e}'\mathrm{h}'}_{(\mathbf{k}_1,z,z')} \left\langle \psi^{\mathrm{h}'}_{\mathbf{k}_1}(z')\psi^{\mathrm{e}'}_{\mathbf{k}_2}(z)\psi^{\mathrm{h}}_{\mathbf{k}_3}(z_\mathrm{h})\psi^{\mathrm{e}}_{\mathbf{k}_4}(z_\mathrm{e})\right\rangle + \mathcal{O}(E^5)\,. \qquad \text{(A.9)}
\end{aligned}$$

The hole-screened transition amplitude factorizes according to:

$$\begin{aligned}
&\left\langle \psi^{\mathrm{h}'\dagger}_{\mathbf{k}_1}(z)\psi^{\mathrm{h}'}_{\mathbf{k}_2}(z)\psi^{\mathrm{h}}_{\mathbf{k}_3}(z_\mathrm{h})\psi^{\mathrm{e}}_{\mathbf{k}_4}(z_\mathrm{e})\right\rangle \\
&\qquad = \sum_{\mathrm{e}'\mathbf{k}} \int \mathrm{d}z' \left\langle \psi^{\mathrm{e}'\dagger}_{\mathbf{k}}(z')\psi^{\mathrm{h}'\dagger}_{\mathbf{k}_1}(z)\right\rangle \left\langle \psi^{\mathrm{h}'}_{\mathbf{k}_2}(z)\psi^{\mathrm{e}'}_{\mathbf{k}}(z')\psi^{\mathrm{h}}_{\mathbf{k}_3}(z_\mathrm{h})\psi^{\mathrm{e}}_{\mathbf{k}_4}(z_\mathrm{e})\right\rangle \delta_{\mathbf{k}\mathbf{k}_1} + \mathcal{O}(E^5) \\
&\qquad = \sum_{\mathrm{e}'} \int \mathrm{d}z' p^{*\mathrm{e}'\mathrm{h}'}_{(\mathbf{k}_1,z',z)} \left\langle \psi^{\mathrm{h}'}_{\mathbf{k}_2}(z)\psi^{\mathrm{e}'}_{\mathbf{k}_1}(z')\psi^{\mathrm{h}}_{\mathbf{k}_3}(z_\mathrm{h})\psi^{\mathrm{e}}_{\mathbf{k}_4}(z_\mathrm{e})\right\rangle + \mathcal{O}(E^5)\,. \qquad \text{(A.10)}
\end{aligned}$$

The consistent factorization of the required expectation values up to third order in the optical field in this section is based on two fundamental assumptions: (i) The system is in its ground state prior to the optical excitation. The Coulomb interaction conserves the particle numbers in conduction and valence bands individually and consequently does not cause the system to leave its ground state. Coulomb scattering processes that change the particle numbers in the bands are very unlikely due to the large band-gap energy and thus can be neglected in a very good approximation. Therefore, unless optical excitation takes place, the electronic system is found in its ground state for zero temperature. (ii) Exclusively optical excitation is applied to the system. Coherence of the electronic system with respect to the exciting light field is required. Violation of one of these assumptions destroys the exact relations (A.7)-(A.10) for the density matrix elements.

A.3. The Two-Exciton Product Basis

In this work a description of biexcitons in terms of two-exciton product states is used. A transition of the quantum mechanical formulation with respect to a discrete one-particle basis to a two-particle basis is applied. In principle, this transition is exact as long as the complete set of basis states is taken into account. Complications may arise from a truncation of the considered set of basis states as already discussed in Section 5.2. To guarantee at least the fermionic symmetry of the resulting states with respect to the truncated basis, it is included in the formulation in advance.

For the given geometry, with translation invariance in the x-y-plane, the optical excitation of single excitons requires the description of excitons with vanishing in-plane COM momentum only. For the description of two interacting excitons, namely the two-electron-two-hole system, exciton states with finite COM momentum must be taken into account. The system symmetry yields a vanishing total in-plane momentum of the resulting four-particle states. Fortunately, in momentum space, excitons with finite COM momentum can be described in terms of exciton wave functions $\phi_m(\mathbf{k}, z_{\mathrm{e}}, z_{\mathrm{h}})$ for the electron-hole relative motion with a shifted momentum argument and with shifted eigenenergies as outlined in the following. In general, an electron with momentum $\mathbf{k}+\mathbf{q}$ and a hole with momentum $\mathbf{k}$ obey the stationary two-particle Schrödinger equation

$$\left[\varepsilon^{\mathrm{e}}_{\mathbf{k}+\mathbf{q},z_{\mathrm{e}}} + \varepsilon^{\mathrm{h}}_{\mathbf{k},z_{\mathrm{h}}}\right]\tilde{\phi}_n(\mathbf{k},\mathbf{q},z_{\mathrm{e}},z_{\mathrm{h}}) - \sum_{\mathbf{k}'} V^{z_{\mathrm{e}}z_{\mathrm{h}}}_{\mathbf{k}-\mathbf{k}'}\tilde{\phi}_n(\mathbf{k}',\mathbf{q},z_{\mathrm{e}},z_{\mathrm{h}}) = \tilde{E}_n\tilde{\phi}_n(\mathbf{k},\mathbf{q},z_{\mathrm{e}},z_{\mathrm{h}})\,, \tag{A.11}$$

which is the formulation of the eigenvalue problem corresponding to Eq. (3.8) but for finite COM momentum $\mathbf{q}$. The one-particle energies $\varepsilon^{\mathrm{e}}_{\mathbf{k}+\mathbf{q},z_{\mathrm{e}}}$ and $\varepsilon^{\mathrm{h}}_{\mathbf{k},z_{\mathrm{h}}}$ are defined according to Eq. (2.3). With the kinetic energy of electron and hole,

$$\frac{\hbar^2(\mathbf{k}+\mathbf{q})^2}{2m^*_{\mathrm{e}}} + \frac{\hbar^2\mathbf{k}^2}{2m^*_{\mathrm{h}}} = \frac{\hbar^2(\mathbf{k}+\alpha\mathbf{q})^2}{2\mu^*} + \frac{\hbar^2\mathbf{q}^2}{2M^*}\,, \tag{A.12}$$

and $\alpha = m^*_{\mathrm{h}}/M^*$, Eq. (A.11) is transformed into

$$\left[\varepsilon^{\mathrm{e}}_{\mathbf{k}+\alpha\mathbf{q},z_{\mathrm{e}}} + \varepsilon^{\mathrm{h}}_{\mathbf{k}+\alpha\mathbf{q},z_{\mathrm{h}}} + \frac{\hbar^2\mathbf{q}^2}{2M^*}\right]\tilde{\phi}_n(\mathbf{k},\mathbf{q},z_{\mathrm{e}},z_{\mathrm{h}}) - \sum_{\mathbf{k}'} V^{z_{\mathrm{e}}z_{\mathrm{h}}}_{\mathbf{k}-\mathbf{k}'}\tilde{\phi}_n(\mathbf{k}',\mathbf{q},z_{\mathrm{e}},z_{\mathrm{h}}) \\ = \tilde{E}_n\tilde{\phi}_n(\mathbf{k},\mathbf{q},z_{\mathrm{e}},z_{\mathrm{h}})\,.$$

The reduced and the total exciton mass are denoted by μ^* and M^*, respectively. Since the in-plane exciton relative motion in this equation only depends on the momentum $\mathbf{k}+\alpha\mathbf{q}$, the substitutions $\tilde{\phi}_n(\mathbf{k},\mathbf{q},z_{\mathrm{e}},z_{\mathrm{h}}) = \phi_n(\mathbf{k}+\alpha\mathbf{q},z_{\mathrm{e}},z_{\mathrm{h}})$ and $\varepsilon_n(q) = \tilde{E}_n = \varepsilon_n + \frac{\hbar^2\mathbf{q}^2}{2M^*}$ are applied here. The resulting equation has the formal structure of the eigenvalue equation (3.12) on page 33 for the exciton relative motion with a shifted momentum argument $\mathbf{k}+\alpha\mathbf{q}$ and shifted eigenvalues $\varepsilon_n(q)$:

$$\left[\varepsilon^{\mathrm{e}}_{\mathbf{k}+\alpha\mathbf{q},z_{\mathrm{e}}} + \varepsilon^{\mathrm{h}}_{\mathbf{k}+\alpha\mathbf{q},z_{\mathrm{h}}} + \frac{\hbar^2\mathbf{q}^2}{2M^*}\right]\phi_n(\mathbf{k}+\alpha\mathbf{q},z_{\mathrm{e}},z_{\mathrm{h}}) - \sum_{\mathbf{k}'} V^{z_{\mathrm{e}}z_{\mathrm{h}}}_{\mathbf{k}-\mathbf{k}'}\phi_n(\mathbf{k}'+\alpha\mathbf{q},z_{\mathrm{e}},z_{\mathrm{h}}) \\ = \varepsilon_n(q)\phi_n(\mathbf{k}+\alpha\mathbf{q},z_{\mathrm{e}},z_{\mathrm{h}})\,.$$

Here ε_n and $\phi_n(\mathbf{k},z_{\mathrm{e}},z_{\mathrm{h}})$ are eigenenergies and wave functions for the exciton relative motion with vanishing COM momentum, respectively, introduced in Eq. (3.12). Therefore, in general, the eigenstate $\tilde{\phi}_n(\mathbf{k},\mathbf{q},z_{\mathrm{e}},z_{\mathrm{h}})$ of an exciton with finite COM momentum $\mathbf{q}$ equals the eigenstate $\phi_n(\mathbf{k}+\alpha\mathbf{q},z_{\mathrm{e}},z_{\mathrm{h}})$ that corresponds to an exciton with relative momentum $\mathbf{k}+\alpha\mathbf{q}$ and vanishing COM momentum with the shifted eigenvalue $\varepsilon_n(q) = \varepsilon_n + \frac{\hbar^2\mathbf{q}^2}{2M^*}$ according to Eq. (3.13).

The biexcitonic correlation function $b^{\mathrm{e'h'}}_{\mathrm{eh}}$ is expressed in terms of the auxiliary quantity $\tilde{b}^{\mathrm{e'h'}}_{\mathrm{eh}}$,

$$b^{\mathrm{e'h'}\;(\mathbf{k}',z_{\mathrm{e'}},\mathbf{k}'+\mathbf{q},z_{\mathrm{h'}})}_{\mathrm{eh}\;(\mathbf{k}+\mathbf{q},z_{\mathrm{e}},\mathbf{k},z_{\mathrm{h}})} = \tilde{b}^{\mathrm{e'h'}\;(\mathbf{k}',z_{\mathrm{e'}},\mathbf{k}'+\mathbf{q},z_{\mathrm{h'}})}_{\mathrm{eh}\;(\mathbf{k}+\mathbf{q},z_{\mathrm{e}},\mathbf{k},z_{\mathrm{h}})} + \tilde{b}^{\mathrm{eh}\;(\mathbf{k}+\mathbf{q},z_{\mathrm{e}},\mathbf{k},z_{\mathrm{h}})}_{\mathrm{e'h'}\;(\mathbf{k}',z_{\mathrm{e'}},\mathbf{k}'+\mathbf{q},z_{\mathrm{h'}})} \\ - \tilde{b}^{\mathrm{eh'}\;(\mathbf{k}+\mathbf{q},z_{\mathrm{e}},\mathbf{k}'+\mathbf{q},z_{\mathrm{h'}})}_{\mathrm{e'h}\;(\mathbf{k}',z_{\mathrm{e'}},\mathbf{k},z_{\mathrm{h}})} - \tilde{b}^{\mathrm{e'h}\;(\mathbf{k}',z_{\mathrm{e'}},\mathbf{k},z_{\mathrm{h}})}_{\mathrm{eh'}\;(\mathbf{k}+\mathbf{q},z_{\mathrm{e}},\mathbf{k}'+\mathbf{q},z_{\mathrm{h'}})}\,, \tag{A.13}$$

which guarantees the required antisymmetry with respect to electron or hole interchange in the following. Making use of Eq. (A.12), the auxiliary quantity $\tilde{b}^{\mathrm{e'h'}}_{\mathrm{eh}}$ is expanded in terms of exciton product states for general electron and hole momenta:[b]

$$\tilde{b}^{\mathrm{e'h'}\,(\mathbf{k}_2,z_2,\mathbf{k}_1,z_1)}_{\mathrm{eh}\,(\mathbf{k}_4,z_4,\mathbf{k}_3,z_3)} = \sum_{nm} \phi_n(\alpha\mathbf{k}_4+\beta\mathbf{k}_3,z_4,z_3)\,\phi_m(\alpha\mathbf{k}_2+\beta\mathbf{k}_1,z_2,z_1)\,B^{\mathrm{ehe'h'}}_{nm}(\mathbf{k}_4-\mathbf{k}_3)\,, \tag{A.14}$$

where $\beta = m^*_{\mathrm{e}}/M^*$, and $\alpha+\beta=1$. Due to the system in-plane translation symmetry, in praxis, only terms contribute to the biexcitonic correlations with vanishing in-plane total momentum $\mathbf{k}_4-\mathbf{k}_1+\mathbf{k}_2-\mathbf{k}_1=0$.[c] Since the internal excitonic quantum numbers n, m are only sufficient to characterize the in-plane relative motion for each exciton state, the expansion coefficients $B^{\mathrm{ehe'h'}}_{nm}(\mathbf{q})$ additionally depend on the exciton COM momenta $\mathbf{k}_4-\mathbf{k}_3 = -(\mathbf{k}_2-\mathbf{k}_1)$ to obtain a general description of the two-exciton state. The expansion (A.14) together with Eq. (A.13) yields:

$$\begin{aligned}
&b^{\mathrm{e'h'}\,(\mathbf{k}',z_{\mathrm{e'}},\mathbf{k}'+\mathbf{q},z_{\mathrm{h'}})}_{\mathrm{eh}\,(\mathbf{k}+\mathbf{q},z_{\mathrm{e}},\mathbf{k},z_{\mathrm{h}})} = \\
&\quad\sum_{nm}\phi_n(\mathbf{k}+\alpha\mathbf{q},z_{\mathrm{e}},z_{\mathrm{h}})\Big[\phi_m(\mathbf{k}'+\beta\mathbf{q},z_{\mathrm{e'}},z_{\mathrm{h'}})B^{\mathrm{ehe'h'}}_{nm}(\mathbf{q}) \\
&\quad+\phi_n(\mathbf{k}'+\beta\mathbf{q},z_{\mathrm{e'}},z_{\mathrm{h'}})\phi_m(\mathbf{k}+\alpha\mathbf{q},z_{\mathrm{e}},z_{\mathrm{h}})B^{\mathrm{e'h'eh}}_{nm}(-\mathbf{q}) \\
&\quad-\phi_n(\alpha\mathbf{k}'+\beta\mathbf{k},z_{\mathrm{e'}},z_{\mathrm{h}})\phi_m(\alpha\mathbf{k}+\beta\mathbf{k}'+\mathbf{q},z_{\mathrm{e}},z_{\mathrm{h'}})B^{\mathrm{e'heh'}}_{nm}(\mathbf{k}'-\mathbf{k}) \\
&\quad-\phi_n(\alpha\mathbf{k}+\beta\mathbf{k}'+\mathbf{q},z_{\mathrm{e}},z_{\mathrm{h'}})\phi_m(\alpha\mathbf{k}'+\beta\mathbf{k},z_{\mathrm{e'}},z_{\mathrm{h}})B^{\mathrm{eh'e'h}}_{nm}(\mathbf{k}-\mathbf{k}')\Big] \\
&=\sum_{nm}\Big[\phi_n(\mathbf{k}+\alpha\mathbf{q},z_{\mathrm{e}},z_{\mathrm{h}})\phi_m(\mathbf{k}'+\beta\mathbf{q},z_{\mathrm{e'}},z_{\mathrm{h'}})\big(B^{\mathrm{ehe'h'}}_{nm}(\mathbf{q})+B^{\mathrm{e'h'eh}}_{mn}(-\mathbf{q})\big) \\
&\quad-\phi_n(\alpha\mathbf{k}'+\beta\mathbf{k},z_{\mathrm{e'}},z_{\mathrm{h}})\phi_m(\alpha\mathbf{k}+\beta\mathbf{k}'+\mathbf{q},z_{\mathrm{e}},z_{\mathrm{h'}})\times \\
&\qquad\qquad\qquad\times\big(B^{\mathrm{e'heh'}}_{nm}(\mathbf{k}'-\mathbf{k})+B^{\mathrm{eh'e'h}}_{mn}(\mathbf{k}-\mathbf{k}')\big)\Big] \\
&=\sum_{nm}\Big[\phi_n(\mathbf{k}+\alpha\mathbf{q},z_{\mathrm{e}},z_{\mathrm{h}})\phi_m(\mathbf{k}'+\beta\mathbf{q},z_{\mathrm{e'}},z_{\mathrm{h'}})b^{\mathrm{ehe'h'}}_{nm}(\mathbf{q}) \\
&\quad-\phi_n(\alpha\mathbf{k}'+\beta\mathbf{k},z_{\mathrm{e'}},z_{\mathrm{h}})\phi_m(\alpha\mathbf{k}+\beta\mathbf{k}'+\mathbf{q},z_{\mathrm{e}},z_{\mathrm{h'}})b^{\mathrm{e'heh'}}_{nm}(\mathbf{k}'-\mathbf{k})\Big]\,,
\end{aligned}$$

with the expansion coefficients $b^{\mathrm{ehe'h'}}_{nm}(\mathbf{q}) = B^{\mathrm{ehe'h'}}_{nm}(\mathbf{q}) + B^{\mathrm{e'h'eh}}_{mn}(-\mathbf{q})$ that determine the contributions to the biexcitonic correlation function (A.13). In direct analogy to the Hydrogen molecule problem a classification of the biexcitonic contributions by their total electronic spin S_{e} is convenient. Electronic singlet ($S_{\mathrm{e}} = 0 \mathrel{\hat{=}} \lambda = -1$) and triplet ($S_{\mathrm{e}} = 1 \mathrel{\hat{=}} \lambda = +1$) contributions $b^{\mathrm{e'h'}\lambda}_{\mathrm{eh}}$ are given by

$$b^{\mathrm{e'h'}\lambda\,(\mathbf{k}',z_{\mathrm{e'}},\mathbf{k}'+\mathbf{q},z_{\mathrm{h'}})}_{\mathrm{eh}\,(\mathbf{k}+\mathbf{q},z_{\mathrm{e}},\mathbf{k},z_{\mathrm{h}})} = \frac{1}{2}\Big(b^{\mathrm{e'h'}\,(\mathbf{k}',z_{\mathrm{e'}},\mathbf{k}'+\mathbf{q},z_{\mathrm{h'}})}_{\mathrm{eh}\,(\mathbf{k}+\mathbf{q},z_{\mathrm{e}},\mathbf{k},z_{\mathrm{h}})} + \lambda b^{\mathrm{eh'}\,(\mathbf{k}',z_{\mathrm{e'}},\mathbf{k}'+\mathbf{q},z_{\mathrm{h'}})}_{\mathrm{e'h}\,(\mathbf{k}+\mathbf{q},z_{\mathrm{e}},\mathbf{k},z_{\mathrm{h}})}\Big)\,,$$

---

[b] Fermionic symmetry is guaranteed by the ansatz (A.13) for each term in the expansion separately.

[c] By definition, hole momenta come with a minus sign compared to the corresponding electronic one.

in terms of the biexcitonic correlation function (A.13). Therefore, the original biexcitonic correlation function (A.13) is just the sum of electronic singlet and triplet contribution. The final expansion in terms of two-exciton product states reads

$$\begin{aligned} b_{\mathrm{eh}}^{\mathrm{e'h'}\lambda}{}^{(\mathbf{k}',z_{\mathrm{e}'},\mathbf{k}'+\mathbf{q},z_{\mathrm{h}'})}_{(\mathbf{k}+\mathbf{q},z_{\mathrm{e}},\mathbf{k},z_{\mathrm{h}})} = \sum_{nm} \Big[& \phi_n(\mathbf{k}+\alpha\mathbf{q}, z_{\mathrm{e}}, z_{\mathrm{h}}) \phi_m(\mathbf{k}'+\beta\mathbf{q}, z_{\mathrm{e}'}, z_{\mathrm{h}'}) b_{nm}^{\mathrm{ehe'h'}\lambda}(\mathbf{q}) \\ & - \lambda \phi_n(\alpha\mathbf{k}'+\beta\mathbf{k}, z_{\mathrm{e}'}, z_{\mathrm{h}}) \phi_m(\alpha\mathbf{k}+\beta\mathbf{k}'+\mathbf{q}, z_{\mathrm{e}}, z_{\mathrm{h}'}) b_{nm}^{\mathrm{ehe'h'}\lambda}(\mathbf{k}'-\mathbf{k}) \Big] , \end{aligned} \tag{A.15}$$

with expansion coefficients $b_{nm}^{\mathrm{ehe'h'}\lambda}(\mathbf{q}) = \frac{1}{2}\big(b_{nm}^{\mathrm{ehe'h'}}(\mathbf{q}) + \lambda b_{nm}^{\mathrm{e'heh'}}(\mathbf{q})\big)$ for electronic singlet and triplet configuration. Using expansion (A.15) together with Eq. (5.9), the corresponding equations of motion for the excitonic p_m^{eh} (5.12) and biexcitonic $b_{nm}^{\mathrm{ehe'h'}\lambda}(\mathbf{q})$ (5.13) coefficients are deduced with

$$i\hbar\frac{\partial}{\partial t} b_{\mathrm{eh}}^{\mathrm{e'h'}\lambda}{}^{(\mathbf{k}',z_{\mathrm{e}'},\mathbf{k}'+\mathbf{q},z_{\mathrm{h}'})}_{(\mathbf{k}+\mathbf{q},z_{\mathrm{e}},\mathbf{k},z_{\mathrm{h}})} = i\hbar\frac{1}{2}\frac{\partial}{\partial t} b_{\mathrm{eh}}^{\mathrm{e'h'}}{}^{(\mathbf{k}',z_{\mathrm{e}'},\mathbf{k}'+\mathbf{q},z_{\mathrm{h}'})}_{(\mathbf{k}+\mathbf{q},z_{\mathrm{e}},\mathbf{k},z_{\mathrm{h}})} + \lambda i\hbar\frac{1}{2}\frac{\partial}{\partial t} b_{\mathrm{e'h}}^{\mathrm{eh'}}{}^{(\mathbf{k}',z_{\mathrm{e}'},\mathbf{k}'+\mathbf{q},z_{\mathrm{h}'})}_{(\mathbf{k}+\mathbf{q},z_{\mathrm{e}},\mathbf{k},z_{\mathrm{h}})} .$$

The two subspaces ($\lambda = \pm 1$) are decoupled because of the conservation of the total electron spin S_{e}. Using the expansion presented in this section, by construction, proper fermionic symmetry of the biexciton states is guaranteed in advance. All biexcitonic contributions to the system dynamics fulfill the required fermionic symmetry even within a truncated exciton basis. All other properties, e.g., selection rules, follow from the equations of motion (5.12) and (5.13).

B. Numerical Techniques and Results

This chapter is dedicated to the discussion of numerical problems that arose during the preparation of the present work. Some fundamental numerical concepts and techniques for their solution are presented. Section B.1 gives an insight into the direct discretization of the excitonic Hamiltonian in real space and momentum space and into concepts for the numerical integration of the time evolution of the excitonic dynamics. In Section B.2 the numerical discretization of the one-dimensional Maxwell equations, which are coupled partial differential equations in space and time, is summarized. Section B.3 is devoted to the calculation of the biexcitonic Hamiltonian matrix with respect to the two-exciton product basis.

B.1. The Exciton Equation

In this section the numerical approach to the solution of the inhomogeneous exciton equation (3.8) on page 29 is summarized. First of all, we consider a general equation, that has the formal structure of the inhomogeneous exciton equation regarding its time-dependence:

$$i\hbar\frac{\partial}{\partial t}\left|\psi(t)\right\rangle = \mathcal{H}\left|\psi(t)\right\rangle + \phi(t)\,. \tag{B.1}$$

$\mathcal{H}$ denotes the Hamiltonian of the considered system and $\phi(t)$ is a time-dependent driving term that, in case of the exciton equation contains the dipole coupling to the external field. The free[a] time evolution of the state $|\psi(t)\rangle$ is determined by the action of the Hamiltonian $\mathcal{H}$. Formally, the time evolution of the state $|\psi(t_0)\rangle$ to a time $t \geq t_0$ can be expressed in terms of the time evolution operator $\mathcal{U}(t,t_0)$ acting on the state $|\psi(t_0)\rangle$:

$$\left|\psi(t)\right\rangle = \mathcal{U}(t,t_0)\left|\psi(t_0)\right\rangle\,.$$

As long as $\mathcal{H}$ does not contain an explicit time-dependence, formal integration of the time evolution yields the time evolution operator in the form:

$$\mathcal{U}(t,t_0) = \mathcal{U}(t-t_0) = \mathrm{e}^{-\frac{i}{\hbar}\mathcal{H}\cdot(t-t_0)}\,.$$

---

[a] The free time evolution of $|\psi(t)\rangle$ is determined by the corresponding homogeneous equation $i\hbar\frac{\partial}{\partial t}\left|\psi(t)\right\rangle = \mathcal{H}\left|\psi(t)\right\rangle$ and is not coupled to the external driving term $\phi(t)$.

Starting from

$$|\psi(t+\Delta t)\rangle - |\psi(t-\Delta t)\rangle = \left(\mathrm{e}^{-\frac{i}{\hbar}\mathcal{H}\Delta t} - \mathrm{e}^{+\frac{i}{\hbar}\mathcal{H}\Delta t}\right)|\psi(t)\rangle \;,$$

and expanding the exponentials for a small time step Δt up to linear order in Δt, an explicit scheme can be deduced for the calculation of the state $|\psi(t+\Delta t)\rangle$ at time $t+\Delta t$:

$$|\psi(t+\Delta t)\rangle = |\psi(t-\Delta t)\rangle - 2\frac{i}{\hbar}\mathcal{H}\,|\psi(t)\rangle\,\Delta t\,.$$

This formulation is equivalent to a symmetric substitution of the time derivative in Eq. (B.1) at time t by a difference quotient with a finite step size Δt. Therefore, the scheme requires the solutions at times t and $t-\Delta t$ to calculate the solution at time $t+\Delta t$. Due to this symmetric formulation, the accuracy of the result is exact in second order in the step size Δt.[79] Therefore, it is called Second Order Differencing (SOD) scheme.[80] The stability limit is determined by the spectral properties of the operator $\mathcal{H}$. Stable behavior of the solution is obtained for

$$\Delta t < \hbar/|E_{\max}|\,, \tag{B.2}$$

where $E_{\max}$ denotes the eigenvalue of $\mathcal{H}$ with largest magnitude.[80] The inclusion of the inhomogeneity in Eq. (B.1) yields the more general result:

$$|\psi(t+\Delta t)\rangle = |\psi(t-\Delta t)\rangle - 2\frac{i}{\hbar}\big[\mathcal{H}\,|\psi(t)\rangle + \phi(t)\big]\Delta t\,. \tag{B.3}$$

The great advantage of the SOD scheme is its simplicity, paired with a comparatively high accuracy. The calculation requires the evaluation of the action of $\mathcal{H}$ on the state $|\psi(t)\rangle$ only once for each time step. For instance, the Euler algorithm, where a non-symmetric time derivative is used requires a similar numerical effort but only yields results being correct in first order in the step size Δt. In particular, the SOD scheme conserves the norm of the state for a hermitian Hamiltonian $\mathcal{H}$.[80] For the time evolution that is determined by a non hermitian operator $\mathcal{H}$ this scheme does not yield a stable result. Strictly speaking, the hermicity of the Hamiltonian $\mathcal{H}^{\mathrm{X}}$ for the excitonic polarization is lost by introduction of a phenomenological dephasing constant. Nevertheless, in favor of its simplicity, the SOD scheme is used for the integration of the time evolution of the exciton equation (3.8). The decay of the macroscopic polarization is sufficiently fast to obtain convergence of the optical spectra before exponentially growing contributions in the solution yield an artificial growth of the polarization which would influence the final result. A fourth order Runge-Kutta algorithm[81] has some shortcomings in comparison to the SOD scheme. The numerical effort is much higher since it requires four evaluations of the action of the Hamiltonian on the state for each time step. Furthermore, it does not exactly conserve the norm of the state during the time evolution. Nevertheless, the advantage of a fourth order Runge-Kutta scheme is its high accuracy and in particular its stability for a system with a non hermitian Hamiltonian $\mathcal{H}$.

For the direct integration of Eq. (3.8) the SOD scheme is applied to avoid a waste of computing time, whereas in nonlinear optics we apply a fourth order Runge-Kutta algorithm in favor of its higher stability.

For a numerical calculation of the time-evolution of Eq. (3.8) an explicit matrix representation of the excitonic Hamiltonian $\mathcal{H}^{\mathrm{X}}$ is required. Therefore, all relevant quantities are discretized on a grid with finite step size in real and momentum space. The spatial derivatives of the excitonic polarization are substituted according to their definition, here given for a general function $f(x)$ at grid point x_n with a finite step size h:

$$\frac{\mathrm{d}^2}{\mathrm{d}x^2} f(x)\Big|_{x_n} \approx \frac{2f(x_n) - f(x_{n-1}) - f(x_{n+1})}{h^2} \,. \tag{B.4}$$

In the following, the indices for the different coordinate grids for electron $\{z_{\mathrm{e}}^u\}$ and hole $\{z_{\mathrm{h}}^v\}$ z-coordinates and for the in-plane relative momentum $\{k_j\}$ are abbreviated by $i \hat{=} \{u, v, j\}$. This yields the formal structure of the exciton equation (3.8) on the discrete coordinate grid

$$i\hbar \frac{\partial}{\partial t} p_i(t) = \sum_l H_{il} p_l(t) + \phi_i(t) \,,$$

and, according to Eq. (B.3), for discrete time steps Δt denoted by the upper index n:

$$p_i^{n+1} = p_i^{n-1} - 2\frac{i}{\hbar}\left[\sum_l H_{il} p_l^n + \phi_i^n\right]\Delta t \,. \tag{B.5}$$

The structure of the spatial derivatives (B.4) yields a Hamiltonian matrix which only couples $p^n(k_j, z_{\mathrm{e}}^u, z_{\mathrm{h}}^v)$ to the four neighboring grid points $(z_{\mathrm{e}}^{u+1}, z_{\mathrm{h}}^v)$, $(z_{\mathrm{e}}^{u-1}, z_{\mathrm{h}}^v)$, $(z_{\mathrm{e}}^u, z_{\mathrm{h}}^{v+1})$, $(z_{\mathrm{e}}^u, z_{\mathrm{h}}^{v-1})$ in real space.[b)] The Coulomb interaction is diagonal with respect to the real space coordinates, thus it only couples all different momentum contributions k_j for fixed spatial coordinates. An efficient numerical implementation of the coupled space-time dynamics in Eq. (B.5) on a parallel computer architecture has been achieved by use of the Message Passing Interface[82,83] (MPI) following Ref. 84.

In case of the exciton equation (3.8) the Coulomb matrix elements contain a singular contribution on the diagonal of the Hamiltonian matrix H_{il} in Eq. (B.5) for $k_j = k_{j'}$. Therefore, to obtain reliable numerical results, a very large number of grid points in k-space would be necessary, resulting in a very large matrix H_{il}. To overcome this problem, the singularity is removed numerically as outlined in the following. This way, a formulation is achieved where the evaluation of the Coulomb singularity can be performed independently of the underlying momentum space grid for the discretization of the excitonic Hamiltonian.

[b)] The structure of the spatial derivatives (B.4) yields a Hamiltonian matrix H_{il} with a low density of non-zero matrix elements, a so-called sparse matrix.

To demonstrate the numerical removal of the Coulomb singularity in momentum space we suppress time and real space arguments in the notation in the following example. The structure of the exciton equation (3.8) regarding the momentum space dependence of the Coulomb interaction corresponds to the following expression:

$$f(k) = \int \mathrm{d}k' \, V(k,k')g(k') \,. \tag{B.6}$$

This relation of $f(k)$ and $g(k)$ can be expressed by a term that is regular for $k = k'$ and an additional contribution that still contains the singularity for $k = k'$:

$$\begin{aligned} f(k) = \int \mathrm{d}k' \, V(k,k')g(k') = \int \mathrm{d}k' \, & \underbrace{V(k,k')[g(k') - g(k)\alpha(k,k')]}_{\text{regular for } k=k'} \\ + g(k) \int \mathrm{d}k' \, & \underbrace{V(k,k')\alpha(k,k')}_{\text{singular for } k=k'} \\ \text{with} \quad \alpha(k,k') = 1 \quad \text{for} \quad & k = k' \,. \end{aligned}$$

The transition to an arbitrary grid in momentum space with discrete values $\{k_j\}$ yields the formulation:

$$f(k_i) = \sum_{j \neq i} V(k_i,k_j)g(k_j)w_{k_j} + \sum_j (-I^{\alpha}_{k_j} + I^{\text{sing}}_{k_j})g(k_j)\delta_{ij} \,, \tag{B.7}$$

with

$$I^{\alpha}_{k_j} = \sum_{l \neq j} V(k_j,k_l)\alpha(k_j,k_l)w_{k_l} \quad , \quad I^{\text{sing}}_{k_j} = \int \mathrm{d}k' \, V(k,k')\alpha(k,k') \,, \tag{B.8}$$

and the step size (weight factor) w_{k_j} for each grid point k_j. Equation (B.7) can be rewritten as a matrix equation of the form

$$f(k_i) = \sum_j V_{k_i k_j} g(k_j) \,, \tag{B.9}$$

with the definition of the Coulomb matrix

$$V_{k_i k_j} = \begin{cases} V(k_i,k_j)w_{k_j} & \text{for} \quad k_i \neq k_j \\ -I^{\alpha}_{k_j} + I^{\text{sing}}_{k_j} & \text{for} \quad k_i = k_j \end{cases} \,. \tag{B.10}$$

An appropriate choice of the factor $\alpha(k,k')$ is given by

$$\alpha(k,k') = \frac{4k^4}{(k^2 + k'^2)^2} \,.$$

It fulfills the requirement $\alpha(k,k) = 1$ and provides a cut-off in the integration of the Coulomb singularity in Eq. (B.8) since it rapidly falls of in the limit $k' - k \to \infty$.

The great advantage of treating the Coulomb singularity in the way presented above, is the formal transfer of the singularity in the evaluation of the Coulomb integral (B.6) to the function $I^{\text{sing}}_{k_j}$ in Eq. (B.10). Therefore the evaluation of the Coulomb singularity can be performed independently of the discrete momentum space grid $\{k_j\}$ on which the action of the Coulomb matrix $V_{k_i k_j}$ on the function $g(k_j)$ is defined according to Eq. (B.9). The integration in $I^{\text{sing}}_{k_j}$ is done by use of Gaussian quadrature points accumulated around the singularity at $k = k'$, while $\alpha(k, k')$ provides a cut-off for large $k' - k$.

In Section 3.2, the transition to the exciton eigenbasis requires the diagonalization of the matrix H_{il} corresponding to the discretized excitonic Hamiltonian $\mathcal{H}^{\text{X}}$. As described in this section, the discretization is applied to the real space coordinates $z_{\text{e}}, z_{\text{h}}$ as well as to the electron-hole relative momentum k. For the investigated layer thicknesses typical matrix dimensions are of the order $N \approx 10^5 - 10^6$. As already mentioned, corresponding to Eq. (B.4), the derivatives in real space only couple neighboring points on the real space grid. This results in a Hamiltonian matrix where the number of non-zero matrix elements is only of order N. For the C++ programming language, efficient algorithms for the calculation of a certain part of the eigenspectrum of these so-called sparse matrices are provided by Arpack++.[85] Since the basic routines are based on Fortran code, Arpack++ provides an object oriented interface in terms of a template class library. The possibility for efficient parallelization is provided with parpack which supports the MPI concept. Economic storage of sparse matrices regarding the required amount of memory is done in the Compressed Sparse Column[85] (CSC) format which is supported by Arpack++ routines. The CSC format requires storage of the row index of each matrix element not being equal zero, the value of the matrix element itself, and the storage position of he first non-zero element in each column in the matrix. Zero entries are not explicitly stored.

B.2. Maxwell's Equations

The solution of a partial differential equation can be found by the method of characteristics.[c)] The free solutions of Maxwell's equations in a material with background refractive index n_{bg} propagate in space with the velocity of light $c = c_0/n_{\text{bg}}$. Making use of this characteristic knowledge about the desired solutions, a certain relation is obtained for the discretization of space and time: The step sizes Δz and Δt on a discrete space and time grid are connected by the velocity of light c in the material, $\Delta z = c \cdot \Delta t$. For the numerical solution, this relation allows a formal transformation of Maxwell's equations to an equivalent set of ordinary differential equations as outlined in this section. Furthermore, for the application in this work the use of Hartree's method[86] is advantageous for the discretization since it avoids an artificial reflection of light at the boundaries of the numerical space grid.[84]

[c)] Details, concerning this method, going beyond the solution of the one-dimensional Maxwell equations are given in Ref. 86.

The macroscopic Maxwell equations with a permeability $\mu_\mathrm{r} = 1$ and without free charges $\rho_\mathrm{free} = 0$ are[d)]

$$\nabla\mathbf{E} = 0\,, \tag{B.11}$$

$$\nabla\mathbf{B} = 0\,, \tag{B.12}$$

$$\nabla\times\mathbf{B} = \mu_0\mathbf{j} + \mu_0\varepsilon_0\varepsilon_\mathrm{r}\frac{\partial\mathbf{E}}{\partial t} + \mu_0\frac{\partial\mathbf{P}}{\partial t}\,, \tag{B.13}$$

$$\nabla\times\mathbf{E} = -\frac{\partial\mathbf{B}}{\partial t}\,. \tag{B.14}$$

The ansatz $\mathbf{E}(\mathbf{r},t) = E_+(z,t)\mathbf{e}_+ + E_-(z,t)\mathbf{e}_-$ for the electric field and $\mathbf{B}(\mathbf{r},t) = B_+(z,t)i\mathbf{e}_+ + B_-(z,t)i\mathbf{e}_-$ for the magnetic field for a transversal electromagnetic wave propagating in the z-direction solves the homogeneous Eqs. (B.11) and (B.12). With $\mathbf{j} = j_+(z,t)\mathbf{e}_+ + j_-(z,t)\mathbf{e}_-$ and $\mathbf{P} = P_+(z,t)\mathbf{e}_+ + P_-(z,t)\mathbf{e}_-$ in terms of circularly polarized components ($\pm$), the one-dimensional Maxwell equations are obtained:

$$n_\mathrm{bg}^2(z)\frac{\partial E_\pm(z,t)}{\partial t} = -c_0^2\frac{\partial B_\pm(z,t)}{\partial z} - \frac{1}{\varepsilon_0}\left(j_\pm(z,t) + \frac{\partial P_\pm(z,t)}{\partial t}\right)\,, \tag{B.15}$$

$$\frac{\partial B_\pm(z,t)}{\partial t} = -\frac{\partial E_\pm(z,t)}{\partial z}\,, \tag{B.16}$$

with the background refractive index profile $n_\mathrm{bg}^2(z) = \varepsilon_\mathrm{r}(z)$. Note, that these scalar equations are decoupled for the different circularly polarized components ($\pm$) of electric and magnetic field. Therefore, in the following, the index $\pm$ is suppressed and the discussion is done for one of the circularly polarized components. The velocity of light in the material is $c = c_0/n_\mathrm{bg} = 1/(n_\mathrm{bg}\sqrt{\mu_0\varepsilon_0})$. The solution of Maxwell's equations (B.15) and (B.16) is coupled to the solution of the material equations which determine the macroscopic polarization $P(z,t)$. For the numerical solution, the explicit occurrence of the band-gap energy E_gap in the material equations (3.2) or (5.8) and (5.9) is inconvenient regarding the stability limit (B.2) for the numerical integration of the time evolution as discussed in the previous section. The resulting fast oscillations of the desired solutions in time necessitate very small time steps in the numerical integration. To eliminate the occurrence of E_gap all dynamic quantities $X(t)$ are transformed to the rotating picture via $X(t) = \mathrm{e}^{-i\omega_0 t}\tilde{X}(t)$, with $\omega_0 = E_\mathrm{gap}/\hbar$. Application of this transformation to the one-dimensional Maxwell equations yields the Maxwell equations in the rotating picture:[e)]

$$\frac{\partial\tilde{E}}{\partial t} + \frac{c_0^2}{n_\mathrm{bg}^2}\frac{\partial\tilde{B}}{\partial z} = -\tilde{J} + i\omega_0\tilde{E} \qquad \text{with} \qquad \tilde{J} = \frac{1}{\varepsilon_0 n_\mathrm{bg}^2}\left(\tilde{j} + \frac{\partial\tilde{P}}{\partial t} - i\omega_0\tilde{P}\right)\,, \tag{B.17}$$

$$\frac{\partial\tilde{B}}{\partial t} + \frac{\partial\tilde{E}}{\partial z} = i\omega_0\tilde{B}\,. \tag{B.18}$$

[d)] For the numerical simulation, the current density **j** is included here in the description as an appropriate device for laser pulse generation outside of the investigated sample.

[e)] In the following, the transformation of the dynamic quantities will not be made explicit in the notation, so the tilde symbol is suppressed.

Discrete version of the one-dimensional Maxwell equations:

To find a numerical solution of Eqs. (B.17) and (B.18) the method of characteristics is applied, following Ref. 86. The dynamic quantities $E \rightarrow u$ and $B \rightarrow v$ and their total derivatives form a system of linear equations:

$$au_x + ev_y = f_1\,, \tag{B.19}$$

$$bu_y + cv_x = f_2\,, \tag{B.20}$$

$$u_x\mathrm{d}x + u_y\mathrm{d}y = \mathrm{d}u\,, \tag{B.21}$$

$$v_x\mathrm{d}x + v_y\mathrm{d}y = \mathrm{d}v\,, \tag{B.22}$$

with the definitions $z \rightarrow x$, $t \rightarrow y$, $u_x = \frac{\partial u}{\partial x}$, $u_y = \frac{\partial u}{\partial y}$, $v_x = \frac{\partial v}{\partial x}$, $v_y = \frac{\partial v}{\partial y}$ and $a = b = e = 1$, $c = c_0^2/n_{\mathrm{bg}}^2$, $f_2 = -J + i\omega_0 E$, $f_1 = i\omega_0 B$. This yields a linear system of equations in the quantities u_x, u_y, v_x, v_y:

$$\underbrace{\begin{pmatrix} a & 0 & 0 & e \\ 0 & b & c & 0 \\ \mathrm{d}x & \mathrm{d}y & 0 & 0 \\ 0 & 0 & \mathrm{d}x & \mathrm{d}y \end{pmatrix}}_{A} \begin{pmatrix} u_x \\ u_y \\ v_x \\ v_y \end{pmatrix} = \begin{pmatrix} f_1 \\ f_2 \\ \mathrm{d}u \\ \mathrm{d}v \end{pmatrix},$$

with the matrix A. For a unique solution, a characteristic equation is found by the requirement $\det A = 0$:[f)]

$$\det A = 0 \rightarrow ac(\mathrm{d}y)^2 - be(\mathrm{d}x)^2 = 0\,,$$

$$\rightarrow \frac{\mathrm{d}x}{\mathrm{d}y} = \pm\sqrt{\frac{ac}{be}} = \pm\frac{c_0}{n_{\mathrm{bg}}} = F_\pm(x) = F_\pm\,. \tag{B.23}$$

This characteristic equation represents the propagating $F_+(x)$ and counter-propagating $F_-(x)$ solutions of light. The solution at a time-space point R (space $x_R \mathrel{\widehat{=}} z_R$ and time $y_R \mathrel{\widehat{=}} t_R$) only depends on the solutions with $x_P < x_R < x_Q$ ($z_P < z_R < z_Q$) at time $y_P = y_Q$ ($t_P = t_Q$), as illustrated in Fig. B.1. The time-space evolution of electromagnetic waves obeys the characteristic equation (B.23). For $\det A = 0$ there is a linear dependence of the columns in A.[87] To find a solution for the system of linear equations (B.19)-(B.22) with non-vanishing inhomogeneity on the right hand side, the inhomogeneity is chosen as a particular linear combination in terms of the columns of A. This approach yields a linear system where the columns still linearly depend on each other and which fulfills

$$\det \begin{pmatrix} f_1 & 0 & 0 & e \\ f_2 & b & c & 0 \\ \mathrm{d}u & \mathrm{d}y & 0 & 0 \\ \mathrm{d}v & 0 & \mathrm{d}x & \mathrm{d}y \end{pmatrix} = 0\,.$$

[f)] At this point, the formulation is restricted to optical homogeneity $n_{\mathrm{bg}}(z) = n_{\mathrm{bg}}$ of the considered material. Nevertheless, in principle the inclusion of a background refractive index profile $n_{\mathrm{bg}}(z)$ is possible within this approach.

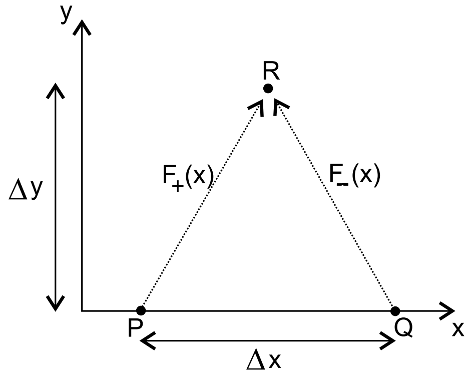

Figure B.1: Illustration of the discrete time-space grid for the application of Hartree's method to the one-dimensional Maxwell equations.

Use of the characteristic equation (B.23) yields

$$\mathrm{d}v + G_\pm \mathrm{d}u + H_\pm \mathrm{d}y = 0 \quad \text{with} \quad G_\pm = \frac{b}{c}F_\pm \quad \text{and} \quad H_\pm = -\Big(\frac{f_1}{e} + \frac{f_2}{c}F_\pm\Big)\,.$$

Maxwell's equations (B.17) and (B.18) can now be discretized with respect to the characteristic equation, following Hartree's method in Ref. 86 according to Fig. B.1 for the time-space grid points P, Q, R:

$$x_R - x_P = \frac{1}{2}\left[F_+(R) + F_+(P)\right]\Delta y\,, \tag{B.24}$$

$$x_R - x_Q = \frac{1}{2}\left[F_-(R) + F_-(Q)\right]\Delta y\,, \tag{B.25}$$

$$v_R - v_P + \frac{1}{2}\left[G_+(R) + G_+(P)\right](u_R - u_P) + \frac{1}{2}\left[H_+(R) + H_+(P)\right]\Delta y = 0\,, \tag{B.26}$$

$$v_R - v_Q + \frac{1}{2}\left[G_-(R) + G_-(Q)\right](u_R - u_Q) + \frac{1}{2}\left[H_-(R) + H_-(Q)\right]\Delta y = 0\,. \tag{B.27}$$

In case of the one-dimensional Maxwell equations the abbreviations introduced here, are explicitly given by:

$$G_\pm = \frac{b}{c}F_\pm = \pm\frac{c_0}{n_{\mathrm{bg}}}\,,$$

$$H_\pm = -\Big(\frac{f_1}{e} + \frac{f_2}{c}F_\pm\Big) = -i\omega_0 v \pm \frac{n_{\mathrm{bg}}}{c_0}(J - i\omega_0 u)\,.$$

Equations (B.24) and (B.25) yield

$$x_R - x_P = \frac{c_0}{2}\Big(\frac{1}{n_{\mathrm{bg}}} + \frac{1}{n_{\mathrm{bg}}}\Big)\Delta y\,,$$

$$x_Q - x_R = \frac{c_0}{2}\Big(\frac{1}{n_{\mathrm{bg}}} + \frac{1}{n_{\mathrm{bg}}}\Big)\Delta y\,,$$

which is just the characteristic equation (B.23) in its discretized form:

$$\Delta x = x_R - x_P = x_Q - x_R = \frac{c_0}{n_{\text{bg}}}\Delta y\,.$$

The electromagnetic fields at point R are obtained from Eqs. (B.26) and (B.27):

$$v_R - v_P + (u_R - u_P)\frac{n_{\text{bg}}}{c_0} + \frac{\Delta y}{2}\left[\frac{n_{\text{bg}}}{c_0}J_R - i\omega_0\frac{n_{\text{bg}}}{c_0}u_R - i\omega_0 v_R\right] + \frac{\Delta y}{2}H_+(P) = 0\,,$$

$$v_R - v_Q - (u_R - u_Q)\frac{n_{\text{bg}}}{c_0} + \frac{\Delta y}{2}\left[-\frac{n_{\text{bg}}}{c_0}J_R + i\omega_0\frac{n_{\text{bg}}}{c_0}u_R - i\omega_0 v_R\right] + \frac{\Delta y}{2}H_-(Q) = 0\,,$$

which yields

$$v_R\Big(1 - i\omega_0\frac{\Delta y}{2}\Big) + u_R\Big(1 - i\omega_0\frac{\Delta y}{2}\Big)\frac{n_{\text{bg}}}{c_0} = v_P + u_P\frac{n_{\text{bg}}}{c_0} - \frac{\Delta y}{2}\left[\frac{n_{\text{bg}}}{c_0}J_R + H_+(P)\right]\,, \tag{$*$}$$

$$v_R\Big(1 - i\omega_0\frac{\Delta y}{2}\Big) - u_R\Big(1 - i\omega_0\frac{\Delta y}{2}\Big)\frac{n_{\text{bg}}}{c_0} = v_Q - u_Q\frac{n_{\text{bg}}}{c_0} + \frac{\Delta y}{2}\left[\frac{n_{\text{bg}}}{c_0}J_R - H_-(Q)\right]\,. \tag{$**$}$$

Sum and difference of these equation are:

$$\begin{aligned}(*) - (**) \quad & 2u_R\Big(1 - i\omega_0\frac{\Delta y}{2}\Big)\frac{n_{\text{bg}}}{c_0} = \\ & \quad v_P + u_P\frac{n_{\text{bg}}}{c_0} - v_Q + u_Q\frac{n_{\text{bg}}}{c_0} - \Delta y J_R\frac{n_{\text{bg}}}{c_0} - \frac{\Delta y}{2}\left[H_+(P) - H_-(Q)\right]\,, \\ (*) + (**) \quad & 2v_R\Big(1 - i\omega_0\frac{\Delta y}{2}\Big) = v_P + u_P\frac{n_{\text{bg}}}{c_0} + v_Q - u_Q\frac{n_{\text{bg}}}{c_0} - \frac{\Delta y}{2}\left[H_+(P) + H_-(Q)\right]\,.\end{aligned}$$

Using the definition of $H_\pm$ again yields

$$\begin{aligned}2u_R\Big(1 - i\omega_0\frac{\Delta y}{2}\Big)\frac{n_{\text{bg}}}{c_0} = \; & (v_P - v_Q)\Big(1 + \frac{\Delta y}{2}i\omega_0\Big) + (u_P + u_Q)\Big(1 + \frac{\Delta y}{2}i\omega_0\Big)\frac{n_{\text{bg}}}{c_0} \\ & - \frac{\Delta y}{2}\left(2J_R + J_P + J_Q\right)\frac{n_{\text{bg}}}{c_0}\,,\end{aligned}$$

$$\begin{aligned}2v_R\Big(1 - i\omega_0\frac{\Delta y}{2}\Big) = \; & (v_P + v_Q)\Big(1 + \frac{\Delta y}{2}i\omega_0\Big) + (u_P - u_Q)\Big(1 + \frac{\Delta y}{2}i\omega_0\Big)\frac{n_{\text{bg}}}{c_0} \\ & - \frac{\Delta y}{2}\left(J_P - J_Q\right)\frac{n_{\text{bg}}}{c_0}\,.\end{aligned}$$

The discrete form of Maxwell's equations defined on a discrete space $\{z_j\}$ and time $\{t_n\}$ grid is obtained with the following transitions:

$$\begin{array}{lclcl} R = t_{n+1}, z_j & & u_R = E_j^{n+1} & & v_R = B_j^{n+1} \\ P = t_n, z_{j-1} & \to & u_P = E_{j-1}^{n} & & v_P = B_{j-1}^{n} \\ Q = t_n, z_{j+1} & & u_Q = E_{j+1}^{n} & & v_Q = B_{j+1}^{n} \end{array}$$

Therefore, the final result for the numerical implementation is given by:

$$
\begin{aligned}
E_j^{n+1} &= \frac{c_0}{2n_{\text{bg}}}\frac{\eta}{\eta^*}\left(B_{j-1}^n - B_{j+1}^n\right) + \frac{\eta}{2\eta^*}\left(E_{j-1}^n + E_{j+1}^n\right) - \frac{\Delta t}{4\eta^*}\left(2J_j^{n+1} + J_{j-1}^n + J_{j+1}^n\right) \, , \\
B_j^{n+1} &= \frac{\eta}{2\eta^*}\left(B_{j-1}^n + B_{j+1}^n\right) + \frac{n_{\text{bg}}}{2c_0}\frac{\eta}{\eta^*}\left(E_{j-1}^n - E_{j+1}^n\right) - \frac{n_{\text{bg}}}{c_0}\frac{\Delta t}{4\eta^*}\left(J_{j-1}^n - J_{j+1}^n\right) \, , \\
&\text{with} \quad \eta = 1 + i\omega_0\frac{\Delta t}{2} \quad \text{and} \quad J = \frac{1}{\varepsilon_0 n_{\text{bg}}^2}\Big(j + \frac{\partial P}{\partial t} - i\omega_0 P\Big) \, .
\end{aligned}
$$

The index n corresponds to the discrete steps in time and the index j denotes the position on the discrete space grid.

B.3. The Biexciton Equation

The evaluation of the Coulomb matrix elements in the two-exciton product basis turns out to be numerically very demanding, especially parts of the exchange interaction matrix element $W^{\text{XC}}_{nmn'm'}(q,q')$ (5.16) with its four-fold real space integral cannot be factorized at all. For the spatially inhomogeneous system care must be taken for a proper treatment of the Coulomb singularity in $W^{\text{C}}_{nmn'm'}(\mathbf{q},\mathbf{q}')$ and $W^{\text{XC}}_{nmn'm'}(\mathbf{q},\mathbf{q}')$. It has been removed numerically in analogy to Appendix B.1. All told, the numerical calculation is a challenge. Being well-suited for a parallel evaluation on several processing units, it has been performed on a modern IBM Regatta supercomputer system. A very efficient distribution to several processing units is possible since each matrix element does not depend on the others and therefore only a very small amount of communication is needed. Once evaluated, the matrix elements can be stored for each given set of material parameters. Using this input data the solution of the equations of motion can be performed on a desktop computer, using a fourth order Runge-Kutta algorithm for the material equations (5.12) and (5.13) and Hartree's method for the discretization of Maxwell's equations (3.4a) and (3.4b). The solutions are obtained in the rotating picture to eliminate the large band-gap energies in the material equations. More general details concerning Hartree's method are given in Ref. 86 and their application to the one-dimensional Maxwell equations is summarized in the previous section.

For a proper evaluation of the matrix elements, the numerical discretization scheme of real space coordinates and in-plane momenta has to be chosen very carefully. To avoid a waste of computing resources for the very time consuming calculations, Gaussian quadrature points are chosen for the evaluation of momentum space integrals. This way, compared to an equidistantly chosen grid, much better numerical convergence with a comparably small number of quadrature points is obtained. In the end, good numerical convergence for the nonlinear transmission spectra and the biexciton binding energy is reached using the following sets of grid points for the solution of the excitonic and biexcitonic problem. For the exciton wave functions, typically a real space step size of $\approx 0.1\,\mathrm{a}_0^{\mathrm{X}}$ and 70 Gaussian quadrature points in momentum space accumulated below $k = 20/a_0^{\mathrm{X}}$ are used.

Biexciton grid points are typically chosen to 16 angle points, 32 Gaussian q and k quadrature points, and 24 equidistant points for real space integrals. Contributions from in plane momenta k with $k > 20/a_0^{\mathrm{X}}$ can be neglected in a very good approximation because all relevant wave functions and Coulomb matrix elements vanish for large momenta, compare Figs. 5.1, 5.2 on pages 81, 82 and Figs. B.2-B.5.

B.3.1. Coulomb Matrix Elements

In addition to the results shown in Section 5.3.1 on page 81, Figs. B.2-B.5 show examples for inter-site diagonal and off-diagonal blocks of the direct $W^{\mathrm{C}}_{nmn'm'}(q,q')$ (5.15) and exchange $W^{\mathrm{XC}}_{nmn'm'}(q,q')$ (5.16) two-exciton Coulomb interaction. Even qualitatively different shapes are found, depending on the internal exciton quantum numbers n, m, n', m' and therefore depending on the space-dependence of the contributing exciton states $\phi_m(\mathbf{k}, z_{\mathrm{e}}, z_{\mathrm{h}})$. The two-exciton exchange matrix elements $W^{\mathrm{XC}}_{nmn'm'}(q,q')$ show a similar shape for all on-site and inter-site diagonal matrix elements, only quantitative differences are obtained. Two typical examples are shown in Figs. 5.2 and B.4. Figure B.5 gives an example for an off-diagonal block. The grid lines on the surface plots are connected to the discretization of the exciton-exciton relative momenta q according to Section B.3. These grid points are accumulated in momentum space regions with large variation of the magnitude of the Coulomb matrix elements.

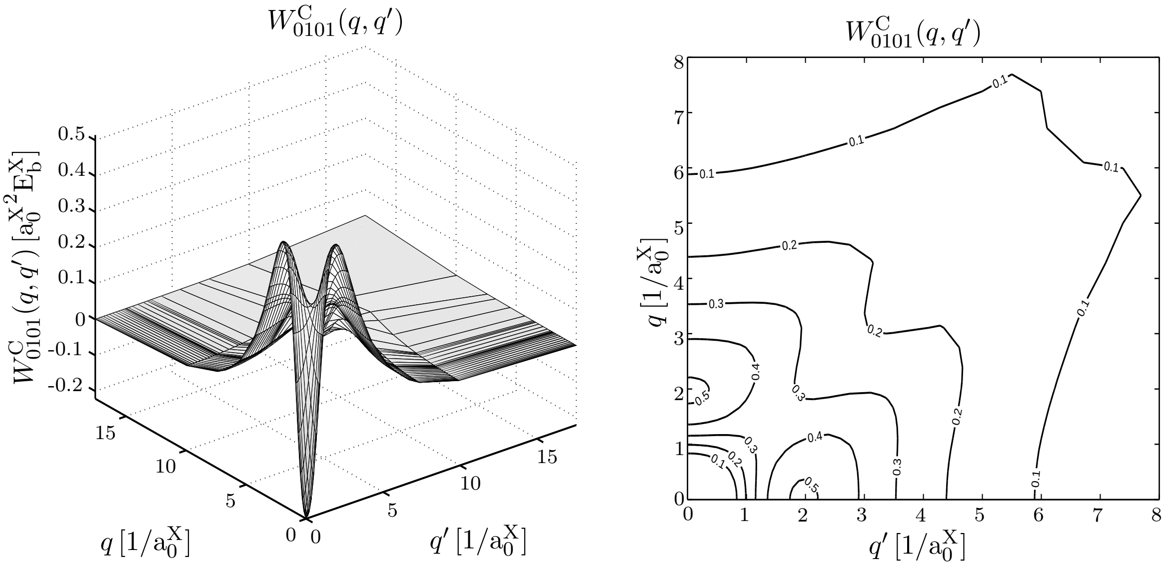

Figure B.2: Inter-site diagonal matrix element $W^{\mathrm{C}}_{0101}(q,q')$ of the direct exciton-exciton Coulomb interaction (5.15). Left: Surface plot. Right: Contour plot.

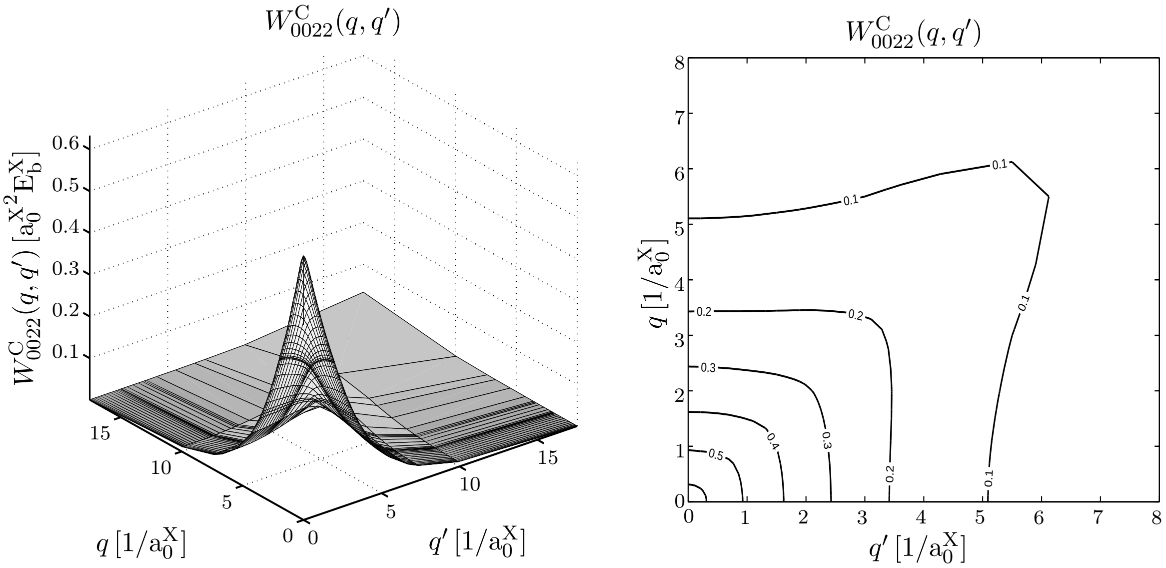

Figure B.3: Off-diagonal matrix element $W^{\mathrm{C}}_{0022}(q,q')$ of the direct exciton-exciton Coulomb interaction (5.15). Left: Surface plot. Right: Contour plot.

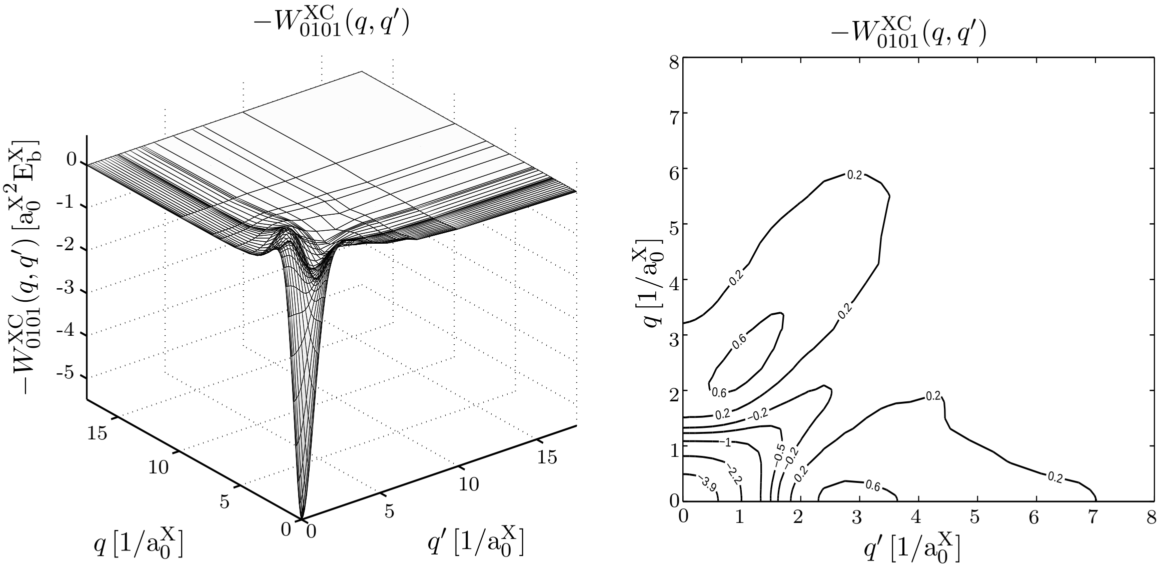

Figure B.4: Inter-site diagonal matrix element $W^{\mathrm{XC}}_{0101}(q,q')$ of the exchange exciton-exciton Coulomb interaction (5.16). Left: Surface plot. Right: Contour plot.

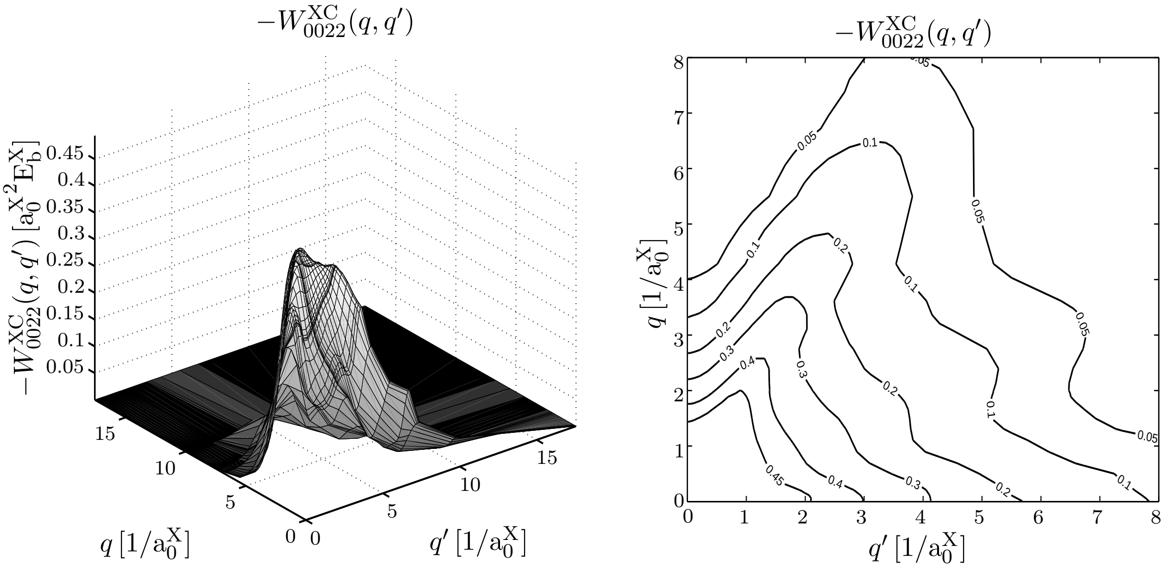

Figure B.5: Off-diagonal matrix element $W^{\mathrm{XC}}_{0022}(q,q')$ of the exchange exciton-exciton Coulomb interaction (5.16). Left: Surface plot. Right: Contour plot.

B.3.2. Matrix Elements in the One-Particle Product Basis

An alternative method for the calculation of the matrix elements in the two-exciton product basis is discussed in this section. Expanding the real space dependence of the exciton eigenfunctions $\phi_m(\mathbf{k}, z_\mathrm{e}, z_\mathrm{h})$ in terms of products of one-particle eigenstates $\chi_i(z_\mathrm{e})$ for electrons and $\varphi_j(z_\mathrm{h})$ for holes,

$$\phi_m(\mathbf{k}, z_\mathrm{e}, z_\mathrm{h}) = \sum_{ij} a^m_{ij}(\mathbf{k})\chi_i(z_\mathrm{e})\varphi_j(z_\mathrm{h})\,, \tag{B.28}$$

a multi-subband representation of the matrix elements (5.15), (5.16), (5.20) is obtained. The contributions of the subbands i, j are determined by the expansion coefficients

$$a^m_{ij}(\mathbf{k}) = \int \mathrm{d}z_\mathrm{e}\mathrm{d}z_\mathrm{h}\chi^*_i(z_\mathrm{e})\varphi^*_j(z_\mathrm{h})\phi_m(\mathbf{k}, z_\mathrm{e}, z_\mathrm{h})\,. \tag{B.29}$$

The exciton eigenenergy ε_m may serve as an estimate for the convergence of the expansion (B.28) with increasing number of considered one-particle states. ε_m is given by the expectation value of the exciton Hamiltonian $\mathcal{H}^\mathrm{X}$ with respect to the m^th eigenstate $|m\rangle$ [g]

$$\begin{aligned}\varepsilon_m = \langle m|\mathcal{H}^\mathrm{X}|m\rangle &= \sum_{ijkl\mathbf{k}\mathbf{k}'} a^{m*}_{ij}(\mathbf{k})H^{ijkl}_{\mathbf{k}\mathbf{k}'}a^m_{kl}(\mathbf{k}')\\ &= \sum_{ij\mathbf{k}} |a^m_{ij}(\mathbf{k})|^2\Big(\varepsilon^\mathrm{e}_i + \varepsilon^\mathrm{h}_j + E_\mathrm{gap} + \frac{\hbar^2\mathbf{k}^2}{2\mu^*}\Big) + \sum_{ijkl\mathbf{k}\mathbf{k}'} V^{ijkl}_{\mathbf{k}\mathbf{k}'}a^{m*}_{ij}(\mathbf{k})a^m_{kl}(\mathbf{k}')\,.\end{aligned}$$

---

[g] The Coulomb matrix elements $V^{ijkl}_{\mathbf{k}\mathbf{k}'} = \int \mathrm{d}z_\mathrm{e}\mathrm{d}z_\mathrm{h}\chi^*_i(z_\mathrm{e})\varphi^*_j(z_\mathrm{h})V_{\mathbf{k}\mathbf{k}'}(z_\mathrm{e}-z_\mathrm{h})\chi_k(z_\mathrm{e})\varphi_l(z_\mathrm{h})$ and one-particle energies ε^e_i, ε^h_j are defined in analogy to Section 3.4.

This expression can be evaluated with respect to approximated exciton states $a^m_{ij}(\mathbf{k})$ by truncation of the i, j-sum over one-particle states in Eq. (B.28). The calculation of the exciton eigenstates $\phi_m(\mathbf{k}, z_\mathrm{e}, z_\mathrm{h})$ is done in real space. This approach is advantageous to the calculation with respect to a discrete one-particle basis as already discussed in Section 3.4. The contributions $a^m_{ij}(\mathbf{k})$ of the one-particle states i, j are calculated by use of Eq. (B.29).

The coefficients (B.29) are not identical to those that follow from a direct calculation of the exciton eigenstates in a truncated one-particle basis as done in Section 3.4. For the calculations in Section 3.4 Coulomb interaction with particles in higher one-particle states is neglected from the beginning, whereas these contributions are at first taken into account for the calculation of the exciton states $\phi_m(\mathbf{k}, z_\mathrm{e}, z_\mathrm{h})$ in this section. This results in a different $\mathbf{k}$-dependence of the $a^m_{ij}(\mathbf{k})$ compared to the eigenstates obtained in Section 3.4. Neglecting higher one-particle states in Section 3.4 from the very beginning also influences the contributions from lower ones. Nevertheless, the diagonalization of the exciton Hamiltonian in Section 3.4 with respect to a truncated one-particle basis yields exact eigenstates within the considered basis, whereas strictly speaking the $a^m_{ij}(\mathbf{k})$ in Eq. (5.22) are no eigenstates to the Hamiltonian $\mathcal{H}^\mathrm{X}$ in the truncated basis of one-particle states. Agreement of the exciton eigenstates in Section 3.4 and the $a^m_{ij}(\mathbf{k})$ in this section is only obtained if the complete set of one-particle states is taken into account for both calculations. The expansion (B.28) may be used as a numerical technique for the calculation of Coulomb matrix elements. It only yields meaningful results as long as sufficient numerical convergence of the expansion (B.28) with the considered number of one-particle states is reached.

The expansion (B.28), together with (5.15), (5.16), (5.20), results in the biexcitonic matrix elements in the one-particle product basis, here given for infinitely high potential barriers:[h)]

$$\begin{aligned} W^C_{nmn'm'}(\mathbf{q},\mathbf{q}') = &\\ &\sum_{ijkl}\Bigg[V^{ijkl}_{\mathbf{q}^-}\Big[\sum_{\mathbf{k}r}\big(a^{n*}_{rj}(\mathbf{k})a^{n'}_{rk}(\mathbf{k}+\beta\mathbf{q}^-) - a^{n*}_{jr}(\mathbf{k})a^{n'}_{kr}(\mathbf{k}-\alpha\mathbf{q}^-)\big)\Big] \\ &\qquad\times\Big[\sum_{\mathbf{k}'s}\big(a^{m*}_{si}(\mathbf{k}')a^{m'}_{sl}(\mathbf{k}'-\beta\mathbf{q}^-) - a^{m*}_{is}(\mathbf{k}')a^{m'}_{ls}(\mathbf{k}'+\alpha\mathbf{q}^-)\big)\Big]\Bigg], \end{aligned} \tag{B.30}$$

$$\begin{aligned} W^{XC}_{nmn'm'}(\mathbf{q},\mathbf{q}') = &\sum_{\mathbf{k}\mathbf{k}'}\sum_{ijklrs} a^{n*}_{ij}(\mathbf{k}+\alpha\mathbf{q}^-)a^{m*}_{kl}(\mathbf{k}'+\beta\mathbf{q}^+) \\ \times\Bigg[&V^{ijsr}_{\mathbf{k}-\mathbf{k}'}a^{n'}_{ks}(\mathbf{k}')a^{m'}_{rl}(\mathbf{k}'+\alpha\mathbf{q}^-+\beta\mathbf{q}^+) - V^{ljsr}_{\mathbf{k}-\mathbf{k}'}a^{n'}_{ks}(\mathbf{k}')a^{m'}_{ir}(\mathbf{k}+\alpha\mathbf{q}^-+\beta\mathbf{q}^+) \\ &+V^{klsr}_{\mathbf{k}-\mathbf{k}'}a^{n'}_{rj}(\mathbf{k})a^{m'}_{is}(\mathbf{k}+\alpha\mathbf{q}^-+\beta\mathbf{q}^+) - V^{kisr}_{\mathbf{k}-\mathbf{k}'}a^{n'}_{rj}(\mathbf{k})a^{m'}_{sl}(\mathbf{k}'+\alpha\mathbf{q}^-+\beta\mathbf{q}^+)\Bigg], \end{aligned} \tag{B.31}$$

[h)] The inclusion of finite potential barriers in this formulation is no problem in general but further complicates the notation since electron and hole one-particle wave functions which enter the Coulomb matrix elements would no longer be equal.

$$S_{nmn'm'}(\mathbf{q},\mathbf{q}') = \sum_{\mathbf{k}} \sum_{ijkl} a^{n*}_{ij}(\mathbf{k}+\alpha\mathbf{q}) a^{m*}_{kl}(\mathbf{k}+\mathbf{q}'+\beta\mathbf{q}) a^{n'}_{kj}(\mathbf{k}+\alpha\mathbf{q}') a^{m'}_{il}(\mathbf{k}+\mathbf{q}+\beta\mathbf{q}') \,. \tag{B.32}$$

These matrix elements with contributions from several subbands represent a multi-subband version of the matrix elements given in Ref. 67 for a two-dimensional system. The result therein is reproduced by the one-subband limit with $a^{m}_{00}(\mathbf{k})$ being the two-dimensional exciton wave function.

Finally, according to the expansion (B.28), the z-dependence of the system has been expressed in terms of several electronic subbands for the calculation of the biexcitonic matrix elements. Taking into account more than one subband becomes necessary for layers with finite thickness leaving the quasi two-dimensional quantum-well limit. An analysis of the influence of the dimensionality on the contributions from higher subbands has been given in Section 5.3.2. For thin quantum-wells the inclusion of only one subband is sufficient in a very good approximation.

In contradiction to the one-subband version in Ref. 67, the Coulomb singularities in (B.30) and (B.31) do not vanish anymore and have to be removed carefully in analogy to Appendix B.1. The calculation of the exchange matrix (B.31) turns out to be most time-consuming. The numerical effort for its calculation increases with the number of considered one-particle states to the power of six whereas the real space representation led to a four-fold real space integral in Eq. (5.16). For rather thin layers ($L \lesssim 5\,\mathrm{a}_0^{\mathrm{X}}$) with good convergence of the expansion in Eq. (B.28), only a few coefficients $a^{m}_{ij}(\mathbf{k})$ have to be taken into account. In that case the evaluation of a six-fold sum in Eq. (B.31) over one-particle states becomes less demanding than a proper evaluation of the corresponding four-fold real space integral in Eq. (5.16). For thicker layer ($L \gtrsim 5\,\mathrm{a}_0^{\mathrm{X}}$) the situation is just vice versa.

List of Figures

List of Tables

Index

Bibliography

[1] S. L. Chuang. *Physics of optoelectronic devices.* Wiley series in pure and applied optics. Wiley-Interscience publication, New York, 1995.

[2] P. Michler, A. Kiraz, C. Becher, W. V. Schoenfeld, P. M. Petroff, L. D. Zhang, E. Hu, and A. Imamoglu. A quantum dot single-photon turnstile device. *Science*, 290:2282, 2000.

[3] A. D'Andrea and R. Del Sole. Wannier-mott excitons in semi-infinite crystals: Wave functions and normal-incidence reflectivity. *Phys. Rev. B*, 25(6):3714, 1982.

[4] A. D'Andrea and N. Tomassini. Exciton quantization in symmetric and asymmetric quantum wells: Pseudo-two-dimensional behavior. *Phys. Rev. B*, 47(12):7176, 1993.

[5] J. Tignon, T. Hasche, D. S. Chemla, H. C. Schneider, F. Jahnke, and S. W. Koch. Unified picture of polariton propagation in bulk GaAs semiconductors. *Phys. Rev. Lett.*, 84(15):3382, 2000.

[6] H. C. Schneider, F. Jahnke, S. W. Koch, J. Tignon, T. Hasche, and D. S. Chemla. Polariton propagation in high quality semiconductors: Microscopic theory and experiment versus additional boundary conditions. *Phys. Rev. B*, 63:045202, 2001.

[7] V. M. Axt and A. Stahl. A dynamics-controlled truncation scheme for the hierarchy of density matrices in semiconductor optics. *Z. Phys. B*, 93:195, 1994.

[8] V. M. Axt and A. Stahl. The role of the biexciton in a dynamic density matrix theory of the semiconductor band edge. *Z. Phys. B*, 93:205, 1994.

[9] M. Lindberg, Y. Z. Hu, R. Binder, and S. W. Koch. $\chi^{(3)}$ formalism in optically excited semiconductors and its applications in four-wave-mixing spectroscopy. *Phys. Rev. B*, 50(24):18060, 1994.

[10] J. J. Hopfield. Theory of the contribution of excitons to the complex dielectric constant of crystals. *Phys. Rev.*, 112(5):1555, 1958.

[11] H. Haug and S. W. Koch. *Quantum Theory of the Optical and Electronic Properties of Semiconductors.* World Scientific Publishing, Singapore, 3rd edition, 1995.

[12] S. Lankes, M. Meier, T. Reisinger, and W. Gebhardt. Hole mass determination in ZnSe by observation of standing polariton waves. *J. Appl. Phys.*, 80(7):4049, 1996.

[13] U. Neukirch, K. Wundke, J. Gutowski, and D. Hommel. Propagation of femtosecond pulses in thin ZnSe layers. *Phys. Stat. Sol. B*, 196:473, 1996.

[14] Z. K. Tang, A. Yanase, Y Segawa, N. Matsuura, and K. Cho. Quantization of excitons in CuCl epitaxial thin films: Behavior between a two-dimensional quantum well and the bulk. *Phys. Rev. B*, 52(4):2640, 1995.

[15] L. Schultheis and K. Ploog. Quantization of excitonic polaritons in thin GaAs layers. *Phys. Rev. B*, 29(12):7058, 1984.

[16] N. Tomassini, A. D'Andrea, R. Del Sole, H. Tuffigo-Ulmer, and R. T. Cox. Center-of-mass quantization of excitons in CdTe/$\mathrm{Cd_{1-x}Zn_xTe}$ quantum wells. *Phys. Rev. B*, 51(8):5005, 1995.

[17] D. Greco, R. Cingolani, A. D'Andrea, N. Tomassini, L. Vanzetti, and A. Franciosi. Center of mass quantization of excitons in $\mathrm{Zn_{1-x}Cd_xSe}$/ZnSe quantum-wells. *Phys. Rev. B*, 54(23):16998, 1996.

[18] M. L. Cohen and J. R. Chelikowski. *Electronic Structure and Optical Properties of Semiconductors*, volume 75 of *Springer Series in Solid-State Sciences.* Springer, 2nd edition, 1989.

[19] W. Schäfer and M. Wegener. *Semiconductor Optics and Transport Phenomena.* Springer Berlin, 2002.

[20] C. Sieh, T. Meier, F. Jahnke, A. Knorr, S. W. Koch, P. Brick, M. Hübner, C. Ell, J. Prineas, G. Khitrova, and H. M. Gibbs. Coulomb memory signatures in the excitonic optical Stark effect. *Phys. Rev. Lett.*, 82(15):3112, 1999.

[21] N. Baer, P. Gartner, and F. Jahnke. Coulomb effects in semiconductor quantum dots. *Eur. Phys. J. B*, 42:231, 2004.

[22] H. Dierks and G. Czycholl. Tight-binding calculations of the subband structures of zincblende-semiconductor (001) quantum wells. *Z. Phys. B*, 99(2):207, 1996.

[23] H. Dierks and G. Czycholl. Tight-binding calculation of linear excitonic absorption spectra of single quantum wells. *J. Cryst. Growth*, 185:877, 1998.

[24] J. M. Luttinger and W. Kohen. Motion of electrons and holes in perturbed periodic fields. *Phys. Rev.*, 97:869, 1955.

[25] J. M. Luttinger. Quantum theory of cyclotron resonance in semiconductors: General theory. *Phys. Rev.*, 102:1030, 1956.

[26] F. Schwabl. *Quantenmechanik.* Springer, Berlin, 5th edition, 1998.

[27] G. Czycholl. *Theoretische Festkörperphysik: Von den klassischen Modellen zu modernen Forschungsthemen.* Vieweg, Braunschweig/Wiesbaden, 2000.

[28] T. Meier and S. W. Koch. Excitons versus unbound electron-hole pairs and their influence on exciton bleaching: A model study. *Phys. Rev. B*, 59(20):13202, 1999.

[29] M. Buck, L. Wischmeier, S. Schumacher, G. Czycholl, F. Jahnke, T. Voss, I. Rückmann, and J. Gutowski. Light-polarization and intensity dependence of higher-order nonlinearities in excitonic FWM signals. *Eur. Phys. J. B*, 42:175, 2004.

[30] S. R. Bolton, U. Neukirch, L. J. Sham, D. S. Chemla, and V. M. Axt. Demonstration of sixth-order Coulomb correlations in a semiconductor single quantum well. *Phys. Rev. Lett.*, 85(9):2000, 2000.

[31] V. M. Axt, S. R. Bolton, U. Neukirch, L. J. Sham, and D. S. Chemla. Evidence of sixth-particle Coulomb correlations in six-wave-mixing signals from a semiconductor quantum well. *Phys. Rev. B*, 63:115303, 2001.

[32] W. Schäfer, R. Lövenich, N. A. Fromer, and D. S. Chemla. From coherently excited highly correlated states to incoherent relaxation processes in semiconductors. *Phys. Rev. Lett.*, 86(2):344, 2001.

[33] R. Lövenich, C. W. Lai, D. Hägele, D. S. Chemla, and W. Schäfer. Semiconductor polarization dynamics from coherent to incoherent regime: Theory and experiment. *Phys. Rev. B*, 66:045306, 2002.

[34] S. I. Pekar. *Sov. Phys. JETP*, 6:785, 1958.

[35] C. S. Ting, M. J. Frankel, and J. L. Birman. *Solid State Commun.*, 17:1285, 1975.

[36] V. A. Kiselev, B. S. Razbirin, and I. N. Uraltsev. Electrodynamics of bounded spatially dispersive media: The additional boundary conditions. *Phys. Stat. Sol. B*, 72:161, 1975.

[37] E. F. Venger and V. N. Piskovoi. Consistency of boundary conditions in crystal optics with spatial dispersion. *Phys. Rev. B*, 70:115107, 2004.

[38] E. A. Muljarov and R. Zimmermann. Exciton polariton including continuum states: Microscopic versus additional boundary conditions. *Phys. Rev. B*, 66:235319, 2002.

[39] A. D'Andrea and R. Del Sole. Exciton quantization and polariton propagation in semiconductor slabs: From semi-infinite crystals to quantum wells. *Phys. Rev. B*, 41(3):1413, 1990.

[40] M. Combescot, R. Combescot, and B. Roulet. The exciton dead layer revisited. *Eur. Phys. J.*, 23:139, 2001.

[41] E. Butkov. *Mathematical Physics*. Addison-Wesley Series in Advanced Physics. Addison-Wesley Publishing Company, London, 1968.

[42] K. Henneberger. Additional boundary conditions: An historical mistake. *Phys. Rev. Lett.*, 80:2889, 1998.

[43] S. Schumacher, G. Czycholl, F. Jahnke, I. Kudyk, H. I. Rückmann, J. Gutowski, A. Gust, G. Alexe, and D. Hommel. Polariton propagation in shallow-confinement heterostructures: Microscopic theory and experiment showing the breakdown of the dead-layer concept. *Phys. Rev. B*, 70(23):235340, 2004.

[44] S. Lankes, T. Reisinger, B. Hahn, C. Meier, M. Meier, and W. Gebhardt. Composition dependent determination of band offsets in ZnCdSe/ZnSe and ZnSe/ZnSSe SQW by optical means. *J. Cryst. Growth*, 159:480, 1996.

[45] N. Baer. Optische Eigenschaften von Halbleiter-Quantenpunkten. Diplomarbeit, Universität Bremen, Institut für Theoretische Physik, 2003.

[46] J. E. Bernard and A. Zunger. Electronic structure of ZnS, ZnSe, ZnTe, and their pseudobinary alloys. *Phys. Rev. B*, 36:3199, 1987.

[47] K. Shahzad, D. J. Olego, and C. G. Van de Walle. Optical characterization and band offsets in ZnSe-ZnS_xSe_{1-x} strained-layer superlattices. *Phys. Rev. B*, 38:1417, 1988.

[48] Su-Huai Wei and A. Zunger. Calculated natural band offsets of all II-VI and III-V semiconductors: Chemical trends and the role of cation d orbitals. *Appl. Phys. Lett.*, 72(16):2011, 1998.

[49] G. F. Schötz, W. Sedlmeier, M. Lindner, and W. Gebhardt. The pressure dependence of the intraimpurity absorption and the charge transfer process of ZnS:Ni and ZnSe:Ni. *J. Phys. Cond. Mat.*, 7:795, 1995.

[50] C. G. Van de Walle and J. Neugebauer. Universal alignment of hydrogen levels in semiconductors, insulators and solutions. *Nature*, 423:626, 2003.

[51] H. W. Hölscher, A. Nöthe, and C. Uihlein. Investigation of band masses and g values of ZnSe by two-photon magnetoabsorption. *Phys. Rev. B*, 31:2379, 1985.

[52] S. Lankes, B. Hahn, C. Meier, F. Hierl, M Kastner, A. Rosenauer, and W. Gebhardt. Photoreflectance measurements on ZnSe/$ZnS_{0.25}Se_{0.75}$ SQW. *Phys. Stat. Sol. a*, 152:123, 1995.

[53] B. Rockwell, H. R. Chandrasekhar, M. Chandrasekhar, A. K. Ramdas, M. Kobayashi, and R. L. Gunshor. Pressure tuning of strains in semiconductor heterostructures: (ZnSe epilayer)/(GaAs epilayer). *Phys. Rev. B*, 44(20):11307, 1991.

[54] I. Galbraith. Simple formula for exciton binding energy in quantum wells with zero band offsets. *Phys. Rev. B*, 45(12):6950, 1992.

[55] V. M. Axt, A. Stahl, E. J. Mayer, P. Haring Bolivar, S. Nüsse, K. Ploog, and K. Köhler. Four-wave-mixing theory beyond the Semiconductor Bloch Equations. *Z. Phys. B*, 188:447, 1995.

[56] N. H. Kwong, R. Takayama, I. Rumyantsev, M. Kuwata-Gonokami, and R. Binder. Third-order exciton-correlation and nonlinear cavity-polariton effects in semiconductor microcavities. *Phys. Rev. B*, 64:045316, 2001.

[57] N. H. Kwong, R. Takayama, I. Rumyantsev, M. Kuwata-Gonokami, and R. Binder. Evidence of nonperturbative continuum correlations in two-dimensional exciton systems in semiconductor microcavities. *Phys. Rev. Lett.*, 87:027402, 2001.

[58] M. E. Donovan, A. Schülzgen, J. Lee, P.-A. Blanche, N. Peyghambarian, G. Khitrova, H. M. Gibbs, I. Rumyantsev, N. H. Kwong, R. Takayama, Z. S. Yang, and R. Binder. Evidence for intervalence band coherences in semiconductor quantum wells via coherently coupled optical stark shifts. *Phys. Rev. Lett.*, 87:237402, 2001.

[59] J. Förstner, A. Knorr, and S. W. Koch. Nonlinear pulse propagation in semiconductors: Hole burning within a homogeneous line. *Phys. Rev. Lett.*, 86(3):476, 2001.

[60] F. Jahnke. A many-body theory for laser emission and excitonic effects in semiconductor microcavities. Habilitationsschrift, Philipps-Universität Marburg, Fachbereich Physik, 1996.

[61] G. Khitrova, H. M. Gibbs, F. Jahnke, M. Kira, and S. W. Koch. Nonlinear optics of normal-mode-coupling semiconductor microcavities. *Rev. Mod. Phys.*, 71(5):1591, 1999.

[62] A. L. Ivanov and H. Haug. Self-consistent theory of the biexciton optical nonlinearity. *Phys. Rev. B*, 48:1490, 1993.

[63] N. C. Nielsen, S. Linden, J. Kuhl, J. Förstner, A. Knorr, S. W. Koch, and H. Giessen. Coherent nonlinear pulse propagation on a free-exciton resonance in a semiconductor. *Phys. Rev. B*, 64:245202, 2001.

[64] J. S. Nägerl, B. Stabenau, G. Böhne, S. Dreher, R. G. Ulbrich, G. Manzke, and K. Henneberger. Polariton pulse propagation through GaAs: Excitation-dependent phase shifts. *Phys. Rev. B*, 63:235202, 2001.

[65] U. Neukirch and K. Wundke. Propagation of confined excitonic polaritons at high densities. *Phys. Rev. B*, 55(23):15408, 1997.

[66] H. G. Breunig, T. Voss, I. Rückmann, J. Gutowski, V. M. Axt, and T. Kuhn. Influence of higher Coulomb correlations on coherent-control signals from a ZnSe quantum well. *J. Opt. Soc. Am. B*, 20:1769, 2003.

[67] R. Takayama, N. H. Kwong, I. Rumyantsev, M. Kuwata-Gonokami, and R. Binder. T-matrix analysis of biexcitonic correlations in the nonlinear optical response of semiconductor quantum wells. *Eur. Phys. J. B*, 25:445, 2002.

[68] I. Rumyantsev, N. H. Kwong, R. Takayama, and R. Binder. Effects of intervalence band coherences on the coherently coupled heavy-hole-light-hole stark shift in semiconductor quantum wells. *Phys. Rev. B*, 65:245325, 2002.

[69] D. A. Kleinman. Binding energy of biexcitons and bound excitons in quantum wells. *Phys. Rev. B*, 28(2):871, 1983.

[70] J. R. Haynes. Experimental proof of the excistence of a new electronic complex in silicon. *Phys. Rev. Lett.*, 4(7):361, 1960.

[71] R. C. Miller, D. A. Kleinman, A. C. Gossard, and O. Munteanu. Biexcitons in GaAs quantum wells. *Phys. Rev. B*, 25(10):6545, 1982.

[72] J. Zhang, T. Pang, and C. Chen. Biexcitons in quantum wells: A quantum Monte Carlo study. *Phys. Lett. A*, 206:101, 1995.

[73] I.-K. Oh and J. Singh. Geometric approach to determine the binding energy of quasi-two-dimensional biexcitons. *Phys. Rev. B*, 60(4):2528, 1999.

[74] D. Birkedal, J. Singh, V. G. Lyssenko, J. Erland, and J. M. Hvam. Binding of quasi-two-dimensional biexcitons. *Phys. Rev. Lett.*, 76(4):672, 1996.

[75] W. Schäfer, D. S. Kim, J. Shah, T. C. Damen, J. E. Cunningham, K. W. Goossen, L. N. Pfeiffer, and K. Köhler. Femtosecond coherent fields induced by many-particle correlations in transient four-wave mixing. *Phys. Rev. B*, 53(24):16429, 1996.

[76] M. Buck. Theoretische Beschreibung kohärenter optischer Nichtlinearitäten in Halbleiter-Quantenfilmen. Dissertation, Universität Bremen, Institut für Theoretische Physik, 2004.

[77] H. G. Breunig. Einfluss optischer Nichtlinearitäten auf die kohärente Kontrolle von exzitonischen Anregungen in ZnSe-Quantentrögen. Dissertation, Universität Bremen, Institut für Festkörperphysik, 2003.

[78] S. Schumacher. Zeitabhängige Schrödingergleichung für wechselwirkende Elektronensysteme. Diplomarbeit, Universität Bremen, Institut für Theoretische Physik, 2001.

[79] A. Askar and A. S. Cakmak. Explicit integration method for the time-dependent Schrödinger equation for collision problems. *J. Chem. Phys.*, 68:2794, 1978.

[80] C. Leforestier, R. H. Bisseling, C. Cerjan, M. D. Feit, R. Friesner, A. Guldberg, A. Hammerich, G. Jolichard, W. Karrlein, H.-D. Meyer, N. Lipkin, O. Roncero, and R. Kosloff. A comparison of different propagation schemes for the time dependent Schrödinger equation. *J. Comput. Phys.*, 94:59, 1991.

[81] W. H. Press, S. A. Teukolsky, W. T. Vetterling, and B. P. Flannery. *Numerical recipes in C: The art of scientific computing.* Cambridge University Press, New York, 2nd edition, 1988.

[82] P. S. Pacheco. *Parallel programming with MPI.* Morgan Kaufmann Publishers, San Francisco, 1997.

[83] W. Gropp, E. Lusk, and R. Thakur. *Using MPI-2, Advanced features of the Message-Passing Interface.* Scientific and engineering computation series. The MIT Press, Cambridge, Massachusetts, 1999.

[84] H. C. Schneider. Zur Theorie der Lichtausbreitung und Spin-Optik in Halbleitern. Dissertation, Universität Marburg, Fachbereich Physik, 1999.

[85] F. M. Gomes and D. C. Sorensen. Arpack++, An object oriented version of ARPACK eigenvalue package. User guide, 1998.

[86] W. F. Ames. *Numerical Methods for Partial Differential Equations.* Computer Science and Scientific Computing. Academic Press Inc., San Diego, 3rd edition, 1992.

[87] I. N. Bronstein, K. A. Semendjajew, G. Musiol, and H. Mühlig. *Taschenbuch der Mathematik.* Harri Deutsch, Frankfurt am Main, 1991.

Publications connected to this work:

- “Microscopic Description of Exciton-Polaritons in Thin Semiconductor Layers”
  S. Schumacher, G. Czycholl, and F. Jahnke, *Phys. Stat. Sol. B*, 234:172, 2002

- “Light-polarization and intensity dependence of higher-order nonlinearities in excitonic FWM signals”
  M. Buck, L. Wischmeier, S. Schumacher, G. Czycholl, F. Jahnke, T. Voss, I. Rückmann, and J. Gutowski, *Eur. Phys. J. B*, 42:175, 2004

- “Polariton propagation in shallow-confinement heterostructures: Microscopic theory and experiment showing the breakdown of the dead-layer concept”
  S. Schumacher, G. Czycholl, F. Jahnke, I. Kudyk, H. I. Rückmann, J. Gutowski, A. Gust, G. Alexe, and D. Hommel, *Phys. Rev. B*, 70:235340, 2004

- “Coherent Propagation of Polaritons in Semiconductor Heterostructures: Nonlinear Pulse Transmission in Theory and Experiment”
  S. Schumacher, G. Czycholl, F. Jahnke, I. Kudyk, L. Wischmeier, I. Rückmann, T. Voss, J. Gutowski, A. Gust, and D. Hommel, submitted

Conference contributions with publication:

- 26th International Conference on the Physics of Semiconductors (ICPS), Edinburgh (UK), 2002
  “Microscopic description of exciton-polaritons in thin semiconductor layers”, S. Schumacher, G. Czycholl, and F. Jahnke

- 14th International Conference on Ultrafast Phenomena, Niigata (Japan), 2004
  “Evidence of higher-order nonlinearities on excitonic FWM signals in microscopic theory and experiment”,
  L. Wischmeier, I. Rückmann, J. Gutowski, M. Buck, S. Schumacher, G. Czycholl, and F. Jahnke, in print

- 27th International Conference on the Physics of Semiconductors (ICPS), Flagstaff, Arizona (USA), 2004
  “Microscopic Theory for Nonlinear Polariton Propagation”, S. Schumacher, G. Czycholl, and F. Jahnke, in print

- Conference on lasers and electro-optics / Quantum electronic & laser-science conference (CLEO/QELS), Baltimore, Maryland (USA), 2005
  “Polariton Propagation in Shallow-Confinement Heterostructures”,
  S. Schumacher, G. Czycholl, F. Jahnke, I. Kudyk, H. I. Rückmann, J. Gutowski, A. Gust, G. Alexe, and D. Hommel, accepted

Conference contributions:

- Frühjahrstagung der Deutschen Physikalischen Gesellschaft, Regensburg (Germany), 2002
  "Mikroskopische Beschreibung von Exziton-Polaritonen in dünnen Halbleiter-Schichten", S. Schumacher, G. Czycholl, and F. Jahnke
- Frühjahrstagung der Deutschen Physikalischen Gesellschaft, Dresden (Germany), 2003
  "Polariton-Propagation in dünnen Halbleiterschichten", S. Schumacher, G. Czycholl, and F. Jahnke
- Marchmeeting of the American Physical Society, Austin, Texas (USA), 2003,
  "Polariton-Propagation in Thin Semiconductor Layers", S. Schumacher, G. Czycholl, and F. Jahnke
- Frühjahrstagung der Deutschen Physikalischen Gesellschaft, Regensburg (Germany), 2004
  "Nichtlineare Polariton-Propagation in dünnen Halbleiterschichten", S. Schumacher, G. Czycholl, and F. Jahnke
- Frühjahrstagung der Deutschen Physikalischen Gesellschaft, Berlin (Germany), 2005
  "Polariton Propagation in Semiconductor Heterostructures", S. Schumacher, G. Czycholl, F. Jahnke, I. Kudyk, I. Rückmann, and J. Gutowski
- Frühjahrstagung der Deutschen Physikalischen Gesellschaft, Berlin (Germany), 2005
  "Nonlinear transmission and pump-and-probe experiments on ZnSe/ZnSSe heterostructures", I. Kudyk, I. Rückmann, J. Gutowski, S. Schumacher, G. Czycholl, and F. Jahnke

Danksagung

In erster Linie danke ich meinem Doktorvater, Herrn Prof. Dr. Gerd Czycholl, für die gute Betreuung und die Unterstützung bei meiner interessanten Arbeit.

Weiter danke ich Herrn Prof. Dr. Frank Jahnke für die Anfertigung des zweiten Gutachtens, sowie für die produktive und angenehme Zusammenarbeit während der letzten Jahre.

Für viele fruchtbare Diskussionen und die erfolgreiche gemeinsame Arbeit möchte ich mich bei Michael Buck bedanken.

Stefan Schulz danke ich für die angenehme Zeit und freundschaftliche Zusammenarbeit in unserem gemeinsamen Büro und für das ein oder andere gesellige Zusammensein nach getaner Arbeit. Außerdem danke ich ihm für das gründliche, und wahrscheinlich sehr mühsame Korrekturlesen der ersten Version meines Manuskriptes.

Norman Baer möchte ich besonders für die schönen gemeinsamen Tagungs- und Urlaubsreisen danken, aber natürlich auch für die freundschaftliche Zusammenarbeit, und dafür, dass er sich die Arbeit gemacht hat Teile meines Manuskriptes zu lesen und kritisch zu kommentieren.

Allen anderen Mitgliedern der Arbeitsgruppen *Theoretische Festkörperphysik* und *Theoretische Halbleiterphysik* danke ich für die gute Arbeitsatmosphäre und die ständige Diskussions- und Hilfsbereitschaft im dritten Stock Ost des NW1.

Bei den Mitarbeitern der Arbeitsgruppe von Herrn Prof. Dr. Jürgen Gutowski bedanke ich mich für die Unterstützung. Der Vergleich mit experimentellen Ergebnissen hat diese Arbeit erst richtig abgerundet. Besonders danke ich hier Iryna Kudyk, die für die Messungen immer wieder im Labor stehen musste. Tobias Voss danke ich für die ein oder andere fruchtbare Diskussion.

Arne Gust, aus der Arbeitsgruppe von Herrn Prof. Dr. Detlef Hommel, danke ich dafür, dass er mit viel Engagement und Sorgfalt die Proben für die Experimente hergestellt hat, sowie für die gemeinsame Studienzeit. Gabriela Alexe danke ich für ihre Mühe bei der Charakterisierung der Proben.

Meiner Freundin Katrin danke ich für ihre Geduld in der Schlussphase dieser Arbeit, aber besonders für die vielen schönen gemeinsamen Jahre.